

G PROTEIN-COUPLED PEPTIDE RECEPTORS
AS MOLECULAR TARGETS
IN NEUROENDOCRINE TUMORS

Inaugural-Dissertation
to obtain the academic degree
Doctor rerum naturalium (Dr. rer. nat.)

submitted to the Department of Biology, Chemistry and Pharmacy
of Freie Universität Berlin

by
Samantha Exner
from Dresden

Berlin, 2018

♪ ...all you got to do is do it... ♪

Wandering Eye, Fat Freddy's Drop

Die vorliegende Arbeit wurde von Juli 2013 bis Dezember 2017 unter der Leitung von Dr. Carsten Grötzinger an der Charité – Universitätsmedizin Berlin, Campus Virchow-Klinikum, in der Medizinischen Klinik mit Schwerpunkt Gastroenterologie und Hepatologie, angefertigt.

1. Gutachter: Dr. Carsten Grötzinger
2. Gutachter: Prof. Dr. Rupert Mutzel

Disputation am 29.05.2018

TABLE OF CONTENTS

ABSTRACT	XI
ZUSAMMENFASSUNG	XIII
DANKSAGUNG	XV
LIST OF FIGURES	XVII
LIST OF TABLES	XIX
LIST OF ABBREVIATIONS	XX
1 INTRODUCTION	1
1.1 The concept of personalized oncology	1
1.2 G protein-coupled receptors as drug targets	2
1.2.1 Signal transduction of GPCRs	3
1.2.2 Somatostatin and its receptors	5
1.2.3 Angiotensin II and its receptors	6
1.3 Peptide-based probes for GPCR targeting	8
1.4 Neuroendocrine tumors	8
1.4.1 SSTR-based diagnostic imaging	9
1.4.2 Peptide receptor radionuclide therapy (PRRT)	11
1.4.3 Targeted mTOR inhibition	12
1.4.4 Alternative GPCR targets in NETs	13
1.5 Preclinical tumor models	14
2 AIMS OF THESIS	15
3 MATERIAL	16
3.1 Instruments	16
3.2 Chemicals	17
3.2.1 Cell culture reagents	17
3.2.2 Buffers and solutions	17
3.2.3 Peptides and small molecules	19
3.2.4 Radionuclides	19
3.3 Oligonucleotides	20
3.4 Antibodies	21
3.5 Kits and ready-to-use reagents	21
3.6 Organisms	22
3.6.1 Eukaryotic cell lines	22
3.6.2 Stable eukaryotic cell lines	23
3.6.3 Mouse strains	23
3.7 Software	23
4 METHODS	24

4.1	Cell culture.....	24
4.1.1	Cultivation	24
4.1.2	Cryopreservation.....	24
4.1.3	Stable transfection	24
4.2	Molecular Biology.....	25
4.2.1	RNA/DNA isolation	25
4.2.2	Polymerase chain reaction (PCR)	25
4.2.3	Agarose gel electrophoresis	25
4.2.4	Reverse transcription quantitative real-time PCR (RT-qPCR)	26
4.3	Protein biochemistry	27
4.3.1	Cell lysis	27
4.3.2	Protein determination.....	27
4.3.3	SDS-PAGE.....	27
4.3.4	Western blotting	28
4.3.5	Immunofluorescence	28
4.3.6	ELISA	28
4.4	Cellular assays.....	29
4.4.1	Drug and radiation treatment.....	29
4.4.2	Calcium mobilisation	29
4.4.3	Cell cycle analysis	30
4.4.4	Cell viability - metabolic activity and cell number	31
4.4.5	Clonogenic survival.....	31
4.4.6	Intracellular signaling array	31
4.5	Radioactive studies.....	32
4.5.1	Iodination of peptides	32
4.5.2	Radiosynthesis of ¹⁷⁷ Lu-coupled peptides	32
4.5.3	Radioactive binding and internalization studies	33
4.5.4	In vitro receptor autoradiography	34
4.6	In vivo experiments	35
4.6.1	Cell line xenografts	35
4.6.2	Establishment of patient-derived xenografts (PDX)	35
4.6.3	Near-infrared fluorescent optical imaging.....	36
4.7	Curve fitting and statistics	36
5	RESULTS	37
5.1	Identification and validation of AGTR1 as a novel target in NETs.....	37
5.1.1	Gene expression analysis of AGTR1 in NET tissue and cell lines.....	37
5.1.2	Establishment of in vitro receptor autoradiography	39
5.1.3	Protein expression analysis of AGTR1 in NET tissue	43
5.1.4	Near-infrared in vivo imaging with ITCC-labeled AGTR1 ligands.....	48
5.1.5	Biological effects of angiotensin II on AGTR1 expressing NET cell lines	51
5.1.6	Generation of patient-derived xenografts as preclinical models	54
5.2	The combinatorial potential of mTOR inhibitors and PRRT in NET cells.....	59
5.2.1	Effect of mTOR inhibitors on NET cells.....	59
5.2.2	Radiation-induced effects on NET cells.....	63

5.2.3	Additive effect of temsirolimus and irradiation on NET cells.....	65
5.2.4	SSTR expression of NET cells	70
5.2.5	Combination of mTOR inhibitors with PRRT	74
6	DISCUSSION	77
6.1	Expression analyses of AGTR1 in NETs	77
6.2	Suitability of AGTR1 as a molecular target for optical imaging.....	79
6.3	Effects of angiotensin II on tumor signaling and biology	81
6.4	Patient-derived NET xenografts for future studies.....	83
6.5	Sensitivity of NET cell lines to mTOR inhibitors.....	84
6.6	Evaluation of radiation-induced effects in NET cell lines	86
6.7	Combinatorial potential of mTOR inhibitors with radiation.....	87
6.8	Combinatorial potential of mTOR inhibitors with PRRT	88
	BIBLIOGRAPHY	91
	PUBLICATIONS AND PRESENTATIONS.....	110
	SELBSTÄNDIGKEITSERKLÄRUNG	113
	SUPPLEMENTARY	115

ABSTRACT

Effective cancer therapy relies on early diagnosis and treatment decisions based on patient-specific tumor profile and biology. Peptide receptor targeting proved to be a pivotal tool for imaging, staging and therapy of neuroendocrine tumors, which frequently express G protein-coupled somatostatin receptors (SSTRs) on their cell surface. Optimized somatostatin analogs such as octreotide are successfully utilized for the clinical management of these tumors.

However, it is estimated that around 30 % of patients do not profit from SSTR-based approaches, making the characterization of alternative cell surface targets necessary. Previous cell-based screening assays conducted in our group had shown a clear response of human NET cell lines to angiotensin II. In the presented study, expression analyses of the cognate angiotensin II receptor type 1 (AGTR1) revealed an upregulation of both mRNA and protein levels in patient NET tissues compared to healthy controls. To assess the applicability of AGTR1 for *in vivo* imaging, the receptor ligands saralasin and valsartan were coupled to the near-infrared dye ITCC and tested for their biodistribution in a mouse model bearing receptor-positive and -negative xenograft tumors. Both probes showed promising results and represent a good basis for further development to optimize their physicochemical profile as well as tumor accumulation. Functional assays evaluating signaling cascades and processes such as proliferation and secretion upon receptor stimulation complemented this project.

Diagnostic imaging selects eligible patients with SSTR-positive tumors for following peptide receptor radionuclide therapy (PRRT). For this purpose, somatostatin analogs are coupled to therapeutic radionuclides like lutetium-177, which are specifically bound and uptaken by NETs after injection. Although PRRT can deliver radiation doses of up to 250 Gy to the tumors, complete remission is very rare. The additional use of established NET therapies such as targeted mTOR inhibition can be a promising approach. Therefore, the second part of this study assessed a potential radiosensitizing effect of temsirolimus and everolimus in five NET cell line models. Treatment with these mTOR inhibitors alone resulted in antiproliferative effects, modulation of downstream signaling and G1 cell cycle arrest. On the other hand, undirected external beam irradiation induced a G2/M arrest in all tested cell lines. In combination, mTOR inhibitors abrogated the radiation-induced G2/M arrest with further reduction of cell viability and survival. As the investigated NET cell lines revealed a lack of SSTR2 expression, two receptor-positive cell lines were established for further SSTR2-targeted PRRT studies. Although the combination of mTOR inhibitors with the agonistic ¹⁷⁷Lu-DOTATOC did not reveal any beneficial effect, the superiority of the recently developed antagonist ¹⁷⁷Lu-DOTA-JR11 was demonstrated.

This work contributes to the understanding of NET-specific target expression and treatment response. The obtained insights might be further refined by preclinical studies to pave the way for a significant increase of the diagnostic and therapeutic efficacy.

ZUSAMMENFASSUNG

Entscheidend für eine effektive Krebstherapie sind die rechtzeitige Diagnose und eine Behandlungsstrategie, die auf den jeweiligen Patienten und sein Tumorprofil abgestimmt wird. Die zielgerichtete Erkennung von Peptidrezeptoren spielt für die Bildgebung und Therapie von neuroendokrinen Tumoren (NETs) eine zentrale Rolle. NETs exprimieren auf ihrer Zelloberfläche häufig G-Protein-gekoppelte Somatostatin-Rezeptoren (SSTRs), die den klinischen Einsatz optimierter Somatostatin-Analoga wie Octreotid ermöglichen.

Allerdings profitieren Schätzungen zufolge etwa 30 % der Patienten nicht von SSTR-basierten Ansätzen. Dies macht die Charakterisierung alternativer Oberflächenrezeptoren notwendig. In Screening-Experimenten mit NET-Zelllinien ergaben sich erste Hinweise auf eine potentielle Rolle von Angiotensin II und dem Angiotensin-II-Rezeptor Typ 1 (AGTR1). Die vorgelegte Arbeit bestätigte dies durch weitere Analysen an humanen NET-Proben. Im Vergleich zu gesunden Kontrollen wiesen NET-Gewebe eine erhöhte Gen- sowie Proteinexpression des AGTR1 auf. Des Weiteren wurde die Eignung des Rezeptors für die optische Bildgebung überprüft. Dazu wurden die AGTR1-Liganden Saralasin und Valsartan an den Nahinfrarotfarbstoff ITCC gekoppelt und in einem NET-Mausmodell auf ihre Bioverteilung untersucht. Beide Konjugate zeigten vielversprechende Ergebnisse und bilden eine gute Basis für eine weitere Optimierung. Die Analyse von Liganden-induzierten Signalwegen sowie Proliferation und Sekretion rundeten dieses Projekt ab.

Die diagnostische Bildgebung ermöglicht die Identifikation von Patienten mit SSTR-positiven Tumoren, die für eine folgende Peptidrezeptor-Radiotherapie (PRRT) in Frage kommen. Zu diesem Zweck werden Somatostatin-Analoga an ein therapeutisches Radionuklid wie Lutetium-177 gekoppelt. Obwohl dadurch bis zu 250 Gy selektiv den Tumor erreichen ist eine vollständige Remission selten. Die Kombination mit etablierten NET-Therapien wie mTOR-Inhibitoren ist daher ein vielversprechender Ansatz. Im zweiten Teil dieser Arbeit wurde daher an fünf NET-Zelllinien unterschiedlichen Ursprungs untersucht, inwieweit die mTOR-Inhibitoren Temsirolimus und Everolimus radiosensibilisierend wirken. Beide Substanzen wirkten antiproliferativ und führten zur Modulation beteiligter Signalwege sowie zum G1-Zellzyklusarrest. Im Gegensatz dazu hatte die ungerichtete externe Bestrahlung in allen Zelllinien einen G2/M-Arrest zur Folge. In der Kombination verringerten die mTOR-Inhibitoren den strahlungsinduzierten G2/M-Arrest und reduzierten Zellviabilität und -überleben stärker als mit der jeweiligen Monotherapie. Da in den verwendeten NET-Zelllinien keine SSTR2-Expression nachgewiesen werden konnte, wurden für die folgenden Versuche mit zielgerichteter Radiotherapie zwei SSTR2-positive NET-Zelllinien etabliert. Die kombinierte Behandlung mit mTOR-Inhibitoren und dem agonistischen Radiopeptid ¹⁷⁷Lu-DOTATOC ließen im verwendeten Modell zwar keinen Vorteil erkennen, allerdings konnte die Überlegenheit des kürzlich entwickelten Antagonisten ¹⁷⁷Lu-DOTA-JR11 demonstriert werden.

Die vorliegende Arbeit leistet somit einen Beitrag zum besseren Verständnis der NET-spezifischen Rezeptorexpression und zur Evaluierung möglicher neuer Therapieansätze. Die gewonnenen Ergebnisse erfordern eine weitere Validierung durch präklinische Studien, um die Effizienz von Diagnose und Therapie in Zukunft zu verbessern.

DANKSAGUNG

Über die letzten Jahre durfte ich viele Menschen kennenlernen, die mich auf meinem Weg ein kleines oder großes Stück begleitet haben, die mir hilfsbereit zur Seite standen, die mich und meine Arbeitsweise geprägt haben.

Ein herzlicher Dank geht zunächst an Professor Bertram Wiedenmann, in dessen Klinik und Forschungsabteilung ich diese Arbeit durchführen konnte und an Professor Rupert Mutzel für die Übernahme des Zweitgutachtens. Mein Dank gilt auch der Sonnenfeldstiftung, die mir durch ein Abschlussstipendium die Fertigstellung dieser Promotion ermöglichte.

Besonders möchte ich mich bei Dr. Carsten Grötzinger bedanken. Für die vielfältige Methodik, die ich im Labor erlernen und selbständig anwenden konnte. Für die Umsetzung eigener Ideen, die vielleicht auch mal auf Abwege führten. Für die Teilnahme an so zahlreichen Kongressen, die mir wertvollen wissenschaftlichen Austausch ermöglichten. Für die stetige Forderung und vor allem Förderung meiner Kenntnisse und Fähigkeiten.

Danke an Sarah und Jan, die mir Kollegen und Freunde waren und von denen ich unheimlich viel gelernt habe. An Yvonne, die mit ihren Kontakten und Tipps so einiges möglich gemacht hat. An Sandy, Lars und Asja, für die angenehme Zeit im Labor. Und an Teresa, mit der ich zum Ende hin eine ganz besondere Gemeinsamkeit teilen konnte.

Vielen Dank an alle Freunde des radioaktiven Arbeitens: Eva, Jakob, Sonal, Nicola. Herzlichen Dank an Professor Winfried Brenner und Dr. Vikas Prasad für die gute Kooperation und die Möglichkeit am BERIC zu experimentieren. Für die Überwindung vieler strahlungsbedingter Hürden möchte ich Rita Geppert, Kerstin Winkler, Dr. Hugo Sanchez-Ruderisch und Dr. Günther Niggemann danken.

Nicht zu vergessen die vielen Tierpfleger und Mitarbeiter der FEM, besonders aber Andrea und Erika, die sich ganz besonders um meine felligen Patienten kümmerten.

Für die Synthese und Bereitstellung des Farbstoffkonjugates Valsartan-ITCC möchte ich mich herzlich bei Dr. Kai Licha und Isabelle Heing-Becker bedanken.

Vielen lieben Dank auch an „meine“ Studenten Timo, Duygu und Gerard, denen ich etwas von meinem Wissen mitgeben konnte und die mich wiederum in meiner Arbeit unterstützt und auf neue Ideen gebracht haben.

Vor allem aber möchte ich mich bei meinen Freunden und meiner Familie bedanken. Ihr habt meine Doktorandenzeit außerhalb des Labors zu einer ganz besonderen gemacht. Die vielen gemeinsamen Gespräche, Momente und Erlebnisse gaben mir viel Energie und Motivation.

Ich weiß nicht wie ich meinen Dank an Enrico in Worte fassen kann. Auf dieser großen Reise warst und bist du mir der beste Gefährte. Ohne dich wäre ich wohl irgendwo auf dem Weg stecken geblieben, aber du hast mich immer weiter mitgenommen und ich bin gespannt wohin es als nächstes gehen wird.

LIST OF FIGURES

Figure 1 The hallmarks of cancer.....	1
Figure 2 GPCR drug targeting.	3
Figure 3 G protein-dependent signaling in GPCRs.	4
Figure 4 Arrestin-dependent internalization and signaling in GPCRs.	4
Figure 5 Structure of somatostatin and its analogs.	6
Figure 6 Components and inhibitors of the renin-angiotensin system.....	7
Figure 7 Different modalities of neuroendocrine tumor imaging.....	10
Figure 8 mTOR signaling and inhibition in cancer.	13
Figure 9 Cell cycle analysis by flow cytometry.	30
Figure 10 Iodination of tyrosine residues by chloramine T.....	32
Figure 11 Generation of patient-derived xenografts from primary patient tumor material.	35
Figure 12 AGTR1 gene expression is increased in NET tissues.....	38
Figure 13 Comparison of AGTR1 and SSTR2 gene expression for selected samples.....	38
Figure 14 AGTR1 gene expression is increased in two NET cell lines.....	39
Figure 15 Radiolabeled angiotensin II binds to AGTR1-positive NET cell lines BON and H727.....	40
Figure 16 Saturation binding assay with BON and H727 cells.....	41
Figure 17 BON and H727 cells specifically bind AGTR1, but not AGTR2 antagonists.	41
Figure 18 BON and H727 xenograft tumors specifically express AGTR1.....	42
Figure 19 In vitro receptor autoradiography of pancreatic NET tissues.	44
Figure 20 In vitro receptor autoradiography of ileal NET tissues.....	45
Figure 21 In vitro receptor autoradiography of pancreatic and ileal control tissues.....	46
Figure 22 Quantification of autoradiography by two methods.	47
Figure 23 Correlation of autoradiography with gene expression data.	47
Figure 24 ITCC-labeled AGTR1 ligands bind with lower affinity.....	48
Figure 25 In vivo NIRF imaging with AGTR1-targeting ITCC-ligands.....	50
Figure 26 Angiotensin II induces calcium signaling in BON and H727 cells.....	51
Figure 27 Intracellular signaling array after 5 min of angiotensin II stimulation.	52
Figure 28 Angiotensin II stimulates chromogranin A secretion in BON cells.	53
Figure 29 Metabolic activity is not altered by angiotensin II, valsartan and azilsartan.	54
Figure 30 Patient-derived NET xenografts maintain human origin.....	56
Figure 31 Two PDX models maintain AGTR1 gene expression levels over several passages.....	56

XVIII | List of Figures

Figure 32 In vitro receptor autoradiography of AGTR1-positive PDX tissues.	57
Figure 33 Treatment with mTOR inhibitors results in a biphasic inhibition of NET cell viability. .	59
Figure 34 Clonogenic survival of NET cell lines is affected by mTOR inhibitors.	61
Figure 35 Increased accumulation of cells in G1 phase after mTOR inhibitor treatment.	61
Figure 36 Effect of everolimus on intracellular signaling molecules.	63
Figure 37 Irradiation leads to reduced cell viability and G2/M accumulation of NET cells.	64
Figure 38 Additive effect of temsirolimus and irradiation on NET cell numbers.	65
Figure 39 Detailed analysis of cell numbers for combined treatment of temsirolimus and 4 Gy. 66	
Figure 40 Additive effect of temsirolimus and irradiation on NET cell survival.	67
Figure 41 Detailed analysis of cell survival for combined treatment of temsirolimus and 4 Gy... 67	
Figure 42 Temsirolimus pretreatment abrogates radiation-induced G2/M cell accumulation.	68
Figure 43 Gene expression analysis of SSTR subtypes in NET cell lines.	70
Figure 44 Binding analysis confirms insufficient SSTR2 expression of NET cell lines.	71
Figure 45 Validation of SSTR2 reintroduction in two NET cell lines.	72
Figure 46 SSTR2-expression and internalization in SSTR2-transfected NET cell lines.	72
Figure 47 SSTR2-transfection did not alter sensitivity for mTOR inhibitor treatment.	73
Figure 48 DOTA-conjugated somatostatin analogs bind to BON-SSTR2.	74
Figure 49 Cell cycle is not affected by combination of mTOR inhibitors and ¹⁷⁷ Lu-DOTATOC.	75
Figure 50 Cell survival is not affected by combination of mTOR inhibitors and ¹⁷⁷ Lu-DOTATOC.. 75	
Figure 51 Binding and internalization of ¹⁷⁷ Lu-DOTATOC and ¹⁷⁷ Lu-DOTA-JR11.	76
Figure 52 Cell cycle distribution after treatment with ¹⁷⁷ Lu-DOTATOC and ¹⁷⁷ Lu-DOTA-JR11.	76
Figure 53 SPECT/CT imaging with ¹⁷⁷ Lu-DOTATOC in different mouse models.	89
Figure S1 Structure of saralasin-ITCC.	115
Figure S2 Structure of valsartan-ITCC.	115
Figure S3 Intracellular signaling array after 10 min of angiotensin II stimulation.	118
Figure S4 Intracellular signaling array after 15 min of angiotensin II stimulation.	118
Figure S5 Intracellular signaling array after 30 min of angiotensin II stimulation.	119
Figure S6 Chromogranin A secretion of NET cell lines.	119
Figure S7 Accumulation of cells in G1 after mTOR inhibitor treatment after 48, 72 and 96 h. ..	120
Figure S8 Irradiation leads to G2/M accumulation of NET cells after 48, 72 and 96 h.	120
Figure S9 Cell cycle distribution at 48, 72 and 96 h after combined treatment.	121
Figure S10 Chromatographic purification of radioiodinated somatostatin-14.	121

LIST OF TABLES

Table 1 Descriptive values of RT-qPCR data.....	37
Table 2 Binding parameters for BON and H727 cells.....	40
Table 3 Calculated K_i values for ITCC-labeled ligands.....	49
Table 4 Clinical characteristics of the tissues injected for PDX generation.....	55
Table 5 Summary of IC_{50} values for mTOR inhibitors.....	60
Table 6 Percentages of cells in G1 phase after mTOR inhibitor treatment.....	62
Table 7 Percentages of cells in G2/M cell cycle after irradiation.....	64
Table 8 Percentages of cells in G1 and G2/M cell cycle 24 h after irradiation.....	68
Table 9 Median values of SSTR gene expression analysis.....	70
Table S1 Amino acid code.....	116
Table S2 Clinical characteristics of the tissues analyzed by in vitro receptor autoradiography.....	117

LIST OF ABBREVIATIONS

^{125}I	iodine-125
^{137}Cs	caesium-137
^{177}Lu	lutetium-177
4EBP1	eukaryotic translation initiation factor 4E-binding protein 1
^{68}Ga	gallium-68
7TM	seven-transmembrane
^{90}Y	yttrium-90
ACE	angiotensin converting enzyme
AGTR1	angiotensin II receptor type 1
AGTR2	angiotensin II receptor type 2
AHX	aminohexanoic acid
ALG9	alpha-1,2-mannosyltransferase
AP2	adaptor protein 2
ARB	angiotensin II receptor type 1 blocker
ATII	angiotensin II
BCA	bicinchoninic acid
B_{max}	maximum number of binding sites
BSA	bovine serum albumin
cAMP	cyclic adenosine monophosphate
CCK	cholecystokinin
cDNA	complementary DNA
cpm	counts per minute
CT	computer tomography
CUP	cancer of unknown primary
DAG	diacylglycerol
DMSO	dimethyl sulfoxid
DNA	deoxyribonucleic acid
dNTP	deoxynucleoside triphosphate
DOTA	1,4,7,10-tetraazacyclododecane-1,4,7,10-tetraacetic acid
DTPA	diethylenetriaminepentaacetic acid
EDTA	ethylenediaminetetraacetic acid

EGFR	epidermal growth factor receptor
eIF4E	eukaryotic translation initiation factor 4E
ELISA	enzyme-linked immunosorbent assay
ERK 1/2	extracellular signal-regulated kinase 1/2
FCS	fetal calf serum
FDA	Food and Drug Administration
FGFR4	fibroblast growth factor receptor 4
FKBP12	FK506 binding protein
GAP	GTPase-activating proteins
GAPDH	glyceraldehyde-3-phosphate dehydrogenase
GDP	guanosine diphosphate
GEF	guanine nucleotide exchange factor
GEP-NET	gastroenteropancreatic neuroendocrine tumor
GIP	gastric inhibitory polypeptide, glucose-dependent insulinotropic polypeptide
GLP-1	glucagon-like peptide-1
GPCR	G protein-coupled receptor
GRK	G protein-coupled receptor kinase
GTP	guanosine triphosphate
HPRT1	hypoxanthine phosphoribosyltransferase 1
HRP	horseradish peroxidase
IDCC	indodicarbocyanine
IGF-1	insulin-like growth factor
iNET	ileal neuroendocrine tumor
IP3	inositol 1,4,5-triphosphate
IRS	insulin receptor substrate
ITCC	indotricarbocyanine
JAK/STAT	janus kinase/signal transducer and activator of transcription
JNK	c-Jun N-terminal kinase
K_d	dissociation constant
K_i	inhibitory constant
MAPK	mitogen-activated protein kinase
MRI	magnetic resonance imaging
mTOR	mammalian target of rapamycin
mTORC1	mammalian target of rapamycin complex 1
mTORC2	mammalian target of rapamycin complex 2

XXII | List of Abbreviations

NET	neuroendocrine tumor
NIRF	near-infrared fluorescence/fluorophore
NK	natural killer
NMRI	Naval Medical Research Institute
NOD	non-obese diabetic
NSG	nod scid gamma
PARP	poly ADP ribose polymerase
PCR	polymerase chain reaction
PDX	patient-derived xenograft
PEG	polyethylene glycol
PET	positron emission tomography
PI	propidium iodide
PI3K	phosphatidylinositol-4,5-biphosphate 3-kinase
PIP2	phosphatidylinositol 4,5-biphosphate
PKC	phosphokinase C
PLC	phospholipase C
PMSF	phenylmethylsulfonyl fluoride
pNET	pancreatic neuroendocrine tumor
PRRT	peptide receptor radionuclide therapy
PTEN	phosphatase and tensin homolog
PTP	phosphotyrosine phosphatase
RAS	renin angiotensin system
RIN	RNA integrity number
RNA	ribonucleic acid
RTK	receptor tyrosine kinase
RT-qPCR	reverse transcription quantitative real-time PCR
S6K1	ribosomal protein S6 kinase beta-1, also known as p70S6K
SAR	structure activity relationship
Scid	severe combined immunodeficiency
SDS	sodium dodecyl sulfate
SNARE	soluble N-ethylmaleimide-sensitive factor attachment receptor
SNP	single-nucleotide polymorphism
SPECT	single photon emission computed tomography
SRIF	somatotropin release-inhibiting factor
SSA	somatostatin analog

SST	somatostatin
SSTR	somatostatin receptor
STR	short tandem repeats
TRF	time-resolved fluorescence
TRP	transient receptor potential
TTDS	trioxatridecansuccinamic acid
UBC	ubiquitin C
VIP	vasoactive intestinal peptide
w	with
w/o	without
w/v	weight per volume

1 INTRODUCTION

1.1 The concept of personalized oncology

For a long time, cancer was perceived as one disease, and researchers were hoping for a universal therapy. The increasing knowledge of cancer development and biology revealed its heterogeneous and very complex nature, based on successively gained genetic alterations. The identification of underlying mutations in oncogenes, tumor-suppressor genes and stability genes defined cancer as a genetic disorder [1]. Today, cancer describes a whole class of diseases that share certain characteristics while keeping their own individual and unique features. In 2000, Hanahan and Weinberg postulated the hallmarks of cancer [2]. They comprise six traits that are acquired by normal cells as they progress to neoplasia and malignancy: sustaining proliferative signaling, evading growth suppressors, enabling replicative immortality, activating invasion and metastasis, inducing angiogenesis as well as resisting cell death. The original concept was complemented in 2011 by four additional capabilities (avoiding immune destruction, tumor-promoting inflammation, genome instability and mutation, deregulating cellular energetics) that further contribute to cancer cell transformation (Figure 1) [3].

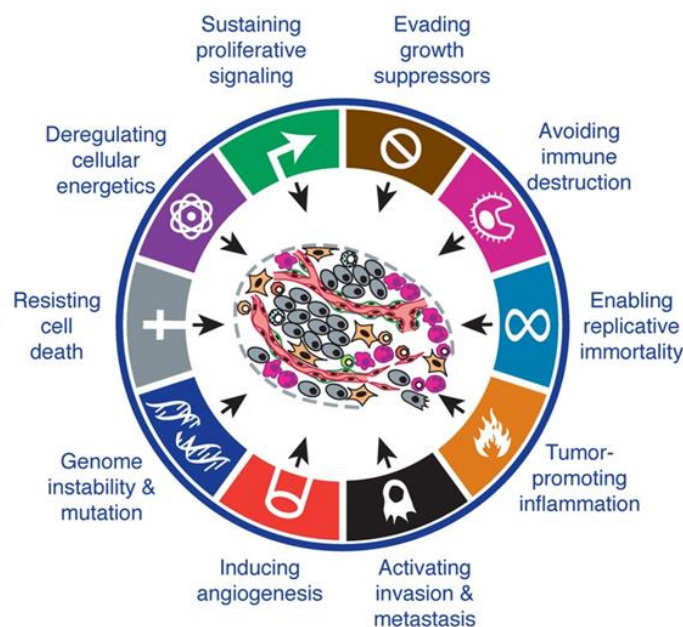


Figure 1 | The hallmarks of cancer. Hanahan and Weinberg introduced their concept of common cancer traits in 2000 and updated it to the depicted version in 2011. It combines ten capabilities that cells sequentially acquire during their transformation to cancer. Adapted by permission from Hanahan and Weinberg [3].

2 | Introduction

The specific targeting of one or more hallmarks by interference with underlying molecular changes has become a major strategy of cancer therapy. The idea of targeted drugs has evolved from Paul Ehrlich over 100 years ago. He introduced the concept of magic bullets, which exclusively attack target positive cells or pathogens with no effect on healthy tissue [4]. Since then, new technologies led to the rapid discovery of a constantly growing number of molecular targets for cancer specific drug development [5]. The molecular and genetic profiling of tumor biopsies together with functional ex vivo drug screenings further allows the design and translation of patient-tailored therapies. In that way, patients profit from precise and personalized medicine by turning general therapy approaches into individualized treatment strategies [6], [7].

Apart from the inter-tumoral heterogeneity between patients, every tumor itself demonstrates intra-tumoral heterogeneity, caused by the spatial and temporal transformation of cancer cells. This clonal evolution, first described in 1976 by Peter Nowell [8], is not only driven by intrinsic factors as genetic predispositions, the immune system or the tumor microenvironment. Targeted agents impose selective pressure on distinct molecules or pathways. They might enrich for mutations in single cells that circumvent inhibition and drug sensitivity, in that way leading to the emergence of resistant subclones. Drug resistance and clinical relapse require further refinement of existing therapies and rationally designed multidimensional treatment regimens. The combination of drugs affecting several targets or pathways, selected on the basis of the individual cancer profiles might permit more effective and stable responses [8]–[13].

1.2 G protein-coupled receptors as drug targets

G protein-coupled receptors (GPCRs) represent the largest family of cell surface receptors, with more than 800 identified members so far. On the basis of their sequence and structure human GPCRs are divided into five major classes: rhodopsin (A), secretin (B), glutamate (C), adhesion and Frizzled/Taste2 [14].

Although receptor sequences are highly variable, they share a characteristic structure of seven transmembrane (7TM) α -helices linked by three loops on both the extracellular N-terminal and intracellular C-terminal side. As integral membrane proteins, GPCRs respond to a great variety of extracellular signals including peptides, proteins, amines, lipids, nucleotides as well as sensory stimuli, and transduce those into intracellular reaction patterns [14]–[16]. They are involved in the regulation of pivotal processes such as neurotransmission, hormone and enzyme secretion, immunity, sensory perception or cell metabolism, differentiation and growth [16], [17]. Consequently, aberrant GPCR expression or dysregulated signaling pathways cause or promote many human diseases, including cancer [17], [18].

Due to their easy accessibility at the cell surface and their functional role in pathophysiological processes, GPCRs represent attractive drug targets for therapeutic intervention. Recent analyses from 2017 identified almost 500 drugs targeting GPCRs, which account for around one third of all FDA-approved drugs (Figure 2) [19], [20]. Since 2000, when bovine rhodopsin was crystallized as the first GPCR, technical advances facilitated the elucidation of 44 receptor structures [19], [21]. Rational structure-based drug design and further deorphanizing of GPCRs with yet unknown ligands will further accelerate GPCR drug discovery in the future.

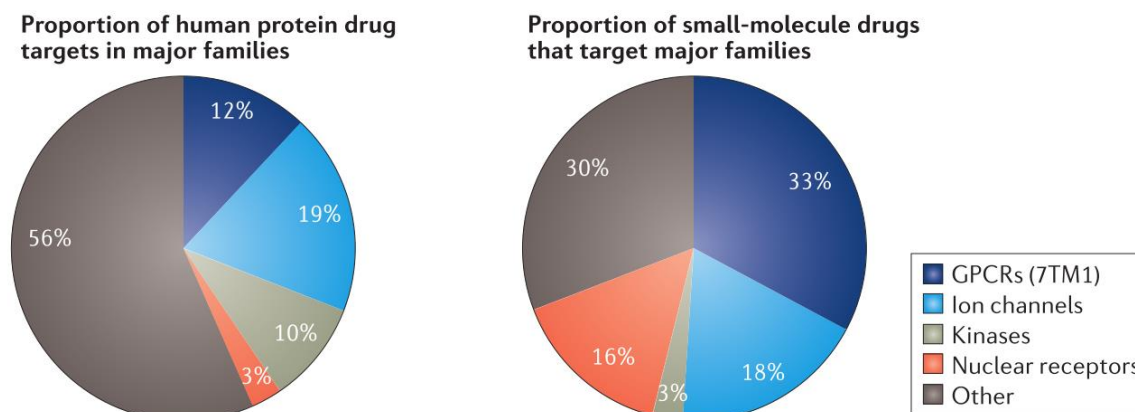


Figure 2 | GPCR drug targeting. Depicted are the fractions of human protein drug targets according to gene family (left) and the percentages of drugs targeting the single families (right). GPCRs represent 12 % of the so far identified human drug targets, while 33 % of drugs target GPCRs. Adapted by permission from Santos et al. [20].

1.2.1 Signal transduction of GPCRs

As soon as an extracellular stimulus activates its cognate GPCR, distinct signaling cascades are triggered, depending on the interacting heterotrimeric G protein. These G proteins consist of three associated subunits $G\alpha$, $G\beta$ and $G\gamma$ and are divided into four families based on the incorporated $G\alpha$ subunit (G_s , $G_{i/o}$, $G_{q/11}$, $G_{12/13}$). More than 21 $G\alpha$ as well as multiple $G\beta$ and $G\gamma$ isoforms are known, allowing a certain combinatorial diversity [22]. In the inactive heterotrimeric state, $G\alpha$ is bound to GDP. Receptor activation induces a conformational change, leading to the exchange of GDP for GTP and the subsequent dissociation of $G\alpha$ and $G\beta\gamma$ subunits. Both of them engage downstream effector molecules such as adenylyl cyclase, phospholipase C (PLC), RhoGEFs or ion channels and further lead to the production of second messengers as depicted in Figure 3. Signaling is interrupted by GTP hydrolysis, which is mediated by the intrinsic GTPase activity of the $G\alpha$ subunit itself, and results in the reassembly of the heterotrimeric G protein [22], [23]. GTPase-activating proteins (GAPs) are able to increase GTP hydrolysis by direct interference with $G\alpha$ and act as additional modifiers of GPCR signaling [24], [25].

Apart from the classical G protein-dependent signal transduction, GPCRs also couple to GPCR kinases (GRKs) and arrestins (Figure 4). So far, seven kinases and four arrestins were identified,

4 | Introduction

hence further increasing the diversity of GPCR activated signaling networks. In general, GRKs phosphorylate activated GPCRs on their intracellular C-terminus, leading to the subsequent recruitment of arrestins to the receptor. Thereby, various signaling molecules are attracted to the activated GPCR turning on additional pathways such as ERK, JNK, p38 and Akt. On the other hand, receptor bound arrestins undergo a conformational change and reveal C-terminal binding sites for clathrin and AP2, the key components of coated pits. These clathrin-coated invaginations of the plasma membrane facilitate the internalization, desensitization, degradation and recycling of activated ligand-receptor complexes [23], [26]–[28]. Early after their discovery, arrestins were thought to primarily terminate G protein-dependent signaling and desensitize GPCRs. Today, they are known to act as multifunctional adaptor proteins not only involved in GPCR regulation but also in a variety of receptor-independent signaling pathways [22], [27].

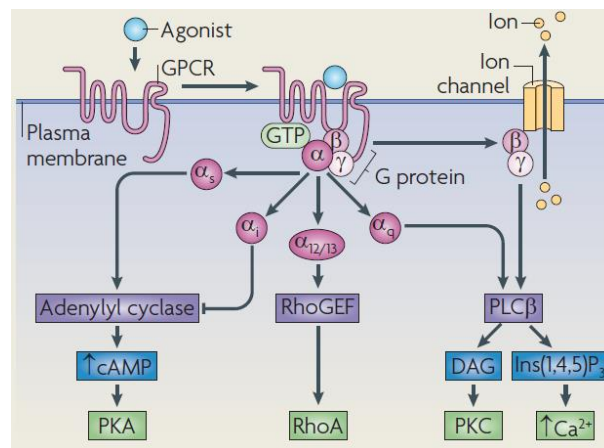


Figure 3 | G protein-dependent signaling in GPCRs. Activated receptors associate with distinct heterotrimeric G proteins and exchange bound GDP for GTP. The induced dissociation of $G\alpha$ and $G\beta\gamma$ subunits regulates distinct downstream effectors, depending on the $G\alpha$ subunit. Reprinted by permission from Ritter and Hall [23].

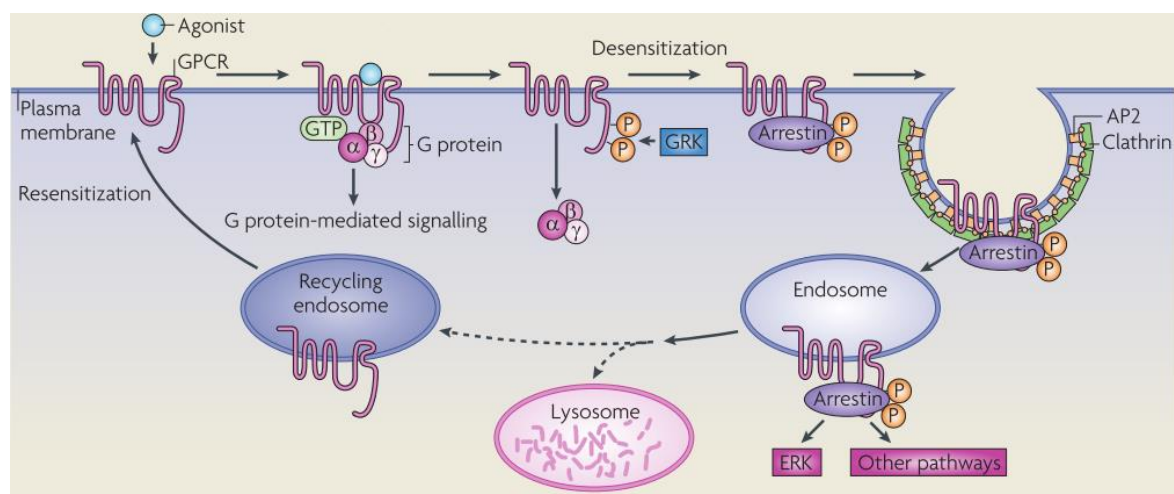


Figure 4 | Arrestin-dependent internalization and signaling in GPCRs. Receptor desensitization and internalization is mediated through arrestins, which translocate the activated GPCR to clathrin-coated pits. Receptors are internalized by endocytosis, degraded in lysosomes or recycled and relocated to the plasma membrane. Reprinted by permission from Ritter and Hall [23].

1.2.2 Somatostatin and its receptors

The versatile peptide somatostatin (SST), also known as somatotropin-release inhibiting factor (SRIF), appears in two biologically active forms: SST-14 with a length of 14 amino acids, and SST-28 with 28 amino acids [29], [30]. Both are cleaved from the precursor prosomatostatin and contain disulfide bridges, hence forming cyclic structures. Although isolated from the central nervous system for the first time, somatostatin is also produced in peripheral tissues such as the gastrointestinal tract and endocrine glands. It regulates neurotransmission and inhibits not only the secretion of various hormones and peptides, but also cell proliferation, immune cells, smooth muscle contraction and other functions [31], [32].

SST-14 and SST-28 bind with high affinity to their cognate G protein-coupled somatostatin receptors, of which five subtypes have been identified and cloned in the early 1990s (SSTR1-5) [33]. The encoding genes are located on different chromosomes, and contain no introns except for SSTR2, which is alternatively spliced into the variants SSTR2A and SSTR2B. Based on their sequence homology SSTRs are divided into the two groups SRIF1 (SSTR2, 3, 5) and SRIF2 (SSTR1, 4). Within each subgroup sequences show evolutionary conservation of up to 90 %, in comparison to 40-60 % across all subtypes [32], [34], [35].

Despite their differences, all SSTRs have been shown to couple via the G_i pathway, leading to downstream inhibition of adenylyl cyclase and decreased cAMP production. In addition, Ca^{2+} levels are lowered by inhibition of voltage-dependent Ca^{2+} channels and activation of K^+ channels by certain receptor subtypes, which further negatively affects exocytotic processes. The mentioned pathways mainly mediate antisecretory effects of SST, while modulation of different phosphotyrosine phosphatases (PTP) and MAPK induces antiproliferative mechanisms. Besides the pathways they share, subtype specific signaling and arrestin recruitment ensures ligand and cell specific receptor functions [36], [37].

Similar to somatostatin, SSTRs are detectable in many tissues throughout the body, including brain, the gastrointestinal tract and pancreas. Depending on the tissue, only one or all five subtypes may be present in a distinct expression pattern. Interestingly, SSTRs and in particular SSTR2, are expressed in a variety of human tumors, for instance in pituitary adenomas, small cell lung cancer, breast cancer or neuroendocrine tumors [38], [39].

SSTR expression in normal and tumor tissue as well as the antisecretory and antiproliferative effects of somatostatin have made this peptide-receptor pair an attractive pharmacological target. However, somatostatin exhibits a very short half-life of only 1-3 minutes, which led to the development of a variety of long-lasting stable analogs, such as octreotide and lanreotide

(Figure 5). Both analogs show subtype selective binding, with high affinity for SSTR2, lower affinity for SSTR5 and SSTR3 and no affinity for SSTR1 and SSTR4 [40], [41]. They are clinically used for medical intervention and as radiolabeled peptides for the diagnosis and therapy of receptor-positive tumors (see chapter 1.4) [42].

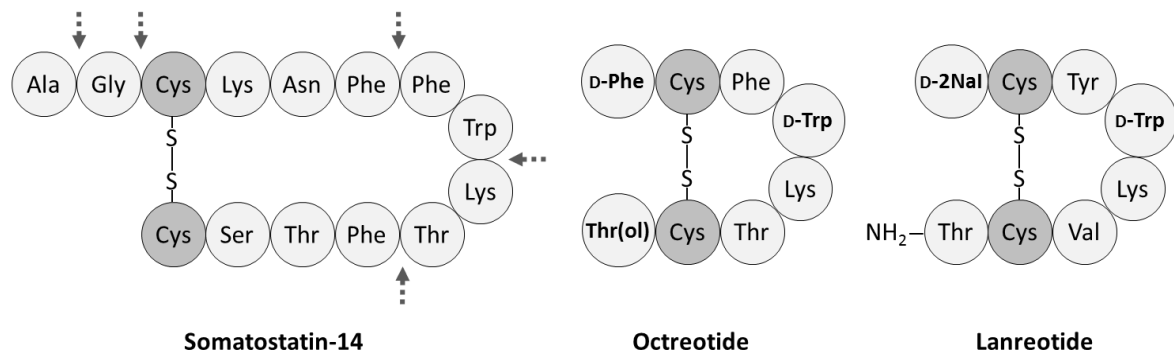


Figure 5 | Structure of somatostatin and its analogs. Depicted are the sequences of somatostatin-14 and of its optimized stable and clinically used analogs octreotide and lanreotide. Arrows indicate potential cleavage sites for proteases. The amino acid code can be found in supplementary Table S1. Adapted by permission from Froidevaux and Eberle [43].

1.2.3 Angiotensin II and its receptors

The octapeptide angiotensin II (ATII, AngII) is the major effector of the systemic renin-angiotensin system (RAS), regulating blood pressure and cardiovascular homeostasis. It is cleaved from angiotensin I (AngI) by the angiotensin converting enzyme (ACE) (Figure 6). Angiotensin I on the other hand is the cleavage product of angiotensinogen (AGT) by renin as a reaction towards low blood pressure. Angiotensin II binds to at least two receptors, the angiotensin II receptors type 1 (AGTR1, AT₁R) and type 2 (AGTR2, AT₂R), of which AGTR1 is ubiquitously expressed and mediates most functions of the peptide. Both subtypes belong to the GPCR family, but share only 34 % of their sequence [44]. The signal transduction of AGTR1 is well studied, coupling in particular to G_{q/11} and thus, leading to an increase of intracellular calcium levels. Protein kinases such as MAPK, JAK/STAT, Akt and PKC as well as small G proteins including Ras, Rho and Rac are also activated [45], [46]. Furthermore, AGTR1 has been shown to stimulate receptor tyrosine kinase (RTK) signaling through cleavage of RTK ligands presented at the cell surface. This ligand shedding, induced by metalloproteinases, results in the subsequent transactivation of RTKs as for instance EGFR [47], [48]. In contrast, AGTR2 signaling and function is still controversial. This subtype is detected in high densities in fetal tissue and is re-expressed during wound healing, hence it might play a role in development and repair. It is thought to act as a counter-regulator to AGTR1 by antagonizing some of its functions [49], [50]. The picture of RAS became more complex with the discovery of additional effectors and receptors, and with the developing concept of a local RAS mediating non-cardiovascular effects in tissues and organs [47].

Dysregulation of this balanced system was mainly implicated in hypertension and cardiovascular pathologies, which yielded in the development of some of the most prescribed drugs worldwide, ACE inhibitors and AGTR1 blockers (ARBs) (Figure 6) [51]. Moreover, receptor-selective small molecules like valsartan and azilsartan (AGTR1 antagonists), PD123319 and novokinin (AGTR2 antagonists) as well as the peptide saralasin (partial agonist of AGTR1 and AGTR2) proved to be valuable tools for scientific research.

Apart from its classical role, increasing evidence indicated that the RAS is also involved in angiogenesis, inflammation, cell proliferation, differentiation and tissue remodeling. Consequently, an inappropriate activation of ATII and other components may be relevant to carcinogenesis [47], [52]. For instance, AGTR1 was found to be overexpressed in various cancers, such as breast [53], gastric [54] and pancreatic cancer [55], [56]. Furthermore, epidemiological data and retrospective meta-analyses suggest that administration of ARBs or ACE inhibitors contributes to cancer prevention or better survival of cancer patients. However, other studies could not confirm any beneficial effect or even observed an increased risk for cancer, raising the need for randomized and controlled clinical trials to gain relevant results [47].

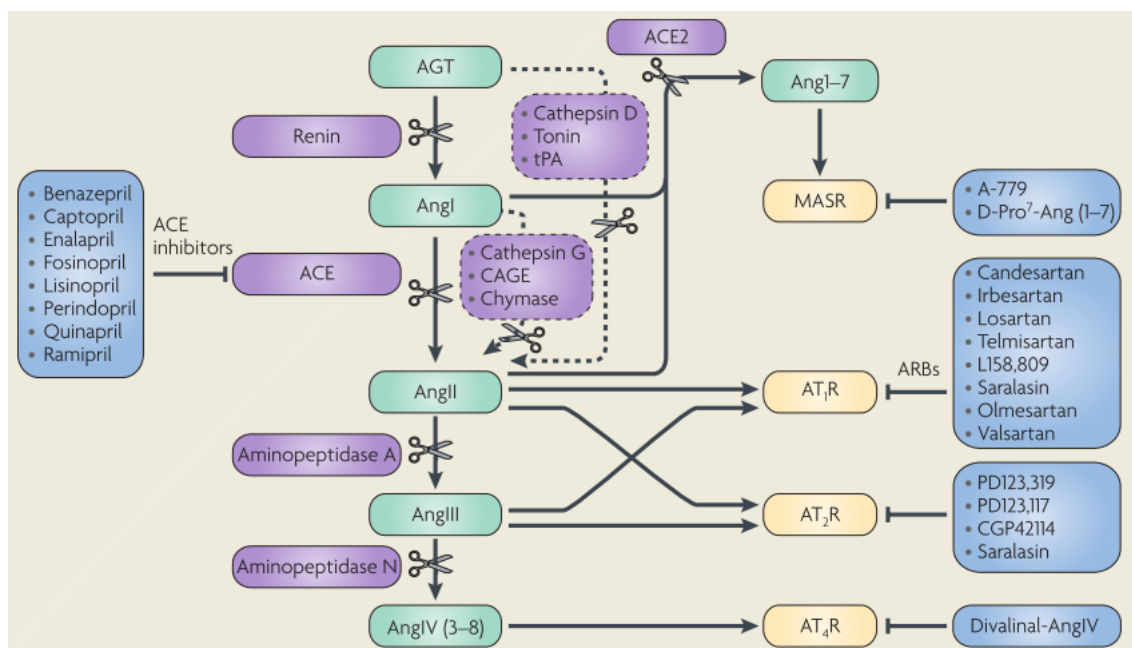


Figure 6 | Components and inhibitors of the renin-angiotensin system. Cardiovascular homeostasis is regulated by a complex network of different hormones, enzymes and receptors. With decreasing blood pressure, renin cleaves angiotensinogen (AGT). The resulting angiotensin I (AngI) is subsequently processed by the angiotensin converting enzyme (ACE) to angiotensin II (ATII or AngII). AngII primarily mediates its functions through the angiotensin II receptors subtype 1 (AGTR1 or AT₁R) and 2 (AGTR2 or AT₂R). Associated dysregulations as hypertension and heart failure can be treated by AGTR1 blockers (ARBs) and ACE inhibitors. Reprinted by permission from George et al. [47].

1.3 Peptide-based probes for GPCR targeting

Around 120 of the known GPCRs bind peptide ligands, which have many advantages and hold great potential for peptide-based clinical applications [57]. Being much smaller than antibodies, these molecules easily reach the target site due to their good tissue permeability and biodistribution after injection. Their high affinity and target specificity leads to high accumulation in the target tissue while they are rapidly removed from the circulation by renal and/or hepatobiliary excretion. Their size and physiological occurrence in the body results in a favorable safety and immunogenicity profile. If at all, side effects occur as the result of the peptide's biologically mediated functions. However, for diagnostic imaging, very low peptide doses are administered with insignificantly expected effects [58]–[60].

Natural peptides exhibit high affinity and selectivity for their cognate receptors, providing useful lead structures for further development. Technical advances enabled the easy synthesis of large peptide libraries for high-throughput screening or of individually designed peptides allowing specific applications. Modifications as methylation and acetylation as well as labels such as fluorescent dyes or radioisotope complexing chelators can be incorporated during the synthesis. Despite their manifold advantages, natural peptide ligands are highly susceptible to proteases and frequently exhibit very short half-lives in serum. Consequently, the development of metabolically stable analogs for instance by amino acid substitution or cyclization is required for peptide-based receptor targeting [61]–[63]. The most prominent example for successful lead structure optimization is somatostatin and its stable analogs (see chapter 1.2.2). Peptide drugs are developed for many different indications including metabolic diseases and cancer. They can be directly administered to block or activate endogenous receptor actions. On the other hand, peptides are used as vehicles for the delivery of fluorophores, radioisotopes or chemotoxins to receptor-positive tumors. The receptor should be present in sufficient quantity particularly in malignant cells to enable efficient diagnostic and therapeutic tumor targeting. Radioisotopes can be applied for both approaches by coupling different emitters to the same peptide (see chapter 1.4.2) [59], [63]–[65]. This emerging theranostic concept links the molecular target identification with the subsequent therapy based on the patient-specific receptor expression as it is already performed for neuroendocrine tumors [66].

1.4 Neuroendocrine tumors

Neuroendocrine tumors (NETs) represent a very heterogeneous group of neoplasms, with a moderate but steadily increasing incidence of around 5/100,000 in 2004 [67], which might reflect improved diagnostics. They can arise from different neuroendocrine cells at diverse locations throughout the body, but mostly occur in the lung and the gastroenteropancreatic system (GEP-

NETs). Patients suffer from the tumor burden and around half of them show additional symptoms caused by the abnormal hormone secretion of functional NETs [68]. Secreted biologically active substances include insulin, glucagon, gastrin, vasoactive intestinal peptide (VIP), somatostatin or serotonin and raise the need for symptomatic treatment besides tumor growth control [69], [70]. NETs grow rather slowly and might develop to an aggressive phenotype while being undetected. Clinical symptoms are often unnoticed and diagnosis is still delayed for many years after the onset of disease, until metastatic spread of the tumor. At this point, local surgery as the only curative therapy is not feasible anymore [71]. Among treatment options for advanced tumors are targeted therapies with mTOR inhibitors (everolimus), tyrosine kinase inhibitors (sunitinib) or somatostatin based analogs [72]–[74].

As mentioned in chapter 1.2.2, NETs frequently express SSTRs, in particular SSTR2. The overexpression of SSTRs in NETs has been described for the first time during the 1980s. Autoradiographic receptor detection, in-situ hybridization and immunohistochemistry could demonstrate high overexpression in tumors with little background in other tissues [75]–[78]. Since then, somatostatin analogs as octreotide and lanreotide were used as antisecretory and antiproliferative medication. Apart from direct pharmacological intervention, SSTR overexpression in NETs has also been utilized for targeted molecular imaging and peptide receptor radionuclide therapy (PRRT) [79]–[82].

1.4.1 SSTR-based diagnostic imaging

The use of radiolabeled somatostatin analogs to localize primary and metastatic neuroendocrine tumors in vivo proved to be an essential tool for non-invasive diagnostic imaging, staging, treatment selection and follow-up. For this purpose, the targeting peptide needs to be linked to a chelator such as DTPA or DOTA, which complexes the radiometal during the labeling procedure. The chosen composition of peptide analog, chelator and radiometal greatly influences receptor affinity, internalization and stability of the conjugate [37], [41]. The first FDA-approved radiopeptide routinely used in the clinic was ^{111}In -DTPA⁰-octreotide (OctreoScan, Figure 7), which can be imaged by whole body receptor scintigraphy around 24 h to 48 h after intravenous injection [83], [84]. For this planar imaging technique (2D), γ -emitters such as ^{111}In or $^{99\text{m}}\text{Tc}$ are used and detected by scintillation crystals of a γ -camera. More recently, advanced 3D imaging technologies as single photon emission computed tomography (SPECT) and positron emission tomography (PET) are implemented in the clinics. Similar to scintigraphy, SPECT detects γ -rays, but from different angles, which can be reconstructed to 3D images [85]. In contrast, PET imaging requires positron emitters (β^+) as ^{68}Ga , tracers include ^{68}Ga -DOTATOC or ^{68}Ga -DOTATATE [86]–[88]. After interaction of the positron with an electron in the body, two photons are emitted in a

180° angle. They are detected simultaneously by a PET camera and thereby provide information about the spatial and temporal distribution of the tracer [85]. PET imaging provides not only better resolution, sensitivity and image quality (Figure 7), but also reduced scanning times (2-3 h) and lower exposure of the patient [89]–[91]. Functional SPECT and PET imaging is usually combined with anatomical techniques as computer tomography (CT) or magnetic resonance imaging (MRI) to correlate tracer signals with morphology and to receive maximal information by only one imaging [92].

One major drawback of nuclear medical imaging is the application of ionizing radiation and the associated logistical and safety issues. In addition, the dependency on 3D image reconstruction impedes the instant signal tracking. In contrast, *in vivo* fluorescence imaging allows for a real-time image acquisition with non-hazardous radiation, a large field of view, inexpensive cameras and a great variety of available labels. So far, image-guided surgery is the primary application field, as the restricted tissue penetration depth prevents the use of optical imaging probes for whole body scans [93], [94]. However, the advancing development of camera systems and the use of near-infrared (NIR) dyes improved light penetration to several centimeters [95], [96]. Fluorophore emission in the near-infrared window (650-900 nm) reduces photon scattering, absorption by water and hemoglobin as well as tissue autofluorescence [93], [97], [98]. These dyes can be easily conjugated to targeting molecules such as peptides, small molecules or antibodies [99]. In general, a linker of variable length is introduced in between them to create distance and to maintain high affinity binding. Optical imaging with affinity agents coupled to NIR cyanine dyes was successfully approached by several groups, but is still confined to preclinical and clinical studies (Figure 7) [100], [101].

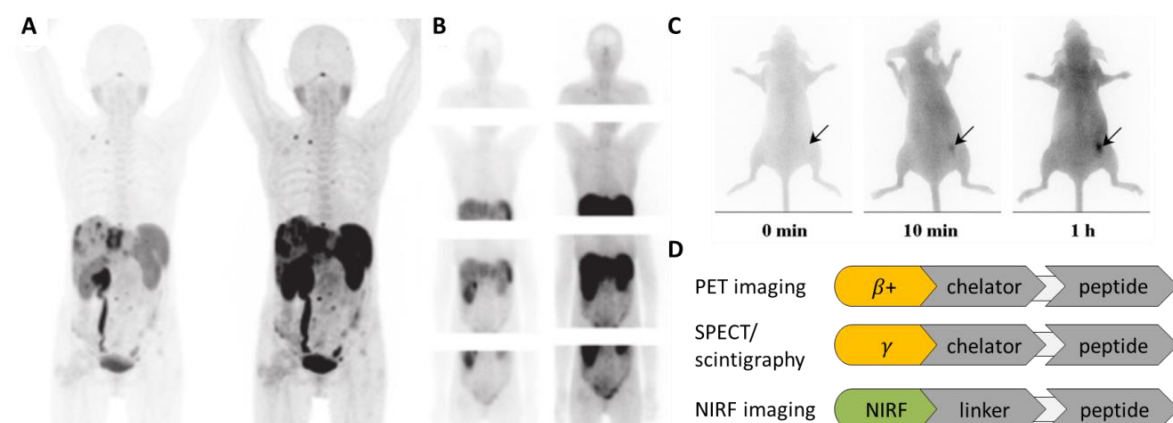


Figure 7 | Different modalities of neuroendocrine tumor imaging. PET imaging with ^{68}Ga -DOTATATE (A) results in higher resolution and more detectable lesions in comparison to planar scintigraphy (B). (C) Near-infrared imaging of a SSTR2-tumor bearing mouse after injection of indotricarbocyanine labeled octreotate. (D) General structure of targeted probes for PET, SPECT or NIRF imaging. The same peptide can be coupled via a chelator or linker to different effector molecules such as radioisotopes or near-infrared fluorophores (NIRF). Figures A and B were adapted by permission from van Essen et al. [85], Figure C was adapted by permission from Grötzinger and Wiedenmann [96].

1.4.2 Peptide receptor radionuclide therapy (PRRT)

Diagnostic imaging identifies patients with SSTR-positive tumors before they are selected for the following therapy with SSAs or peptide receptor radionuclide therapy (PRRT). Treatment of neuroendocrine tumors with radiolabeled somatostatin analogs is based on the same principle as imaging and utilizes identical peptide conjugates, for example DOTATATE or DOTATOC [102]. However, the peptide is bound to therapeutic radioisotopes with short tissue penetration ranges of a few millimeters. The most widely used isotopes for PRRT are the beta-particle emitters yttrium-90 (^{90}Y) and lutetium-177 (^{177}Lu), with half-lives of 2.5 and 6.7 days, respectively. Whereas ^{90}Y is a pure, high-energy β -emitter with a tissue range of up to 10 mm, ^{177}Lu is a combined β/γ -emitter of medium energy, reaching 2 mm penetration depth and also allowing for imaging after therapy [103]–[105].

PRRT has evolved as an important second-line treatment option in the management of inoperable and metastatic NETs. Administration of the radiopharmaceutical is performed in repeated cycles every 6 to 10 weeks. In one of the earliest studies, comprising 310 GEP-NET patients, treatment with ^{177}Lu -DOTATATE resulted in complete tumor remission in 2 % and partial tumor remission in 28 % of the patients, with a median progression-free survival of 40 months. Side effects were considered to be mild [106]. Recently, the first randomized multicenter PRRT trial (NETTER-1) evaluated the effect of combined SSA and PRRT treatment in comparison to SSA alone in patients with advanced, progressive midgut NETs. This phase III trial confirmed the previously obtained results of various studies, showing high response rates and increased progression-free survival after PRRT [107].

Despite its success, complete remissions are still very rare, raising the need for further improvement strategies. So far, PRRT was performed exclusively with agonistic somatostatin analogs, as internalization of the radiopharmaceutical was considered as a key point of therapeutic receptor targeting. However, a new development in the field is the use of antagonists, showing the contrary. Antagonists as DOTA-JR11 demonstrated higher and longer lasting tumor binding and accumulation in vitro and in preclinical mouse models [108], [109]. Recently, a first clinical pilot study confirmed the indicated superiority of antagonists in four patients, larger studies are in preparation [110]. Another promising approach to improve the outcome of PRRT might be the combination with chemotherapy or targeted agents such as mTOR inhibitors that possibly “sensitize” tumor cells for the following radiotherapy.

1.4.3 Targeted mTOR inhibition

The serine/threonine kinase mTOR (mammalian target of rapamycin) is a central element in the cell, which integrates environmental signals such as nutrients, growth factors or stress to coordinate cell growth and proliferation. Depending on the proteins it is interacting with, it can form the two complexes mTORC1 and mTORC2 with distinct downstream effectors (Figure 8A). Activated mTORC1 initiates protein translation by phosphorylation of S6K1 (also known as p70S6K) and 4EBP1, which in turn further engage S6 ribosomal protein and eIF4E. At the same time, activated S6K1 negatively regulates the PI3K-Akt pathway by inhibition of IRS. Furthermore, mTORC1 promotes cell cycle progression, inhibits autophagy and controls transcription and the DNA damage response. On the other hand, mTORC2 is in charge of cell survival, metabolism and the actin cytoskeleton [111], [112].

Dysregulated mTOR signaling has been demonstrated in various cancers, which made mTOR a promising target and facilitated the development of derivatives of rapamycin, a naturally occurring mTOR inhibitor. Two examples for FDA-approved rapalogs with improved pharmacological and solubility qualities are temsirolimus (CCI-779) and everolimus (RAD001) [113]. They form a complex with FKBP12 before binding to mTORC1. Inhibition of mTORC1 leads to G1 cell cycle arrest, reduced tumor angiogenesis, apoptosis induction and enhanced sensitivity towards DNA-damaging agents [111]. However, rapalogs interrupt not only downstream functions, but also the S6K1 feedback loop. This results in an upregulation of Akt-mediated pro-survival signaling and may counteract the antitumor activity of the inhibitor (Figure 8B) [114]. While rapalogs act as universal inhibitors of mTORC1, Akt downregulation was observed only in a few cancer cell lines, indicating a cell-type specific inhibition of mTORC2 [115]. Possibly, cells with PTEN loss and hyperactive PI3K-Akt signaling may be more dependent on mTORC1 and show higher sensitivity towards rapalogs [116]. Also, other signaling pathways such as the MAPK cascade seem to be activated by mTOR inhibition, although this is less well investigated [117].

Mutations as well as aberrant activations in the PI3K-Akt-mTOR network were also observed in NETs [118]. A series of clinical trials (RADIANT) resulted in the FDA-approval of everolimus for advanced pancreatic, non-functional gastrointestinal and lung NETs [119]–[122]. Treatment with everolimus prolonged median progression-free survival by 6.4 to 7.1 months when compared to the placebo group. Response rates of temsirolimus were similar to those observed with everolimus, as evaluated in a phase II study in advanced NETs [73]. However, the authors concluded that temsirolimus, when applied as a single drug, may yield only modest clinical benefit [123]. In addition, it has to be administered intravenously, whereas everolimus is available as an oral formulation [124], [125].

Recently, a small phase I study assessed the safety and optimal dose for a combined treatment of NETs with everolimus and PRRT (^{177}Lu -DOTATATE) in 16 patients. Overall response was observed in 44 % of patients, and the maximum tolerated dose for everolimus in combination was found to be 7.5 mg daily [126].

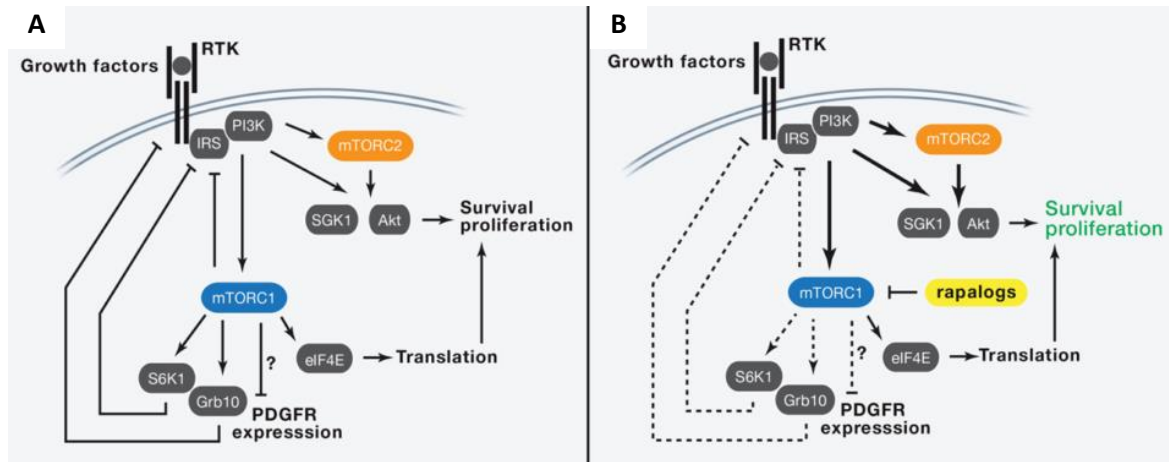


Figure 8 | mTOR signaling and inhibition in cancer. (A) Activation of mTOR promotes tumor development by increased cell growth and proliferation. Signaling of mTORC1 is characterized by several feedback mechanisms inhibiting the PI3K-pathway. (B) The treatment with rapalogs may lead to selective inhibition of mTORC1, resulting in the loss of feedback regulation and upregulated cell survival controlled by mTORC2. Adapted by permission from Laplante and Sabatini [112].

1.4.4 Alternative GPCR targets in NETs

SSTR-based imaging and therapy proved to be a successful and important option in the management of NETs. However, it is estimated that around 30 % of patients do not profit from these approaches. The expression of SSTR is associated with well-differentiated tumors of grade 1 or 2, whereas it is less detectable in poorly differentiated tumors or carcinomas of grade 3 [85], [127]. On the other hand, benign insulinomas have been shown to express SSTR2 to a much lower extent (50-70 %) in comparison to most GEP-NETs (80-100 %) [40], [128], [129]. Whereas some tumors may completely lack SSTR expression, others exhibit a nonhomogeneous receptor distribution, which results in residual tumor mass after treatment and subsequent resistance to SSAs [130], [131]. Other possible resistance mechanisms include: receptor desensitization, downregulation or loss-of-function as well as altered signaling pathways [40], [131]. Most patients develop SSA resistance within weeks to months of treatment, with recurrent symptoms and tumor growth [132]. As a consequence, alternative peptide GPCRs are investigated to extend the repertoire of available ligands for imaging and therapy. Among these targets are glucagon-like peptide-1 (GLP-1), gastric inhibitory polypeptide (GIP), cholecystikinin (CCK) or neurotensin receptors, for which overexpression in NETs has been confirmed [133]–[136]. In this context, the idea of simultaneous multireceptor targeting with a cocktail of different radioligands is a promising approach to increase diagnostic sensitivity and therapeutic efficiency [128], [137].

1.5 Preclinical tumor models

Preclinical models that imitate human disease are essential for in vitro and in vivo target identification, drug testing and therapy prediction. Due to their easy accessibility established cell lines or transgenic mice are widely used, although they represent the inter- and intra-tumoral heterogeneity of cancer only to a very low extent [138], [139]. The development of innovative models that reflect certain aspects of tumor biology in a more realistic way provided useful tools for translational research. In vitro drug testing transitions from monolayer permanent cell cultures to three-dimensional primary cultures, organoids and vital tissue-slices, freshly prepared from human material. These ex vivo models typically maintain their growth pattern, their tumor microenvironment as well as interactions with surrounding tissue [140], [141].

In vivo mouse models are of particular interest for studying receptor-targeted imaging and therapy. The generation of immunodeficient mouse strains enabled the injection and transplantation of xenografts without rejection. Tumors can be grown subcutaneously directly under the skin or orthotopically at the original tissue site, for example pancreas or colon. While subcutaneous xenografts can be easily established and monitored, orthotopic tumors are technically advanced, but are also more likely to metastasize [142], [143]. It is possible to generate classical cell-line based xenografts or to implant human primary material to establish patient-derived xenografts (PDX), which more accurately mimic the endogenous tumor heterogeneity [144]. The initial engraftment of PDX tumors often requires the use of specific mouse strains such as scid beige or nod scid gamma (NSG). These animals are severely immunocompromised with non-functional T-, B- and NK cells, besides additional defects in cytokine signaling [145], [146]. Their use increases the efficiency of xenotransplantation and leads to higher take rates, when compared to nude mice [147]. Nude mice (NMRI nu/nu) on the other hand display a mutation in the *Foxn1* gene, resulting in an athymic phenotype and a lack of T-cells, which need to mature in the thymus [148]. This strain is in particular valuable for the classical cell-line xenografts. Depending on the scientific background of the study, the appropriate model system needs to be carefully selected. So far, for slow growing neuroendocrine tumors the availability of PDX models is very limited [149].

2 AIMS OF THESIS

Somatostatin receptor-based diagnostic imaging and radiotherapy represent standard options for the clinical management of neuroendocrine tumors (NETs). For these approaches, eligible patients are only selected in the case of sufficient target expression, to ensure an individualized treatment strategy.

As not all patients profit from these approaches due to low receptor expression or desensitization, alternative GPCR ligand systems need to be investigated to broaden the spectrum of applicable targets. Preliminary cellular screening assays revealed a clear response of neuroendocrine tumor cell lines towards angiotensin II, the natural ligand of the angiotensin II receptor type 1 (AGTR1). Therefore, the first part of this thesis was conceived to assess the potential of AGTR1 as a novel target in neuroendocrine tumors. Study objectives were to validate the receptor mRNA and protein expression in neuroendocrine tumor tissue; to investigate the biological effects of angiotensin II in the cell line model and to evaluate the suitability of AGTR1 as a target for optical near-infrared imaging in a mouse xenograft model. It also included the establishment of two methods: 1) the in vitro receptor autoradiography to replace antibody-based immunohistochemistry and 2) the generation of patient-derived xenografts to obtain in vivo models that better reflect the heterogeneity of neuroendocrine tumors.

The second part of the thesis was designed in collaboration with the Department of Nuclear Medicine at Charité, Campus Virchow. Although peptide receptor radionuclide therapy (PRRT) delivers up to 250 Gy to somatostatin receptor-positive NETs, complete remission is still very rare. Radiosensitizing agents such as mTOR inhibitors could potentially improve therapy outcome. Therefore, the objectives of this study were to initially characterize the response of a panel of NET cell lines to mTOR inhibitors and secondly, to evaluate a potential additive or synergistic effect by combining them with either undirected external beam irradiation or targeted PRRT. For PRRT, the intention was to not only apply the agonistic DOTATOC, but also the recently developed antagonist DOTA-JR11 to assess its efficacy.

Both projects aim at contributing to the fundamental understanding of NET-specific target expression and treatment response. The results might be further integrated into extended preclinical studies with appropriate tumor models.

3 MATERIAL

3.1 Instruments

Name	Manufacturer
Analytic HPLC 1200 Series	Agilent Technologies (Santa Clara, US)
Bioanalyzer 2100	Agilent Technologies (Santa Clara, US)
Biometra TGradient, Thermal Cycler	Analytik Jena (Jena, DE)
CellLux, Cellular Imaging System	Perkin Elmer (Waltham, US)
CFX96 Touch™ Real-Time PCR Detection System	Bio-Rad Laboratories (Hercules, US)
Countess™ II Automated Cell Counter	Thermo Fisher Scientific (Waltham, US)
Cryostat CM3050S	Leica (Wetzlar, DE)
Cytospin 3	Thermo Fisher Scientific (Waltham, US)
EnVision 2103 Multilabel Plate Reader	Perkin Elmer (Waltham, US)
FACSCalibur flow cytometer	Beckton Dickinson (Franklin Lakes, US)
FlowStar LB513, Radio flow detector for HPLC	Berthold (Wildbad, DE)
GeneFlash, Imaging device	Syngene (Bangalore, IN)
GSR D1 gamma irradiator	Gamma-Service Medical GmbH (Leipzig, DE)
IN Cell Analyzer 1000	GE Healthcare (Buckinghamshire, GB)
LSM510, Laser scanning confocal microscope	Zeiss (Oberkochen, DE)
MicroBeta 2	Perkin Elmer (Waltham, US)
Microscope Axiovert	Zeiss (Oberkochen, DE)
Microscope Observer Z1	Zeiss (Oberkochen, DE)
Mini Trans-Blot® Cell	Bio-Rad Laboratories (Hercules, US)
Mini-PROTEAN Tetra Cell	Bio-Rad Laboratories (Hercules, US)
Odyssey Infrared Imaging System	LI-COR Biosciences (Lincoln, US)
Pearl Imager	LI-COR Biosciences (Lincoln, US)
Power Washer 384	Tecan (Männedorf, CH)
SimpliNano Spectrophotometer	GE Healthcare (Buckinghamshire, GB)
SpectraMax Plus 384 Microplate Reader	Molecular Devices (Sunnyvale, US)
Ultra-Turrax T8, Rotor-stator homogenizer	IKA-Werke (Staufen, DE)
VersaDoc Imaging system	Bio-Rad Laboratories (Hercules, US)
Wallac Wizard 1470, Gamma Counter	Perkin Elmer (Waltham, US)

3.2 Chemicals

3.2.1 Cell culture reagents

Name	Manufacturer
DMEM w 3.7 g/l NaHCO ₃ , w 1.0 g/l D-Glucose, w stable glutamine, low endotoxin	Biochrom AG (Berlin, DE)
DMEM/Ham's F-12 (1:1) w stable glutamine, low endotoxin	Biochrom AG (Berlin, DE)
Fetal Calf Serum (FCS)	Biochrom AG (Berlin, DE)
G418-BC (30,000 U/ml)	Biochrom AG (Berlin, DE)
PBS Dulbecco w/o Ca ²⁺ , w/o Mg ²⁺ , low endotoxin	Biochrom AG (Berlin, DE)
Penicillin/Streptomycin 10,000 U/ml, 10,000 µg/ml	Biochrom AG (Berlin, DE)
Poly-D-Lysine 50 µg/ml in PBS Dulbecco	Corning (Corning, US)
RPMI 1640 w 2.0 g/l NaHCO ₃ , w stable glutamine	Biochrom AG (Berlin, DE)
Trypsin/EDTA Solution 0.05 %/0.02 % (w/v) in PBS w/o Ca ²⁺ , w/o Mg ²⁺	Biochrom AG (Berlin, DE)

3.2.2 Buffers and solutions

Name	Recipe
5x SDS-PAGE Sample Buffer	250 mM Tris-HCl pH 6.8 5 % w/v SDS 45 % Glycerol 500 mM DTT 0.12 % w/v Bromophenol blue
Acid Solution	50 mM Glycine 100 mM NaCl pH 2.8
C1 Buffer	130 mM NaCl 5 mM KCl 10 mM Na-Hepes 2 mM CaCl ₂ 10 mM Glucose
Crystal Violet Solution	0.2 % w/v Crystal violet 20 % Methanol
Iodination Buffer	0.5 M Sodium phosphate buffer, pH 7.4

Phosphate-buffered Saline (PBS) pH 7.4	137 mM NaCl 10 mM Na ₂ HPO ₄ 2.7 mM KCl 1.8 mM KH ₂ PO ₄ <i>add 0.1 % Tween-20 for PBST</i>
Ponceau S	0.1 % w/v Ponceau S 0.5 % Acetic acid
Propidium Iodide (PI) Solution	20 µg/ml Propidium iodide 20 µg/ml RNaseA in PBS
Radioligand Binding Buffer	50 mM Hepes pH 7.4 5 mM MgCl ₂ 1 mM CaCl ₂ 0.5 % w/v BSA cOmplete Protease Inhibitors (Roche, Basel, CH)
Radioligand Wash Buffer	50 mM Tris-HCl pH 7.4 125 mM NaCl 0.05 % w/v BSA
SDS-PAGE Bottom Buffer	0.2 M Tris-HCl, pH 8.8
SDS-PAGE Top Buffer	0.1 M Tris-HCl 0.1 M Tricine, pH 8.25 0.1 % w/v SDS
Stripping Buffer	0.5 M Glycin, pH 2.67
Tris-Acetate-EDTA (TAE)	40 mM Tris 20 mM Acetic acid 1 mM EDTA (0.5 M, pH 8.0)
Tris-buffered Saline (TBS) pH 7.4	25 mM Tris 150 mM NaCl 2 mM KCl <i>add 0.1 % Tween-20 for TBST</i>
Western Blot Transfer Buffer	100 ml Rotiphorese 10x SDS-PAGE 200 ml 96 % Ethanol ad 1l H ₂ O
Western Blot Blocking Buffer	5 % w/v nonfat dry milk powder in TBST
Loading medium	10 ml serum-free medium 100 µl Probenicid (250 mM in 1 N NaOH) 10 µl Fluo-4 AM (50 µg in 22 µl DMSO)

3.2.3 Peptides and small molecules

Name	Manufacturer	Sequence/Formula
Angiotensin II	Sigma Aldrich (Deisenhofen, DE)	Asp-Arg-Val-Tyr-Ile-His-Pro-Phe
Azilsartan	Tocris (Bristol, GB)	2-Ethoxy-1-[[2'-(4,5-dihydro-5-oxo-1,2,4-oxadiazol-3-yl)biphenyl-4-yl]methyl]benzimidazole-7-carboxylic acid
DOTA-JR11	Helmut Mäcke (Uni Freiburg, DE)	DOTA-Cpa-c[D-Cys-Aph(Hor)- D-Aph(Cbm)-Lys-Thr-Cys]- D-Tyr-NH ₂
DOTATOC (DOTA-Tyr ³ -octreotide)	ABX (Radeberg, DE)	DOTA- D-Phe-c[Cys-Tyr- D-Trp-Lys-Thr-Cys]-Thr(ol)
Everolimus	Selleckchem (Houston, US)	42-O-(2-hydroxyethyl)-rapamycin
Novokinin	Tocris (Bristol, GB)	Arg-Pro-Leu-Lys-Pro-Trp
Octreotide	p&e (Hennigsdorf, DE)	D-Phe-c[Cys-Phe- D-Trp-Lys-Thr-Cys]-Thr(ol)
PD123319	Tocris (Bristol, GB)	1-[[4-(Dimethylamino)-3-methylphenyl]methyl]-5-(diphenylacetyl)-4,5,6,7-tetrahydro-1H-imidazo[4,5-c]pyridine-6-carboxylic acid ditrifluoroacetate
Saralasin-ITCC	p&e (Hennigsdorf, DE)	ITCC-TTDS-Sar-Arg-Val-Tyr-Val-His-Pro-Ala-COOH (see supplementary Figure S1)
Temsirolimus	Sigma Aldrich (Deisenhofen, DE)	42-[3-hydroxy-2-(hydroxymethyl)-2-methylpropanoate]-rapamycin
Tyr ¹¹ -Somatostatin-14	Bachem (Bubendorf, CH)	Ala-Gly-c[Cys-Lys-Asn-Phe-Phe-Trp-Lys-Thr-Tyr-Thr-Ser-Cys]
Valsartan	Tocris (Bristol, GB)	(S)-3-methyl-2-[N-({4-[2-(2h-1,2,3,4-tetrazol-5-yl)phenyl]phenyl)methyl}pentanamido]butanoic acid
Valsartan-ITCC	Kai Licha (FU Berlin, DE)	see supplementary Figure S2

3.2.4 Radionuclides

Name	Radiation	Half-life
Iodine-125	Gamma	59.6 days
Lutetium-177	Beta, Gamma	6.7 days

3.3 Oligonucleotides

Name	Sequence	Species	Amplicon length
<i>Primer for qPCR</i>			
AGTR1_for	TTTTCGTGCCGGTTTTTCAGC	Homo sapiens	100 bp
AGTR1_rev	TGCAACTTGACGACTACTGC		
SSTR1_for	TGAGTCAGCTGTCCGGTCATC	Homo sapiens	184 bp
SSTR1_rev	ACACTGTAGGCACGGCTCTT		
SSTR2_for	CCCCTCACCATCATCTGTCT	Homo sapiens	247 bp
SSTR2_rev	AGGTGAGGACCACCACAAAG		
SSTR3_for	TGCTCAACATCGTCAACGTG	Homo sapiens	115 bp
SSTR3_rev	TAAAGGATGGGGTTGGCACAG		
SSTR4_for	TCAACCACGTGTCCCTTATCC	Homo sapiens	91 bp
SSTR4_rev	AAGAATCGGCGGAAGTTGTC		
SSTR5_for	TCACCGTCAACATCGTCAAC	Homo sapiens	145 bp
SSTR5_rev	TGGCGGAAGTTGTCAGAGAG		
UBC_for	ATTTGGGTCGCAGTTCTTG	Homo sapiens	133 bp
UBC_rev	TGCCTTGACATTCTCGATGGT		
HPRT1_for	TGACACTGGCAAACAATGCA	Homo sapiens	94 bp
HPRT1_rev	GGTCCTTTTCACCAGCAAGCT		
ALG9_for	GTCTTCTGGCTTTTGTGAGCTG	Homo sapiens	78 bp
ALG9_rev	TCACGTGCAACCCAAACTTC		
GAPDH_for	TGCACCACCAACTGCTTAGC	Homo sapiens	87 bp
GAPDH_rev	GGCATGGACTGTGGTCATGAG		
<i>Primer for PCR</i>			
GAPDH_HS_for	TGAGTGCTACATGGTGAGCC	Homo sapiens	256 bp
GAPDH_HS_rev	AGCCACACCATCCTAGTTGC		
GAPDH_MM_for	GTCCTCGGGCATAATGCGTA	Mus musculus	356 bp
GAPDH_MM_rev	TAACCTCAGATCAGGGCGGA		

All oligonucleotides were designed by using Primer3Plus, NCBI Primer-BLAST and UCSC BLAT software. They were manufactured by Tib MolBiol (Berlin, DE).

3.4 Antibodies

Name	Species	Dilution	Cat No/Manufacturer
<i>Primary antibodies</i>			
Akt	Rabbit, polyclonal	1:1000 in 5 % BSA/TBST	#9272, Cell Signaling (Danvers, US)
Caspase-3	Rabbit, polyclonal	1:1000 in 5 % milk/TBST	#9662, Cell Signaling (Danvers, US)
P44/42 MAPK (ERK1/2) (3A7)	Mouse, monoclonal	1:2000 in 5 % milk/TBST	#9107, Cell Signaling (Danvers, US)
p70 S6 Kinase	Rabbit, polyclonal	1:1000 in 5 % BSA/TBST	#9202, Cell Signaling (Danvers, US)
PARP	Rabbit, polyclonal	1:1000 in 5 % milk/TBST	#9542, Cell Signaling (Danvers, US)
Phospho-Akt (Ser473) (D9W9U)	Mouse, monoclonal	1:1000 in 5 % BSA/TBST	#12694, Cell Signaling (Danvers, US)
Phospho-p44/42 MAPK (ERK1/2) (Thr202/Tyr204) (D13.14.4E) XP	Rabbit, monoclonal	1:2000 in 5 % BSA/TBST	#4370, Cell Signaling (Danvers, US)
Phospho-p70 S6 Kinase (Thr389) (1A5)	Mouse, monoclonal	1:1000 in 5 % milk/TBST	#9206, Cell Signaling (Danvers, US)
SSTR2	Mouse, monoclonal	1:50 in PBS	#sc-365502, Santa Cruz Biotechnology (Dallas, US)
<i>Secondary antibodies</i>			
Anti-rabbit IgG (H+L) horseradish peroxidase conjugated	Goat, polyclonal	1:5000 in 5 % milk/TBST	#111035003 Jackson ImmunoResearch (West Grove, US)
Anti-mouse IgG (H+L) horseradish peroxidase conjugated	Goat, polyclonal	1:2000 in 5 % milk/TBST	#115035003 Jackson ImmunoResearch (West Grove, US)
Anti-mouse IgG (H+L) Cy3 conjugated	Goat, polyclonal	1:1000 in PBS	#115165146 Jackson ImmunoResearch (West Grove, US)

3.5 Kits and ready-to-use reagents

Name	Manufacturer
Chromogranin A ELISA Kit	Dako (Glostrup, DK)
BSA (10 mg/ml)	New England Biolabs (Ipswich, US)
DAPI	Sigma Aldrich (Deisenhofen, DE)
DNase I Kit	Sigma Aldrich (Deisenhofen, DE)
DNeasy Blood & Tissue Kit	Qiagen (Hilden, DE)

Eosin Y Solution	Sigma Aldrich (Deisenhofen, DE)
Hematoxinilin	Sigma Aldrich (Deisenhofen, DE)
GeneRuler 100 bp Plus DNA Ladder	Thermo Fisher Scientific (Waltham, US)
DNA Gel Loading Dye (6x)	Thermo Fisher Scientific (Waltham, US)
High Capacity cDNA Reverse Transcription Kit	Applied Biosystems (Waltham, US)
jetPEI Transfection Reagent	Polyplus-transfection (Illkirch, F)
Matrigel® Matrix Basement Membrane HC	Corning (Corning, US)
PathScan® Cell Lysis Buffer (#7018)	Cell Signaling (Danvers, US)
PathScan® Intracellular Signaling Array Kit (Fluorescent Readout, #7744)	Cell Signaling (Danvers, US)
Phusion High-Fidelity DNA Polymerase Kit	Thermo Fisher Scientific (Waltham, US)
Pierce BCA Protein Assay Kit	Thermo Fisher Scientific (Waltham, US)
Precision Plus Protein™ Kaleidoscope™ Prestained Protein Standard	Bio-Rad Laboratories (Hercules, US)
RNeasy Mini Kit	Qiagen (Hilden, DE)
SSoFast™ EvaGreen® Supermix	Bio-Rad Laboratories (Hercules, US)
SuperSignal™ West Dura Substrate	Thermo Fisher Scientific (Waltham, US)
SYTOX™ Orange Nucleic Acid Stain	Thermo Fisher Scientific (Waltham, US)
Fluo-4, AM, cell permeant	Thermo Fisher Scientific (Waltham, US)
QIAshredder Homogenizer	Qiagen (Hilden, DE)
RNA 6000 Nano Kit	Agilent Technologies (Santa Clara, US)
Trypan Blue Stain 0.4 %	Thermo Fisher Scientific (Waltham, US)
Tissue-Tek® O.C.T.™ Compound	Sakura Finetek (Torrance, US)

3.6 Organisms

3.6.1 Eukaryotic cell lines

Cell line	Species	Origin	Culture medium
BON	Homo sapiens	Pancreas, carcinoid	DMEM/Ham's F-12 (1:1), 10 % FCS
H727	Homo sapiens	Lung, carcinoid	RPMI 1640, 10 % FCS
LCC-18	Homo sapiens	Colon, carcinoma	RPMI 1640, 10 % FCS
QGP-1	Homo sapiens	Pancreas, islet cell carcinoma	RPMI 1640, 10 % FCS
UMC-11	Homo sapiens	Lung, carcinoid	RPMI 1640, 10 % FCS
KRJ-1	Homo sapiens	Ileal, carcinoid	RPMI 1640, 10 % FCS
CM17	Homo sapiens	Pancreas, insulinoma	RPMI 1640, 10 % FCS

3.6.2 Stable eukaryotic cell lines

Cell line	Plasmid	Antibiotics
BON-SSTR2	pcDNA3.1-huSSTR2 (#SSTR200000, cDNA Resource Center, Bloomsberg, US)	G418 (600 µg/ml)
QGP-1-SSTR2	pcDNA3.1-huSSTR2 (#SSTR200000, cDNA Resource Center, Bloomsberg, US)	G418 (600 µg/ml)

3.6.3 Mouse strains

Strain	Distributor	Characteristics
Fox Chase SCID® Beige	Charles River	CB17.Cg-Prkdc ^{scid} Lyst ^{bg-J} /Crl defective T cells, B cells and NK cells
NMRI-nu	Janvier Labs	Rj:NMRI-Foxn1 ^{nu/nu} lack of T cells
NSG (JAX™), NOD scid gamma	Charles River	NOD.Cg-Prkdc ^{scid} Il2rg ^{tm1Wjl} /SzJ lack of T cells, B cells, functional NK cells and cytokine signalling

3.7 Software

Name	Manufacturer
AssayPro	Perkin Elmer (Waltham, US)
ChemStation	Agilent Technologies (Santa Clara, US)
ImageJ version 1.50	Open Source
Bio-Rad CFX Manager	Bio-Rad Laboratories (Hercules, US)
Bio-Rad Image Lab™	Bio-Rad Laboratories (Hercules, US)
EnVision Software	Perkin Elmer (Waltham, US)
qbase+ 3.1	Biogazelle (Ghent, BE)
GraphPad Prism 5.3	GraphPad Software, Inc. (La Jolla, US)
SoftMax Pro 5.3	Molecular Devices (Sunnyvale, US)
WinPrep 2.4	Perkin Elmer (Waltham, US)
IN Cell Analyzer 1000 Workstation 3.5	GE Healthcare (Buckinghamshire, GB)
CellQuest™ Pro	Beckton Dickinson (Franklin Lakes, US)
Pearl Cam Software 2.9	LI-COR Biosciences (Lincoln, US)

4 METHODS

4.1 Cell culture

4.1.1 Cultivation

Cells were grown in tissue culture treated polystyrene dishes in a humidified atmosphere at 37 °C with 5 % CO₂. Medium was supplemented with FCS at a final concentration of 10 % as indicated in 3.6.1, unless stated otherwise. Cells were subcultured twice a week. For this purpose the culture medium was removed, the cells briefly rinsed with PBS and incubated for 3-5 min with Trypsin/EDTA solution at 37 °C. The enzyme reaction was stopped by addition of complete medium. After centrifugation for 3 min at 800 x g the cell pellet was resuspended in fresh culture medium and the desired volume added to a new culture vessel.

For cell seeding at defined densities 10 µl of a 1:1 trypan blue mixed sample of the resuspended cell suspension were added to the chamber port of a Countess™ cell counting slide. Cell numbers were calculated by the automated cell counter and cells seeded accordingly.

4.1.2 Cryopreservation

For long term storage cells were resuspended in freezing medium (FCS/10 % DMSO) after trypsinization and centrifugation and aliquoted into cryovials. Cells were frozen slowly in an insulated box containing isopropanol at -80 °C and finally stored in liquid nitrogen.

Frozen cells were thawed rapidly in a water bath and diluted with complete medium. Cells were centrifuged to remove DMSO, carefully resuspended in fresh medium and transferred to a culture vessel.

4.1.3 Stable transfection

The recombinant cell lines BON-SSTR2 and QGP-1-SSTR2 were generated by transfecting wildtype BON and QGP-1 cells in a 6-well with a plasmid encoding for human SSTR2 and jetPEI transfection reagent according to the manufacturer's recommendations. Antibiotic selection to specifically expand positive cells was started 24 h after transfection with medium containing 600 µg/ml G418. After another 48 h cells were trypsinized and seeded into a 10 cm dish to obtain single cells. Monoclonal clones were picked, grown in 96-well plates first and tested for their SSTR2 expression by radioligand binding.

4.2 Molecular Biology

4.2.1 RNA/DNA isolation

Nucleic acids were isolated from cell lysates or tissues using the RNeasy Mini Kit (total RNA) or the DNeasy Blood & Tissue Kit (genomic DNA) according to the manufacturer's protocol.

For homogenization, disrupted cell lysates were pipetted into a QIAshredder spin column and centrifuged for 2 min at maximum speed. Tissues were grinded in liquid nitrogen and further homogenized in disruption buffer using a rotor-stator homogenizer for 30 sec, the lysate was centrifuged for 3 min at maximum speed and the supernatant used for the subsequent isolation.

Integrity of RNA prepared from primary patient tissues was assessed with a Bioanalyzer 2100. It allows the rapid analysis of purity, size and quantity of the sample by automated microcapillary electrophoretic RNA separation. Quality evaluation is based on the calculation of the RIN (RNA integrity number), which can range from 0 (totally degraded) to 10 (intact) [150]. For subsequent analyses RNA with a RIN equal to or higher than 5.9 was used.

4.2.2 Polymerase chain reaction (PCR)

For the verification of the human origin of patient derived xenograft tumors, 100 ng genomic DNA were amplified in 20 μ l reaction volume containing 5x reaction buffer, 0.5 μ M of the respective forward and reverse primers, 200 μ M dNTPs and 0.02 U/ μ l Phusion DNA Polymerase using the following conditions:

Step	Temperature	Time	Cycles
Initial denaturation	98 °C	30 sec	1
Denaturation	98 °C	10 sec	
Annealing	60 °C	20 sec	30
Extension	72 °C	20 sec	
Final extension	72 °C	10 min	1
Hold	4 °C	∞	

4.2.3 Agarose gel electrophoresis

PCR amplicates were analyzed by agarose gel electrophoresis for their length and purity. For this, 1.5 % w/v agarose powder was dissolved in TAE buffer and mixed with the intercalating dye ethidium bromide (1:10,000 dilution from stock: 1 mg/ml). Samples, mixed with 6x loading buffer, were separated on the polymerized gels for 40 min at 100 V and visualized by a GeneFlash UV transilluminator. The GeneRuler 100 bp Plus DNA ladder was used for sizing.

4.2.4 Reverse transcription quantitative real-time PCR (RT-qPCR)

Prior to reverse transcription, RNA was DNase I treated to remove contaminating DNA. For this, 2 µg RNA were incubated with 10x reaction buffer and DNase I for 15 min at room temperature. The reaction was stopped by addition of 10x stop solution and heating for 10 min at 70 °C. The RNA was directly transcribed into cDNA in a total volume of 40 µl (final concentration: 50 ng/µl) by using the High Capacity cDNA Reverse Transcription Kit. In addition to DNase I digestion a minus reverse transcriptase control was included for each sample to check for amplification of contaminating DNA, especially when using non intron spanning primers. The cycler was programmed as follows:

Step	Temperature	Time
Annealing	25 °C	10 min
Extension	37 °C	120 min
Inactivation	85 °C	5 min
Hold	4 °C	∞

For quantitative real-time PCR (qPCR), 2x SSoFast EvaGreen Supermix, 0.5 µM of the respective forward and reverse primer as well as 30 ng cDNA in 10 µl total reaction volume were pipetted per well. Amplification was carried out in Hard-Shell 96-well Plates/Clear Wells, sealed with Microseal B Adhesive Optical Sealing Film (both Bio-Rad Laboratories, Hercules, US) under the following conditions:

Step	Temperature	Time	Cycles
Initial denaturation	95 °C	30 sec	1
Denaturation	95 °C	3 sec	
Annealing/Extension	60 °C	30 sec	45
Plate read			
Melting curve	65-95 °C	10 sec/0.5 °C	

The obtained Ct values were corrected for different primer efficiencies and then normalized according to the $\Delta\Delta C_t$ method on the geometric mean of at least two reference genes, which were validated and chosen using the geNorm algorithm by qbase+ software [151], [152]. In case of single target expression analyses final relative quantities were calculated by qbase+ [153]. To compare expression levels between multiple targets these values were calculated manually with Excel. Quality control included melting curve analysis for specific target amplification and amplicon length, technical replicates as well as addition of minus reverse transcriptase and non-template samples as negative controls. All primer pairs were tested for their optimal annealing

temperature by running a thermal gradient and the correct amplicon length was checked by agarose gel electrophoresis.

4.3 Protein biochemistry

4.3.1 Cell lysis

Seeded cells were treated as desired, washed with ice cold PBS and incubated with appropriate amounts of PathScan lysis buffer supplemented with 1 mM PMSF for at least 5 min on ice. Cells were collected with the help of a cell scraper, transferred into tubes and centrifuged for 3 min at 4 °C and maximum speed. The supernatant was used for further analyses or stored at -20 °C.

4.3.2 Protein determination

Protein concentration of cell lysates was determined by using the Pierce BCA Protein Assay Kit based on protein-copper chelation known as biuret reaction and subsequent detection of the reduced copper ions (Cu^{1+}) by bicinchoninic acid (BCA). The colorimetric changes were measured at 562 nm and the obtained OD values used to interpolate protein concentrations from a standard curve prepared with BSA (0-10 mg/ml).

4.3.3 SDS-PAGE

Protein gel electrophoresis was performed according to standard protocols. Cell lysates were separated on discontinuous SDS-polyacrylamide gels, which were prepared as follows:

<i>for 2 gels</i>	12 % separating gel	4 % stacking gel
Water	1610 μl	2080 μl
40 % Acrylamide	2700 μl	400 μl
2 M Tris, pH 8.45	4500 μl	1440 μl
10 % SDS	90 μl	40 μl
10 % APS	90 μl	40 μl
Temed	9 μl	4 μl

In general, 10 μg of protein were diluted in 5x sample buffer and water in 10 μl total volume, denatured for 5 min at 95 °C and spun down shortly. Polymerized gels were assembled in a Mini-PROTEAN Tetra tank, the upper chamber filled with top buffer and the samples loaded into the lanes. The lower chamber was filled with bottom buffer and the gels run at 100 V. The Precision Plus Kaleidoscope Standard was used as molecular weight marker.

4.3.4 Western blotting

Electrophoretically separated proteins (see 4.3.3) were transferred to nitrocellulose membranes by the wet blot technique to detect and quantify specific molecules in complex cell lysates. For this, polyacrylamide gel, membrane, fiber pads and filter paper were equilibrated in transfer buffer for 15 min, stacked and locked into a cassette. The cassette was placed into a mini Trans-Blot tank together with an ice pad and a stir bar and filled with transfer buffer. Blotting was performed for 1 h at 100 V and constant 350 mA on a magnetic stirrer. Membrane was stained with ponceau S for assessment of homogeneous protein transfer, destained with water and incubated in blocking buffer for 60 min. After a short wash with TBST, membrane was incubated with primary antibody, in the desired dilution and diluent as indicated in 3.4, overnight at 4 °C. Membrane was washed three times for 5 min with TBST, incubated with HRP-coupled secondary antibody diluted in blocking buffer for 60 min at room temperature and again, washed three times for 5 min with TBST. Chemiluminescence was induced by addition of 500 µl SuperSignal West Dura substrate and captured with a VersaDoc imaging system. Protein signals were analyzed and quantified with Image Lab software.

4.3.5 Immunofluorescence

For immunofluorescent detection of specific proteins or epitopes, cells were grown on glass coverslips (Ø 12 mm, R. Langenbrinck, Emmendingen, DE) for at least 24 h. Antibody dilutions and diluents can be taken from section 3.4.

For staining of membrane receptor SSTR2, cells were washed with PBS, fixated in 1:1 acetone/methanol for 2 min at room temperature and directly incubated with the primary antibody overnight at 4 °C. After three washes with PBS, cells were incubated with a Cy3 goat anti-mouse secondary antibody for 1 h at room temperature and washed again. Finally, cells were briefly dipped into water and 96 % ethanol, air-dried and mounted on glass slides with Immu-Mount (Thermo Fisher Scientific, Waltham, US). Mounted cells were imaged using a confocal laser-scanning microscope equipped with a helium-neon laser at 543 nm, LP560 emission filter and 40x and 63x NeoFluar oil immersion objectives.

4.3.6 ELISA

For the detection of secreted proteins in cell supernatants, 30,000 cells per well were seeded in 96-well plates and grown overnight. The next day, ligands were diluted in serum-free medium supplemented with 0.5 % BSA and the medium aspirated before adding 250 µl of the respective dilution to each well. Cells were incubated for 6 h at 37 °C, then, supernatants were transferred into an U-bottom plate, centrifuged for 3 min at 800 x *g* and carefully transferred into another U-

bottom plate. Supernatants were directly used for ELISA measurements according to the manufacturer's protocol or the plate was sealed with adhesive film and stored at -20 °C until further use. Inhibitor experiments were performed in complete medium for 24 h after ligand application and supernatants processed as described.

4.4 Cellular assays

4.4.1 Drug and radiation treatment

Cells were seeded at distinct densities in 96-, 12- or 6-well plates, depending on the experimental setup and grown overnight. In general, substances were added in medium on top of the wells in double concentration for the indicated final concentrations.

Irradiation was performed with an external caesium-137 source at a dose rate of 1 Gy/min and further incubation without medium change. Beside external radiation, cells were alternatively treated with ¹⁷⁷Lu-coupled peptides to imitate PRRT in vitro. The indicated activities were added in medium on top of the wells. Cells were washed twice with warm PBS after 4 h at 37 °C and further incubated in fresh medium.

For combination treatments, cells were incubated for 24 h with the respective substance before radiation or radioligand treatment was applied.

4.4.2 Calcium mobilisation

This assay measures changes of intracellular calcium levels during the application of peptides or small molecules on living cells. Activated GPCRs, that couple to the G $\alpha_{q/11}$ subunit, regulate downstream effectors that eventually lead to an influx of calcium ions (Ca²⁺) from the endoplasmic reticulum. Calcium indicators such as fluo-4 increase their fluorescence intensity upon Ca²⁺ binding and are thereby used to assess ligand induced receptor activation.

Optical ViewPlate microplates (Perkin Elmer, Waltham, US) were coated with poly-D-lysine (see 3.2.1, 50 μ l/well) for 30 min at 37 °C, washed twice with PBS and air dried before seeding 40,000 cells per well. The next day, medium was exchanged for serum-free medium for 30 min. Then, cells were incubated in loading medium (see 3.2.2) with the AM ester form of fluo-4, which is intracellularly de-esterified after cell uptake. Probenecid was added to further reduce dye leakage. After a loading time of 45 min, cells were washed 3 times with 100 μ l C1 buffer followed by 20 min incubation in the dark. The washing and incubation step was repeated once more. Meanwhile, the corresponding ligands were prepared in C1 buffer/0.5 % BSA in double concentration and pipetted in a U-bottom plate. Finally, ligand and cell plate were stacked in a CellLux Calcium Imager and the protocol started. After a baseline measurement for 30 sec the

ligands were added on top of the cells and the fluorescence intensity recorded for further 60 sec. Obtained raw data were analyzed with AssayPro software. After a spatial uniformity correction, maximum response values (F) were normalized on the baseline values (F_0) of each well to reduce well to well variations. For this the following equation was used:

$$response = \frac{\Delta F}{F_0} = \frac{(F - F_0)}{F_0}$$

4.4.3 Cell cycle analysis

Cell cycle analysis was performed on the basis of DNA content measurement by flow cytometry. The fluorescence intensity of DNA binding dyes such as propidium iodide is proportional to the DNA content of the cell, thereby allowing the discrimination of cells in sub-G1, G1, S and G2/M cell cycle phases [154].

Cells were seeded in 12-well plates at a density between 100,000 to 200,000 cells per well and grown overnight before treatment (see 4.4.1). Both supernatant and cells were harvested at distinct time points and fixated with ice cold 70 % ethanol, which was added dropwise while vortexing to avoid cell aggregation. After fixation at $-20\text{ }^{\circ}\text{C}$ for at least 24 h, samples were washed with PBS and stained with propidium iodide solution, additionally containing RNaseA to remove interfering RNA. For each sample 10,000 events were counted with a flow cytometer measuring forward and sideward scatter as well as integrated (area, FL2-A) and pulse (width, FL2-W) red fluorescence. Doublet discrimination was performed by gating the cells using FL2-A vs. FL2-W, in that way excluding two aggregating G1 cells that appear to be one single G2/M cell [155]. The gate was applied to the PI histogram, cell cycle phases marked and the percentages of cells in each phase quantified with CellQuest Pro software.

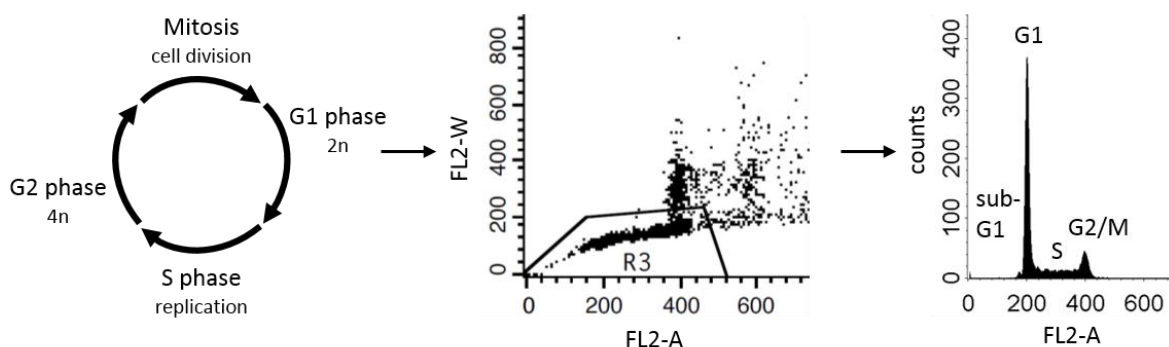


Figure 9 | Cell cycle analysis by flow cytometry. For visualization of the different cell cycle phases (left), PI stained and counted cells were gated according to FL2-A and FL2-W signals (middle), resulting in the exemplarily histogram (right).

4.4.4 Cell viability - metabolic activity and cell number

Cells were seeded in quadruplicates and a density of 5,000 cells in 50 μ l medium per well in 96-well plates, grown overnight and treated as described in 4.4.1. After 96 h, first, metabolic activity was determined by addition of 100 μ l medium containing 0.4 mM of the redox indicator resazurin. Cells were incubated for 3-4 h and the resulting fluorescence was measured with an EnVision Multilabel Plate Reader (excitation filter: TRF 495 nm, emission filter: dysprosium 572 nm). Following, the supernatant was removed, cells were fixated with 4 % formaldehyde for 10 min, stained with DAPI (1 μ g/ml in PBS/0.1 % Triton) for another 10 min and wells covered with 80 μ l PBS for image acquisition. Four fields per well were imaged on an IN Cell Analyzer 1000 using the 4x objective. Image stacks were analyzed and nuclei counted by IN Cell software. The values were averaged and normalized as percent of control treated with vehicle.

4.4.5 Clonogenic survival

In comparison to short term cell viability assays, the clonogenic survival assay evaluates the ability of single cells to reproduce and build colonies, so called clones. Cells were seeded in duplicates and a density of 5,000 cells in 500 μ l medium per well in 12-well plates and treated as described in 4.4.1. Cells were incubated without medium change for 1-2 weeks. Finally, colonies were fixated with 70 % ethanol for 10 min, stained with crystal violet solution for another 10 min and carefully rinsed with tap water. Plates were dried overnight and digitized with an Odyssey infrared scanner (700 nm channel, intensity 3, 84 μ m resolution and medium quality). For quantification, images were analyzed using the ColonyArea plugin for ImageJ [156].

4.4.6 Intracellular signaling array

The PathScan intracellular signaling array kit (see 3.5) allows the simultaneous detection of 18 phosphorylated or cleaved target molecules in a single cell lysate. Up to 750,000 cells were seeded in 6-well plates, grown overnight and incubated in serum-free medium 24 h before treatment with vehicle, positive control or angiotensin II. After 5, 10, 15 and 30 min cells were washed with ice cold PBS and lysed on ice with 100 μ l PathScan lysis buffer supplemented with 1 mM PMSF for 5 min. Cells were collected with the help of a cell scraper and centrifuged for 3 min at 4 $^{\circ}$ C and maximum speed. The supernatants were used for the analysis according to the manufacturer's protocol. The fluorescent signals were captured with an Odyssey infrared scanner (700 nm channel, intensity L1.0, 21 μ m resolution and medium quality) and the integrated intensities quantified with the software.

4.5 Radioactive studies

4.5.1 Iodination of peptides

Radioactive iodination of peptides was performed by the chloramine T method [157]. Soluble chloramine T serves as an oxidizing agent for Na^{125}I forming iodine monochloride, which reacts directly with tyrosyl residues of the peptide by electrophilic substitution (Figure 10).

For labeling, 10 nmol of the respective peptide in 25 μl iodination buffer were mixed with 1 mCi carrier-free Na^{125}I (NEZ033L010MC, Perkin Elmer, Waltham, US) in an HPLC glass vial with microvolume insert. The reaction was started by addition of 4 μl chloramine T (1 mg/ml in water). After 20-30 seconds, 4 μl sodium metabisulfite (2 mg/ml in water) were added to stop the iodination. HPLC purification was performed to separate unlabeled from labeled radioactive peptide on an Agilent ZORBAX 300 Extend-C18 column using a gradient from 20 to 50 % acetonitrile (+0.1 % TFA) against water (+0.1 % TFA) for 20 min. First, 1-2 μl of the reaction mixture were preanalyzed to determine the retention time of the radioactive peptide. This fraction was then collected during the main run, diluted with radioactive binding buffer to prevent radioautolysis, aliquoted and stored at $-20\text{ }^\circ\text{C}$.

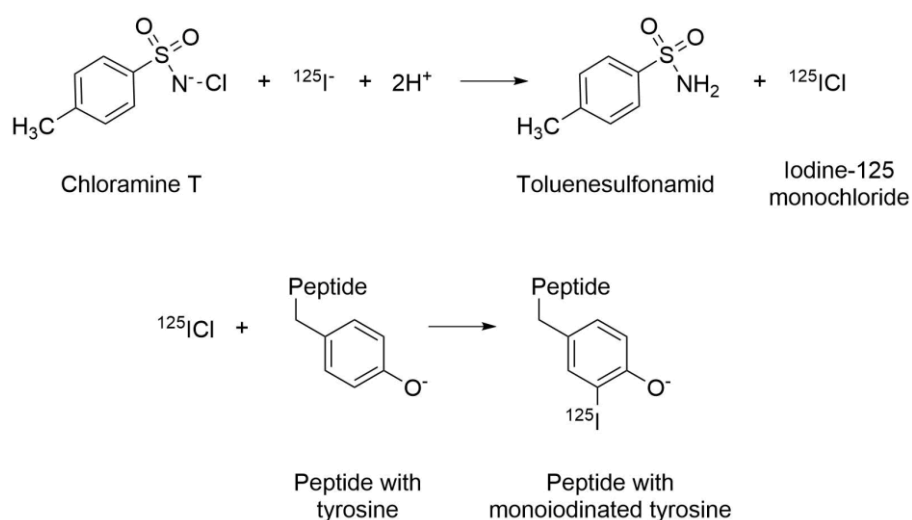


Figure 10 | Iodination of tyrosine residues by chloramine T. The iodination process is started by addition of chloramine T, which oxidizes radioactive iodine-125. The resulting iodine monochloride directly reacts with the tyrosine residue of a peptide. Adapted from Lane and Richardson [158].

4.5.2 Radiosynthesis of ^{177}Lu -coupled peptides

Labeling of the somatostatin analogs DOTATOC and DOTA-JR11 with lutetium-177 was kindly performed by Sonal Prasad in the Department of Nuclear Medicine, Campus Virchow Klinikum. All experiments involving ^{177}Lu -coupled radioligands were carried out in the laboratories of the Berlin Experimental Radionuclide Imaging Center (BERIC).

4.5.3 Radioactive binding and internalization studies

Radioactive experiments with ^{125}I -labeled peptides were performed in 96-well plates with 40,000 cells per well, grown overnight. In general, cells were incubated with 100 μl radioligand binding buffer containing certain amounts of both labeled (see 4.5.1) and unlabeled peptide. After 30 min at 37 $^{\circ}\text{C}$, cells were washed three times with 100 μl ice cold radioligand wash buffer, lysed with 80 μl 1 N NaOH, transferred to tubes and measured in a gamma counter for 60 sec per sample. Variations of this protocol are described below.

Saturation binding was performed to determine the dissociation constant K_d of the radioligand and the maximum number of binding sites B_{max} . Therefore, binding buffer was prepared with varying concentrations of labeled peptide from 0-4 nM, either with (non-specific binding) or without 1 μM of additional unlabeled peptide (total binding). Non-specific binding was subtracted from total binding to obtain specific binding. All three datasets were plotted with GraphPad Prism and fitted using nonlinear regression (one site - total and non-specific, one site - specific binding). The software provides B_{max} in the same value as the respective y-axis, in this case cpm. The following calculations were performed to obtain B_{max} in receptor sites per cell. In the first step, the specific activity of ^{125}I (2175 Ci/mmol) was transformed into dpm/mmol by multiplication with $2.22 \cdot 10^{12}$. This was multiplied with the counter efficiency of 65 % to get cpm/mmol and subsequently converted to cpm/fmol:

$$\text{cpm/fmol} = \frac{2175 \text{ Ci/mmol} * 2.22 * 10^{12} * 0.65}{10^{12}}$$

In a second step, the B_{max} value, calculated by the software in cpm, was divided by cpm/fmol to get the number of fmols. This was multiplied with the Avogadro constant ($6.02 \cdot 10^8$ /fmol) to get the number of molecules before division by seeded cells (40,000 in this case):

$$\text{sites/cell} = \frac{B_{\text{max}} (\text{cpm}) * 6.02 * 10^8 \text{ fmol}^{-1}}{\text{cpm/fmol} * 40,000}$$

Competitive binding was used to record dose-response curves of different unlabeled peptides and to determine their dissociation constant K_i or, in case of an unknown K_d of the radioligand, their IC_{50} . For this, cells were incubated with a single concentration of labeled peptide (0.32 nM or 100,000 cpm/well) and increasing concentrations of unlabeled peptide. Obtained cpm values were plotted with GraphPad Prism and the data fitted using nonlinear regression (one site - fit K_i , one site - fit $\log\text{IC}_{50}$).

For experiments with ^{177}Lu -coupled peptides cells were seeded in 12-well plates at a density of 250,000 cells per well and grown overnight. Incubation with the indicated activities was performed in culture medium for 4 h at 37 °C. To distinguish between membrane-bound and internalized fraction, cells were washed three times with ice cold PBS. Membrane-bound radioligand was washed off with an acid solution for 10 min before cells were lysed with 1 N NaOH to obtain the internalized radioligand fraction. Both fractions were collected in tubes and measured in a gamma counter.

4.5.4 In vitro receptor autoradiography

In vitro receptor autoradiography is a very sensitive technique to visualize and localize tissue bound radiolabeled peptides. In that way, receptor expression and distribution can be determined in distinct anatomical structures within the tissue in high resolution [159].

Flash-frozen human and mouse tissue samples were cut into 10-20 μm thick sections with a cryostat, mounted on glass slides, dried and stored at -80 °C. On the day of the experiment, slides were thawed, tissue sections encircled with a Dako Pen and equilibrated in radioligand binding buffer for 15 min. The buffer was removed and residual liquid carefully absorbed with filter paper. For angiotensin II receptor autoradiography, tissue sections were incubated with 200 μl radioligand binding buffer containing 0.5 nM radiolabeled ^{125}I -angiotensin II (total binding). Non-specific binding was assessed on successive sections by additional incubation with 1 μM of unlabeled displacer. After 1-2 h at 37 °C, slides were transferred to glass cuvettes, washed three times for 1 min with radioligand wash buffer and shortly dipped into water. Sections were immediately dried under a stream of air, the hydrophobic circle removed with paper and the slides arranged in an autoradiography cassette. In a darkroom, the tissue sections were exposed to Amersham Hyperfilm MP (GE Healthcare, Buckinghamshire, GB) for 1-2 weeks at room temperature. Finally, films were successively swayed in developer (G-153, AGFA, Mortsel, BE), water, fixer (G-354, AGFA, Mortsel, BE), rinsed with tap water and dried. Developed films were scanned and analyzed with ImageJ software. In addition to densitometric quantification, single tissue sections were carefully wiped off the slides with filter paper and measured in a gamma counter.

Additional tissue sections were stained with hematoxylin and eosin for comparison with the corresponding autoradiograms. For this, thawed sections were shortly washed with PBS, stained with hematoxylin for 4 min, rinsed with tap water, counterstained with eosin for 1 min and again carefully rinsed with tap water. Slides were dried and embedded with Kaiser's glycerol gelatin (Roth, Karlsruhe, DE). Specimens were digitized with an Axiovert microscope using the Mosaic acquisition mode.

4.6 In vivo experiments

4.6.1 Cell line xenografts

Immunodeficient NMRI nude mice were inoculated with NET cell lines to generate xenografts for in vivo experiments. Tumor cells were harvested as usual, counted and the pellet resuspended in the appropriate volume of serum-free medium for a concentration of 10 million cells/100 μ l. Immediately before injection, the precooled cell suspension was mixed 1:1 with matrigel, which was slowly thawed on ice. Cells were subcutaneously injected with a 27 G needle into the shoulder of anesthetized mice (100 μ l, 5 million cells) and grown for 2 to 3 weeks.

4.6.2 Establishment of patient-derived xenografts (PDX)

Besides xenografting permanent NET cell lines, neuroendocrine tumor tissue was directly injected into immunodeficient mice to obtain PDX models for future in vivo studies and to propagate primary tumor material as depicted in Figure 11.

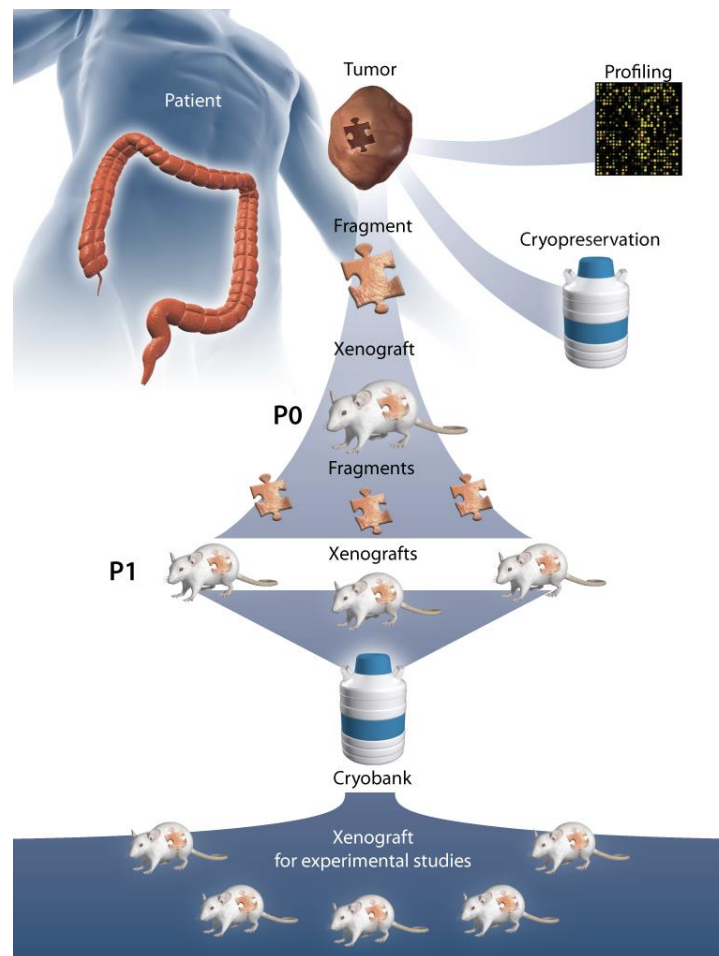


Figure 11 | Generation of patient-derived xenografts from primary patient tumor material. Human tumor fragments are xenografted into immunodeficient mice. Successfully grown tumors are further propagated in additional mice. Primary and PDX tumor fragments of different passages are withdrawn for cryopreservation and genetic and molecular profiling. Reprinted from Constant et al. [160].

Under a laminar flow hood, fresh or cryopreserved human tumor fragments were rinsed twice in PBS and transferred to a sterile 6 cm dish. Around 1 ml of serum-free DMEM was added and the fragment minced with two sterile scalpels into a cell suspension. If necessary, the suspension was further homogenized by using a cell strainer (100 μ m, Corning, Corning, US) and an appropriate syringe plunger. Finally, the volume was adjusted as needed with serum-free DMEM and the cells were transferred to a 2 ml tube and kept on ice. Just before injection, cells were carefully mixed 1:1 with high concentrated matrigel and withdrawn into a syringe. By using a 27 G needle, 100-200 μ l were injected into each flank of NSG or scid beige mice. Mice were kept under specific pathogen free (SPF) conditions, body weight and tumor size were monitored twice a week. After the first successful engraftment, mice were sacrificed, the xenografts processed as described above and injected into NMRI nude mice for all following passages.

Very firm tumors, which could not be dissected into homogeneous cell suspensions, were minced as far as possible and finally injected into the mice with a 24 G needle. The human origin of the obtained mouse xenografts was confirmed by PCR, target expression was validated by RT-qPCR analysis (see 4.2.2 and 4.2.4).

4.6.3 Near-infrared fluorescent optical imaging

For in vivo receptor targeting, fluorescent ITCC-labeled ligands were applied intravenously via the tail vein into tumor bearing NMRI nude mice (per animal: 1 nmol in 100 μ l 0.9 % NaCl). Images were acquired prior and at different time points after injection with a Pearl near-infrared imaging system (0 min, 10 min, 20 min, 30 min, 1 h, 2 h, 3 h, 4 h, 5 h, 6 h and 24 h). Animals were imaged under isoflurane anesthesia with an excitation at 785 nm and an emission at 820 nm. Images were analyzed with the Pearl Cam Software by defining regions of interest to obtain mean fluorescence intensities. From these, the ratio of signal (tumor) to background (neck) was calculated and plotted over time.

4.7 Curve fitting and statistics

If not indicated otherwise, dose-response curves were plotted with GraphPad Prism 5.3 and the data fitted using nonlinear regression and the variable slope model (four-parameters). As X values, base 10 logarithms of doses or concentrations were entered.

Statistical analyses were performed with the same software and the applied tests are indicated in the respective figure legends.

5 RESULTS

5.1 Identification and validation of AGTR1 as a novel target in NETs

The first part of the results section focuses on the G protein-coupled angiotensin II receptor type 1 (AGTR1) and its natural ligand angiotensin II (ATII). In search of alternative targets that may be used for the diagnosis and treatment of NET patients, previous experiments in our group had shown a clear response of human NET cell lines to ATII using calcium mobilization, dynamic mass redistribution and impedance assays (unpublished results). In the following, AGTR1 gene and protein expression was analyzed in NET tissue to confirm a potential role of the receptor in NET patients. As there are no specific AGTR1 antibodies available for receptor protein detection, in vitro receptor autoradiography was established as a method in our laboratory. Furthermore, two fluorescent ITCC-labeled AGTR1 ligands were used to evaluate the suitability of the target for in vivo optical imaging. Besides the verification of target expression, biological effects of ATII on tumor related processes were investigated, such as signaling, cell growth and secretion. Finally, patient-derived xenografts (PDX) were established and analyzed for their AGTR1 expression for the use in future in vivo studies.

5.1.1 Gene expression analysis of AGTR1 in NET tissue and cell lines

The existence of a receptor in tumor tissue is a prerequisite for targeting approaches. Pancreatic and ileal NET samples of patients were analyzed for their AGTR1 gene expression by RT-qPCR (Figure 12). NETs, and in particular ileal NETs, showed significantly increased AGTR1 transcript levels, with an overall 3.6-fold higher median value in comparison to healthy control tissues (Table 1). The same samples were analyzed for expression of the established target SSTR2, as a positive control and to relate AGTR1 levels to those of a known gene. As expected, SSTR2 mRNA was significantly upregulated in both pancreatic and ileal NET tissues. The ratio between control and tumor median values was much higher for SSTR2 (8.5 versus 3.6 for AGTR1). On the other hand, AGTR1 levels were detected in a 10-fold higher expression range.

Table 1 | Descriptive values of RT-qPCR data.

	AGTR1						SSTR2					
	pancreatic		ileal		all		pancreatic		ileal		all	
	control	NET	control	NET	control	NET	control	NET	control	NET	control	NET
n	12	42	13	71	25	113	12	42	13	71	25	113
median	2.1	2.6	5.1	14.2	2.9	10.4	0.08	0.71	0.15	1.06	0.11	0.93
ratio	1.2		2.8		3.6		8.9		7.1		8.5	

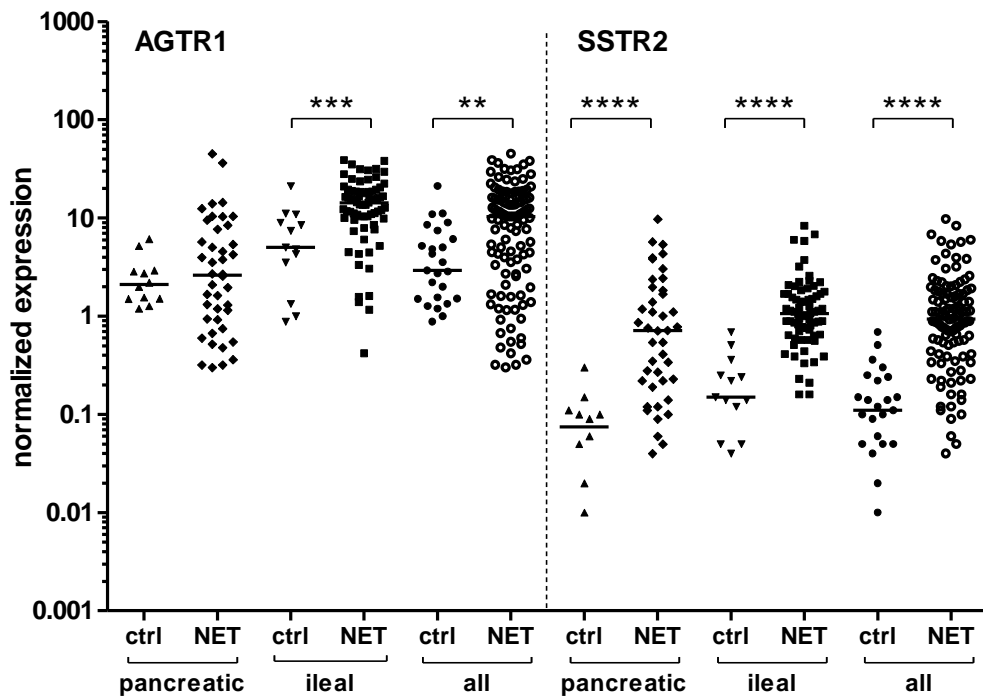


Figure 12 | AGTR1 gene expression is increased in NET tissues. Gene expression levels were measured by RT-qPCR in pancreatic (n=42) and ileal (n=71) NET tissues in comparison to healthy pancreatic (n=12) and ileal (n=13) control tissues. AGTR1 levels are shown in contrast to those of the standard target SSTR2 in the same samples. Values were normalized on ALG9, UBC and HPRT1. Bars represent median. Evaluated with unpaired two-tailed Student’s t-test, **P<0.01, ***P<0.001, ****P<0.0001.

For in vitro receptor autoradiography, 10 control and 17 NET samples were selected and their AGTR1 mRNA levels were individually compared to those of SSTR2 (Figure 13). Tissues with high expression of AGTR1 seemed to have much less SSTR2 mRNA, although this might be due to the overall higher AGTR1 levels.

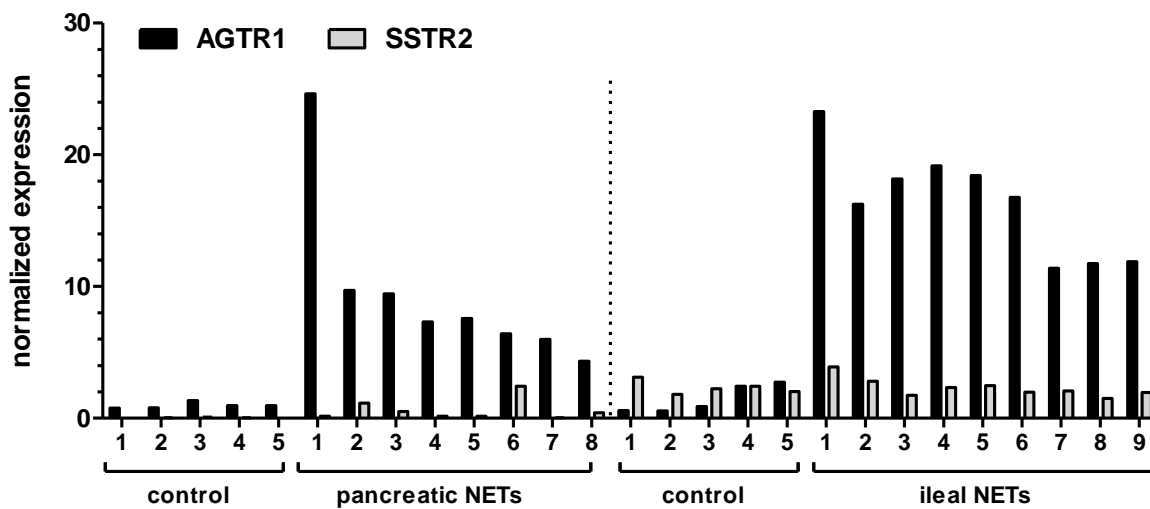


Figure 13 | Comparison of AGTR1 and SSTR2 gene expression for selected samples. From all samples that were analyzed by RT-qPCR in Figure 12, 10 control and 17 NET samples were used for in vitro receptor autoradiography. Their AGTR1 gene expression levels are shown in contrast to those of the established target SSTR2. Values were normalized on ALG9, UBC and HPRT1. Bars represent median.

In order to identify cell line models for in vitro and in vivo experiments, the endogenous AGTR1 expression of seven permanent NET cell lines was assessed and compared to the mRNA levels of various other tumor and non-tumor cell lines (Figure 14). Two AGTR1-positive NET cell lines, BON and H727, could be identified. They were originally isolated from pancreas and lung, respectively, and exhibited the highest mRNA levels of all tested cell lines. On the other hand, QGP-1 (pancreas) and LCC-18 (colon) with at least 1000-fold less expression were employed as AGTR1-negative NET cell lines for further experiments.

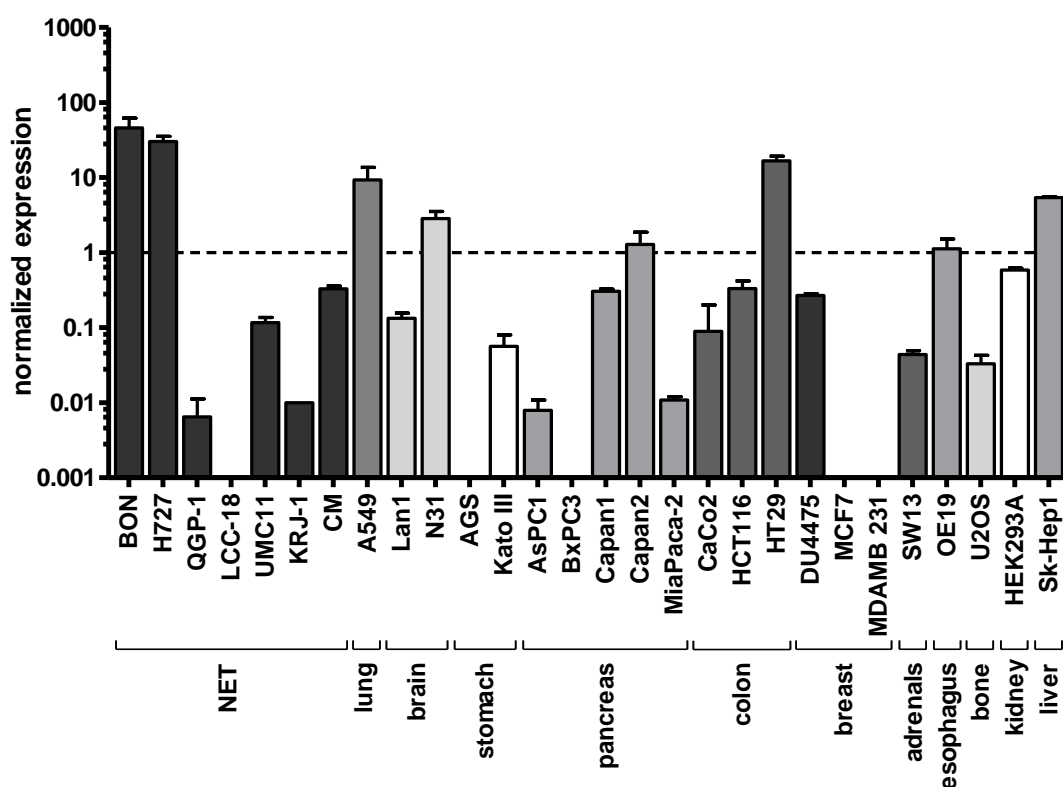


Figure 14 | AGTR1 gene expression is increased in two NET cell lines. Cell lines of different origin were analyzed by RT-qPCR for their AGTR1 gene expression levels. Values were normalized on UBC, HPRT1 and GAPDH. Bars show mean \pm S.E.M (n=2, different passages).

5.1.2 Establishment of in vitro receptor autoradiography

Gene expression data provide a first hint for potential expression changes, but they do not necessarily have to be reflected at protein level. For receptor targeting approaches, it is essential to verify receptor protein expression in tumor tissue. In the case of the G protein-coupled receptor AGTR1, several antibodies were tested but none of them specifically detected the receptor by western blotting or immunofluorescence (data not shown). As a consequence, autoradiography was chosen as an alternative technique for protein detection. This method utilizes a radioactively labeled ligand to visualize the corresponding receptor directly in tissue cryosections. The establishment of the method is described in the following.

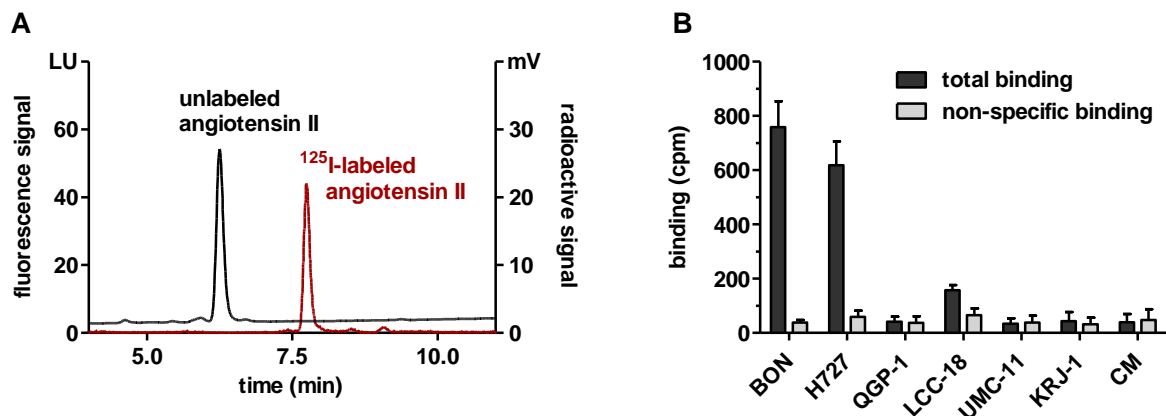


Figure 15 | Radiolabeled angiotensin II binds to AGTR1-positive NET cell lines BON and H727. (A) Angiotensin II was radioactively labeled with iodine-125 and purified from unlabeled peptide by HPLC. Chromatogram showing peptide peaks as recorded by fluorescence detector (black line, $\text{ex}=280\text{ nm}$, $\text{em}=340\text{ nm}$) and radioactive detector (red line). (B) NET cell lines were incubated with ^{125}I -angiotensin II alone (total binding) or in the presence of additional $1\ \mu\text{M}$ unlabeled angiotensin II (non-specific binding). Data represent mean \pm S.E.M. ($n=3$). cpm, counts per minute.

First, it was necessary to obtain a specific radiolabeled peptide with high affinity for AGTR1. The short peptide angiotensin II (8 AA), containing a tyrosine at position four, was well suitable for radioiodination with iodine-125 using chloramine T. The additional iodine changed the retention time of the peptide, allowing the separation of unlabeled from labeled angiotensin II by reversed-phase HPLC [161]. The chromatogram in Figure 15A shows the clear difference of peptide retention times. The fluorescent signal of unlabeled angiotensin II could be detected at 6.2 min, whereas the radioactive signal of labeled angiotensin II was recorded around 7.7 min.

When a radioligand is used for the first time, it is important to verify its characteristics before autoradiography, such as receptor specificity, affinity and non-specific binding [159]. The specificity of ^{125}I -angiotensin II for its receptor was tested by a competitive binding assay with seven available NET cell lines (Figure 15B). As expected from gene expression data, the AGTR1-positive NET cell lines BON and H727 showed binding that could be displaced by unlabeled angiotensin II (non-specific binding), whereas the others demonstrated only background levels of ^{125}I -angiotensin binding.

Table 2 | Binding parameters for BON and H727 cells.

	K_d (nM)	B_{max} (cpm) (sites/cell)		K_i (nM)				
				angiotensin II	valsartan	azilsartan	novokinin	PD123319
BON	0.6	10,583	50,748	0.1	4.3	2.2	-	-
H727	1.2	3,405	16,327	0.2	9.4	3.8	-	-

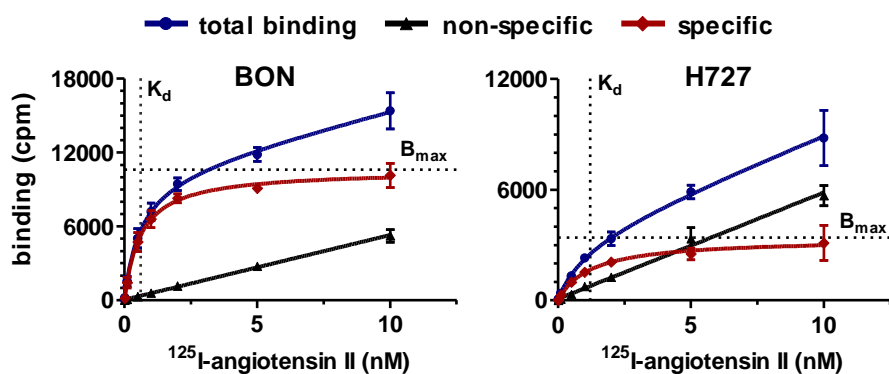


Figure 16 | Saturation binding assay with BON and H727 cells. Cells were incubated with increasing concentrations of ^{125}I -angiotensin II in the absence (total binding, blue) or presence of $1\ \mu\text{M}$ unlabeled angiotensin II (non-specific binding, black) for the determination of K_d and B_{max} values (see Table 2). Non-specific binding was subtracted from total binding to obtain specific binding (red). cpm, counts per minute.

BON and H727 cells were further analyzed by saturation binding to determine two parameters: 1) the dissociation constant K_d , which is a measure for ligand affinity and indicates the concentration at which half the receptors are occupied, and 2) the maximum number of binding sites B_{max} , which is a measure for the receptor density on the cell surface (Figure 16). For both cell lines, K_d values were in the nanomolar range with $0.6\ \text{nM}$ for BON and $1.2\ \text{nM}$ for H727 cells, respectively (Table 2). In contrast, the cell lines differed in their receptor density as indicated by the calculated B_{max} value, which was 3-fold higher for BON cells (around 50,000 sites/cell) in comparison to H727 cells (around 16,000 sites/cell).

Angiotensin II does not only bind to AGTR1, although this is the major physiological target, it is also the ligand for the angiotensin II receptor type 2 (AGTR2). AGTR2 mRNA levels could not be detected in the four NET cell lines BON, H727, QGP-1 and LCC-18 and there was no difference in expression levels for pancreatic and ileal NET tissues either (data not shown). Nevertheless, the two subtypes needed to be distinguished for autoradiographic protein detection. This was achieved by displacement of the radioligand with subtype specific ligands, such as AGTR1 antagonists valsartan and azilsartan or the AGTR2 antagonists PD123319 and novokinin.

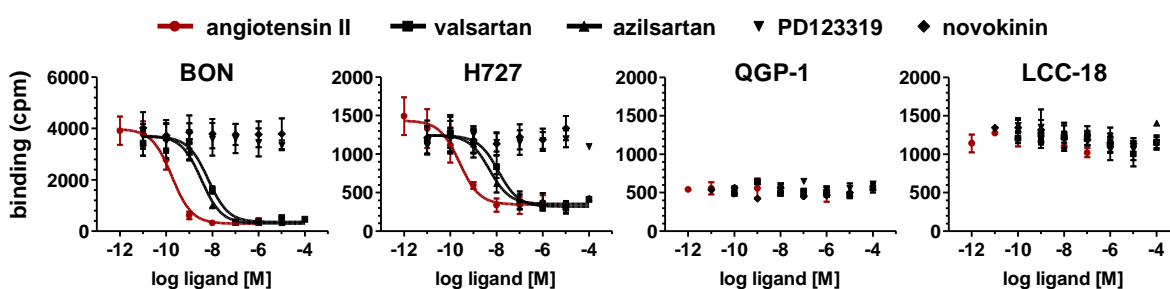


Figure 17 | BON and H727 cells specifically bind AGTR1, but not AGTR2 antagonists. AGTR1-positive (BON, H727) and AGTR1-negative (QGP-1, LCC-18) NET cells were incubated with ^{125}I -angiotensin II and increasing concentrations of either unlabeled angiotensin II, AGTR1 antagonists valsartan and azilsartan or AGTR2 antagonists PD123319 and novokinin. Data show mean \pm S.E.M. for BON and H727 ($n=3$) or mean \pm S.D. for QGP-1 and LCC-18 ($n=1$). cpm, counts per minute.

As depicted in Figure 17, ^{125}I -angiotensin II binding to AGTR1-positive BON and H727 cells could be displaced in a dose-dependent fashion by angiotensin II and AGTR1 specific antagonists, but not by the two AGTR2 specific antagonists. The AGTR1-negative QGP-1 and LCC-18 cells were included in a control experiment, but no dose-response curves could be recorded. The calculated K_i values (inhibitory constants), listed in Table 2, reflected the high affinity of angiotensin II for AGTR1 (BON: 0.1 nM, H727: 0.2 nM). K_i values of valsartan and azilsartan were slightly higher, but still in the low nanomolar range, whereas it was not possible to obtain K_i values for the AGTR2 antagonists PD123319 and novokinin. This further confirms a specific AGTR1 expression in these cell lines.

The validated radioligand was finally used for autoradiographic experiments with xenograft tumors of the four NET cell lines. Tumors were grown in nude mice for a few weeks before mice were sacrificed, the tissue was flash frozen and cut into 20 μm cryosections. Adjacent sections were incubated with the radioligand in absence (total binding) or in presence of the different ligands (non-specific binding). Autoradiograms as well as the quantification by a gamma counter verified previous results (Figure 18). Binding of ^{125}I -angiotensin II was only observed in the receptor-positive xenografts of BON and H727 cells and could be displaced by angiotensin II and the AGTR1 antagonists, whereas the incubation with additional AGTR2 antagonists exhibited the same signal strength as for total binding. Binding to QGP-1 and LCC-18 cells could only be detected at background levels. The conditions used for radioactive binding assays with cells also applied to autoradiographic experiments with more complex tissues, resulting in receptor subtype specific signals and a good signal-to-background ratio.

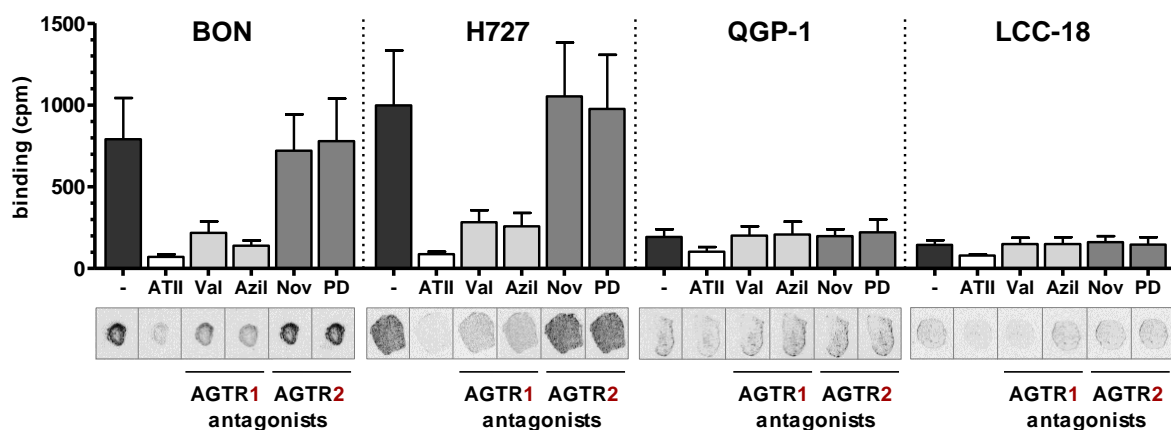


Figure 18 | BON and H727 xenograft tumors specifically express AGTR1. Cryosections of NET xenograft tumors were either incubated with ^{125}I -angiotensin II alone (-, total binding) or in the presence of additional 1 μM unlabeled angiotensin II (ATII), AGTR1 antagonists valsartan (Val) and azilsartan (Azil) or AGTR2 antagonists novokinin (Nov) and PD123319 (PD). Sections were wiped off after autoradiography and counts per minute (cpm) were measured with a gamma counter. Depicted is the mean \pm S.E.M. of three independent experiments (n=3) and one representative autoradiogram.

5.1.3 Protein expression analysis of AGTR1 in NET tissue

After the establishment of autoradiography utilizing AGTR1-positive NET cell lines and their corresponding xenograft tumors, the technique was applied to primary patient NET tissue. Based on gene expression analyses, ten control as well as eight pancreatic and nine ileal NET samples were selected for the verification of the previous results at protein level. The clinical characteristics of the samples are listed in supplementary Table S2. Tissues of both male and female as well as of primary and metastatic tumors have been chosen for the following experiment. Adjacent cryosections of each tissue were incubated with the validated radioligand in absence or in presence of angiotensin II, the AGTR1 specific antagonist valsartan or the AGTR2 specific antagonist PD123319 (Figure 19 to Figure 21). The binding patterns of the different tissues were quite heterogeneous. Pancreatic NET tissues depicted in Figure 19 showed a rather weak overall binding of ^{125}I -angiotensin II. Nevertheless, in tissues 1, 4, 6 and 8, it could be clearly displaced by angiotensin II and valsartan, but not or only partly by PD123319, indicating an AGTR1 expression. Ileal NETs (Figure 20) on the other hand demonstrated a strong binding in more than half of the samples (1-5), which was also AGTR1 specific as it could only be displaced by valsartan. PD123319 was not able to compete with ^{125}I -angiotensin II resulting in similar signal strengths. Autoradiograms of pancreatic and ileal control tissues are depicted in Figure 21. Interestingly, a few pancreatic samples exhibited strong radioligand binding. In comparison to pancreatic NET samples, normal pancreas seems to specifically express AGTR2 instead of AGTR1, as the signals were eliminated solely by PD123319. On the other hand, ileal control samples showed no binding at all (1, 3) or if so, it was not possible to displace it by any of the ligands (2, 4, 5).

To evaluate the autoradiograms in a more precise way, two methods were utilized for quantification. Directly after film development, cryosections were wiped off with filter paper and measured by a gamma counter. In addition, digitized autoradiograms were analyzed with the software ImageJ to obtain mean signal intensities per area. In either case, ratios of total binding to non-specific binding were calculated for angiotensin II, valsartan and PD123319. The results of both quantification approaches are depicted in Figure 22. The higher a ratio, the higher the expression of the respective receptor subtype. For example, a high ratio of total binding to valsartan binding indicates a high AGTR1 expression in the sample. Indeed, valsartan ratios were increased up to 5-fold in NET tissues, especially in ileal NETs, when compared to their respective control tissues (Figure 22A). As already supposed after visual evaluation of the autoradiograms, pancreatic control tissues showed up to 5-fold higher PD123319 ratios compared to NETs, which related to an increased AGTR2 expression. Similar results were observed for both quantification methods, however, image analysis revealed overall higher ratios (Figure 22B).

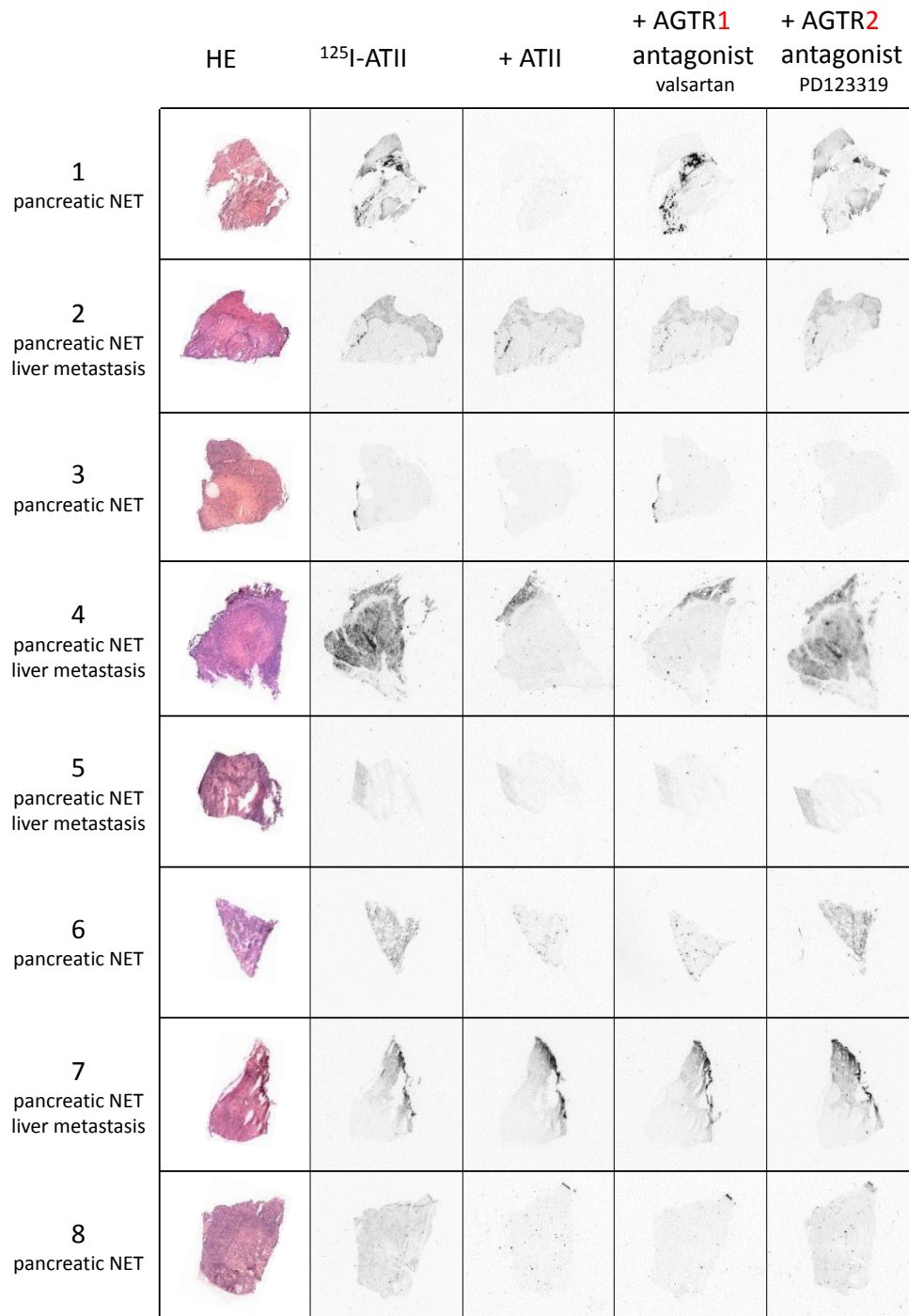


Figure 19 | In vitro receptor autoradiography of pancreatic NET tissues. For each tissue, HE staining and autoradiograms of adjacent cryosections are displayed. Cryosections were either incubated with ^{125}I -angiotensin II alone (^{125}I -ATII, total binding) or in the presence of additional $1\ \mu\text{M}$ unlabeled angiotensin II (ATII), AGTR1 antagonist valsartan or AGTR2 antagonist PD123319 (non-specific binding).

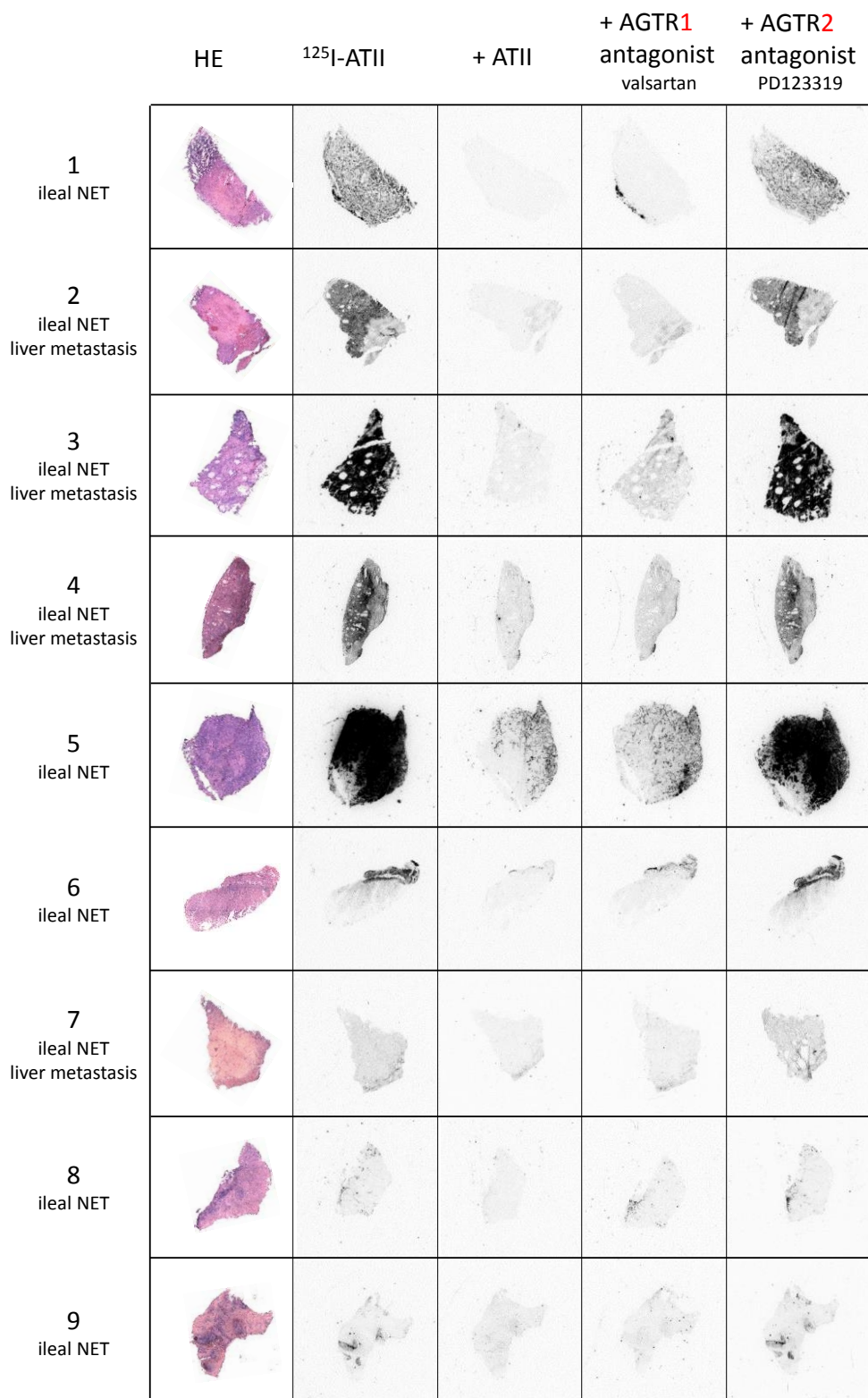


Figure 20 | In vitro receptor autoradiography of ileal NET tissues. For each tissue, HE staining and autoradiograms of adjacent cryosections are displayed. Cryosections were either incubated with ^{125}I -angiotensin II alone (^{125}I -ATII, total binding) or in the presence of additional $1\ \mu\text{M}$ unlabeled angiotensin II (ATII), AGTR1 antagonist valsartan or AGTR2 antagonist PD123319 (non-specific binding).

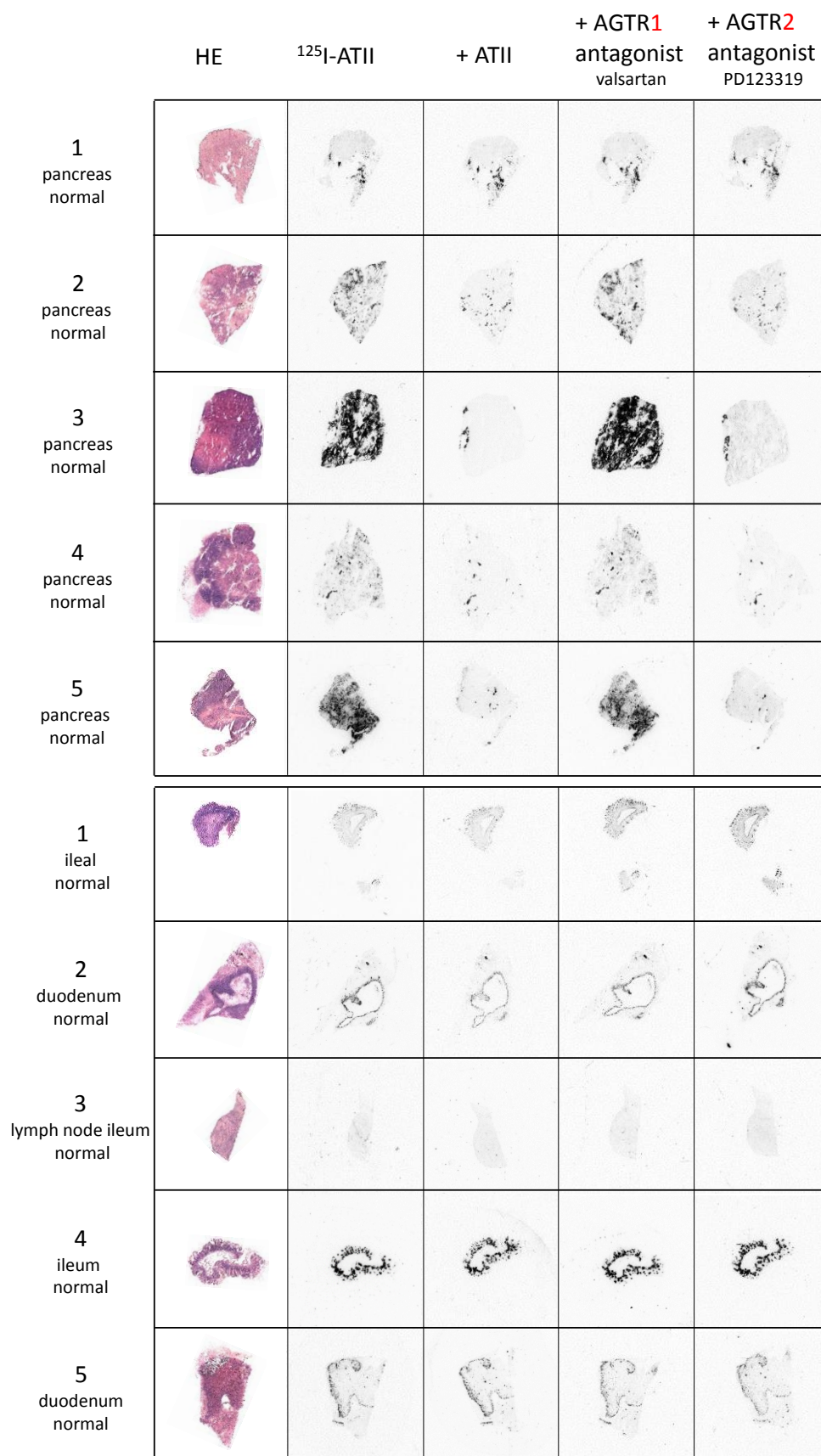


Figure 21 | In vitro receptor autoradiography of pancreatic and ileal control tissues. For each tissue, HE staining and autoradiograms of adjacent cryosections are displayed. Cryosections were either incubated with ^{125}I -angiotensin II alone (^{125}I -ATII, total binding) or in the presence of additional $1\ \mu\text{M}$ unlabeled angiotensin II (ATII), AGTR1 antagonist valsartan or AGTR2 antagonist PD123319 (non-specific binding).

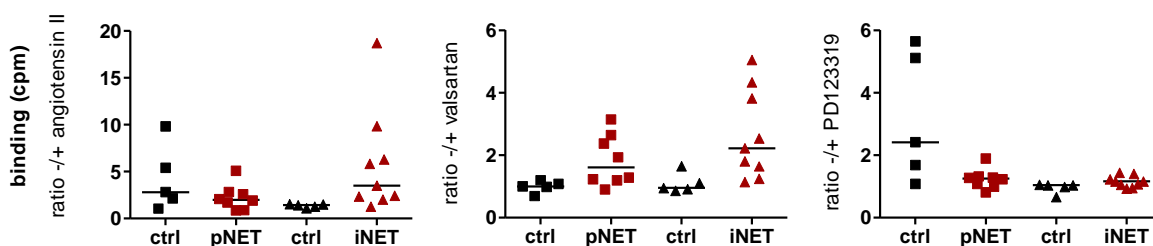
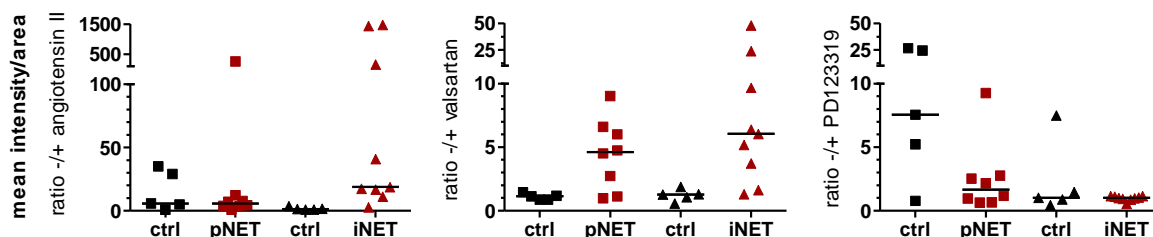
A gamma counter**B image analysis**

Figure 22 | Quantification of autoradiography by two methods. Sections were either wiped off after film development and the counts per minute (cpm) measured with a gamma counter (**A**) or mean signal intensities per area were calculated using ImageJ (**B**). For both, ratios of total to non-specific binding are shown for angiotensin II, valsartan and PD123319. ctrl, control; pNET, pancreatic NET; iNET, ileal NET.

Finally, the quantitative data of autoradiography was compared to gene expression data from chapter 5.1.1 for the selected samples. As depicted in Figure 23, mRNA levels (RT-qPCR) could be well correlated with protein levels (autoradiography) for most tissues. Especially, the difference between control and NET tissues was obvious. Whereas controls showed low mRNA and low protein levels, NETs generally had relatively high mRNA and high protein levels. Nevertheless, a few NET tissues with high mRNA levels, exhibited only low to moderate valsartan ratios as readout for AGTR1 protein expression.

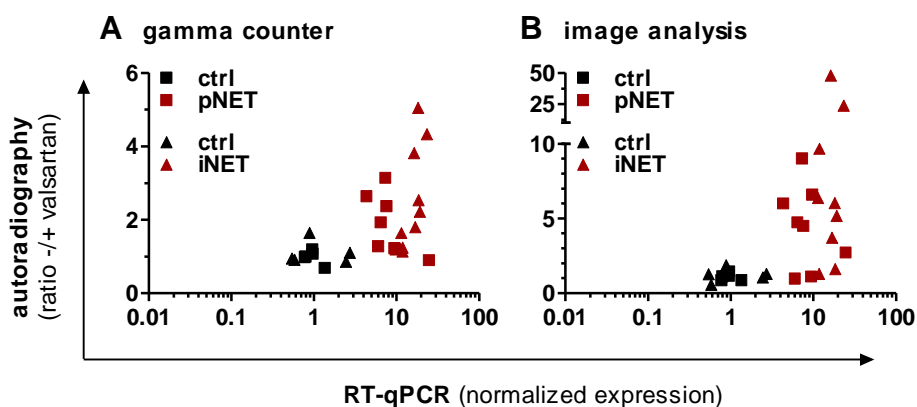


Figure 23 | Correlation of autoradiography with gene expression data. Scatter plot showing the correlation of AGTR1 gene expression (x-axis, RT-qPCR) with receptor protein expression (y-axis, autoradiography), the latter was analyzed by gamma counter measurement (**A**) or ImageJ (**B**).

5.1.4 Near-infrared in vivo imaging with ITCC-labeled AGTR1 ligands

After target verification in NET tissues by gene and protein expression analyses, the suitability of AGTR1 as a target for in vivo molecular imaging was assessed. Two ligands were chosen for a first imaging attempt: 1) the peptide saralasin, a partial AGTR1/2 agonist with three amino acid substitutions in comparison to angiotensin II, and 2) the small molecule valsartan, an AGTR1 antagonist, which is already clinically used for the treatment of hypertension. Both ligands exhibit binding affinities in the low nanomolar range and are metabolically more stable than angiotensin II, with half-lives of 4 min for saralasin [162] or around 6 h for valsartan [163]. Imaging probes were generated by coupling the ligands to the near-infrared dye indotricarbocyanine (ITCC), either directly in the case of valsartan or indirectly via a linker in the case of saralasin (see supplementary Figure S1 and Figure S2). For the following experiments, the two NET cell lines BON (AGTR1-positive) and QGP-1 (AGTR1-negative) were used.

First, the binding capacity of the fluorescent probes was determined in vitro utilizing a competitive radioactive binding assay. Their dose-response curves in comparison to angiotensin II are displayed in Figure 24, calculated K_i values can be obtained from Table 3. In receptor-positive BON cells, angiotensin II showed binding with high affinity ($K_i = 0.1$ nM) as determined before. In contrast, curves for valsartan-ITCC and saralasin-ITCC were shifted to the right, indicating lower binding affinities with K_i values of 18.6 nM and 246.5 nM, respectively. The introduction of ITCC had a considerable impact on molecule properties, affecting the binding affinity especially of saralasin. In contrast, receptor-negative QGP-1 cells did not show binding at all, as expected.

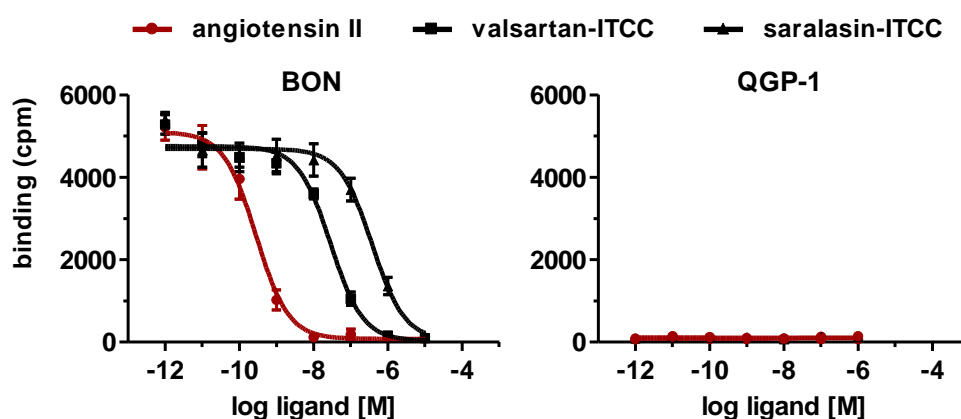


Figure 24 | ITCC-labeled AGTR1 ligands bind with lower affinity. AGTR1-positive BON and AGTR1-negative QGP-1 cells were incubated with 125 I-angiotensin II and increasing concentrations of unlabeled angiotensin II, valsartan-ITCC or saralasin-ITCC. Data show mean \pm S.E.M. for BON (n=3-4) or mean \pm S.D. for QGP-1 (n=1). cpm, counts per minute.

Table 3 | Calculated K_i values for ITCC-labeled ligands.

	angiotensin II	valsartan-ITCC	saralasin-ITCC
BON	0.1 nM	18.6 nM	246.5 nM
QGP-1	-	-	-

For in vivo imaging, immunodeficient nude NMRI-nu mice were subcutaneously injected with BON cells on the right and QGP-1 cells on the left shoulder. Near-infrared fluorescent imaging was performed after sufficient tumor growth and each ITCC-labeled probe was tested in three to four animals. The time-dependent biodistribution of saralasin-ITCC and valsartan-ITCC after intravenous probe application is exemplarily displayed for one animal in Figure 25A and B. The fluorescent gain was equally adjusted for all images to compare signals over time, except for the ventral signals of saralasin-ITCC, which were too strong and had to be lowered. For quantification, ratios of tumor-to-background signals were calculated and plotted over time (Figure 25C).

Visual evaluation of the images already suggested a target-specific accumulation of saralasin-ITCC in AGTR1-positive BON tumors, which proved to be significant at three, four, five and six hours post-injection after quantitative analysis (Figure 25A and C). Tumor-to-background ratios were 2- to 3-fold higher when compared to the image acquired prior injection. In contrast, only low uptake was detected in receptor-negative QGP-1 tumors. As shown by ventral images of the mouse, the majority of the probe was rapidly excreted via the kidneys and the bladder. The detectable fluorescence returned almost to background levels already after a few hours and by this possibly enhanced the visibility of the tumor signal (dorsal images).

On the other hand, valsartan-ITCC differed in its biodistribution. Tumor accumulation of the probe was relatively weak with similar signals in receptor-positive and -negative tumors. Quantitative analysis confirmed this impression, as a significant probe accumulation was detected in both tumors at one, two, three, four, five and six hours with 2-fold higher ratios compared to background levels (Figure 25B and C). Excretion of valsartan-ITCC primarily took place via liver and intestines. It was also noticeable, that the probe remained much longer in the mouse, and even 24 h post-injection fluorescence was detectable, especially in liver and receptor-positive BON tumors.

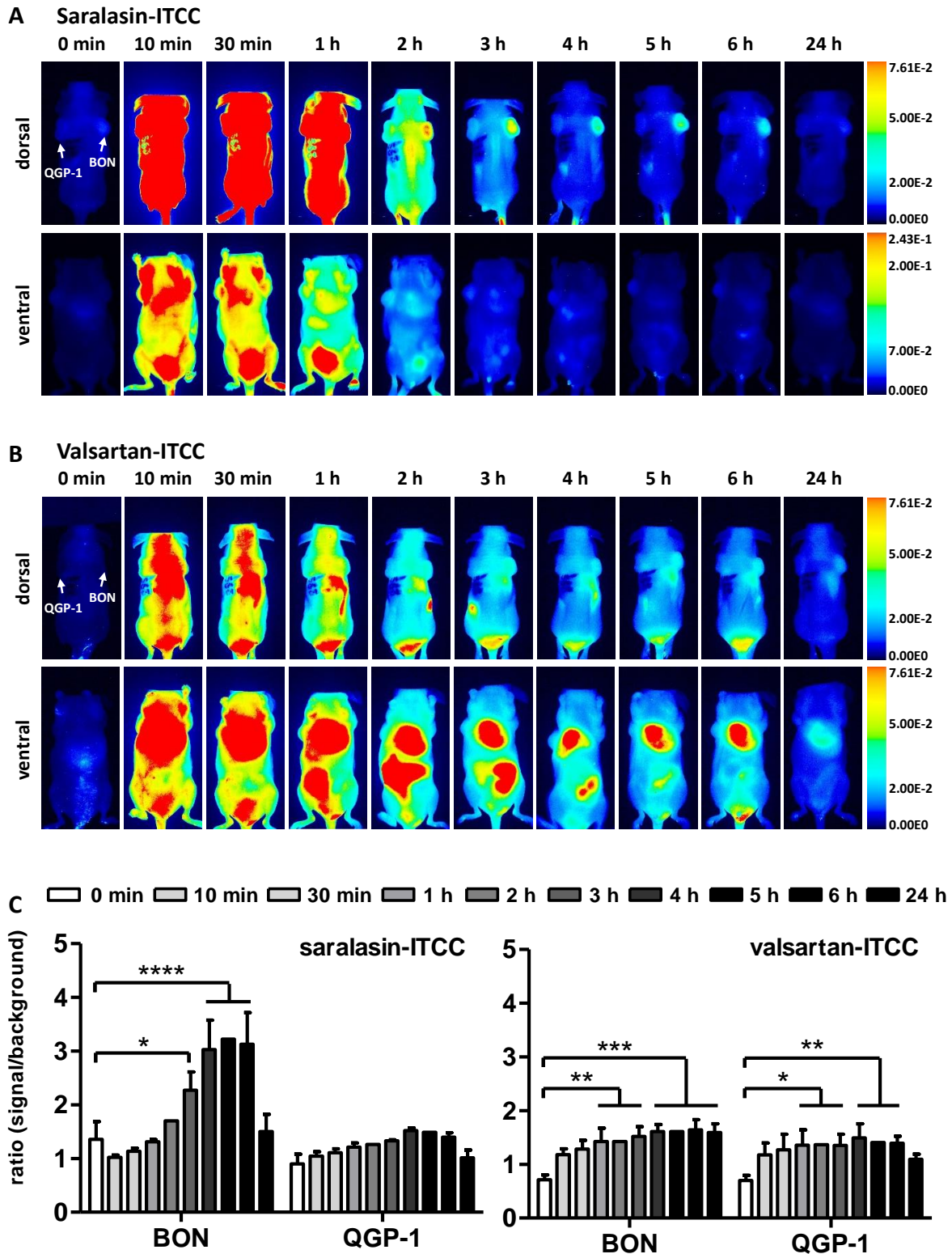


Figure 25 | In vivo NIRF imaging with AGTR1-targeting ITCC-ligands. Biodistribution of 1 nmol i.v. saralasin-ITCC (A) or valsartan-ITCC (B) in a mouse model subcutaneously injected with AGTR1-positive BON cells (right shoulder) or negative QGP-1 cells (left shoulder). Images were acquired at the indicated time points before or after injection and are displayed with an equally adjusted gain for either dorsal or ventral signals. (C) Signals from in vivo NIRF imaging were quantified by calculating the ratio of signal (tumor) to background (neck) for saralasin-ITCC (left, n=4) and valsartan-ITCC (right, n=3). Bars represent mean \pm S.E.M. of different animals. Evaluated with matched two-way ANOVA and Bonferroni post-hoc test, * $P \leq 0.05$, ** $P \leq 0.01$, *** $P \leq 0.001$, **** $P \leq 0.0001$. ITCC, indotricarbocyanine.

5.1.5 Biological effects of angiotensin II on AGTR1 expressing NET cell lines

Most peptides applied for tumor targeting remain to be receptor agonists, although recent studies suggested superior efficacy when using antagonists [58], [108]. However, it is of great relevance to investigate the biological functions of the peptide to avoid unwanted side effects triggered by activation of the receptor. In this section, the effects of angiotensin II on AGTR1 were investigated in more detail, including cell signaling, secretion and cell viability. The NET cell lines BON and H727, endogenously expressing AGTR1, as well as receptor-negative QGP-1 and LCC-18 were used as model cell lines for the following experiments.

Upon stimulation by external ligands, the G protein-coupled receptor AGTR1 primarily activates $G_{q/11}$ and subsequently phospholipase C, which eventually leads to an increase of the second messenger Ca^{2+} in the cell [47]. This influx can be measured by an intracellular calcium mobilization assay, which was already applied for the preliminary screening that identified angiotensin II as an interesting ligand in NET cells.

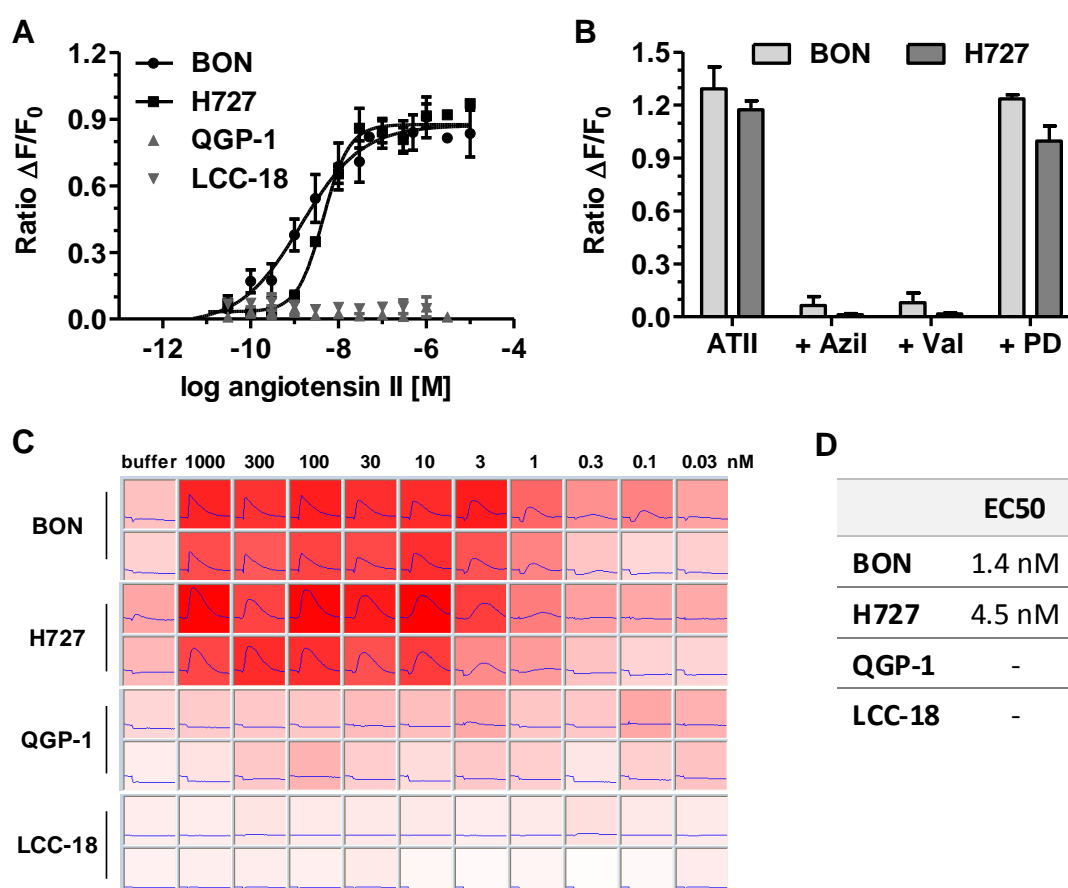


Figure 26 | Angiotensin II induces calcium signaling in BON and H727 cells. NET cell lines were loaded with the calcium indicator fluo-4 and the increased fluorescence after ligand application was recorded. **(A,D)** Dose-response curves after stimulation with angiotensin II and calculated EC₅₀ values for AGTR1-positive (BON, H727) and AGTR1-negative (QGP-1, LCC-18) NET cell lines. Data show mean \pm S.E.M. ($n \geq 3$). **(B)** BON and H727 cells were preincubated with 1 μ M of the AGTR1 antagonists valsartan (Val) and azilsartan (Azil) or the AGTR2 antagonist PD123318 (PD) for 15 min before application of angiotensin II. Data show mean \pm S.E.M. ($n = 3$). **(C)** One representative recording of the fluorescent kinetics after angiotensin II application.

In section 5.1.2, binding analyses revealed high affinities of angiotensin II for its receptor in BON and H727 cells. Here, functional activation of the receptor was evaluated by a calcium assay. The cells, preloaded with a calcium indicator increasing its fluorescence upon Ca^{2+} binding, were incubated with different concentrations of angiotensin II. As expected, dose-response curves could be obtained for AGTR1-positive BON and H727, but not for AGTR1-negative QGP-1 and LCC-18 cells (Figure 26A). The calculated EC_{50} values, 1.4 nM for BON and 4.5 nM for H727 (Figure 26D), were in the same range as the K_i values, which were determined before (Table 2). In addition, AGTR1 antagonists valsartan and azilsartan were able to diminish the angiotensin II induced Ca^{2+} mobilization, whereas preincubation with AGTR2 antagonist PD123319 did not influence receptor activation (Figure 26B).

Besides activation of the phospholipase C pathway, other signaling cascades possibly involved in angiotensin II receptor activation were investigated by an intracellular signaling array. This kit enabled the simultaneous detection of 18 phosphorylated or cleaved targets in a single cell lysate. Figure 27 gives an overview of the outcome after 5 min of angiotensin II stimulation in BON and H727 cells. The positive control phorbol 12,13-dibutyrate (PDBu) was included as a known activator of MAPK/ERK signaling to exclude experimental errors. Data were normalized to the untreated sample for every respective target and are depicted as percentages of control. Angiotensin II stimulation resulted in phosphorylation of growth-stimulating ERK 1/2, Akt and GSK-3 beta in BON cells, whereas H727 almost exclusively showed increased phospho-Akt levels.

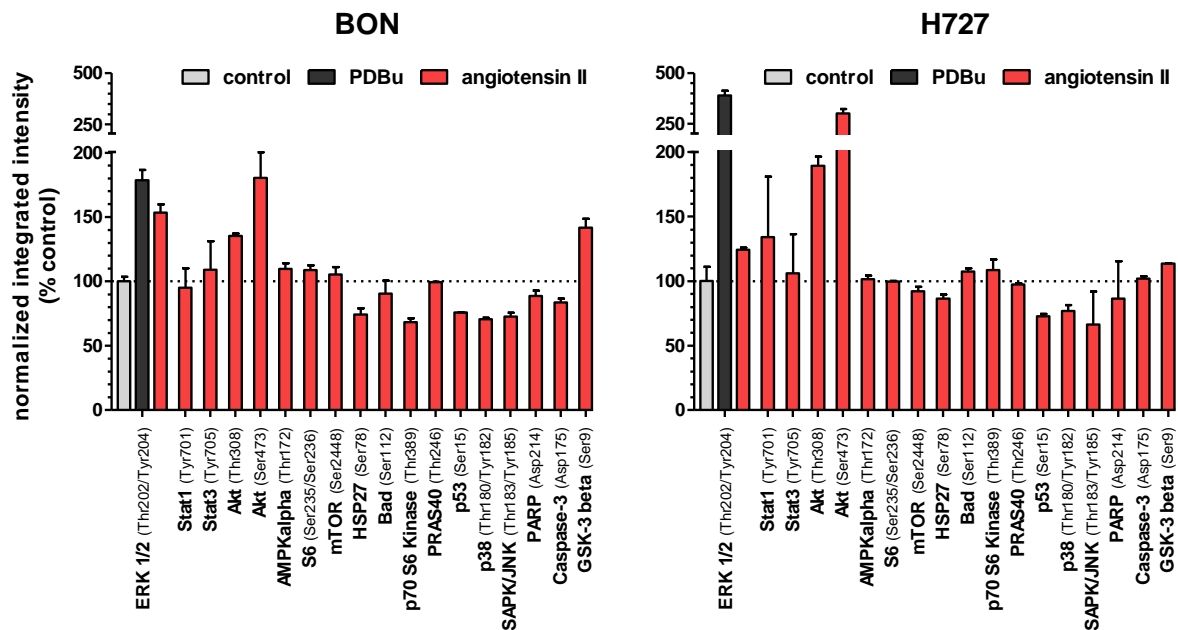


Figure 27 | Intracellular signaling array after 5 min of angiotensin II stimulation. BON and H727 cells were incubated with vehicle, 1 μM PDBu or 1 μM angiotensin II for 5 min. Cell lysates were analyzed for the phosphorylation and cleavage status of intracellular molecules. For each target, fluorescence intensities were normalized on the untreated control lysate, here exemplarily shown for ERK 1/2. Data showing mean \pm S.D. of one experiment, measured in duplicates. PDBu, phorbol 12,13-dibutyrate.

However, longer stimulation with angiotensin II for 10, 15 or 30 min led to enhanced phosphorylation of Bad and cell cycle promoting p70S6K in H727 (see supplementary Figure S3 to Figure S5). Other targets were only marginally influenced.

NETs are known to secrete a variety of molecules, including chromogranin A (CgA), which serves as a tumor marker for diagnosis and therapeutic monitoring [164]. BON cells are widely used for secretion studies, as they express and secrete CgA, which was also confirmed by our group (see supplementary Figure S6). Interestingly, angiotensin II stimulates CgA secretion of BON cells in a dose-dependent manner ($EC_{50} = 1.64$ nM) as measured by ELISA in cell supernatants (Figure 28A). Moreover, this effect was diminished when incubating the cells with AGTR1 antagonists valsartan or azilsartan for 15 min before angiotensin II application (Figure 28B). AGTR2 antagonist PD123319 on the other hand did not influence CgA levels. Again, PDBu served as a positive control and led to highly increased CgA secretion, as expected.

Finally, it was investigated, whether angiotensin II affected tumor related processes such as cell growth. For this, BON and H727 cells were treated with increasing concentrations of the peptide for 96 h and metabolic activity was measured by addition of the redox indicator resazurin. As shown in Figure 29, no change in metabolic activity was detected, even with 10 μ M of angiotensin II. Similarly, cells were not affected by treatment with AGTR1 antagonists valsartan or azilsartan, the metabolic activity continuously remained on the same level.

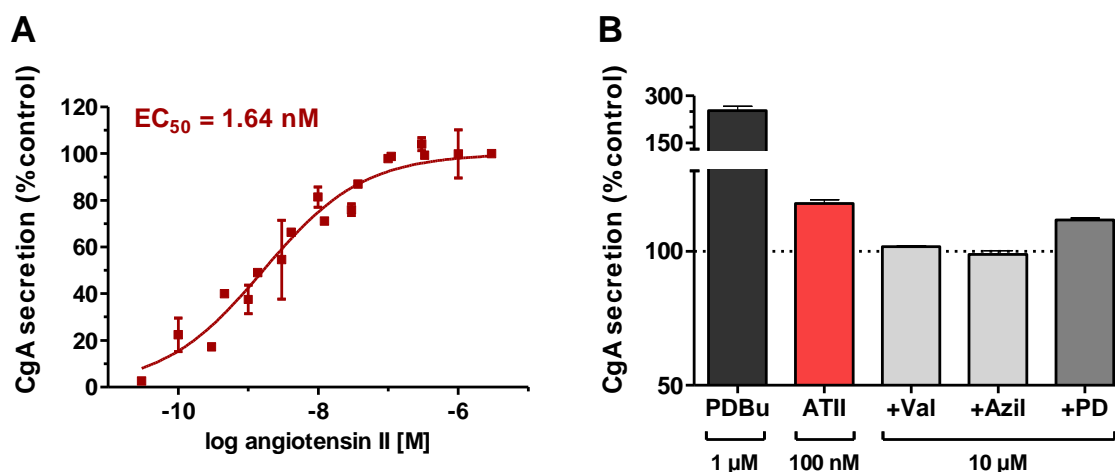


Figure 28 | Angiotensin II stimulates chromogranin A secretion in BON cells. (A) BON cells were incubated with increasing concentrations of angiotensin II for 6 h, the supernatants were collected and CgA secretion was determined by ELISA. (B) BON cells were preincubated with 10 μ M of the AGTR1 antagonists valsartan (Val) and azilsartan (Azil) or the AGTR2 antagonist PD123318 (PD) for 15 min before application of 100 nM angiotensin II (ATII). PDBu served as a positive control. After 24 h supernatants were collected and CgA secretion determined by ELISA. Data show mean \pm S.E.M. of n=3 (A) or n=2 (B). Obtained values were normalized on untreated control samples.

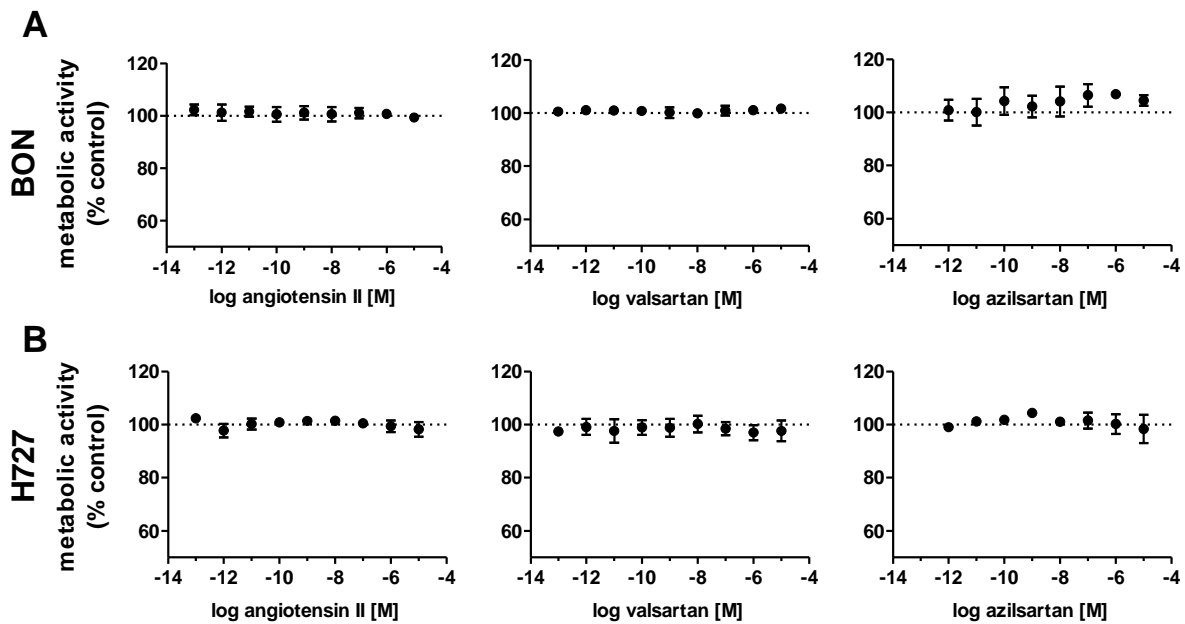


Figure 29 | Metabolic activity is not altered by angiotensin II, valsartan and azilsartan. BON (A) and H727 (B) cells were treated with increasing concentrations of angiotensin II (left), valsartan (middle) or azilsartan (right), incubated for 96 h and analyzed for metabolic activity. Data represent mean \pm S.E.M. (n=2-4).

In summary, stimulation of NET cells with angiotensin II induced changes in second messenger levels (Ca^{2+}) or phosphorylation of central kinases (ERK 1/2, Akt). Secretion of CgA, a biomarker for NETs, could be demonstrated, whereas no effect on tumor-related cell growth was detectable in the chosen experimental setup.

5.1.6 Generation of patient-derived xenografts as preclinical models

In search of preclinical models, that resemble human tumors more closely than permanent cell cultures, large panels of patient-derived xenografts (PDX) were developed over the past years. However, for rather slow growing neuroendocrine tumors, there is limited availability of such models so far. One aim of this work was the generation of NET xenografts in immunodeficient mice, to propagate tumor material and to use these models for future in vivo studies.

Table 4 gives an overview of the 16 NET tissues, which were obtained for PDX development. Tumor fragments were cryopreserved after surgery and thawed again prior to tissue preparation. The list comprises NETs of different origins such as stomach, colon, pancreas or ovaries, with Ki-67 levels ranging from 5 to 70 %. Most of them were metastatic tumors of grade two or three. Tissues were prepared as described in 4.6.2, until formation of rather homogeneous cell suspensions. They were subcutaneously injected into NOD scid gamma or scid beige mice and after weeks to months, depending on the tissue, tumor growth was observed in 6 of 16 cases, resulting in a take rate of 37 %. Successfully grown PDX tumors (highlighted in green, Table 4)

were mainly classified as poorly differentiated tumors of grade three, with high proliferation rates as indicated by their Ki-67 values, and five of them being from metastatic tissue.

Table 4 | Clinical characteristics of the tissues injected for PDX generation.

ID	Sex	Tissue type	Primary	Origin of tissue	Ki-67	Grade
T1S	m	primary	stomach	stomach	30 %	G3
T2P	f	metastasis	stomach	liver	20 %	G3
T3S	m	metastasis	rectum	liver	10 %	G2
T4J	m	metastasis	colon	liver	40 %	G3
T0	m	metastasis	pancreas	spleen	20 %	G2
T1	f	metastasis	CUP	ovary	66 %	G3
T2	f	metastasis	stomach	liver	20 %	G3/G2
T3	m	metastasis	ileum	liver	5 %	G2
T4	m	primary	stomach	stomach	30 %	G3
T5	m	metastasis	jejunum	liver	5 %	G2
T6	m	metastasis	CUP	liver	5 %	G2
T7	f	metastasis	rectum	ovary	10 %	G2
T8	f	metastasis	CUP	ovary	66 %	G3
T9	m	metastasis	pancreas	liver	70 %	G3
T10	f	metastasis	ileum	liver	10 %	G2
T11	f	metastasis	ileum	liver	1-15 %	G1/G2

After the initial engraftment (passage 0), mice were sacrificed and tumors explanted for analyses and further tissue propagation in additional mice. To verify the human origin of the xenograft, genomic DNA was isolated from both patient and xenograft (passage 0) tumors. PCR amplification was performed with species specific primers for GAPDH resulting in amplicon lengths of 256 bp (human) or 356 bp (mouse) as shown in Figure 30. Human and mouse DNA isolated from cell lines was included as a positive control for every run, but is only depicted exemplarily on the left. The upper panel visualizes the amplicons obtained for primary patient tissues, and as expected all of them only revealed one distinct band for human GAPDH. For the respective xenograft in the lower panel, bands appeared for human and mouse specific GAPDH. This indicated the preservation of the human origin of the tumor in the mouse, but also the infiltration of the xenograft with murine cells such as fibroblasts, endothelial cells and lymphocytes, which could be detected as well.

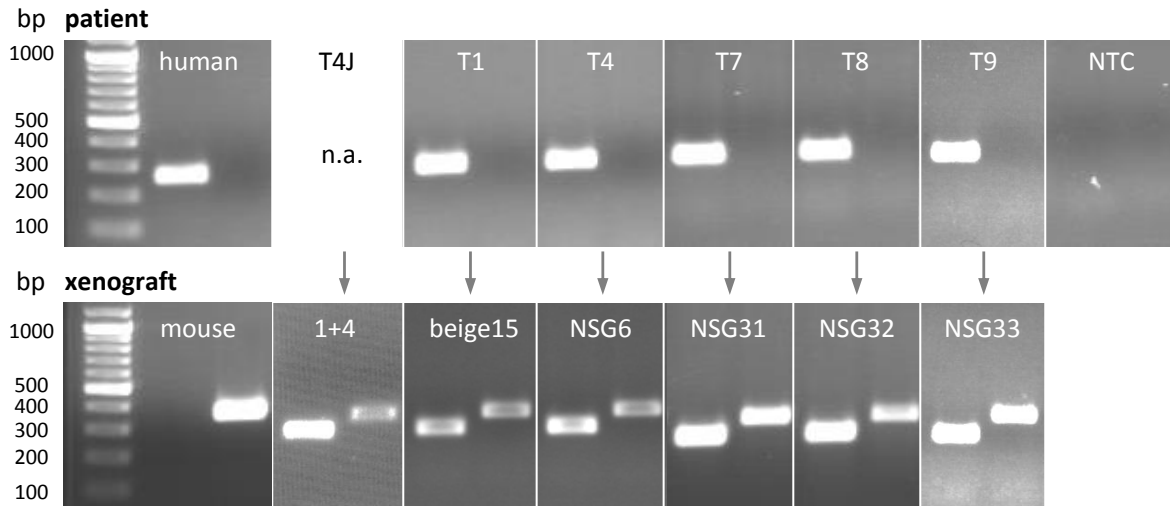


Figure 30 | Patient-derived NET xenografts maintain human origin. Genomic DNA was isolated from primary tumor patient (upper panel) and the corresponding xenograft mouse (lower panel) tissue. Human (left band, 256 bp) or mouse (right band, 356 bp) specific GAPDH was amplified by PCR and visualized on agarose gels. Bands are exemplarily shown for the first passage in mouse (passage 0). For tumor T4J, primary tumor tissue was not available (n.a.).

To obtain further insights into specific target expression of the xenografts, RNA was isolated from patient and xenograft tumors and investigated by RT-qPCR for their AGTR1 mRNA levels. Figure 31 shows an overview of AGTR1 gene expression in the primary tumor (if available) and the following xenografts in the mouse (up to passage 3) for all six engrafted NETs. They were compared to the NET cell lines BON, H727, QGP-1 and LCC-18 and to two pancreatic NET samples (pNET 1, 2) with high receptor expression.

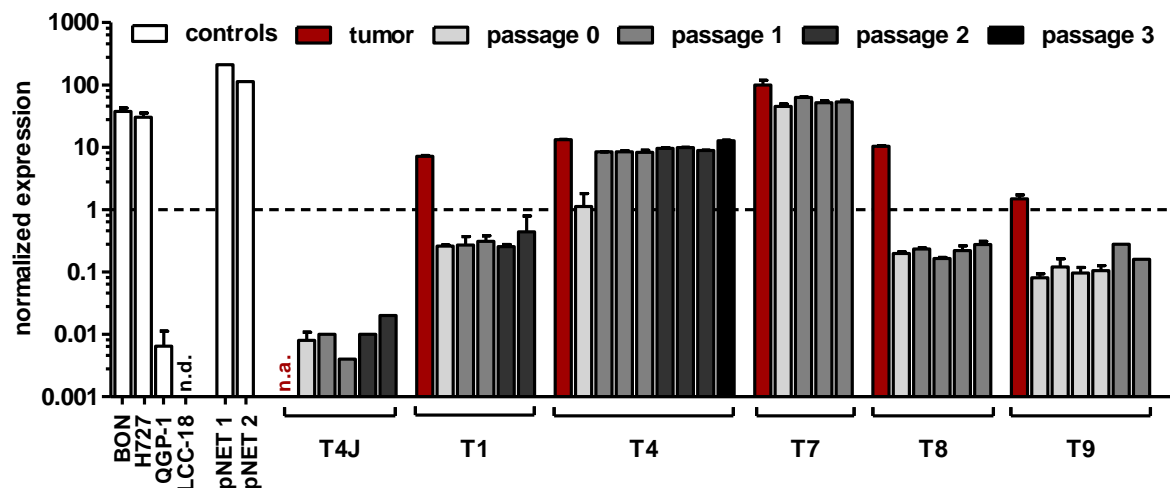


Figure 31 | Two PDX models maintain AGTR1 gene expression levels over several passages. Primary patient tumor and subsequent passages of mouse xenograft tissues were analyzed by RT-qPCR for their AGTR1 gene expression. They were compared to NET cell lines and two receptor-positive pancreatic NET samples (controls) for a better evaluation of expression levels. Values were normalized on UBC, HPRT1 and GAPDH. Bars show mean \pm S.D. (n=1-4). n.d., not detectable; n.a., not available.

Interestingly, AGTR1 levels seemed to be relatively high in the primary tumors, but were maintained over time only in two of them, namely T4 and T7. Their levels were found to be as high as of AGTR1-positive BON and H727 cells. Especially T7 was comparable to the pancreatic NETs, which exhibited the highest AGTR1 expression in the tested NET sample set. For the other PDX models, AGTR1 expression dropped 10- to 100-fold after their initial engraftment in the mouse, and therefore, these were scored as receptor-negative.

In addition to gene expression analyses, primary and xenograft tumors of T4 and T7 underwent autoradiographic protein detection. Unfortunately, both tumors of passage 0 were fixated before cryosectioning, making the tissue futile for autoradiographic detection. For the other tissues, as previously described, adjacent cryosections were incubated with radiolabeled ^{125}I -angiotensin II (^{125}I -ATII) in absence or in presence of angiotensin II (ATII), the AGTR1 specific antagonist valsartan or the AGTR2 specific antagonist PD123319 (Figure 32A). Although the primary tumor T4 showed only background levels of binding, the respective xenografts up to passage 3 yielded stronger signals, which could be displaced by angiotensin II and valsartan, but not PD123319. This was also reflected in the quantitative data obtained by gamma counter measurements (Figure 32B). Most probably, the lacking signal in the primary tumor was caused by an inadequate tissue quality.

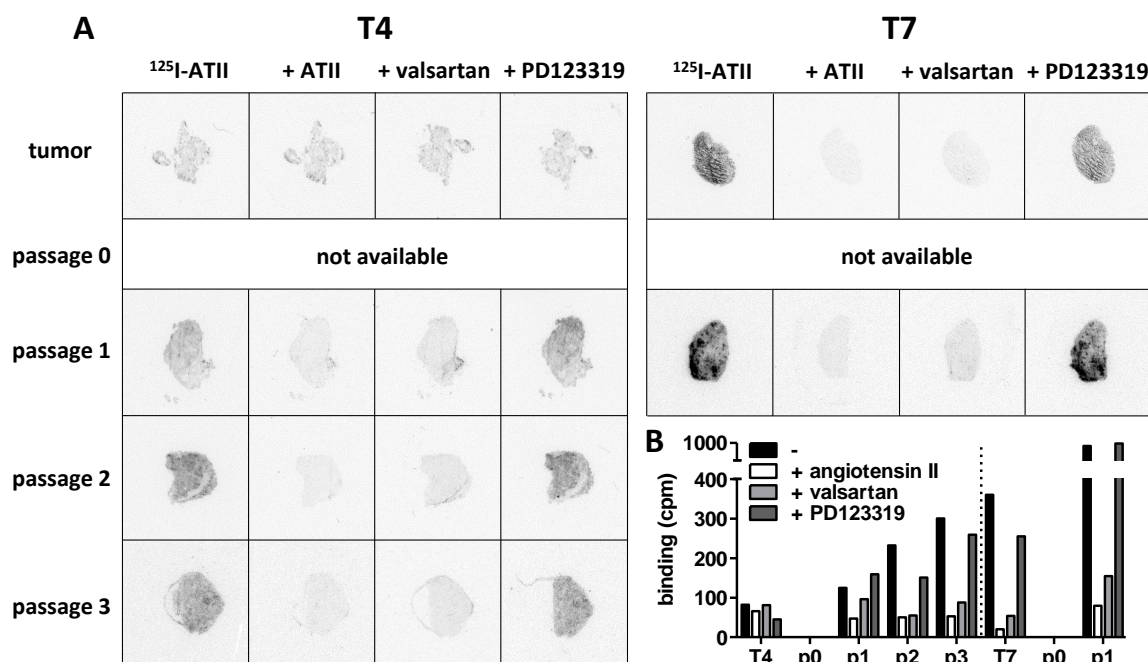


Figure 32 | In vitro receptor autoradiography of AGTR1-positive PDX tissues. (A) Adjacent cryosections of primary (tumor) and PDX NET tumors (passages 0-3, p0-p3) were either incubated with ^{125}I -angiotensin II alone (^{125}I -ATII, total binding) or in the presence of additional 1 μM unlabeled angiotensin II (ATII), AGTR1 antagonist valsartan or AGTR2 antagonist PD123319 (non-specific binding). **(B)** Sections were wiped off after autoradiography and the counts per minute (cpm) measured with a gamma counter. Depicted are the results of one experiment ($n=1$).

In contrast, T7 revealed strong binding in all tested tumors, which was also AGTR1 specific as indicated by successful displacement with valsartan. The elevated AGTR1 mRNA levels as measured by RT-qPCR could be confirmed by autoradiography at protein level as well, especially for T7.

For both PDX models appropriate target expression was verified, making them useful tools for future in vivo imaging or therapeutic studies. In addition to the investigated AGTR1, xenografts could be also tested for expression of other interesting receptors.

5.2 The combinatorial potential of mTOR inhibitors and PRRT in NET cells

Peptide receptor radionuclide therapy (PRRT) showed very promising results in the treatment of NETs so far. Nevertheless, complete remissions are very rare, raising the need for adjuvant agents, which might improve the outcome of PRRT. In this second part of the results section, the effect of the mTOR inhibitors temsirolimus and everolimus on five NET cell lines was investigated. First of all, they were applied as single drugs to evaluate their effects on a comprehensive panel of NET cell lines. In the following, the mTOR inhibitor temsirolimus was preferentially used in combination with radiotherapy. External beam irradiation was utilized as a model system, before preliminary experiments with lutetium-coupled somatostatin analogs were performed in a SSTR2-transfected cell line.

5.2.1 Effect of mTOR inhibitors on NET cells

To evaluate the effect of the mTOR inhibitors temsirolimus and everolimus on neuroendocrine tumor cells, five NET cell lines from different organs of origin were studied: BON, QGP-1 (both pancreas), LCC-18 (colon) as well as H727 and UMC-11 (both pulmonary). The cells were incubated with one of the two mTOR inhibitors and two parameters of cell viability were determined after 96 h: metabolic activity and cell number. In both assays, temsirolimus and everolimus led to a biphasic inhibition of cell viability in all five NET cell lines (Figure 33), displaying similar concentration-response curves. Metabolic activity as well as cell number decreased while inhibitor concentrations increased, with two calculated IC_{50} values in the nanomolar and micromolar range, respectively (Table 5). The low nanomolar IC_{50} differed only slightly between cell lines and assays (around 1 nM), whereas the higher, micromolar IC_{50} demonstrated greater variation.

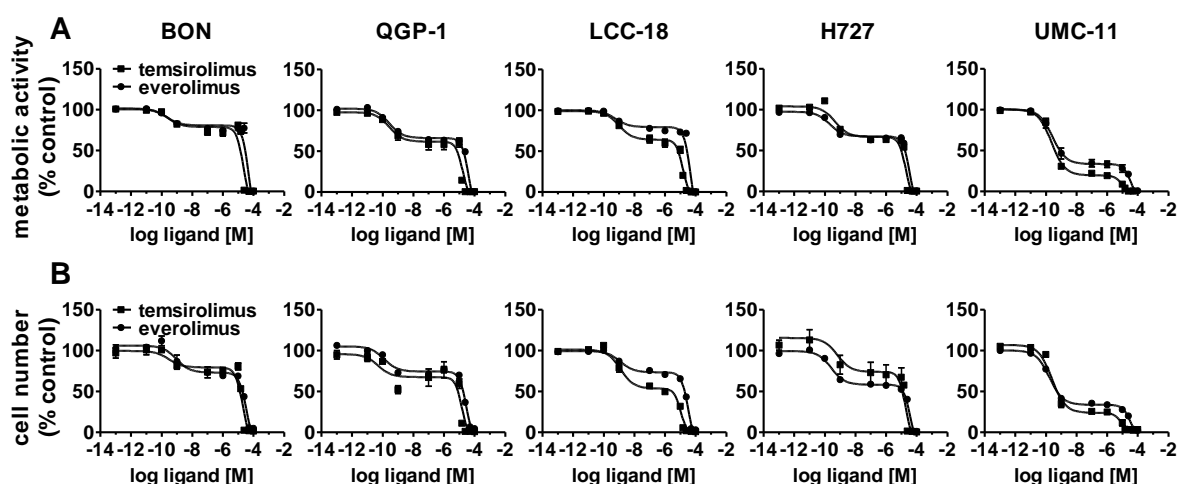


Figure 33 | Treatment with mTOR inhibitors results in a biphasic inhibition of NET cell viability. NET cell lines were treated with increasing concentrations of temsirolimus or everolimus (0.1 pM to 100 μ M), incubated for 96 h and analyzed for metabolic activity (A) and cell number (B). Data represent mean \pm S.E.M. (n=3).

Table 5 | Summary of IC₅₀ values for mTOR inhibitors.

	temsirolimus				everolimus			
	metabolic activity		cell number		metabolic activity		cell number	
	IC ₅₀ low	IC ₅₀ high						
BON	0.26 nM	21.28 µM	0.29 nM	20.61 µM	0.21 nM	48.87 µM	0.92 nM	33.96 µM
QGP-1	0.27 nM	16.67 µM	0.05 nM	15.21 µM	0.27 nM	39.54 µM	0.12 nM	22.28 µM
LCC-18	0.99 nM	15.03 µM	1.23 nM	10.74 µM	0.58 nM	46.24 µM	1.21 nM	31.26 µM
H727	0.47 nM	19.32 µM	0.65 nM	18.85 µM	0.21 nM	34.04 µM	0.26 nM	36.48 µM
UMC-11	0.23 nM	9.08 µM	0.25 nM	8.18 µM	0.27 nM	34.44 µM	0.17 nM	30.76 µM

Here, values ranged from 8 to 21 µM for temsirolimus and from 30 to 48 µM for everolimus. A parameter, which is not included in the IC₅₀ value, is the efficacy of a substance, i.e. the amplitude of the effect. In the nanomolar dose range, the inhibitors affected cell viability by 20-75 %, with BON being the most resistant cell line (20 %) and UMC-11 the most sensitive (75 %). In contrast, when applying high micromolar concentrations, all NET cell lines eventually showed a complete decline of cell viability.

To further investigate the inhibitors' potency regarding long-term cell survival and proliferation, clonogenic assays were performed. Now, cells were followed up for 1-2 weeks and their capability to form colonies after treatment was assessed. Data were quantified as percent covered well area as a measure for colony formation and cell survival. In general, results confirmed the findings obtained from metabolic activity and cell number assays. However, the biphasic pattern could not be reproduced, possibly due to the smaller concentration range used for this assay. Both inhibitors led to similar response curves, with the most profound effect on UMC-11, as expected, but also on H727 cells (Figure 34). In contrast to the cell viability assays, even low nanomolar concentrations (1 nM, 10 nM) strongly inhibited cell proliferation in these pulmonary cell lines by 40-70 % for H727 and even by 85-95 % for UMC-11. When applying micromolar concentrations, no colonies were detectable at all. The other cell lines seemed to be more resistant to treatment with nanomolar concentrations, but showed moderate inhibition by around 30-60 % (BON), 30-70 % (QGP-1) and 20-60 % (LCC-18) in the micromolar range for both substances.

As mTOR inhibitors are known to inhibit cell cycle progression in G1 phase, it was tested, how pronounced this effect would be manifested in the different NET cell lines and whether this could be correlated to the variable reaction pattern seen before. Cell cycle analysis was performed by flow cytometry 24 h to 96 h after treatment. Both inhibitors induced an accumulation of cells in G1 cell cycle phase after 24 h, though to different extents depending on the cell line (Figure 35). QGP-1 demonstrated the highest increase of G1 cells, from 61.1 to 74.7 % for temsirolimus and from 55.4 to 80.1 % for everolimus (Table 6).

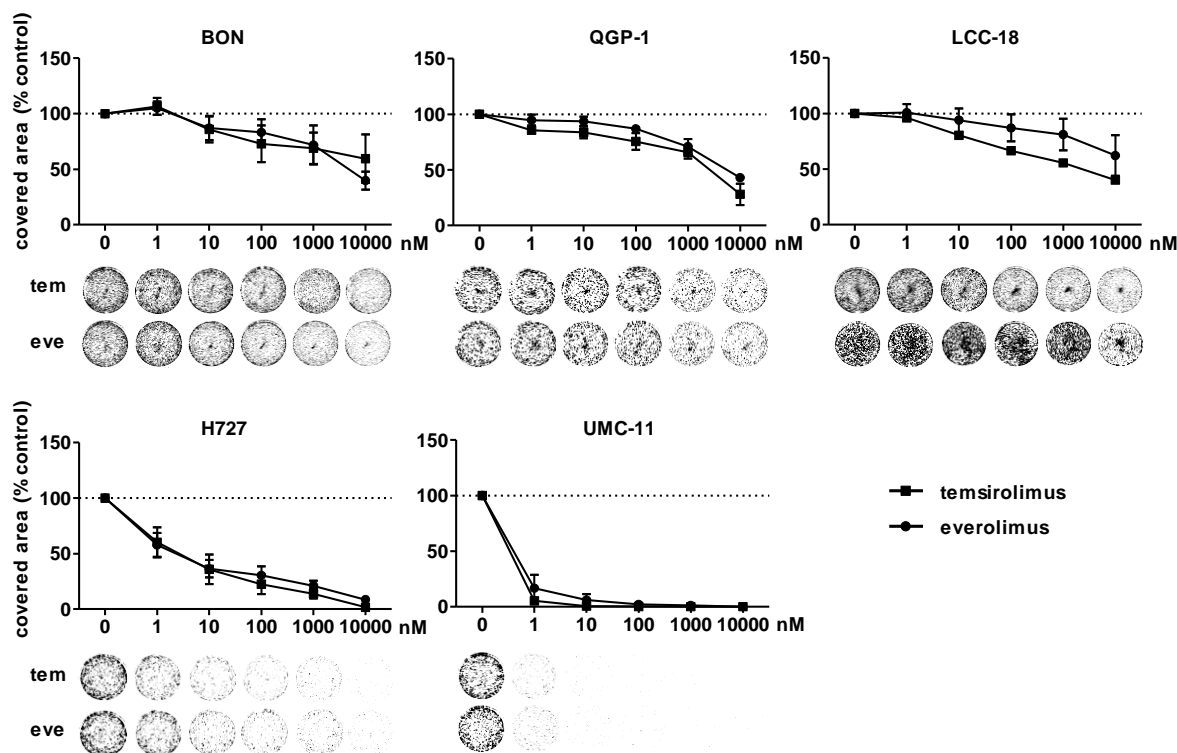


Figure 34 | Clonogenic survival of NET cell lines is affected by mTOR inhibitors. NET cell lines were seeded at low density, treated with increasing concentrations of temsirolimus (tem) or everolimus (eve) and incubated for 1-2 weeks until colony formation. Data were normalized to untreated controls and represent mean \pm S.E.M. (n=3-4) or mean only (LCC-18 treated with temsirolimus, n=1).

However, this seemed to be a rather transient state, as percentages leveled out again after 72 h, at the latest. Graphical representations of the data for 48, 72 and 96 h after treatment can be found in the supplementary Figure S7. Likewise, BON and LCC-18 cells showed an accumulation in G1 of 6-12 % after 24 h, which also adjusted over time. H727 cells were not affected at all, with G1 percentages remaining almost equal during the considered time period.

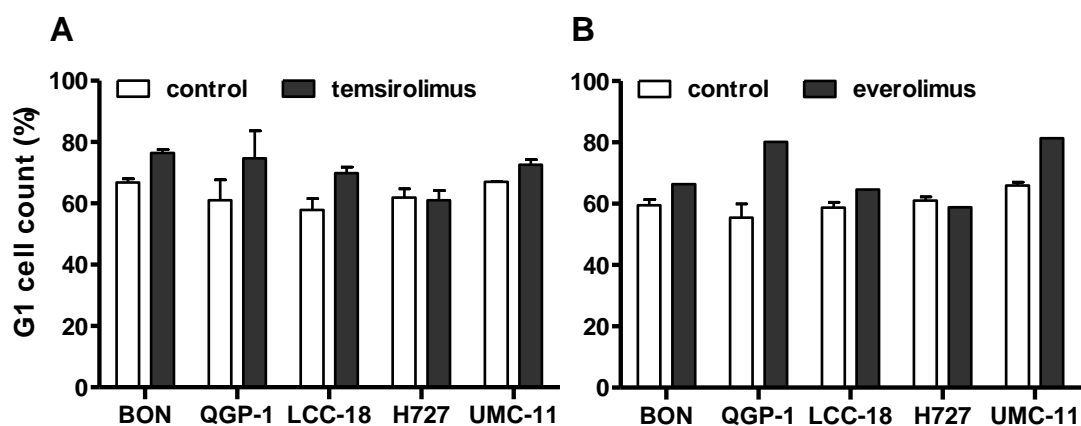


Figure 35 | Increased accumulation of cells in G1 phase after mTOR inhibitor treatment. NET cell lines were treated with vehicle and 1 μ M temsirolimus (A) or everolimus (B). After 24 h incubation samples were collected for cell cycle analysis by flow cytometry. Data are shown as bar diagrams with mean \pm S.E.M. of n=2 (A) or n=1-2 (B).

Table 6 | Percentages of cells in G1 phase after mTOR inhibitor treatment. Data show mean \pm S.E.M. (n=2) or mean only (n=1).

	24h		48h		72h		96h	
	0	1 μ M	0	1 μ M	0	1 μ M	0	1 μ M
temsirolimus								
BON	66.8 \pm 1.2	76.4 \pm 1.1	65.9 \pm 1.8	66.2 \pm 2.1	67.7 \pm 0.1	69.5 \pm 1.4	64.8 \pm 2.7	65.0 \pm 3.3
QGP-1	61.1 \pm 6.7	74.7 \pm 9.0	65.5 \pm 13.8	77.4 \pm 3.8	79.4 \pm 6.4	76.5 \pm 4.4	82.7 \pm 2.3	79.6 \pm 6.0
LCC-18	57.8 \pm 3.7	69.9 \pm 2.0	65.5 \pm 4.8	69.6 \pm 3.9	64.3 \pm 6.1	64.1 \pm 3.3	68.7 \pm 4.6	64.1 \pm 3.3
H727	61.9 \pm 2.8	61.1 \pm 3.1	59.5 \pm 0.6	61.3 \pm 2.5	57.2 \pm 2.3	60.6 \pm 1.0	58.0 \pm 0.8	63.7 \pm 3.4
UMC-11	67.0 \pm 0.2	72.5 \pm 1.7	64.3 \pm 3.7	79.1 \pm 1.8	69.3 \pm 2.3	73.4 \pm 7.4	69.8 \pm 0.2	74.1 \pm 0.5
everolimus								
BON	59.5 \pm 1.9	66.6	63.0 \pm 1.5	68.3	66.9 \pm 0.9	70.6		
QGP-1	55.4 \pm 4.5	80.1	75.9 \pm 0.6	79.6	75.7 \pm 3.1	79.4		
LCC-18	58.7 \pm 1.8	64.6	68.1 \pm 0.1	71.1	63.8 \pm 2.7	67.6		
H727	61.1 \pm 1.1	58.8	60.3 \pm 0.2	66.5	61.3 \pm 0.1	63.4		
UMC-11	65.9 \pm 1.0	81.4	61.3 \pm 0.5	83.0	60.6 \pm 0.5	74.0		

Only UMC-11, identified as the most sensitive cell line when studying cell viability and survival, demonstrated constantly elevated G1 percentages at all time points. They reached an increased accumulation of G1 cells by 5-15 % for temsirolimus and even 14-22 % for everolimus. The effects observed after treatment with 1 μ M could be also reproduced with concentrations of 10 μ M, 100 nM and 10 nM, but to a lesser extent with 1 nM (data not shown). Obviously, the G1 accumulation was induced at a certain threshold and did not increase dose-dependently.

Loss of cell viability and changes in cell cycle progression are cellular reactions towards changed signaling cascades after treatment. Consequently, the effect of an inhibitor is related to the underlying dysregulation of the targeted molecule or pathway in the cell. By western blotting it was analyzed, how selected intracellular effector proteins were affected by mTOR inhibitor treatment in the different NET cell lines. Results are exemplarily shown for everolimus in Figure 36. p70S6 kinase, involved in cell growth and cell cycle progression, is known to be directly activated by mTOR and therefore, mTOR inhibition should lead to its decreased activation or phosphorylation, respectively. As expected, this was confirmed in all five NET cell lines, after incubation with 1 nM or 100 nM everolimus for 6 or 24 h. On the contrary, phospho-Akt levels increased when inhibiting mTOR, especially in BON and H727 cells. In UMC-11, phospho-Akt was barely detected, and also in QGP-1 cells it was very low, although total Akt was constantly expressed. Interestingly, the low dose of everolimus led to higher phospho-Akt levels and the higher dose to less Akt phosphorylation, as seen for BON and H727 cells. Phosphorylation status of ERK 1/2 was not affected in most cell lines, only BON showed slightly increased levels after treatment with everolimus. Both caspase-3 and PARP, markers for apoptosis, were not cleaved

upon treatment with the applied nanomolar concentrations of everolimus. Possibly, changes would be detectable in the micromolar range or after longer incubation times. Since everolimus and temsirolimus showed comparable reaction patterns in all assays before, temsirolimus most likely induces the same signaling cascades in the investigated cell lines.

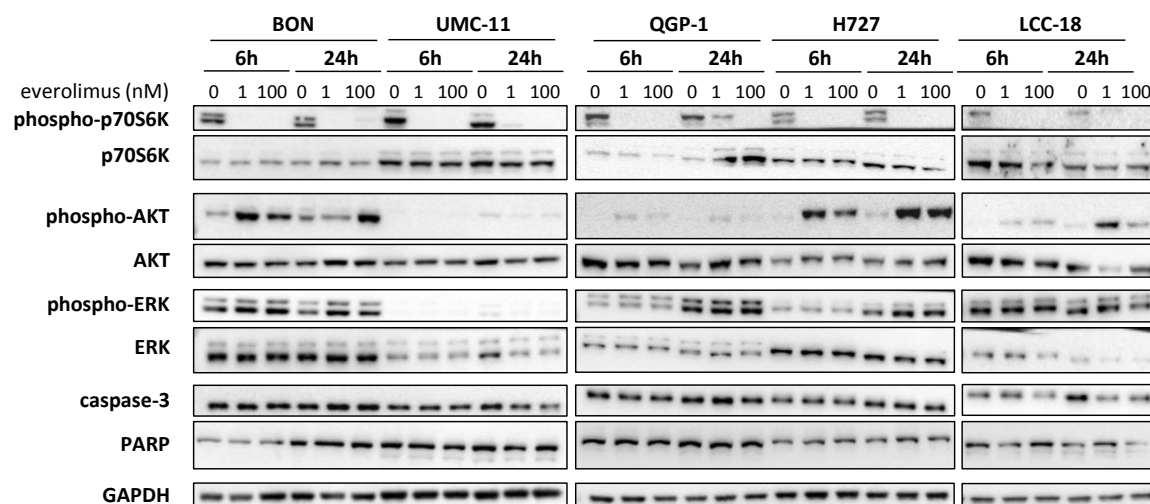


Figure 36 | Effect of everolimus on intracellular signaling molecules. NET cell lines were treated with vehicle or everolimus (1 nM, 100 nM) and harvested after 6 h and 24 h. Equal amounts of protein were separated on SDS gels and the indicated molecules detected after western blotting. Depicted are the blots of one experiment (n=1).

In summary, both mTOR inhibitors showed antiproliferative activity in all five NET cell lines, caused by suppression of the mTOR signaling pathway and G1 cell cycle arrest. However, the cell lines differed in their reaction patterns towards treatment, depending on counteracting regulations and the extent and duration of G1 cell accumulation. Whereas the rather resistant BON cells exhibited only a transient G1 arrest, but increased phospho-Akt levels, the most sensitive UMC-11 cells showed persistent G1 arrest and barely detectable phosphorylation of Akt.

5.2.2 Radiation-induced effects on NET cells

Before combining mTOR inhibitor treatment with irradiation, the sole impact of irradiation on NET cells was assessed by analysis of cell viability and cell cycle distribution. A single radiation dose of 0-10 Gy was applied to the cells using an external caesium-137 source, which is a combined beta and gamma emitter. Cell viability assays revealed a dose-dependent reduction of metabolic activity and cell number in all investigated NET cell lines (Figure 37A). However, cell numbers seemed to be the more appropriate readout, showing a distinct reduction by 60-80 % versus 20-40 % when determining metabolic activity. After irradiation, cells obviously increase their metabolism to counteract radiation-induced damages, leading to a falsification of results shortly after exposure [165], [166].

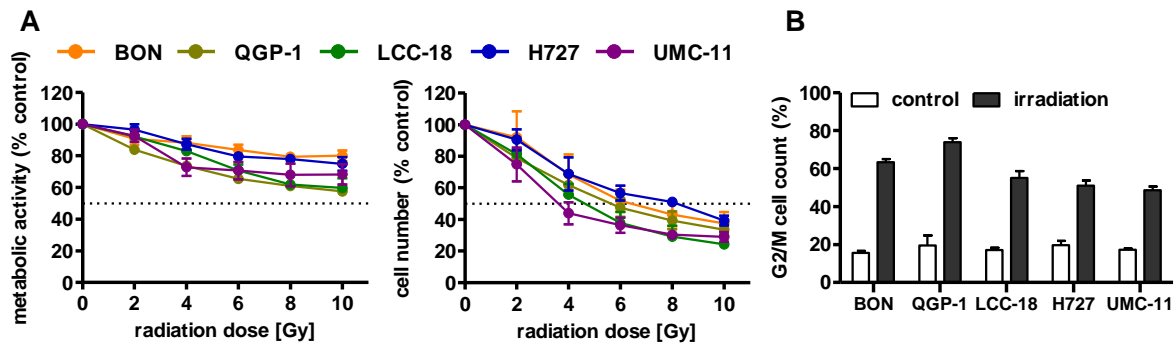


Figure 37 | Irradiation leads to reduced cell viability and G2/M accumulation of NET cells. (A) NET cell lines were irradiated with doses of 0 to 10 Gy, incubated for 96 h and analyzed for metabolic activity and cell number. Data represent mean \pm S.E.M. (n=3). **(B)** NET cell lines were irradiated with 10 Gy and samples were collected after 24 h for cell cycle analysis by flow cytometry. Data are shown as bar diagrams with mean \pm S.E.M. (n=2-3).

The investigated NET cell lines revealed slight differences in their susceptibility to radiation. The dose required to lower cell numbers by 50 % was around 8 Gy for H727, 6 Gy for BON and QGP-1 or 4 Gy for UMC-11 and LCC-18.

In comparison to G1 cell cycle arrest after mTOR inhibitor treatment, irradiation with 10 Gy resulted in a strong accumulation of cells in G2/M cell cycle phase after 24 h (Figure 37B). QGP-1 cells reached the greatest increase by 55 %, followed by BON (48 %), LCC-18 (38 %), H727 (31 %) and UMC-11 (31 %) as indicated in Table 7. This G2/M cell cycle arrest was retained over time until 96 h after irradiation in all cell lines, although percentages partly decreased (also see supplementary Figure S8).

Table 7 | Percentages of cells in G2/M cell cycle after irradiation. Data show mean \pm S.E.M. (n=2-3).

	24h		48h		72h		96h	
	0	10 Gy						
BON	15.6 \pm 1.0	63.3 \pm 1.6	16.3 \pm 0.4	54.5 \pm 2.4	17.0 \pm 0.6	41.7 \pm 2.5	17.0 \pm 1.5	38.1 \pm 0.6
QGP-1	19.4 \pm 5.3	73.9 \pm 2.1	18.7 \pm 7.3	53.0 \pm 3.2	9.9 \pm 3.0	46.9 \pm 3.0	8.9 \pm 1.2	43.2 \pm 1.9
LCC-18	17.0 \pm 1.2	55.0 \pm 3.8	12.5 \pm 2.7	48.0 \pm 0.9	11.5 \pm 1.2	42.8 \pm 2.2	10.0 \pm 1.6	33.9 \pm 0.3
H727	19.6 \pm 2.2	50.9 \pm 2.8	19.8 \pm 1.5	52.4 \pm 1.4	20.1 \pm 1.2	45.1 \pm 1.6	21.1 \pm 2.0	37.9 \pm 2.1
UMC-11	17.1 \pm 0.7	48.5 \pm 2.0	19.1 \pm 2.0	62.7 \pm 1.1	15.5 \pm 0.6	51.2 \pm 3.3	13.9 \pm 0.9	47.5 \pm 2.6

5.2.3 Additive effect of temsirolimus and irradiation on NET cells

After studying the single effects of mTOR inhibitors and irradiation on NET cells, the outcome of their combination was assessed and analyzed by cell number and survival assays as well as cell cycle distribution. All following combinatorial experiments were exemplarily performed with temsirolimus.

The five NET cell lines under investigation were pretreated with temsirolimus for 24 h, subsequently irradiated and incubated for further 96 h. As before, cell numbers declined when applying increasing doses of temsirolimus (Figure 38A, orange line) or radiation (Figure 38B, orange line). However, the combination of both reduced cell numbers to a greater extent, especially in the low nanomolar range. UMC-11 cells were already dramatically affected by temsirolimus alone; therefore, the additive effect of irradiation was rather moderate when compared to BON, QGP-1 or LCC-18. The biphasic inhibition pattern of temsirolimus was retained after irradiation, although the curve slopes flattened out with increasing radiation doses (Figure 38A). For a detailed analysis, Figure 39 exemplarily shows the results when combining temsirolimus at a dose of 1 nM, and 1 μ M respectively, with 4 Gy. For both doses, the sequential treatment resulted in a higher reduction of cell numbers than the respective single treatments. In the case of pretreatment with 1 μ M, cell numbers for BON and UMC-11 decreased significantly when compared to irradiation alone (Figure 39B). However, cell numbers were only slightly higher after pretreatment with 1 nM, indicating that lower doses could be sufficient to achieve a similar effect when applied in combination.

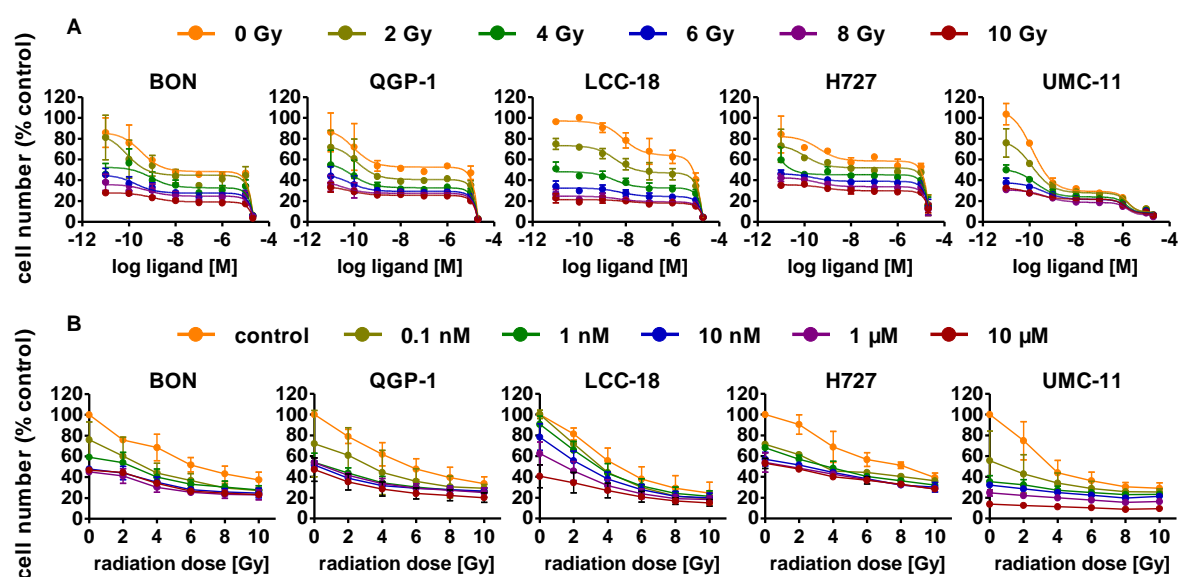


Figure 38 | Additive effect of temsirolimus and irradiation on NET cell numbers. NET cell lines were pretreated with increasing concentrations of temsirolimus (0.01 nM to 20 μ M) for 24 h before irradiation. Cell number was determined 96 h after irradiation with different doses of 0 to 10 Gy. Graphs show mean \pm S.E.M. (n=2-3). Data are represented in two different ways, either with temsirolimus concentration (A) or radiation dose (B) plotted on the x-axis.

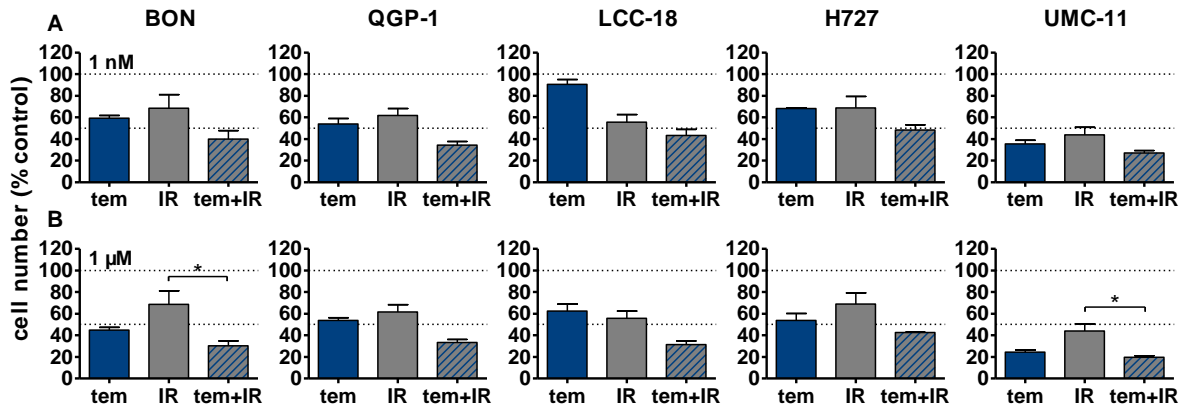


Figure 39 | Detailed analysis of cell numbers for combined treatment of temsirolimus and 4 Gy. NET cell lines were pretreated with 1 nM (A) or 1 μ M (B) temsirolimus for 24 h before irradiation with 4 Gy. Cell number was determined 96 h after irradiation. Graphs show mean \pm S.E.M. (n=2-3). Evaluated with one-way ANOVA (Kruskal-Wallis test) and Dunn's posttest, * $P \leq 0.05$. tem, temsirolimus; IR, irradiation.

In addition, clonogenic survival assays were included to evaluate the impact of combined treatment over a longer time period. For this, NET cells were irradiated with 0 to 4 Gy after preincubation with temsirolimus and followed up for 1-2 weeks. In general, combination of both resulted in clearly impaired cell survival in comparison to the single treatments (Figure 40). Interestingly, curves retained their cell line specific slope and shape independent of the applied radiation dose. Radiation doses higher than 4 Gy resulted in barely visible colonies in the wells (data not shown). This is in strong contrast to the short-term cell number assays, where the highest dose of 10 Gy still resulted in detectable signals (Figure 38). To some extent, cell death could not be measured by the cell number assay, and occurred beyond the observed time frame of only 96 h. Irradiation with 4 Gy inhibited cell numbers only by 30 % (BON), 40 % (QGP-1), 30 % (H727) and 55 % (UMC-11) (compare Figure 39). Cell survival on the other hand was lowered by 45 % (BON), 55 % (QGP-1), 75 % (H727) and 90 % (UMC-11), as depicted in Figure 41. Only LCC-18 cells exhibited a higher reduction of cell numbers (45 %) instead of cell survival (15 %), possibly arising from the semi-adherent nature of this cell line, which hardly generated colonies but rather stayed in single cell formation. In BON and H727, pretreated with 1 nM temsirolimus, and in QGP-1, pretreated with 1 μ M, additional irradiation with 4 Gy significantly decreased cell survival in comparison to temsirolimus alone (Figure 41). The beneficial impact of a combined treatment regimen was visible in all cell lines and lowered cell survival down to ≤ 20 %, especially when applying 1 μ M temsirolimus, but also 1 nM yielded noticeable results, in particular in the pulmonary cell lines H727 and UMC-11. However, in UMC-11, treatment with 1 nM temsirolimus already dramatically impaired cell survival. In consistence with the previously performed cell number assay, additional irradiation only led to marginal alterations.

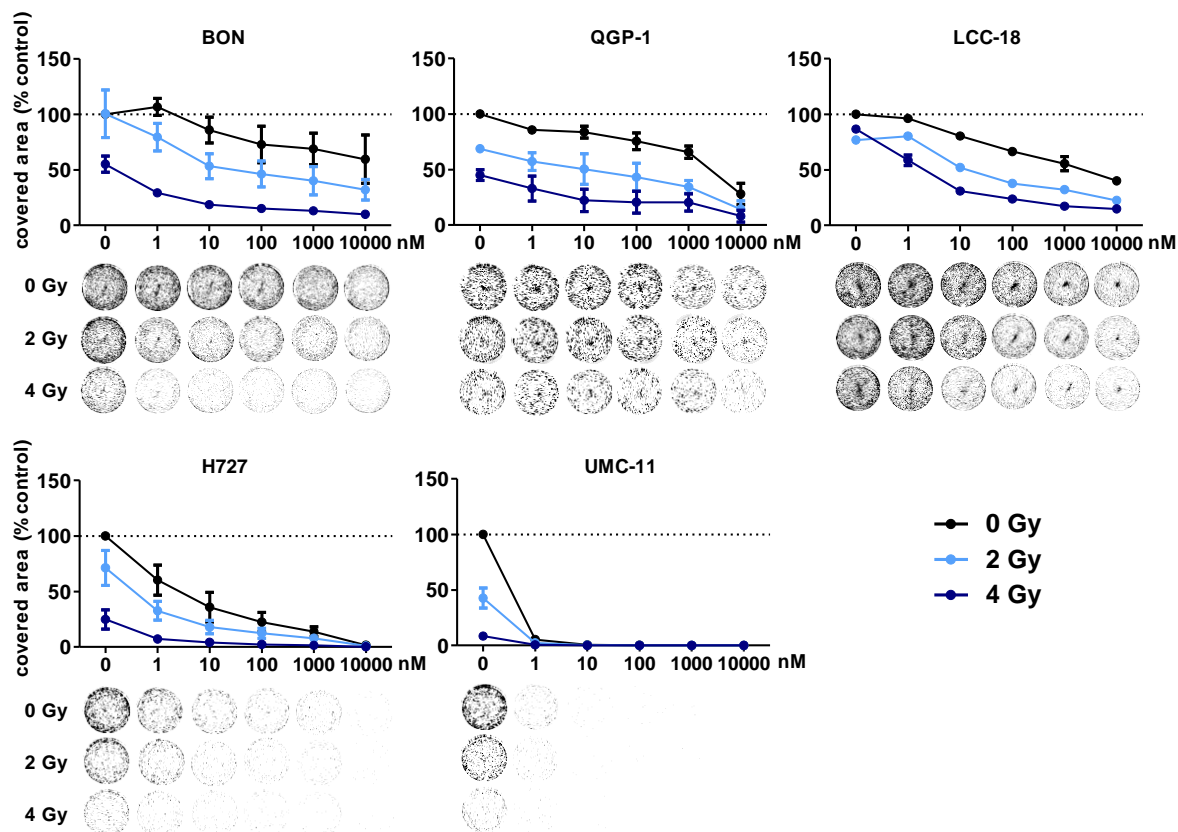


Figure 40 | Additive effect of temsirolimus and irradiation on NET cell survival. NET cell lines were seeded at low density, treated with increasing concentrations of temsirolimus for 24 h before irradiation with 0 to 4 Gy. Cells were incubated for 1 to 2 weeks until colony formation. Data were normalized to untreated controls and represent mean \pm S.E.M. (n=3) or mean \pm S.D. (n=1, LCC-18).

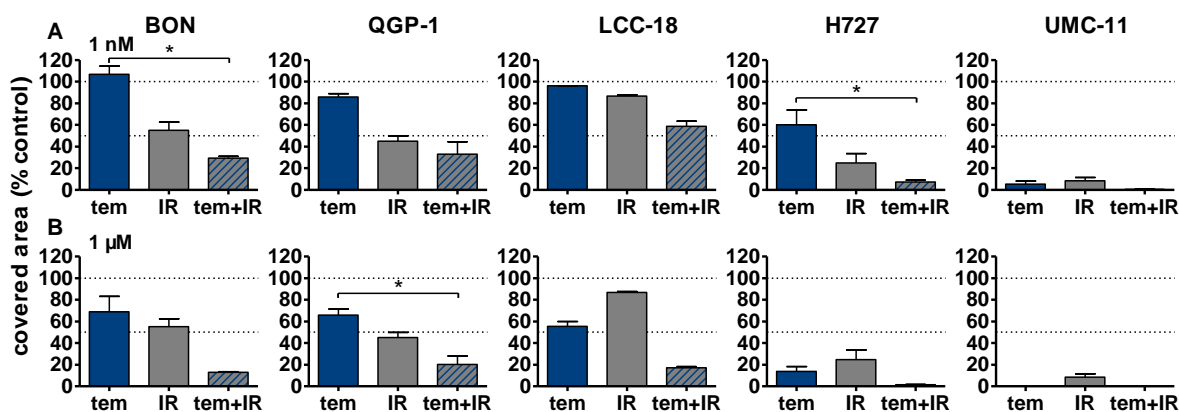


Figure 41 | Detailed analysis of cell survival for combined treatment of temsirolimus and 4 Gy. NET cell lines were pretreated with 1 nM (A) or 1 μ M (B) temsirolimus for 24 h before irradiation with 4 Gy. Cell survival was determined 1-2 weeks after irradiation. Graphs show mean \pm S.E.M. (n=3) or mean \pm S.D. (n=1, LCC-18). Evaluated with one-way ANOVA (Kruskal-Wallis test) and Dunn's posttest, except LCC-18, * $P \leq 0.05$. tem, temsirolimus; IR, irradiation.

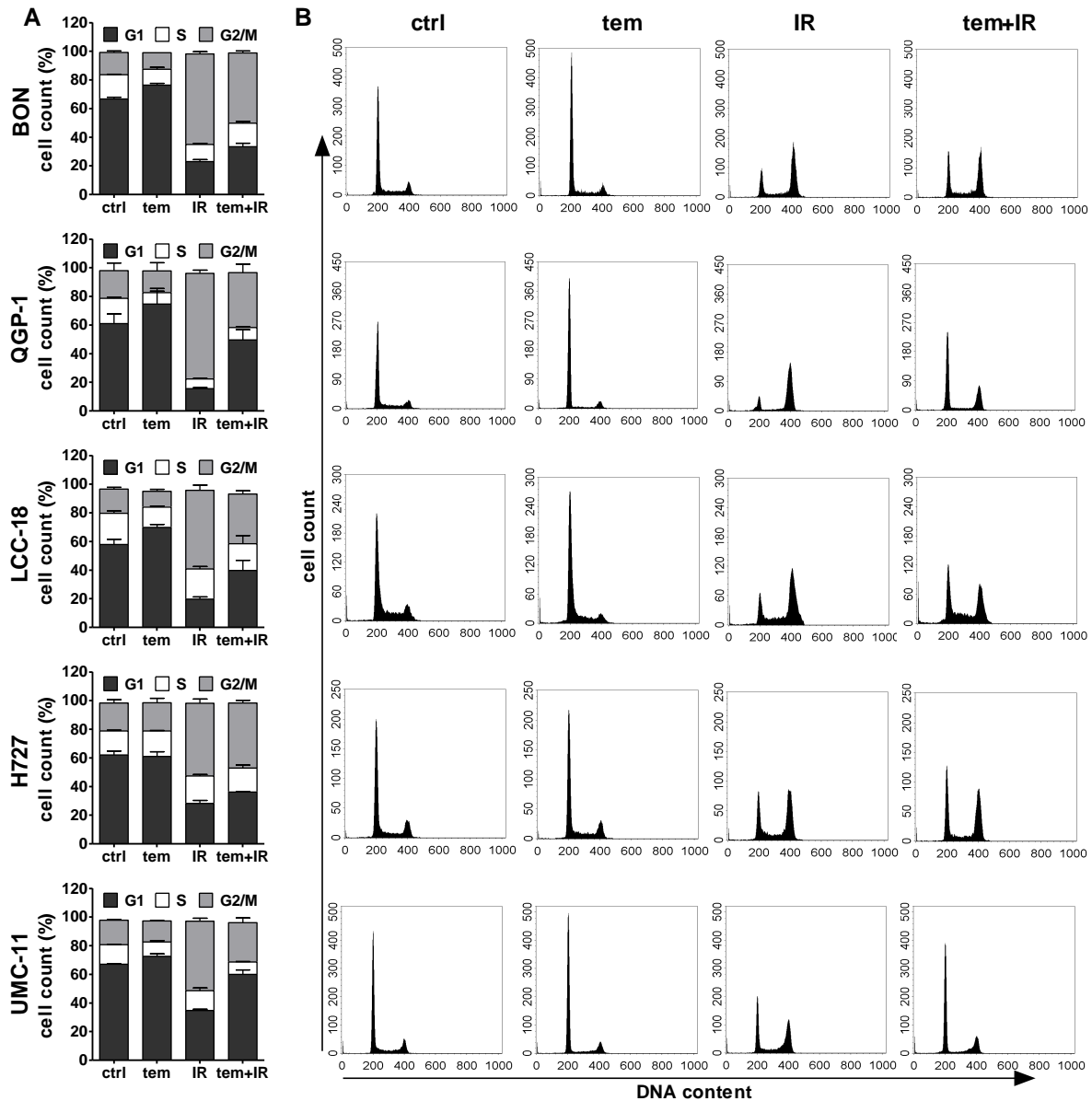


Figure 42 | Temsirolimus pretreatment abrogates radiation-induced G2/M cell accumulation. NET cell lines were incubated with 1 μ M temsirolimus (tem) or vehicle (ctrl) for 24 h before irradiation. For assessment of cell cycle distribution pretreated NET cells were collected 24 h after irradiation with 10 Gy (IR, tem+IR), stained with propidium iodide and analyzed by flow cytometry. Data are shown as bar diagrams with mean \pm S.E.M. (n=2-3) (A) or as DNA histograms of one representative experiment (B).

Table 8 | Percentages of cells in G1 and G2/M cell cycle 24 h after irradiation. Data show mean \pm S.E.M. (n=2-3).

	G1				G2/M			
	ctrl	tem	IR	tem + IR	ctrl	tem	IR	tem + IR
BON	66.7 \pm 1.2	76.4 \pm 1.1	22.9 \pm 1.5	33.4 \pm 2.4	15.6 \pm 1.0	11.5 \pm 0.0	63.3 \pm 1.6	49.1 \pm 1.5
QGP-1	61.1 \pm 6.7	74.7 \pm 9.0	15.6 \pm 0.6	49.5 \pm 7.2	19.4 \pm 5.3	15.2 \pm 5.7	73.9 \pm 2.1	38.4 \pm 5.9
LCC-18	57.8 \pm 3.7	69.9 \pm 2.0	19.7 \pm 1.5	39.7 \pm 7.1	17.0 \pm 1.2	11.0 \pm 1.5	55.0 \pm 3.8	34.8 \pm 2.2
H727	61.9 \pm 2.8	61.1 \pm 3.1	28.2 \pm 1.9	36.3 \pm 0.2	19.6 \pm 2.2	19.8 \pm 3.1	50.9 \pm 2.8	45.3 \pm 1.9
UMC-11	67.0 \pm 0.2	72.5 \pm 1.7	34.7 \pm 0.8	59.9 \pm 3.2	17.1 \pm 0.7	14.7 \pm 0.1	48.5 \pm 2.0	27.4 \pm 3.3

The previous analysis of cell cycle distribution following the respective single treatments revealed increased cell accumulation in G1 cell cycle phase after mTOR inhibitor treatment, or in G2/M cell cycle phase after irradiation. Now, the combined effect of both was evaluated by preincubating the respective cell lines with 1 μ M temsirolimus for 24 h before irradiating them with 10 Gy. In all five NET cell lines, mTOR inhibitor pretreatment resulted in an abrogated radiation-induced G2/M arrest after 24 h (Figure 42). Correspondingly, percentages of cells in G1 increased. In QGP-1 cells, the impact of combined treatment on cell cycle distribution was most profound. Compared to irradiation only, the G2/M fraction decreased by 36 % (from 74 to 38 %), while cells in G1 increased by 34 % (from 16 to 50 %) (Table 8). Similarly, UMC-11 showed reduction of G2/M by 22 % and a G1 increase of 25 %, followed by LCC-18 cells with 20 % G2/M reduction and 20 % G1 increase, as well as BON showing 14 % decrease of G2/M and 10 % increase of G1. Even in H727 cells, which did not show any G1 cell accumulation when applying temsirolimus alone, combined treatment led to an increase of the G1 fraction by 8 % after 24 h. This abrogated G2/M arrest after combinatorial treatment was maintained over time in UMC-11 and H727 up to 96 h (see supplementary Figure S9), whereas it diminished after 48 h in BON and LCC-18 cells. QGP-1 cells slowly returned to the irradiation-like cell cycle distribution with complete adjustment after 96 h. At the later time points, the sub-G1 cell cycle phase as a measure for nuclear debris in this case, was clearly increased after irradiation only or after combination with temsirolimus pretreatment in all investigated cell lines.

In summary, combination of mTOR inhibitor treatment and irradiation indicated superiority compared to the single treatments as proven by decreased cell numbers and cell survival. Preincubation with temsirolimus abrogated the irradiation-induced G2/M arrest in all NET cell lines under investigation.

5.2.4 SSTR expression of NET cells

In comparison to the external beam irradiation used so far, peptide receptor radionuclide therapy (PRRT) with ^{177}Lu -coupled somatostatin analogs is specifically targeting cells with SSTR expression. The most relevant subtype 2 (SSTR2) exhibits the highest affinity for clinically used somatostatin analogs [41]. The presentation of receptor binding sites at the cell surface is a prerequisite for PRRT, and although established NET cell lines are widely used in the field, their SSTR expression profile was initially investigated. First of all, mRNA levels of all five SSTR subtypes were analyzed by RT-qPCR in the five NET cell lines under investigation. For comparison, 10 human normal tissues (5 pancreatic, 5 ileal) as well as 20 human NET tissues (10 pancreatic, 10 ileal) were included. In all NET cell lines, expression of SSTR2, the major target of PRRT, was considerably decreased when compared to human NET samples (median: 6.55) (Figure 43, Table 9). It was at least 10-fold lower in H727 (0.27), and even more than 100-fold lower in BON (0.02), QGP-1 (0.02) and UMC-11 (0.01). In LCC-18 cells, no SSTR2 expression was detectable at all. Median values for SSTR5 were found to be 5-fold higher in BON and H727 than in NET tissues, while it was around the median of normal tissues in QGP-1, LCC-18 and UMC-11. SSTR3 levels were in the range of NET tissues in BON and H727, but also below the median of normal tissues in QGP-1, LCC-18 and UMC-11 cells. SSTR1 was highly increased in UMC-11 cells (median: 38.80), even above NET tissue levels (20.75), whereas in the other cell lines it was detected below normal tissues. SSTR4 expression was similarly low in NET and control tissues and not detectable in any of the cell lines.

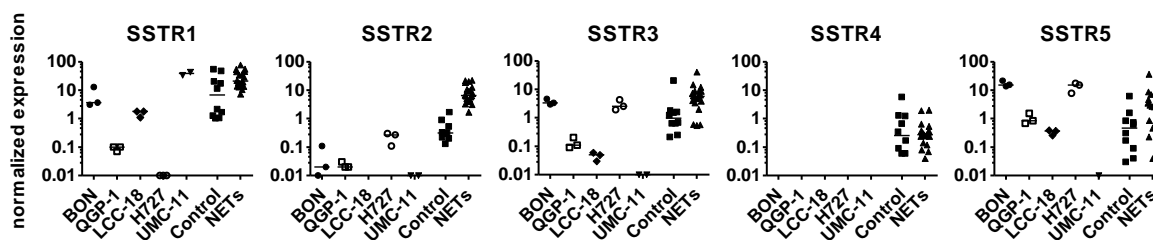


Figure 43 | Gene expression analysis of SSTR subtypes in NET cell lines. Scatter plots showing mRNA levels of SSTR1-5 in NET cell lines (n=3, different passages) in comparison to patient control (n=10) and NET samples (n=20). Values were normalized on ALG9 and HPRT1. Bars represent median.

Table 9 | Median values of SSTR gene expression analysis. Showing median for NET cell lines (n=3, different passages), control (n=10) and NET samples (n=20).

	BON	QGP-1	LCC-18	H727	UMC-11	control	NETs
SSTR1	3.64	0.10	1.79	0.01	38.80	6.76	20.75
SSTR2	0.02	0.02	n.d.	0.27	0.01	0.31	6.55
SSTR3	3.30	0.11	0.05	2.55	0.01	0.97	5.72
SSTR4	n.d.	n.d.	n.d.	n.d.	n.d.	0.26	0.28
SSTR5	15.23	0.84	0.37	15.18	0.01	0.47	3.00

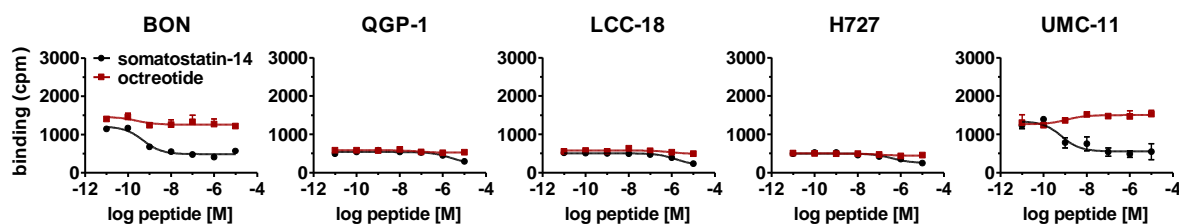


Figure 44 | Binding analysis confirms insufficient SSTR2 expression of NET cell lines. For competitive radioligand binding, NET cell lines were incubated with iodine-125 labeled Tyr¹¹-somatostatin-14 and increasing concentrations of unlabeled Tyr¹¹-somatostatin-14 or SSTR2-specific octreotide (0.01 nM to 10 μ M). Data represent mean \pm S.D. (n=1).

A competitive radioligand binding assay was utilized to validate the obtained gene expression data. For this, Tyr¹¹-somatostatin-14, a universal SSTR ligand binding to all five subtypes, was radioactively labeled with iodine-125, purified by HPLC (see supplementary Figure S10) and incubated with the NET cell lines. QGP-1, LCC-18 and H727 yielded only background levels of radioligand binding with no displacement by increasing amounts of unlabeled Tyr¹¹-somatostatin-14 or SSTR2-specific octreotide (Figure 44). Both BON and UMC-11 demonstrated binding above background that could be displaced by Tyr¹¹-somatostatin-14 with IC₅₀ values of 0.5 nM for BON and 0.7 nM for UMC-11. However, signals were not affected by addition of octreotide. In summary, no octreotide binding was detected in any of the cell lines, thereby confirming the results of gene expression analysis. The findings indicated insufficient expression of SSTR2, therefore, these cell lines were considered as inappropriate models for PRRT with ¹⁷⁷Lu-coupled somatostatin analogs.

As a consequence, the two pancreatic cell lines BON and QGP-1 were stably transfected with a plasmid encoding for human SSTR2. Successful reintroduction of the receptor was verified by RT-qPCR, radioligand binding and immunofluorescence (Figure 45 and Figure 46). In comparison to wildtype cells, SSTR2-transfected BON and QGP-1 exhibited about 1000-fold higher SSTR2 expression, which was now comparable to SSTR2 mRNA levels found in human NET tissues (Figure 45A). Accordingly, SSTR2-transfected cells demonstrated considerably higher radioligand binding when compared to wildtype cells: 2.5-fold higher in BON-SSTR2 and 9-fold higher in QGP-1-SSTR2 (Figure 45B). In both cell lines, binding could be displaced by increasing concentrations of unlabeled octreotide with nanomolar IC₅₀ values of 0.67 nM for BON-SSTR2 and 3.62 nM for QGP-1-SSTR2, respectively. As a third method, immunofluorescent staining with an SSTR2-specific antibody confirmed successful reintroduction, but also functionality of the receptor (Figure 46). While wildtype BON and QGP-1 cells yielded only faint signals, a clear staining was observed in SSTR2-transfected cells with a predominant receptor localization at the plasma membrane (Figure 46A). In addition, functional activity of the reintroduced receptor was verified by an internalization assay. BON-SSTR2 as well as QGP-SSTR2 cells were incubated for 30 min at

37 °C in absence or presence of somatostatin-14 and subsequently stained for SSTR2. In comparison to control, incubation with the agonist resulted in a rather diffuse, punctate staining pattern, indicating ligand-induced receptor internalization into an intracellular vesicular compartment (Figure 46B).

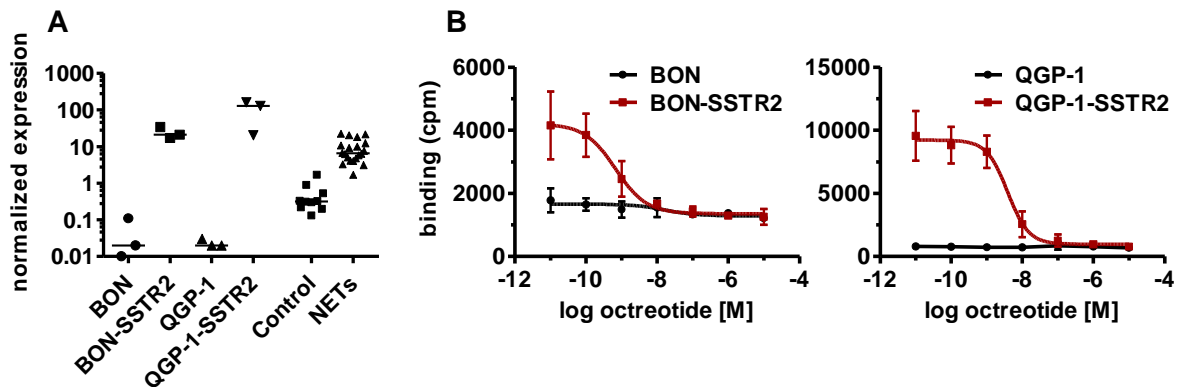


Figure 45 | Validation of SSTR2 reintroduction in two NET cell lines. SSTR2 expression was verified by RT-qPCR (A) and competitive radioligand binding assay (B) in BON-SSTR2 and QGP-1-SSTR2 in comparison to wildtype BON and QGP-1 cells. (A) SSTR2 mRNA levels in NET cell lines (n=3, different passages) in comparison to patient control (n=10) and NET samples (n=20). Values were normalized on ALG9 and HPRT1. Bars represent median. (B) Cells were incubated with iodine-125 labeled Tyr¹¹-somatostatin-14 and increasing concentrations of SSTR2-specific octreotide (0.01 nM to 10 μM). Data represent mean ± S.E.M. (n=2).

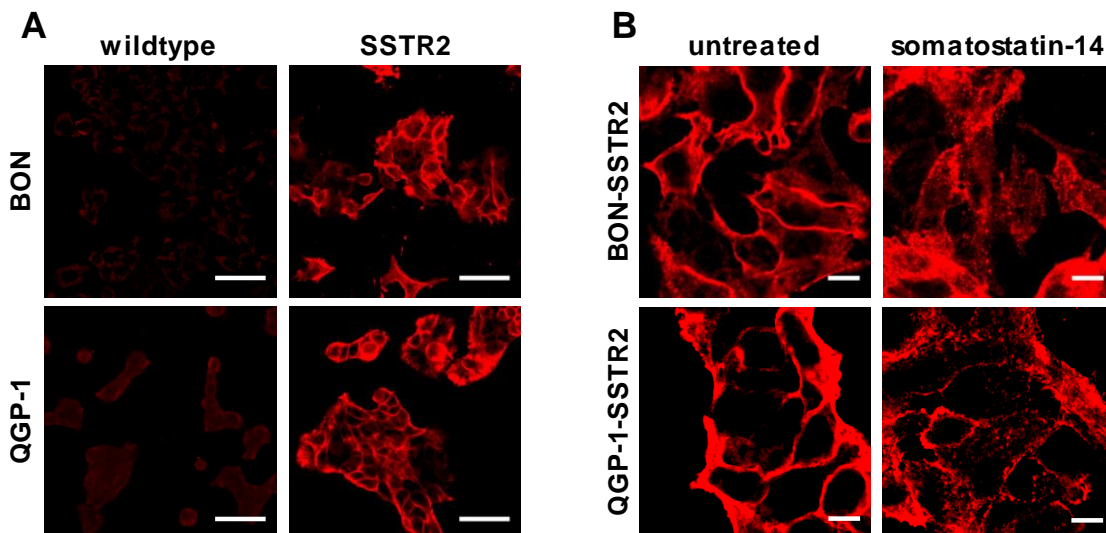


Figure 46 | SSTR2-expression and internalization in SSTR2-transfected NET cell lines. Immunofluorescent SSTR2-stainings show BON-SSTR2 and QGP-SSTR2 in comparison to wildtype cells (A) or after incubation with 1 μM somatostatin-14 for 30 min (B). Scale bars measure 50 μm (A) or 10 μm (B).

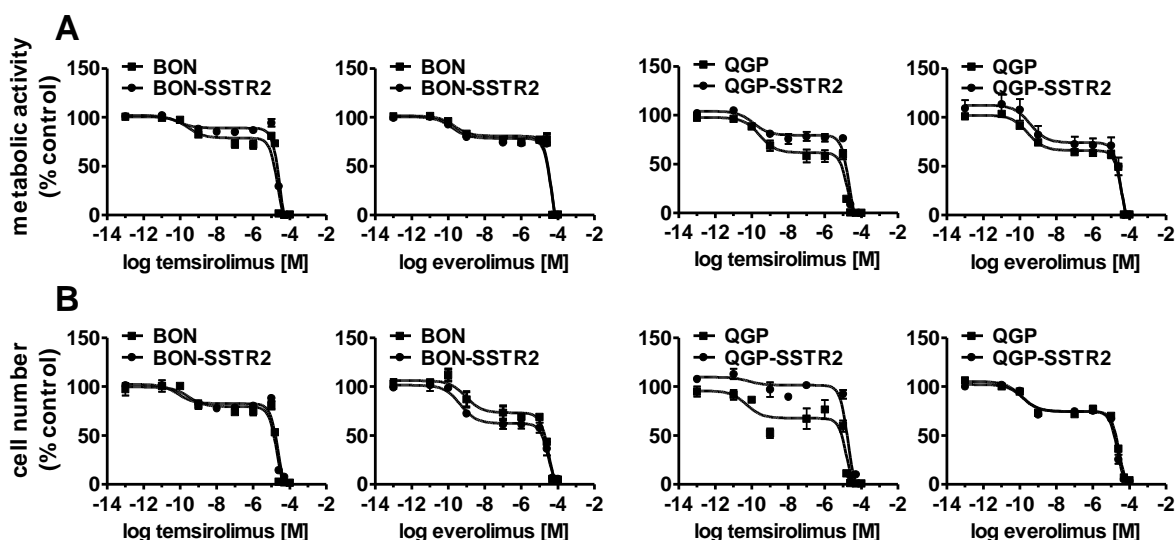


Figure 47 | SSTR2-transfection did not alter sensitivity for mTOR inhibitor treatment. NET cell lines were treated with increasing concentrations of temsirolimus or everolimus (0.1 pM to 100 μ M), incubated for 96 h and analyzed for metabolic activity (A) and cell number (B). Data represent mean \pm S.E.M. (n=3).

Finally, it was tested whether SSTR2-transfection altered sensitivity to mTOR inhibitor treatment. For this, both cell lines were incubated with increasing concentrations of temsirolimus or everolimus and analyzed for cell viability after 96 h. As Figure 47 shows, dose-response curves of metabolic activity and cell numbers had nearly the same shape for wildtype and transfected cells. Only QGP-SSTR2 demonstrated a slight curve shift for cell numbers after treatment with temsirolimus, though this is more likely due to technical variations, as metabolic activity is not changed (Figure 47B).

In summary, RT-qPCR, radioligand binding and immunofluorescent staining validated the successful reintroduction and functionality of SSTR2 in BON and QGP-1 cells. In addition, the sensitivity towards mTOR inhibitors was not influenced by the transfection. The availability of SSTR2-positive cell lines was required for the following experiments with ^{177}Lu -coupled somatostatin analogs.

5.2.5 Combination of mTOR inhibitors with PRRT

So far, the effects of external beam irradiation, alone or in combination with mTOR inhibitors were comprehensively investigated in NET cell lines. After the generation of appropriate cell models for SSTR2-targeted PRRT, preliminary experiments were performed in BON-SSTR2 and BON wildtype cells. Two different somatostatin analogs were applied: 1) the agonistic octreotide, which is clinically used, and 2) the antagonistic JR11, which was recently developed by Mäcke et al. [167]. For PRRT, both octreotide and JR11 were synthesized as the DOTA-conjugated agents DOTATOC and DOTA-JR11. DOTA acts as a chelator and complexes radioisotopes such as lutetium-177.

First of all, both analogs were tested by a radioactive binding assay for their binding capacity in BON-SSTR2 and control wildtype BON. As described in 5.2.4, cells were incubated with radioiodinated Tyr¹¹-somatostatin-14. As expected, BON-SSTR2 demonstrated binding, which could be displaced by DOTATOC (IC₅₀: 13.1 nM) and DOTA-JR11 (IC₅₀: 2.3 nM) in a dose-dependent fashion (Figure 48). Both analogs exhibited nanomolar IC₅₀ values, although the affinity of the antagonist DOTA-JR11 was around 6-fold higher than of the agonist. BON showed only background levels of binding without any displacement.

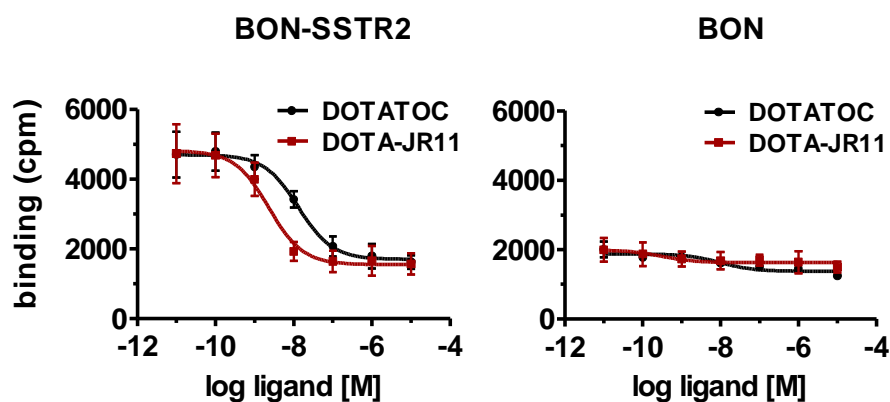


Figure 48 | DOTA-conjugated somatostatin analogs bind to BON-SSTR2. SSTR2-transfected and wildtype BON were incubated with iodine-125 labeled Tyr¹¹-somatostatin-14 and increasing concentrations of unlabeled DOTATOC or DOTA-JR11. Data show mean \pm S.E.M. (n=3) for BON-SSTR2 or mean \pm S.D. (n=1) for BON. cpm, counts per minute.

The access to ¹⁷⁷Lu-DOTATOC was constantly provided by the Department of Nuclear Medicine, as DOTATOC was frequently radiolabeled by the in house radiochemists for therapeutic patient care. On the other hand, radiolabeling of DOTA-JR11 was performed only once so far, as preclinical studies to evaluate its potential just recently started at Charité. For this reason, first combinatorial experiments were conducted with ¹⁷⁷Lu-DOTATOC and analyzed for cell cycle distribution and cell survival. As expected, single treatment with 1 μ M temsirolimus or everolimus increased the G1 cell cycle fraction in both wildtype and SSTR2-transfected BON cells. Surprisingly, single or

combinatorial incubation with 1 MBq of ^{177}Lu -DOTATOC did not result in the expected G2/M arrest in receptor-positive BON-SSTR2, as seen with external beam irradiation (Figure 49). Likewise, ^{177}Lu -DOTATOC only slightly affected cell survival of pretreated NET cells, and also to a similar extent in BON-SSTR2 and BON (Figure 50).

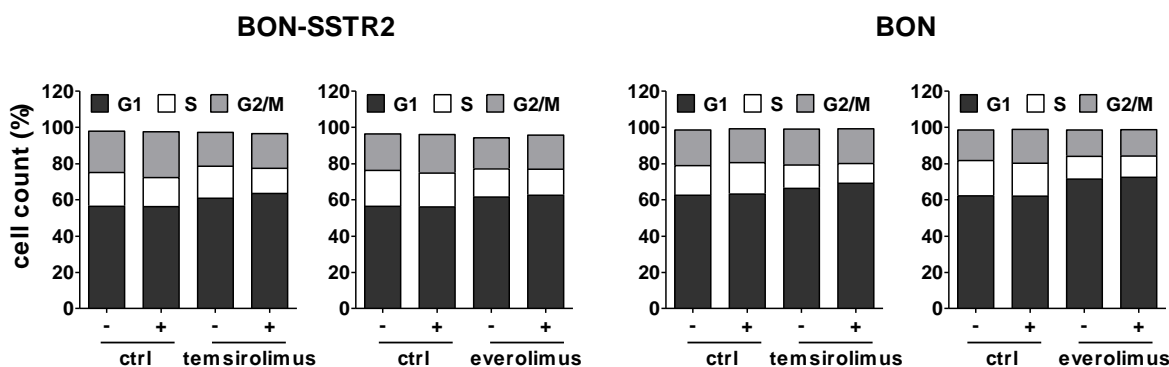


Figure 49 | Cell cycle is not affected by combination of mTOR inhibitors and ^{177}Lu -DOTATOC. SSTR2-transfected and wildtype BON cells were pretreated with 1 μM temsirolimus, everolimus or vehicle (ctrl) for 24 h before addition of medium (-) or 1 MBq ^{177}Lu -DOTATOC (+). Medium was exchanged after 4 h and cells were collected 24 h later, stained with propidium iodide and analyzed by flow cytometry for assessment of cell cycle distribution. Data are shown as bar diagrams with mean \pm S.E.M. (n=2, everolimus) or mean only (n=1, temsirolimus).

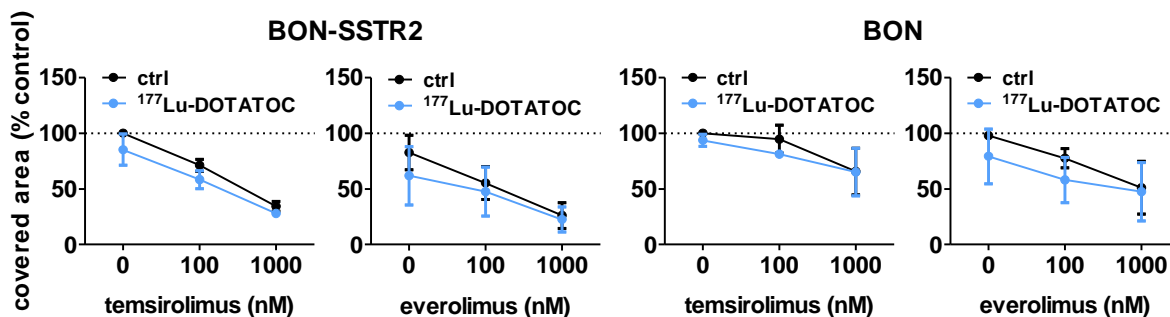


Figure 50 | Cell survival is not affected by combination of mTOR inhibitors and ^{177}Lu -DOTATOC. SSTR2-transfected and wildtype BON cells were pretreated with increasing concentrations of temsirolimus or everolimus for 24 h before addition of medium (ctrl) or 1 MBq ^{177}Lu -DOTATOC. Medium was exchanged after 4 h and cells were incubated for 1-2 weeks until colony formation. Data were normalized to untreated controls and represent mean \pm S.E.M. (n=2-3).

In the following, binding and internalization studies with ^{177}Lu -DOTATOC and ^{177}Lu -DOTA-JR11 were performed to evaluate their binding potential. As indicated in Figure 51, BON-SSTR2 showed accumulation of both radiopeptides. However, the overall detected activity was 10-fold higher for the antagonist ^{177}Lu -DOTA-JR11 when compared to the agonist ^{177}Lu -DOTATOC. As expected, the largest fraction of uptaken ^{177}Lu -DOTA-JR11 was membrane-bound (80%), while ^{177}Lu -DOTATOC was mostly detected in the internalized fraction (80%). This pattern distinctly correlates with the antagonistic and agonistic features of the respective tracers. Signals could be displaced by unlabeled octreotide and in addition, BON wildtype cells only showed background levels of binding with no displacement, confirming the specificity of the radiopeptides.

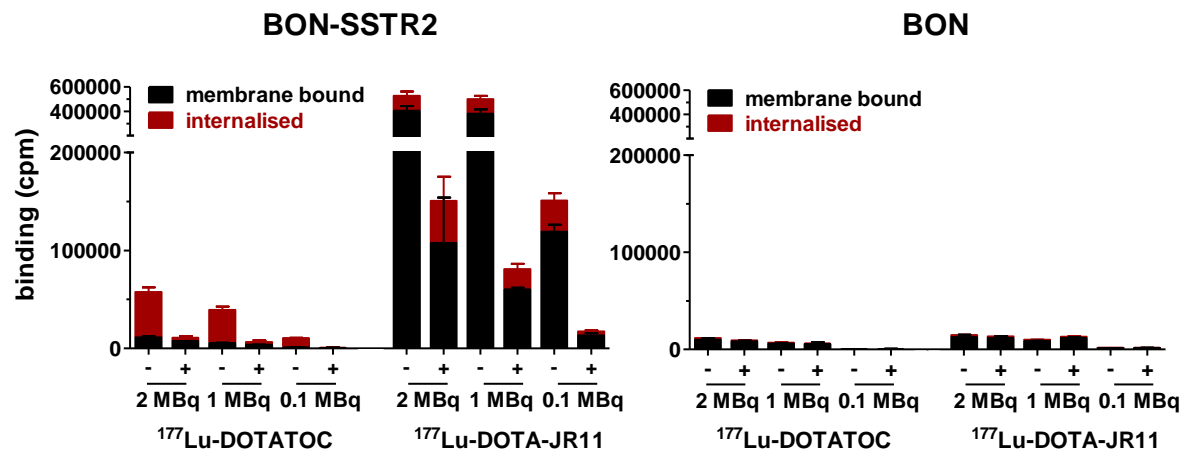


Figure 51 | Binding and internalization of ^{177}Lu -DOTATOC and ^{177}Lu -DOTA-JR11. SSTR2-transfected and wildtype BON were incubated with the indicated doses of agonistic ^{177}Lu -DOTATOC or antagonistic ^{177}Lu -DOTA-JR11 in absence (-) or presence (+) of unlabeled octreotide (1 μM). After 4 h at 37 $^{\circ}\text{C}$, membrane bound and internalized fractions were isolated and measured by a gamma counter. Data show mean \pm S.E.M. (n=2-3). cpm, counts per minute.

Interestingly, activities of 2 MBq could not further enhance binding levels in BON-SSTR2, rather leading to a saturation of receptor sites. In comparison, a low activity of 0.1 MBq resulted in lower total (-), but also non-specific binding (+) and hence, in better signal-to-background ratios.

In addition, cell cycle distribution after incubation with both radiopeptides was analyzed. For ^{177}Lu -DOTATOC, cell cycle phases remained unaffected in BON-SSTR2 and BON wildtype cells (Figure 52). In contrast, in the case of ^{177}Lu -DOTA-JR11, cells accumulated in G2/M in a dose-dependent way and only in the receptor-positive BON-SSTR2 cells. The amount of radioactivity delivered by the antagonist was sufficient to induce a G2/M arrest, as seen with the external radiation source before, but in a target-specific way. Unfortunately, no further combinatorial experiments could be performed with ^{177}Lu -DOTA-JR11 so far.

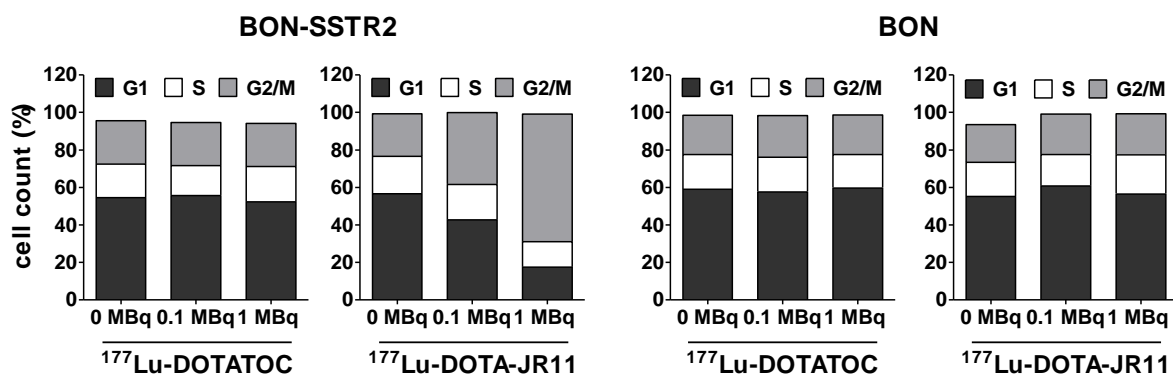


Figure 52 | Cell cycle distribution after treatment with ^{177}Lu -DOTATOC and ^{177}Lu -DOTA-JR11. SSTR2-transfected and wildtype BON cells were incubated with 0, 0.1 or 1 MBq of ^{177}Lu -DOTATOC or ^{177}Lu -DOTA-JR11. Medium was exchanged after 4 h and cells were collected 24 h later, stained with propidium iodide and analyzed by flow cytometry for assessment of cell cycle distribution. Data show the results of single samples (n=1).

6 DISCUSSION

The presented work addressed two related topics. The first project aimed to evaluate the applicability of AGTR1 as a molecular target in NETs as an alternative to the established target SSTR2. Previous experiments in our group indicated a role of AGTR1 in NETs and resulted in the conducted study. The second project focused on the investigation of a potential benefit of combining mTOR inhibitors with PRRT in a panel of NET cell lines. The use of combinatorial treatments proved to be efficient to enhance the outcome of single drug regimens and was therefore evaluated in more detail.

6.1 Expression analyses of AGTR1 in NETs

Angiotensin II and its receptors were recently associated with carcinogenic processes such as cell proliferation, angiogenesis or tissue remodeling. Different studies evaluated the expression profile of AGTR1 in a variety of tumors including breast, pancreatic, gastric and skin cancer. For example, Rhodes et al. found the AGTR1 gene to be overexpressed in 10-20 % of breast cancers in a large meta-analysis of microarray data [53]. Another study detected AGTR1 protein in 75 % of patients with pancreatic ductal adenocarcinoma [55]. The findings of this work also demonstrate an upregulation of AGTR1 in pancreatic and ileal NETs after comprehensive analysis of both AGTR1 gene and protein expression in primary NET patient material. Tumor mRNA levels were significantly increased in comparison to healthy control tissue and, interestingly, samples with high AGTR1 expression were low in SSTR2 expression. However, AGTR1 levels, also of control samples, were found to be in an overall elevated range. This is not necessarily a sign for higher absolute quantities. Although primer efficiencies were included in the calculation, it might still be difficult to compare gene expression data of different targets, owing to varying reaction kinetics and the unequal target sequences the respective primers recognize. It would be of great interest to further validate the results on protein level as expression changes might to some extent reflect the differentiation status of the tissue. SSTR2 expression is known to be decreased in high grade tumors [85]. In contrast, AGTR1 has been shown to be overexpressed in particular in high grade renal clear cell carcinoma [168] and astrocytomas [169] and is associated with poor prognosis in these tumors. However, Piastowska et al. demonstrated significantly decreased AGTR1 levels in high grade endometrial adenocarcinomas when compared with low grade tumors [170]. How AGTR1 gene expression levels influence tumor grade and prognosis of NETs requires further studies and integration of clinical parameters. In addition to NET tissues, a panel of 28 cell lines

was tested for AGTR1 expression to identify appropriate models for following experiments. Indeed, the two cell lines with the highest AGTR1 mRNA expression were of NET origin, whereas only a colon and a lung cell line reached similarly high values. This indicates that AGTR1 overexpression is not a general phenomenon in tumors, but rather depends on their specific genetic profile and biology.

Gene expression data provide important insights into differentially regulated transcripts. Nevertheless, the existence of sufficient receptor protein is a prerequisite for molecular targeting. In a previous study, Fendrich et al. evaluated AGTR1 protein expression in 44 pancreatic NETs by immunohistochemistry staining [171]. Although they observed an expression in 80 % of the patients, pancreatic control tissues were not included in their analysis. Moreover, non-specific binding of most commercially available antibodies against AGTR1 was clearly demonstrated by different groups [172], [173], including the one used in the study by Fendrich et al. This is a frequent issue when investigating GPCRs, which are known to be difficult targets for antibody development. Their extracellularly exposed epitopes are limited, while at the same time, they show high conformational variability in this region. Receptor subtypes often share a high percentage of sequence homology. The major challenge though is to obtain purified antigen preparations, as GPCRs lose their natural conformation and function as soon as they are removed from the cell membrane [174], [175]. Also during this work, none of the commercially obtained AGTR1 antibodies revealed appropriate staining patterns. Therefore, protein expression was evaluated by receptor autoradiography as an alternative and in this case more reliable method than antibody based techniques. Tissue sections of pancreatic and ileal tumors and their respective controls were incubated with radioactively labeled angiotensin II. To discriminate between AGTR1 and AGTR2, subtype selective antagonists were co-applied for signal displacement and assessment of non-specific binding. Quantification revealed an up to 5-fold higher expression of AGTR1 in pancreatic, and in particular ileal NETs, which could be well correlated to gene expression data for most samples. However, a few samples showed high mRNA levels but hardly any ligand binding. This further emphasizes the necessity to determine protein levels, as mRNA underlies various post-transcriptional regulations influencing its stability, its transport into the cytosol and the initiation of translation [176]. Thus, mRNA data only partially predict the actual protein expression in the cell. Besides this, external factors such as sample handling and storage might also explain the observed discrepancy. Especially for pancreatic samples, autoradiographic signal intensities are relatively low. Due to the high amount of autolytic enzymes, tissue processing and preservation of quality can be very challenging and require standardized procedures, which cannot always be followed in clinical routine [177], [178]. However, mRNA may be more affected by an unfavorable preservation of samples than protein.

Strikingly, AGTR2 expression could be detected in several pancreatic control tissues. These findings are in line with a study by Shao et al. reporting high AGTR2 levels in pancreatic islets of adult rats. The authors further concluded that the receptor mediates insulinotropic effects by increasing blood insulin levels through enhanced insulin expression, biosynthesis and secretion [179]. Sadik et al. associated the differentiation of bone-marrow derived mesenchymal stem cells into insulin producing cells with an increased AGTR2 expression [180], underlining its role in development and tissue regeneration. In mouse studies, AGTR2 was found to be a protective counter regulator of AGTR1 signaling in pancreatic fibrosis [181] or to attenuate pancreatic carcinoma growth [182]. Clearly, the distinct role of AGTR2 is still controversial and whether it is expressed under normal and/or pathophysiological conditions in the human pancreas would require further investigation.

6.2 Suitability of AGTR1 as a molecular target for optical imaging

Radiolabeled AGTR1-targeted peptides and small molecules have been primarily assessed for cardiac and cardiovascular imaging so far, to precisely select patients for distinct treatment options and to better predict therapy response [183]. To the best of our knowledge, the presented work is the first study investigating the applicability of AGTR1-based tumor targeting.

The conducted expression analyses confirmed the presence of AGTR1 in NETs and also identified appropriate NET cell lines for in vivo near-infrared optical imaging. The biodistribution of two different ITCC-labeled AGTR1-targeted ligands was evaluated in a xenograft mouse model and revealed a significant accumulation of saralasin-ITCC in receptor-positive BON tumors after a few hours. On the other hand, valsartan-ITCC was taken up to a much lesser extent, but in both BON and receptor-negative QGP-1. The superior performance of saralasin-ITCC was unexpected, as it revealed a 13-fold lower affinity for AGTR1 than valsartan-ITCC as determined by radioactive competitive binding. The published K_i value for saralasin of around 1 nM was decreased 250-fold after introduction of the dye molecule ITCC [184]. Although a slow dissociation rate from the receptor is mostly associated with high affinity binding, both parameters do not necessarily have to correlate [185]. Furthermore, saralasin exhibits a half-life of a few minutes whereas valsartan is stable for a few hours [162], [163]. It is of notice though, that saralasin-ITCC was quite rapidly eliminated via kidney and bladder, while valsartan-ITCC remained much longer in the mouse and was mainly excreted hepatically. The excretion route is dependent on the size, charge and hydrophobicity of a molecule. Small peptides, such as saralasin, and proteins with rather hydrophilic properties are in particular cleared from the body through renal filtration. Xenobiotics and small molecules such as valsartan are typically biotransformed in the liver and converted to more hydrophilic molecules before they are eliminated via urine or bile [186], [187].

Consequently, the physicochemical properties of a peptide or drug dramatically impact its biodistribution, retention time and excretion [188]. A certain retention time in the circulation is favorable to allow for sufficient target binding, however, in the case of valsartan-ITCC this possibly led to high background fluorescence and a worse signal-to-background ratio in comparison to saralasin-ITCC. Moreover, a reason for the low tumor uptake of valsartan-ITCC might be its limited tissue distribution. Obviously, up to 95 % are bound to serum proteins, in particular serum albumin, when applied intravenously [189].

Saralasin on the other hand, is not selective for AGTR1, but binds with similar affinity to AGTR2 as well [190]. The cell line models BON and QGP-1 were found to be AGTR2 negative. Nevertheless, xenografts also consist of host-derived murine cells, which infiltrate the tumor and form stromal environment and vascularizing vessels [191], [192]. While tumor angiogenesis is in particular associated with AGTR1, studies investigating the role of receptor subtype 2 in this process revealed controversial data [47], [193], [194]. However, Walther et al. [195] as well as Clere et al. [196] suggested a contribution of AGTR2 to the development and promotion of tumor vasculature. Therefore, binding of saralasin-ITCC to both tumor tissue and murine vessels cannot be excluded, albeit a different vascularization pattern of BON and QGP-1 tumors was not distinctively observed after surgical excision of the xenografts.

Although the tumor-to-background ratio for saralasin-ITCC was significantly increased in receptor-positive BON tumors, several modifications might further enhance probe performance. The introduction of a more hydrophobic linker between peptide and dye could result in longer retention, and hence, higher uptake and overall fluorescence intensities. Linker molecules such as aminohexanoic acid (AHX) are commonly used to increase the hydrophobicity of a molecule, whereas trioxatridecansuccinamic acid (TTDS) or polyethylene glycol (PEG) are more hydrophilic. In addition, the variation of linker length and thus the distance between peptide and near-infrared dye, might enhance the affinity of the probe [197]. Likewise, the tumor targeting properties of valsartan-ITCC might be improved by introducing a more hydrophilic linker to reduce plasma protein binding and liver uptake. Alternatively, new AGTR1-targeted peptide based probes could be developed on the basis of saralasin, using for example non-natural or D-amino acids. This requires rational peptide design strategies and subsequent structure activity relationship (SAR) analyses with cell based screening and stability assays to evaluate peptide affinity and half-life. However, chemical peptide modifications are limited. New approaches for the development of imaging probes include cysteine knot peptides, also known as knottins. Their basic structure already confers proteolytic resistance and thermal stability and provides a scaffold for the insertion of target-binding motifs. Similar to peptide ligands they can easily be conjugated to dyes or radioisotopes [198], [199].

This first in vivo tumor imaging with AGTR1-targeted probes showed, that it is a feasible approach, which should be pursued further on. Saralasin-ITCC showed convincing results, and based on its high affinity valsartan-ITCC is another promising molecule for continuing development. Tumor targeting properties might be further improved by further probe optimization, linker modification or alternative peptide engineering strategies in favor of longer retention times, higher tumor-to-background ratios and increased overall fluorescence intensities. In addition, nuclear medical PET imaging with radiolabeled DOTA-conjugated AGTR1-ligands might be performed in the established NET mouse model.

6.3 Effects of angiotensin II on tumor signaling and biology

Only very low amounts of a probe are applied for diagnostic imaging, which reduces pharmacological effects by receptor activation to a minimum. For example, the injected dose for OctreoScan scintigraphy is typically 10 μg , which corresponds to a peptide concentration of around 1 nM in the patient's blood pool [200]. However, for a potential therapeutic application, it is necessary to have a thorough understanding of the actions a ligand mediates through its receptor. Therefore, the effects of angiotensin II on tumor signaling and related processes such as proliferation and secretion were investigated.

The signaling cascades involved in AGTR1 activation are well studied, albeit not for NET cells. Calcium mobilization and an intracellular signaling array were utilized to assess the functional response after angiotensin II stimulation in the cell line model.

AGTR1 is known to primarily couple to the heterotrimeric G protein $G_{q/11}$ [47], which could be confirmed for NET cells as well. Both AGTR1-positive NET cell lines BON and H727 revealed a concentration-dependent intracellular calcium increase after receptor activation. This indicates an engagement of $G_{q/11}$ and the subsequent stimulation of phospholipase $C\beta$, which in turn cleaves phosphatidylinositol 4,5-bisphosphate (PIP₂) to inositol 1,4,5-trisphosphate (IP₃) and diacylglycerol (DAG). IP₃ eventually leads to an influx of calcium ions from the endoplasmic reticulum, whereas DAG regulates phosphokinase C as well as some TRP channels [51], [201]. Calcium acts as a versatile second messenger and influences many physiological processes such as cell contraction, metabolism, proliferation, migration and secretion, depending on cell type and function [202]–[204]. In addition, calcium homeostasis has been demonstrated to be disturbed or remodeled in malignant phenotypes [205]. In NET cells, enhanced calcium channel activity was associated with an increased release of chromogranin A as observed in BON cells by Mergler et al. [206], [207].

The performed PathScan signaling array was applied to gain an overall insight into activated downstream signaling pathways. The simultaneous detection of 18 different phosphorylated or cleaved targets enabled a broad analysis of post-translational modifications after angiotensin II stimulation in BON and H727 cells. Whereas BON cells showed enhanced Akt, ERK 1/2 and GSK-3 beta phosphorylation, regulated key targets in H727 primarily included Akt, to a much lesser extent ERK 1/2 and at later time points also Bad and p70S6K. The activation of ERK 1/2 by angiotensin II has been shown in several studies, and is suggested to be mediated mainly but not exclusively by EGFR transactivation, which allows a crosstalk between GPCRs and RTKs [208]–[211]. It was reported that AGTR1 engages not only G protein-dependent, but also β -arrestin-dependent signaling cascades for EGFR transactivation and subsequent ERK phosphorylation [212], [213]. EGFR transactivation could also be demonstrated for neuroendocrine BON cells, but upon stimulation with neurotensin [214]. Although the presented study did not investigate the mechanism of ERK activation in more detail, it is likely to be EGFR associated, as EGFR is frequently overexpressed in NETs as well [215]–[217]. Similar to the MAPK pathway, the PI3K/Akt cascade is stimulated by EGFR transactivation and leads to downstream inhibition of pro-apoptotic Bad and GSK-3 beta, thereby promoting cell survival and growth [46], [218]. Both investigated cell lines exhibited activation of this signaling axis, in particular H727 demonstrated a clear phosphorylation of Akt and sustained Bad inhibition during the considered time frame of 30 min.

The induced signaling cascades resulting in calcium mobilization as well as ERK and Akt activation are associated with a broad range of cellular processes and implicated further functional investigations. In BON cells, angiotensin II dose-dependently stimulated the secretion of chromogranin A (CgA), which serves as a general tumor marker for NETs. Although it was not specifically addressed in this study, hormone secretion by endocrine cells as well as neurotransmitter release by neurons is known to be induced by calcium regulated exocytosis involving a variety of different mediators such as synaptotagmins, complexins and SNARE proteins [219]. Nevertheless, the exact mechanism responsible for the excessive production of secretory granules and the following hypersecretion of neuroendocrine tumor cells is still not fully understood [220], [221]. So far, several reports suggest an important role of different protein kinases of the family C and D as well as an autocrine IGF-1 signaling loop [222]–[224].

Angiotensin II has been shown to facilitate cell proliferation in various human cancer cell lines by activation of MAPK or PI3K pathway, including breast [225], prostate [208] and pancreatic cells [226]. Although BON and H727 cells revealed enhanced ERK and Akt signaling upon angiotensin II stimulation, the proposed pro-proliferative effect could not be confirmed, as metabolic activity and cell number were not affected. Likewise, treatment with AGTR1 antagonists valsartan and

azilsartan revealed no inhibition of cell growth. It could be assumed that the observed timeframe of 96 h was not appropriate and that angiotensin II needs to be constantly present over a longer period for a detectable change of cell proliferation. Autocrine angiotensin II signaling might be another reason why the investigated receptor-positive NET cells did not respond to the treatment. At least BON cells have been shown to secrete various agents such as chromogranin A, IGF-1, serotonin and neurotensin [227], which act as autocrine growth factors through receptors on the secreting cell. By this mechanism, tumor cells often sustain their self-sufficient growth signaling. One could hypothesize that BON and H727 release angiotensin II, which leads to enhanced cell proliferation and make externally added treatment negligible. This would be in line with a study of Fendrich et al., in which treatment with the ACE inhibitor enalapril, and thereby inhibition of angiotensin II production, resulted in decreased BON cell growth in vitro and in vivo [171]. Similarly, the effect of applied antagonists might be impaired as they have to compete with autocrine angiotensin II binding for the receptors [228]. It is also conceivable, that a lack of one or more signaling components prevents the transduction of the signal from the receptor to the cell cycle machinery. Furthermore, angiotensin II mediates its pro-proliferative signaling not only by direct stimulation of tumor cells, but also indirectly affects stromal and vascular cells [47]. Obviously, monolayer cell cultures do not provide such a complex tumor microenvironment. Three-dimensional cell models, organoids and in vivo xenografts might prove to be more suitable for the study of cell proliferation in this case. Fujita et al. reported a decreased tumor growth of sarcoma xenografts in mice after administration of an AGTR1 antagonist [229], [230]. Fendrich et al. could demonstrate an increased survival in a mouse model for islet carcinoma after treatment with enalapril [171]. However, the effect they observed was very weak and could not be directly linked to AGTR1 antagonism as enalapril acts as an ACE inhibitor. Eventually, the proliferative potential of angiotensin II is certainly dependent on the complex genetic profile and signaling of the cell model under investigation and AGTR1 overexpression does not necessarily have to lead to stimulation of cell growth.

6.4 Patient-derived NET xenografts for future studies

NET patients represent with a very heterogeneous phenotype as these tumors can originate from various sites and are characterized by distinct signaling and secretion patterns. It is difficult to obtain permanent cultures, as NET cells are often overgrown by faster replicating fibroblasts and because of their demand for distinctive supplemented culture media [231]. So far, only a few human NET cell lines have been established [227], [232]. Due to a lack of alternative models, these are widely used in the field, although they often show high doubling rates and frequently lack SSTR expression. The availability of well-differentiated cell lines displaying the slow growing

nature of NETs is limited. Recently, Benten et al. reported the successful culture of such a cell line of pancreatic origin [149]. One aim of this work was the generation of patient-derived xenografts (PDX) to extend the spectrum of preclinical NET models. For 6 of 16 primary tissues that were xenografted into immunodeficient mice, tumor growth was observed. In particular for NETs, the resultant take rate of 37 % was strikingly high, owing to the described difficulties. However, the majority of the engrafted tissues originated from grade three NETs with relatively high proliferation rates. The establishment of tumor models of low grade and thereby rather slow growing NETs remains challenging. All PDX tissues were tested for their human origin after initial engraftment and two of them were scored as AGTR1-positive after expression analyses by RT-qPCR and autoradiography. Further molecular characterization such as STR profiling or immunostaining for NET markers would confirm the conservation of primary tumor characteristics as well as xenograft integrity and stability over different passages in more detail [233]. Potential applications for the established PDX models include molecular imaging with specific probes, and therapy studies for the evaluation of novel agents. Moreover, the propagated tumor material could directly be used for in vitro drug screenings with dissociated monolayer cells or three-dimensional spheroids [234], [235].

6.5 Sensitivity of NET cell lines to mTOR inhibitors

Peptide receptor radionuclide therapy (PRRT) has become an essential treatment option for advanced NETs and showed increased progression free survival when compared to chemotherapy, radiation or intervention with somatostatin analogs (SSAs). Objective response rates range between 15 to 35 % [236]. However, complete remissions are still very rare, although PRRT delivers up to 250 Gy specifically to the tumor [237]. In contrast, similar nuclear therapies such as radioiodine therapy for thyroid cancers or radioimmunotherapy for B-cell non-Hodgkin's lymphoma achieve complete remissions in 30 % or 75 % of all cases, respectively [238], [239]. It was hypothesized that other established NET therapies such as mTOR inhibitors may have a beneficial impact on the outcome of PRRT. Several studies have reported a radiosensitizing effect of mTOR inhibitors, which might suppress radiation-induced survival and escape mechanisms of the tumor cell [240], [241]. Therefore, the second part of this work intended to evaluate the combinatorial potential of mTOR inhibitor treatment with PRRT in a panel of NET cell lines of different origin.

In the beginning, the impact of the two mTOR inhibitors temsirolimus and everolimus on cellular processes was validated for the utilized NET cell lines. Proliferation assays revealed a biphasic inhibition of metabolic activity and cell number for both substances in all five cell lines. Whereas nanomolar concentrations led to a moderate antiproliferative effect, micromolar concentrations

suppressed cell viability completely. This is in line with a report from Shor et al., also reporting a low-dose and high-dose effect of temsirolimus in different cancer cell lines [242]. In addition to the well-known FKBP12-dependent binding of temsirolimus to mTOR, they suggested a second, FKBP12-independent mechanism, which might be responsible for the profound high dose effect. Although the determined low-dose IC_{50} values were around 1 nM for all cell lines and both inhibitors, the efficacy i.e. the amplitude of the effect differed between the investigated cell lines. Especially pulmonary UMC-11 cells can be considered to be drug-sensitive as cell viability was strongly reduced by 75 % after treatment with nanomolar concentrations, whereas BON cells seemed to be rather resistant (only 20 % reduction). Long-term clonogenic survival assays over 1-2 weeks confirmed these results. Signaling and cell cycle analysis were conducted to further elucidate the observed response in these cell lines. Similar to a study by Hurvitz et al. in breast cancer cell lines [243], the inhibition of p70S6 kinase, a downstream target of mTOR, was achieved in all NET cell lines, but could not be correlated with their susceptibility as measured by cell viability and survival. On the other hand, phospho-p70S6 kinase levels were only monitored for 24 h after treatment and later time points might reveal divergent response patterns. However, the high sensitivity of UMC-11 might be explained by a constantly elevated fraction of cells in G1 cell cycle phase, up to 96 h after treatment. In addition, mTOR inhibition did not result in a counteracting phospho-Akt upregulation. Due to the loss of the negative S6K feedback loop on IRS and PI3K, this is a frequently observed resistance mechanism in treated tumor cells. In comparison, the rather resistant BON cells show only transient G1 cell accumulation of up to 24 to 48 h and a clear increase of phospho-Akt and phospho-ERK levels, indicating several escape pathways. This is in line with a report by Zitzmann et al., who investigated the effect of everolimus on proliferation, cell cycle distribution and signaling of BON cells [244]. However, in contrast to their results, the here presented study could not confirm apoptosis induction by low nanomolar concentrations, as determined by detection of caspase 3 and cleaved PARP. Interestingly, between these very distinct cases of BON and UMC-11 cells, there seem to be intermediate phenotypes. For example, clonogenic survival of H727 was strongly reduced after mTOR inhibition, despite a clear Akt activation and a rather weak and transient G1 cell accumulation. QGP-1 cells behaved similar to BON cells with regard to cell viability and survival assays, with a transient but very strong G1 cell accumulation. On the other hand QGP-1 cells did not increasingly activate Akt upon mTOR inhibition.

Cell cycle checkpoints at G1/S or G2/M phase transitions are important control mechanisms to maintain genomic integrity within the cell in response to environmental stress and DNA damaging agents such as irradiation. Their activation is mediated by a complex signaling network including cyclins, cyclin-dependent kinases and the key modulator p53, which is primarily involved in G1 cell

cycle arrest [245]. In the case of very extensive and irreparable damage the cells go into apoptosis. It has been shown that mTOR inhibitors induce a p53-independent G1 cell cycle arrest by an impaired translation of cyclin D1 and an enhanced expression of p27Kip1 [246]–[248]. Both molecules were not included in this study, but differences in their expression upon mTOR inhibition might further explain the varying treatment susceptibility of the single cell lines. The permanent G1 cell cycle accumulation of drug-sensitive UMC-11 cells indicates a likely influence of the cells' capability to stay in this arrest over time.

Apart from the evaluated parameters, the results indicate a complex network of genes and proteins that influence sensitivity or resistance to mTOR inhibitors. However, it was not the aim of this study to investigate these mechanisms in detail, but to generally assess the response of the NET cell lines under investigations. Several genetic alterations have been associated with mTOR sensitivity such as PTEN-deficiency [249], a distinct SNP in FGFR4 [250] or PIK3CA mutations [251]. Undoubtedly, an increased basal activation of mTOR and its signaling pathway plays an important role for the outcome of mTOR inhibitor treatment. Nevertheless, clinical biomarkers for a reliable response prediction were not identified so far [252]. In conclusion, this study verifies the expected effects of mTOR inhibitors in vitro and further complements the reported results for BON and QGP-1 cells [244], [249] by evaluating an extended NET cell line panel.

6.6 Evaluation of radiation-induced effects in NET cell lines

In advance of combination treatments, the radiobiological response of NET cell lines was studied in more detail. For this, external beam irradiation with a caesium-137 source was applied as it delivers reproducible, stable and precise dose levels to cultured cells and is easily accessible. Similar to lutetium-177, caesium-137 is a combined beta/gamma emitter. However, in comparison to targeted PRRT with ¹⁷⁷Lu-coupled peptides this type of irradiation is undirected and affects cells independent of their receptor status. In line with many reports that analyzed radiation effects and DNA damage responses in cancer cells [253], [254], all investigated NET cell lines revealed a clear accumulation in the G2/M cell cycle phase, which was retained over time. The radiation susceptibility differed only slightly between cell lines as determined by cell number assays. Although DNA damaging radiation is primarily associated with G1 arrest, it was postulated that most cancer cells lack a functional G1 checkpoint due to mutations in the key molecule p53. Therefore, they are more reliant on the pre-mitotic G2/M checkpoint for repair of potentially lethal damage and display a strong G2/M arrest upon irradiation [255]–[257].

6.7 Combinatorial potential of mTOR inhibitors with radiation

Cell viability and survival assays revealed the superiority of combining mTOR inhibitors with external beam irradiation in comparison to either single application. In all NET cell lines under investigation this treatment strategy exhibited an additive inhibitory effect. Interestingly, only drug-sensitive UMC-11 cells barely profited from this approach as mTOR inhibition already impaired the evaluated parameters to a great extent.

As discussed before, mTOR inhibitors induced a G1 cell cycle accumulation, whereas after irradiation cells accumulated in G2/M. In combination, pretreatment with temsirolimus clearly abrogated the radiation-induced G2/M arrest in all five NET cell lines. Thus, it can be hypothesized that temsirolimus prevents DNA damage repair processes that normally occur during G2/M arrest. Thereby, cells with unrepaired DNA lesions may prematurely enter mitosis and undergo the so called mitotic catastrophe, which is distinct from apoptotic cell death [258], [259]. Although the respective data were not included in the results section, everolimus pretreatment led to similar effects when combined with radiation. Other groups addressing the radiosensitizing effect of everolimus consistently reported an enhanced inhibition of cell growth in vitro and in vivo when applying the combinatorial treatment regimen. However, cell cycle distribution analyses revealed different outcomes. Su et al. observed no difference in G2/M between everolimus with and without radiation in Ras-transformed cells [260]. Possibly, the chosen concentration of 30 nM was too low to uncover the G2/M abrogation. In contrast, Nassim et al. reported an increase of both G1 and G2/M when combining everolimus with radiation in bladder cancer cells [240]. They suggest that the everolimus-induced G1 arrest confers an enhanced sensitivity for the following radiation as fewer cells were counted in the rather radioresistant S-phase [261]. However, in NET cell lines the proportion of S-phase cells was relatively unaffected. It must be further noted, that the length of pretreatment differed between the studies, which might have a significant impact on the evaluated parameters. In line with the presented work, Wang et al. reported an abrogation of the radiation-induced G2/M arrest in pancreatic cells, but after pretreatment with metformin [262].

6.8 Combinatorial potential of mTOR inhibitors with PRRT

In contrast to undirected external beam irradiation, PRRT with ^{177}Lu -coupled somatostatin analogs only targets SSTR2-positive cells. However, for all NET cell lines under investigation RT-qPCR and radioligand binding assays demonstrated low target expression and no binding of SSTR2-specific octreotide. The cells showed 10- to 1000-fold lower SSTR2 mRNA levels than human NET tissues. A few studies investigated the receptor status of selected NET cell lines before, but as far as we know this is the first study to quantitatively compare them with patient tissues [263]–[265]. These findings further confirm the lack of appropriate preclinical NET models for the study of tumor specific biology and treatment response. Original cell lines may undergo molecular transformations, which might be induced by in vitro culture conditions, loss of the tumor microenvironment and proliferative pressure [227]. QGP-1 cells for example have been shown to intrinsically express inhibitory somatostatin [266]. Thereby the loss of the corresponding SSTRs may provide an advantage for single clones, which could then overgrow well-differentiated cells.

In order to obtain appropriate cell lines with sufficient target expression for PRRT, SSTR2 was successfully reintroduced in BON and QGP-1 by stable transfection, of which BON-SSTR2 were further used for the following experiments. However, the combinatorial treatment with mTOR inhibitors and the agonistic somatostatin analog ^{177}Lu -DOTATOC revealed no changes of cell survival and cell cycle distribution between target positive BON-SSTR2 and wildtype BON. Interestingly, direct comparison with the antagonistic ^{177}Lu -DOTA-JR11 demonstrated superior efficacy of the antagonist with 10-fold higher uptake, although both peptides showed similar binding affinities before. In correlation with the agonistic and antagonistic features of the respective radiopeptides, ^{177}Lu -DOTATOC was primarily internalized by the cells, while ^{177}Lu -DOTA-JR11 was mainly detected in the membrane-bound fraction. Furthermore, ^{177}Lu -DOTA-JR11 indeed induced the expected radiation-induced G2/M arrest specifically in SSTR2-positive cells. The results are in line with recent studies evaluating the applicability of somatostatin antagonists for NET targeting. Reubi et al. showed highly increased binding of iodine-125 coupled JR11 to NET tissue samples by in vitro receptor autoradiography [267]. Similar to the presented study Dalm et al. reported a 5-fold higher in vitro uptake of ^{177}Lu -DOTA-JR11 and more DNA double strand breaks in comparison to ^{177}Lu -DOTATOC [109]. Moreover, they observed an enhanced therapeutic response of ^{177}Lu -DOTA-JR11 in a preclinical mouse model.

Antagonistic radiopeptides do not only recognize more receptor sites than agonists, they also exhibit longer lasting accumulation at the tumor, possibly due to the decreased receptor internalization and recycling rate [167]. It was further hypothesized that they target receptors in both active and inactive state, of which the latter one is predominantly present at the cell surface.

On the other hand agonists bind to the active state and thereby only to a small fraction of available receptor sites [40]. According to Cescato et al., the higher sensitivity of somatostatin antagonists not only improved the visualization of NETs, but also increased tumor-to-background ratios in tumor types with rather low target expression such as breast cancer or non-Hodgkin lymphoma [268], [269]. Thereby, the use of antagonists might even extend the number of patients that might profit from SSTR-based approaches.

Unfortunately, the combined effect of mTOR inhibitor treatment with ^{177}Lu -DOTA-JR11 could not be evaluated in this study, as the availability of the radiopeptide was limited. Although the application of agonistic ^{177}Lu -DOTATOC did not yield the expected results, it is an important treatment option for NET patients. This emphasizes the contribution of more complex phenomena than can be evaluated in vitro, such as biodistribution and tissue clearance kinetics of a radiopharmaceutical as well as the specific tumor microenvironment and receptor status. Nevertheless, the experiments performed so far are a solid basis for continuing research. Dr. Eva Koziolok and Jakob Albrecht, members of the BERIC (Berlin Experimental Radionuclide Imaging Center) at Charité, established a BON-SSTR2 mouse model, which is available for in vivo combinatorial treatment approaches. Besides the classical subcutaneous xenografts (Figure 53A and B), they developed an orthotopic pancreatic model (Figure 53C). In line with our in vitro data, only SSTR2-positive cells showed an uptake of ^{177}Lu -DOTATOC as measured with SPECT/CT. The therapeutic response and tumor growth of the animals can also be monitored by non-invasive imaging.



Figure 53 | SPECT/CT imaging with ^{177}Lu -DOTATOC in different mouse models. A dose of 30 MBq was intravenously injected in the tail vein of mice bearing subcutaneous (sc) BON (A) and BON-SSTR2 (B) or orthotopic (ortho) BON-SSTR2 (C). Images were taken after 20 h and kindly provided by Eva Koziolok.

So far, only Bison et al. evaluated the effect of everolimus in combination with ^{177}Lu -DOTATOC preclinically in vivo [270], [271]. In their syngeneic rat model with subcutaneous CA20948 xenografts they observed no beneficial effect on tumor growth. Strikingly, they found more metastatic lesions in animals treated with everolimus alone or in combination, whereas this was not detected in the control or PRRT group. They suggest, this could be due to an incomplete mTOR inhibition as everolimus was only administered twice-weekly, which might have resulted in an upregulation of growth-associated signaling pathways. It would certainly be of great interest to see the experimental outcome in an orthotopic human NET cell line model using BON-SSTR2 or established PDX tumors. In addition to treatment with ^{177}Lu -DOTATOC, the evaluation of ^{177}Lu -DOTA-JR11 should be part of this combinatorial in vivo study. The future application of somatostatin antagonists as single agents or together with mTOR inhibitors as well as other substances may provide new opportunities for SSTR-based therapies with highly improved response rates.

BIBLIOGRAPHY

- [1] B. Vogelstein and K. W. Kinzler, "Cancer genes and the pathways they control," *Nat. Med.*, vol. 10, p. 789, Jul. 2004.
- [2] D. Hanahan and R. A. Weinberg, "The hallmarks of cancer.," *Cell*, vol. 100, no. 1, pp. 57–70, Jan. 2000.
- [3] D. Hanahan and R. A. Weinberg, "Hallmarks of Cancer: The Next Generation," *Cell*, vol. 144, no. 5, pp. 646–674, Mar. 2011.
- [4] K. Strebhardt and A. Ullrich, "Paul Ehrlich's magic bullet concept: 100 Years of progress," *Nat. Rev. Cancer*, vol. 8, no. 6, pp. 473–480, Jun. 2008.
- [5] M. E. Gutierrez, S. Kummar, and G. Giaccone, "Next generation oncology drug development: opportunities and challenges," *Nat. Rev. Clin. Oncol.*, vol. 6, p. 259, May 2009.
- [6] A. A. Friedman, A. Letai, D. E. Fisher, and K. T. Flaherty, "Precision medicine for cancer with next-generation functional diagnostics," *Nat. Rev. Cancer*, vol. 15, p. 747, Nov. 2015.
- [7] C. Kumar-Sinha and A. M. Chinnaiyan, "Precision oncology in the age of integrative genomics," *Nat. Biotechnol.*, vol. 36, p. 46, Jan. 2018.
- [8] P. C. Nowell, "The clonal evolution of tumor cell populations.," *Science*, vol. 194, no. 4260, pp. 23–8, Oct. 1976.
- [9] R. J. Gillies, D. Verduzco, and R. A. Gatenby, "Evolutionary dynamics of carcinogenesis and why targeted therapy does not work.," *Nat. Rev. Cancer*, vol. 12, no. 7, pp. 487–93, Jun. 2012.
- [10] M. Greaves and C. C. Maley, "Clonal evolution in cancer," *Nature*, vol. 481, no. 7381, pp. 306–313, Jan. 2012.
- [11] D. Longley and P. Johnston, "Molecular mechanisms of drug resistance," *J. Pathol.*, vol. 205, no. 2, pp. 275–292, Jan. 2005.
- [12] C. Swanton, "Intratumor Heterogeneity: Evolution through Space and Time," *Cancer Res.*, vol. 72, no. 19, pp. 4875–4882, Oct. 2012.
- [13] I. Dagogog-Jack and A. T. Shaw, "Tumour heterogeneity and resistance to cancer therapies," *Nat. Rev. Clin. Oncol.*, Nov. 2017.
- [14] R. Fredriksson, M. C. Lagerström, L.-G. Lundin, and H. B. Schiöth, "The G-protein-coupled receptors in the human genome form five main families. Phylogenetic analysis, paralogon groups, and fingerprints.," *Mol. Pharmacol.*, vol. 63, no. 6, pp. 1256–72, Jun. 2003.
- [15] M. Lu and B. Wu, "Structural studies of G protein-coupled receptors," *IUBMB Life*, vol. 68, no. 11, pp. 894–903, Nov. 2016.
- [16] M. C. Lagerström and H. B. Schiöth, "Structural diversity of G protein-coupled receptors and significance for drug discovery.," *Nat. Rev. Drug Discov.*, vol. 7, no. 4, pp. 339–57, Apr. 2008.

- [17] R. T. Dorsam and J. S. Gutkind, "G-protein-coupled receptors and cancer.," *Nat. Rev. Cancer*, vol. 7, no. 2, pp. 79–94, Feb. 2007.
- [18] A. Nieto Gutierrez and P. H. McDonald, "GPCRs: Emerging anti-cancer drug targets," *Cell. Signal.*, vol. 41, pp. 65–74, Jan. 2018.
- [19] A. S. Hauser, M. M. Attwood, M. Rask-Andersen, H. B. Schiöth, and D. E. Gloriam, "Trends in GPCR drug discovery: new agents, targets and indications," *Nat. Publ. Gr.*, vol. 16, 2017.
- [20] R. Santos, O. Ursu, A. Gaulton, A. P. Bento, R. S. Donadi, C. G. Bologa, A. Karlsson, B. Al-Lazikani, A. Hersey, T. I. Oprea, and J. P. Overington, "A comprehensive map of molecular drug targets," *Nat. Rev. Drug Discov.*, vol. 16, no. 1, pp. 19–34, Dec. 2016.
- [21] K. Palczewski, T. Kumasaka, T. Hori, C. A. Behnke, H. Motoshima, B. A. Fox, I. Le Trong, D. C. Teller, T. Okada, R. E. Stenkamp, M. Yamamoto, and M. Miyano, "Crystal structure of rhodopsin: A G protein-coupled receptor.," *Science*, vol. 289, no. 5480, pp. 739–45, Aug. 2000.
- [22] D. Hilger, M. Masureel, and B. K. Kobilka, "Structure and dynamics of GPCR signaling complexes," *Nat. Struct. Mol. Biol.*, vol. 25, no. 1, pp. 4–12, Jan. 2018.
- [23] S. L. Ritter and R. a Hall, "Fine-tuning of GPCR activity by receptor-interacting proteins.," *Nat. Rev. Mol. Cell Biol.*, vol. 10, no. 12, pp. 819–30, Dec. 2009.
- [24] A. J. Kimple, D. E. Bosch, P. M. Giguère, and D. P. Siderovski, "Regulators of G-protein signaling and their G α substrates: promises and challenges in their use as drug discovery targets," *Pharmacol. Rev.*, vol. 63, no. 3, pp. 728–49, Sep. 2011.
- [25] D. M. Rosenbaum, S. G. F. Rasmussen, and B. K. Kobilka, "The structure and function of G-protein-coupled receptors," *Nature*, vol. 459, no. 7245, pp. 356–363, May 2009.
- [26] K. E. Komolov and J. L. Benovic, "G protein-coupled receptor kinases: Past, present and future," *Cell. Signal.*, vol. 41, pp. 17–24, 2018.
- [27] S. M. DeWire, S. Ahn, R. J. Lefkowitz, and S. K. Shenoy, " β -Arrestins and Cell Signaling," *Annu. Rev. Physiol.*, vol. 69, no. 1, pp. 483–510, Feb. 2007.
- [28] V. V Gurevich and E. V Gurevich, "Overview of different mechanisms of arrestin-mediated signaling.," *Curr. Protoc. Pharmacol.*, vol. 67, p. Unit 2.10.1-9, Dec. 2014.
- [29] L. Pradayrol, H. Jörnvall, V. Mutt, and A. Ribet, "N-terminally extended somatostatin: The primary structure of somatostatin-28," *FEBS Lett.*, vol. 109, no. 1, pp. 55–58, Jan. 1980.
- [30] P. Brazeau, W. Vale, R. Burgus, N. Ling, M. Butcher, J. Rivier, and R. Guillemin, "Hypothalamic Polypeptide That Inhibits the Secretion of Immunoreactive Pituitary Growth Hormone," *Science (80-.)*, vol. 179, no. 4068, p. 77 LP-79, Jan. 1973.
- [31] V. Martinez, "Somatostatin," in *Handbook of Biologically Active Peptides*, Elsevier, 2013, pp. 1320–1329.
- [32] P. Barnett, "Somatostatin and somatostatin receptor physiology," *Endocrine*, vol. 20, no. 3, pp. 255–264, 2003.
- [33] Y. C. Patel, "Somatostatin and Its Receptor Family," *Front. Neuroendocrinol.*, vol. 20, no. 3, pp. 157–198, 1999.
- [34] S. Pyronnet, C. Bousquet, S. Najib, R. Azar, H. Laklai, and C. Susini, "Antitumor effects of somatostatin," *Mol. Cell. Endocrinol.*, vol. 286, no. 1, pp. 230–237, 2008.

- [35] D. Hoyer, G. I. Bell, M. Berelowitz, J. Epelbaum, W. Feniuk, P. P. A. Humphrey, A.-M. O'Carroll, Y. C. Patel, A. Schonbrunn, J. E. Taylor, and T. Reisine, "Classification and nomenclature of somatostatin receptors," *Trends Pharmacol. Sci.*, vol. 16, no. 3, pp. 86–88, 1995.
- [36] M. Theodoropoulou and G. K. Stalla, "Somatostatin receptors: From signaling to clinical practice," *Front. Neuroendocrinol.*, vol. 34, no. 3, pp. 228–252, 2013.
- [37] F. Barbieri, A. Bajetto, A. Pattarozzi, M. Gatti, R. Würth, S. Thellung, A. Corsaro, V. Villa, M. Nizzari, and T. Florio, "Peptide Receptor Targeting in Cancer: The Somatostatin Paradigm," *Int. J. Pept.*, vol. 2013, pp. 1–20, 2013.
- [38] G. Weckbecker, I. Lewis, R. Albert, H. A. Schmid, D. Hoyer, and C. Bruns, "Opportunities in somatostatin research: biological, chemical and therapeutic aspects," *Nat. Rev. Drug Discov.*, vol. 2, p. 999, Dec. 2003.
- [39] J. C. Reubi, B. Waser, J. C. Schaer, and J. A. Laissue, "Somatostatin receptor sst1-sst5 expression in normal and neoplastic human tissues using receptor autoradiography with subtype-selective ligands," *Eur. J. Nucl. Med.*, vol. 28, no. 7, pp. 836–46, Jul. 2001.
- [40] J. C. Reubi and A. Schonbrunn, "Illuminating somatostatin analog action at neuroendocrine tumor receptors," *Trends Pharmacol. Sci.*, vol. 34, no. 12, pp. 676–688, 2013.
- [41] J. C. Reubi, J.-C. Schär, B. Waser, S. Wenger, A. Heppeler, J. S. Schmitt, and H. R. Mäcke, "Affinity profiles for human somatostatin receptor subtypes SST1-SST5 of somatostatin radiotracers selected for scintigraphic and radiotherapeutic use," *Eur. J. Nucl. Med. Mol. Imaging*, vol. 27, no. 3, pp. 273–282, Mar. 2000.
- [42] G. Olias, C. Viollet, H. Kusserow, J. Epelbaum, and W. Meyerhof, "Regulation and function of somatostatin receptors," *J. Neurochem.*, vol. 89, no. 5, pp. 1057–1091, Jun. 2004.
- [43] S. Froidevaux and A. N. Eberle, "Somatostatin analogs and radiopeptides in cancer therapy," *Biopolymers*, vol. 66, no. 3, pp. 161–83, Jan. 2002.
- [44] M. Mukoyama, M. Nakajima, M. Horiuchi, H. Sasamura, R. E. Pratt, and V. J. Dzau, "Expression cloning of type 2 angiotensin II receptor reveals a unique class of seven-transmembrane receptors," *J. Biol. Chem.*, vol. 268, no. 33, pp. 24539–42, Nov. 1993.
- [45] S. Higuchi, H. Ohtsu, H. Suzuki, H. Shirai, G. D. Frank, and S. Eguchi, "Angiotensin II signal transduction through the AT1 receptor: novel insights into mechanisms and pathophysiology," *Clin. Sci. (Lond.)*, vol. 112, no. 8, pp. 417–28, Apr. 2007.
- [46] P. K. Mehta and K. K. Griendling, "Angiotensin II cell signaling: physiological and pathological effects in the cardiovascular system," *Am. J. Physiol. Cell Physiol.*, vol. 292, no. 1, pp. C82–97, Jan. 2007.
- [47] A. J. George, W. G. Thomas, and R. D. Hannan, "The renin-angiotensin system and cancer: old dog, new tricks," *Nat. Rev. Cancer*, vol. 10, no. 11, pp. 745–59, Nov. 2010.
- [48] N. J. Smith, H.-W. Chan, J. E. Osborne, W. G. Thomas, and R. D. Hannan, "Hijacking epidermal growth factor receptors by angiotensin II: new possibilities for understanding and treating cardiac hypertrophy," *Cell. Mol. Life Sci.*, vol. 61, no. 21, pp. 2695–703, Nov. 2004.
- [49] S. Nouet and C. Nahmias, "Signal transduction from the angiotensin II AT2 receptor," *Trends Endocrinol. Metab.*, vol. 11, no. 1, pp. 1–6, Feb. 2000.

- [50] M. de Gasparo, K. J. Catt, T. Inagami, J. W. Wright, and T. Unger, "International union of pharmacology. XXIII. The angiotensin II receptors.," *Pharmacol. Rev.*, vol. 52, no. 3, pp. 415–72, Sep. 2000.
- [51] M. A. Zaman, S. Oparil, and D. A. Calhoun, "Drugs targeting the renin–angiotensin–aldosterone system," *Nat. Rev. Drug Discov.*, vol. 1, p. 621, Aug. 2002.
- [52] F. Deshayes and C. Nahmias, "Angiotensin receptors: a new role in cancer?," *Trends Endocrinol. Metab.*, vol. 16, no. 7, pp. 293–9, Sep. 2005.
- [53] D. R. Rhodes, B. Ateeq, Q. Cao, S. A. Tomlins, R. Mehra, B. Laxman, S. Kalyana-Sundaram, R. J. Lonigro, B. E. Helgeson, M. S. Bhojani, A. Rehemtulla, C. G. Kleer, D. F. Hayes, P. C. Lucas, S. Varambally, and A. M. Chinnaiyan, "AGTR1 overexpression defines a subset of breast cancer and confers sensitivity to losartan, an AGTR1 antagonist.," *Proc. Natl. Acad. Sci. U. S. A.*, vol. 106, no. 25, pp. 10284–9, Jun. 2009.
- [54] C. Röcken, F.-W. Röhl, E. Diebler, U. Lendeckel, M. Pross, S. Carl-McGrath, and M. P. A. Ebert, "The angiotensin II/angiotensin II receptor system correlates with nodal spread in intestinal type gastric cancer.," *Cancer Epidemiol. Biomarkers Prev.*, vol. 16, no. 6, pp. 1206–12, Jun. 2007.
- [55] H. A. Arafat, Q. Gong, G. Chipitsyna, A. Rizvi, C. T. Saa, and C. J. Yeo, "Antihypertensives as novel antineoplastics: angiotensin-I-converting enzyme inhibitors and angiotensin II type 1 receptor blockers in pancreatic ductal adenocarcinoma.," *J. Am. Coll. Surg.*, vol. 204, no. 5, pp. 996-1005–6, May 2007.
- [56] Y. Fujimoto, T. Sasaki, A. Tsuchida, and K. Chayama, "Angiotensin II type 1 receptor expression in human pancreatic cancer and growth inhibition by angiotensin II type 1 receptor antagonist," *FEBS Lett.*, vol. 495, no. 3, pp. 197–200, 2001.
- [57] F. Wu, G. Song, C. de Graaf, and R. C. Stevens, "Structure and Function of Peptide-Binding G Protein-Coupled Receptors," *J. Mol. Biol.*, vol. 429, no. 17, pp. 2726–2745, 2017.
- [58] M. Fani, H. R. Maেকে, and S. M. Okarvi, "Radiolabeled peptides: valuable tools for the detection and treatment of cancer.," *Theranostics*, vol. 2, no. 5, pp. 481–501, 2012.
- [59] J. C. Reubi, "Peptide Receptors as Molecular Targets for Cancer Diagnosis and Therapy," *Endocr. Rev.*, vol. 24, no. 4, pp. 389–427, Aug. 2003.
- [60] S. M. Okarvi, "Peptide-based radiopharmaceuticals: Future tools for diagnostic imaging of cancers and other diseases," *Med. Res. Rev.*, vol. 24, no. 3, pp. 357–397, 2004.
- [61] R. Soudy, N. Byeon, Y. Raghuwanshi, S. Ahmed, and A. L. and K. Kaur*, "Engineered Peptides for Applications in Cancer-Targeted Drug Delivery and Tumor Detection," *Mini-Reviews in Medicinal Chemistry*, vol. 17, no. 18. pp. 1696–1712, 2017.
- [62] M. F. Powell, T. Stewart, L. Jr Otvos, L. Urge, F. C. A. Gaeta, A. Sette, T. Arrhenius, D. Thomson, K. Soda, and S. M. Colon, "Peptide Stability in Drug Development. II. Effect of Single Amino Acid Substitution and Glycosylation on Peptide Reactivity in Human Serum," *Pharm. Res.*, vol. 10, no. 9, pp. 1268–1273, 1993.
- [63] K. Bellmann-Sickert and A. G. Beck-Sickinger, "Peptide drugs to target G protein-coupled receptors," *Trends Pharmacol. Sci.*, vol. 31, no. 9, pp. 434–441, 2010.
- [64] A. G. B.-S. and I. U. Khan, "Targeted Tumor Diagnosis and Therapy with Peptide Hormones as Radiopharmaceuticals," *Anti-Cancer Agents in Medicinal Chemistry*, vol. 8, no. 2. pp. 186–199, 2008.

- [65] M. Srinivasarao, C. V Galliford, and P. S. Low, "Principles in the design of ligand-targeted cancer therapeutics and imaging agents," *Nat. Rev. Drug Discov.*, vol. 14, p. 203, Feb. 2015.
- [66] P. Choudhury and M. Gupta, "Personalized & Precision Medicine in Cancer: A Theranostic Approach.," *Curr. Radiopharm.*, vol. 10, no. 3, pp. 166–170, Nov. 2017.
- [67] J. C. Yao, M. Hassan, A. Phan, C. Dagohoy, C. Leary, J. E. Mares, E. K. Abdalla, J. B. Fleming, J.-N. Vauthey, A. Rashid, and D. B. Evans, "One hundred years after 'carcinoid': epidemiology of and prognostic factors for neuroendocrine tumors in 35,825 cases in the United States.," *J. Clin. Oncol.*, vol. 26, no. 18, pp. 3063–72, Jun. 2008.
- [68] A. Walenkamp, G. Crespo, F. Fierro Maya, R. Fossmark, P. Igaz, A. Rinke, G. Tamagno, G. Vitale, K. Öberg, and T. Meyer, "Hallmarks of gastrointestinal neuroendocrine tumours: implications for treatment.," *Endocr. Relat. Cancer*, vol. 21, no. 6, pp. R445-60, Dec. 2014.
- [69] J. M. Feldman, "Carcinoid tumors and the carcinoid syndrome," *Curr. Probl. Surg.*, vol. 26, no. 12, pp. 835–885, Dec. 1989.
- [70] G. Rindi, C. Capella, and E. Solcia, "Cell biology, clinicopathological profile, and classification of gastro-enteropancreatic endocrine tumors," *J. Mol. Med.*, vol. 76, no. 6, pp. 413–420, Apr. 1998.
- [71] A. Frilling, G. Akerstrom, M. Falconi, M. Pavel, J. Ramos, M. Kidd, and I. M. Modlin, "Neuroendocrine tumor disease: an evolving landscape," *Endocr. Relat. Cancer*, vol. 19, no. 5, pp. R163–R185, Sep. 2012.
- [72] M. Dong, A. T. Phan, and J. C. Yao, "New Strategies for Advanced Neuroendocrine Tumors in the Era of Targeted Therapy," *Clin. Cancer Res.*, vol. 18, no. 7, pp. 1830–1836, Apr. 2012.
- [73] J. R. Eads and N. J. Meropol, "A new era for the systemic therapy of neuroendocrine tumors.," *Oncologist*, vol. 17, no. 3, pp. 326–38, 2012.
- [74] J. C. Yao, D. R. Lagunes, and M. H. Kulke, "Targeted therapies in neuroendocrine tumors (NET): clinical trial challenges and lessons learned.," *Oncologist*, vol. 18, no. 5, pp. 525–32, 2013.
- [75] T. Fischer, C. Doll, S. Jacobs, A. Kolodziej, R. Stumm, and S. Schulz, "Reassessment of sst₂ Somatostatin Receptor Expression in Human Normal and Neoplastic Tissues Using the Novel Rabbit Monoclonal Antibody UMB-1," *J. Clin. Endocrinol. Metab.*, vol. 93, no. 11, pp. 4519–4524, Nov. 2008.
- [76] J. C. Reubi, R. Maurer, K. von Werder, J. Torhorst, J. G. Klijn, and S. W. Lamberts, "Somatostatin receptors in human endocrine tumors.," *Cancer Res.*, vol. 47, no. 2, pp. 551–8, Jan. 1987.
- [77] J. C. Reubi, A. Kappeler, B. Waser, J. Laissue, R. W. Hipkin, and A. Schonbrunn, "Immunohistochemical Localization of Somatostatin Receptors sst_{2A} in Human Tumors," *Am. J. Pathol.*, vol. 153, no. 1, pp. 233–245, Jul. 1998.
- [78] H. A. Schmid, C. Lambertini, H. H. van Vugt, P. Barzaghi-Rinaudo, J. Schäfer, R. Hillenbrand, A. W. Sailer, M. Kaufmann, and P. Nuciforo, "Monoclonal antibodies against the human somatostatin receptor subtypes 1-5: development and immunohistochemical application in neuroendocrine tumors.," *Neuroendocrinology*, vol. 95, no. 3, pp. 232–47, 2012.
- [79] C. Gröttinger and B. Wiedenmann, "Somatostatin Receptor Targeting for Tumor Imaging and Therapy," *Ann. N. Y. Acad. Sci.*, vol. 1014, no. 1, pp. 258–264, Apr. 2004.

- [80] W. W. de Herder, D. J. Kwekkeboom, R. A. Feelders, M. O. van Aken, S. W. J. Lamberts, A.-J. van der Lely, and E. P. Krenning, "Somatostatin receptor imaging for neuroendocrine tumors," *Pituitary*, vol. 9, no. 3, pp. 243–248, Sep. 2006.
- [81] J. J. M. Teunissen, D. J. Kwekkeboom, R. Valkema, and E. P. Krenning, "Nuclear medicine techniques for the imaging and treatment of neuroendocrine tumours.," *Endocr. Relat. Cancer*, vol. 18 Suppl 1, no. S1, pp. S27-51, Oct. 2011.
- [82] R. J. Hicks, "Use of molecular targeted agents for the diagnosis, staging and therapy of neuroendocrine malignancy.," *Cancer Imaging*, vol. 10 Spec no, no. 1A, pp. S83-91, Oct. 2010.
- [83] E. P. Krenning, D. J. Kwekkeboom, W. H. Bakker, W. A. P. Breeman, P. P. M. Kooij, H. Y. Oei, M. van Hagen, P. T. E. Postema, M. de Jong, J. C. Reubi, T. J. Visser, A. E. M. Reijs, L. J. Hofland, J. W. Koper, and S. W. J. Lamberts, "Somatostatin receptor scintigraphy with [111In-DTPA-d-Phe1]- and [123I-Tyr3]-octreotide: the Rotterdam experience with more than 1000 patients," *Eur. J. Nucl. Med.*, vol. 20, no. 8, pp. 716–731, Aug. 1993.
- [84] S. W. J. Lamberts, W. H. Barker, J.-C. Reubi, and E. P. Krenning, "Somatostatin-Receptor Imaging in the Localization of Endocrine Tumors," *N. Engl. J. Med.*, vol. 323, no. 18, pp. 1246–1249, Nov. 1990.
- [85] M. van Essen, A. Sundin, E. P. Krenning, and D. J. Kwekkeboom, "Neuroendocrine tumours: the role of imaging for diagnosis and therapy," *Nat. Rev. Endocrinol.*, vol. 10, p. 102, Dec. 2013.
- [86] H. R. Maecke, M. Hofmann, and U. Haberkorn, "(68)Ga-labeled peptides in tumor imaging.," *J. Nucl. Med.*, vol. 46 Suppl 1, p. 172S–8S, Jan. 2005.
- [87] I. Kayani, J. B. Bomanji, A. Groves, G. Conway, S. Gacinovic, T. Win, J. Dickson, M. Caplin, and P. J. Ell, "Functional imaging of neuroendocrine tumors with combined PET/CT using 68Ga-DOTATATE (DOTA-DPhe1,Tyr3-octreotate) and 18F-FDG.," *Cancer*, vol. 112, no. 11, pp. 2447–55, Jun. 2008.
- [88] M. Hofmann, H. Maecke, R. Börner, E. Weckesser, P. Schöffski, L. Oei, J. Schumacher, M. Henze, A. Heppeler, J. Meyer, and H. Knapp, "Biokinetics and imaging with the somatostatin receptor PET radioligand (68)Ga-DOTATOC: preliminary data.," *Eur. J. Nucl. Med.*, vol. 28, no. 12, pp. 1751–7, Dec. 2001.
- [89] R. Srirajaskanthan, I. Kayani, A. M. Quigley, J. Soh, M. E. Caplin, and J. Bomanji, "The role of 68Ga-DOTATATE PET in patients with neuroendocrine tumors and negative or equivocal findings on 111In-DTPA-octreotide scintigraphy.," *J. Nucl. Med.*, vol. 51, no. 6, pp. 875–82, Jun. 2010.
- [90] I. Buchmann, M. Henze, S. Engelbrecht, M. Eisenhut, A. Runz, M. Schäfer, T. Schilling, S. Haufe, T. Herrmann, and U. Haberkorn, "Comparison of 68Ga-DOTATOC PET and 111In-DTPAOC (Octreoscan) SPECT in patients with neuroendocrine tumours.," *Eur. J. Nucl. Med. Mol. Imaging*, vol. 34, no. 10, pp. 1617–26, Oct. 2007.
- [91] J. Kowalski, M. Henze, J. Schuhmacher, H. R. Mäcke, M. Hofmann, and U. Haberkorn, "Evaluation of positron emission tomography imaging using [68Ga]-DOTA-D Phe(1)-Tyr(3)-Octreotide in comparison to [111In]-DTPAOC SPECT. First results in patients with neuroendocrine tumors.," *Mol. Imaging Biol.*, vol. 5, no. 1, pp. 42–8, 2003.
- [92] L. Bodei, A. Sundin, M. Kidd, V. Prasad, and I. M. Modlin, "The Status of Neuroendocrine Tumor Imaging: From Darkness to Light?," *Neuroendocrinology*, vol. 101, no. 1, pp. 1–17, Sep. 2014.

- [93] G. Hong, A. L. Antaris, and H. Dai, "Near-infrared fluorophores for biomedical imaging," *Nat. Biomed. Eng.*, vol. 1, p. 10, Jan. 2017.
- [94] C. Wang, Z. Wang, T. Zhao, Y. Li, G. Huang, B. D. Sumer, and J. Gao, "Optical molecular imaging for tumor detection and image-guided surgery," *Biomaterials*, vol. 157, pp. 62–75, 2018.
- [95] W. A. Weber, J. Czernin, M. E. Phelps, and H. R. Herschman, "Technology Insight: novel imaging of molecular targets is an emerging area crucial to the development of targeted drugs," *Nat. Clin. Pract. Oncol.*, vol. 5, p. 44, Jan. 2008.
- [96] C. Grötzinger and B. Wiedenmann, "Somatostatin receptor targeting for tumor imaging and therapy.," *Ann. N. Y. Acad. Sci.*, vol. 1014, pp. 258–64, Apr. 2004.
- [97] V. Ntziachristos, C. Bremer, and R. Weissleder, "Fluorescence imaging with near-infrared light: new technological advances that enable in vivo molecular imaging.," *Eur. Radiol.*, vol. 13, no. 1, pp. 195–208, Jan. 2003.
- [98] R. Weissleder, "A clearer vision for in vivo imaging.," *Nat. Biotechnol.*, vol. 19, no. 4, pp. 316–7, Apr. 2001.
- [99] X. Yi, F. Wang, W. Qin, X. Yang, and J. Yuan, "Near-infrared fluorescent probes in cancer imaging and therapy: an emerging field.," *Int. J. Nanomedicine*, vol. 9, pp. 1347–65, 2014.
- [100] J. E. Bugaj, S. Achilefu, R. B. Dorshow, and R. Rajagopalan, "Novel fluorescent contrast agents for optical imaging of in vivo tumors based on a receptor-targeted dye-peptide conjugate platform.," *J. Biomed. Opt.*, vol. 6, no. 2, pp. 122–33, Apr. 2001.
- [101] A. Becker, C. Hassenius, K. Licha, B. Ebert, U. Sukowski, W. Semmler, B. Wiedenmann, and C. Grötzinger, "Receptor-targeted optical imaging of tumors with near-infrared fluorescent ligands.," *Nat. Biotechnol. Apr2001*, vol. 19, no. 4.
- [102] L. Bodei, M. Kidd, V. Prasad, and I. M. Modlin, "Peptide Receptor Radionuclide Therapy of Neuroendocrine Tumors," in *Frontiers of hormone research*, vol. 44, 2015, pp. 198–215.
- [103] M. de Jong, W. A. P. Breeman, R. Valkema, B. F. Bernard, and E. P. Krenning, "Combination radionuclide therapy using ¹⁷⁷Lu- and ⁹⁰Y-labeled somatostatin analogs.," *J. Nucl. Med.*, vol. 46 Suppl 1, no. 1 suppl, p. 13S–7S, Jan. 2005.
- [104] D. J. Kwekkeboom, W. H. Bakker, B. L. Kam, J. J. M. Teunissen, P. P. M. Kooij, W. W. Herder, R. A. Feelders, C. H. J. Eijck, M. Jong, A. Srinivasan, J. L. Erion, and E. P. Krenning, "Treatment of patients with gastro-entero-pancreatic (GEP) tumours with the novel radiolabelled somatostatin analogue [¹⁷⁷Lu-DOTA₀,Tyr₃]octreotate," *Eur. J. Nucl. Med. Mol. Imaging*, vol. 30, no. 3, pp. 417–422, Mar. 2003.
- [105] H. Bergsma, E. I. van Vliet, J. J. M. Teunissen, B. L. R. Kam, W. W. de Herder, R. P. Peeters, E. P. Krenning, and D. J. Kwekkeboom, "Peptide receptor radionuclide therapy (PRRT) for GEP-NETs," *Best Pract. Res. Clin. Gastroenterol.*, vol. 26, no. 6, pp. 867–881, Dec. 2012.
- [106] D. J. Kwekkeboom, W. W. de Herder, B. L. Kam, C. H. van Eijck, M. van Essen, P. P. Kooij, R. A. Feelders, M. O. van Aken, and E. P. Krenning, "Treatment with the radiolabeled somatostatin analog [¹⁷⁷ Lu-DOTA 0,Tyr₃]octreotate: toxicity, efficacy, and survival.," *J. Clin. Oncol.*, vol. 26, no. 13, pp. 2124–30, May 2008.
- [107] J. Strosberg, G. El-Haddad, E. Wolin, A. Hendifar, J. Yao, B. Chasen, E. Mittra, P. L. Kunz, M. H. Kulke, H. Jacene, D. Bushnell, T. M. O'Dorisio, R. P. Baum, H. R. Kulkarni, M. Caplin, R. Lebtahi, T. Hobday, E. Delpassand, E. Van Cutsem, A. Benson, R. Srirajaskanthan, M. Pavel, J. Mora, J. Berlin, E. Grande, N. Reed, E. Seregni, K. Öberg, M. Lopera Sierra, P. Santoro, T.

- Thevenet, J. L. Erion, P. Ruzsniwski, D. Kwekkeboom, and E. Krenning, "Phase 3 Trial of 177 Lu-Dotatate for Midgut Neuroendocrine Tumors," *N. Engl. J. Med.*, vol. 376, no. 2, pp. 125–135, Jan. 2017.
- [108] M. Ginj, H. Zhang, B. Waser, R. Cescato, D. Wild, X. Wang, J. Erchegeyi, J. Rivier, H. R. Macke, and J. C. Reubi, "Radiolabeled somatostatin receptor antagonists are preferable to agonists for in vivo peptide receptor targeting of tumors," *Proc. Natl. Acad. Sci.*, vol. 103, no. 44, pp. 16436–16441, Oct. 2006.
- [109] S. U. Dalm, J. Nonnekens, G. N. Doeswijk, E. de Blois, D. C. van Gent, M. W. Konijnenberg, and M. de Jong, "Comparison of the Therapeutic Response to Treatment with a 177Lu-Labeled Somatostatin Receptor Agonist and Antagonist in Preclinical Models," *J. Nucl. Med.*, vol. 57, no. 2, pp. 260–5, Feb. 2016.
- [110] D. Wild, M. Fani, R. Fischer, L. Del Pozzo, F. Kaul, S. Krebs, R. Fischer, J. E. F. Rivier, J. C. Reubi, H. R. Maecke, and W. A. Weber, "Comparison of somatostatin receptor agonist and antagonist for peptide receptor radionuclide therapy: a pilot study," *J. Nucl. Med.*, vol. 55, no. 8, pp. 1248–52, Aug. 2014.
- [111] H.-J. Klümper, J. H. Beijnen, H. Gurney, and J. H. M. Schellens, "Inhibitors of mTOR," *Oncologist*, vol. 15, no. 12, pp. 1262–9, Jan. 2010.
- [112] M. Laplante and D. M. Sabatini, "mTOR signaling in growth control and disease," *Cell*, vol. 149, no. 2, pp. 274–93, Apr. 2012.
- [113] D. M. Sabatini, "mTOR and cancer: insights into a complex relationship," *Nat. Rev. Cancer*, vol. 6, no. 9, pp. 729–34, Sep. 2006.
- [114] K. E. O'Reilly, F. Rojo, Q.-B. She, D. Solit, G. B. Mills, D. Smith, H. Lane, F. Hofmann, D. J. Hicklin, D. L. Ludwig, J. Baselga, and N. Rosen, "mTOR inhibition induces upstream receptor tyrosine kinase signaling and activates Akt," *Cancer Res.*, vol. 66, no. 3, pp. 1500–8, Feb. 2006.
- [115] D. D. Sarbassov, S. M. Ali, S. Sengupta, J.-H. Sheen, P. P. Hsu, A. F. Bagley, A. L. Markhard, and D. M. Sabatini, "Prolonged rapamycin treatment inhibits mTORC2 assembly and Akt/PKB," *Mol. Cell*, vol. 22, no. 2, pp. 159–68, Apr. 2006.
- [116] M. S. Neshat, I. K. Mellinshoff, C. Tran, B. Stiles, G. Thomas, R. Petersen, P. Frost, J. J. Gibbons, H. Wu, and C. L. Sawyers, "Enhanced sensitivity of PTEN-deficient tumors to inhibition of FRAP/mTOR," *Proc. Natl. Acad. Sci. U. S. A.*, vol. 98, no. 18, pp. 10314–9, Aug. 2001.
- [117] A. Carracedo, L. Ma, J. Teruya-Feldstein, F. Rojo, L. Salmena, A. Alimonti, A. Egia, A. T. Sasaki, G. Thomas, S. C. Kozma, A. Papa, C. Nardella, L. C. Cantley, J. Baselga, and P. P. Pandolfi, "Inhibition of mTORC1 leads to MAPK pathway activation through a PI3K-dependent feedback loop in human cancer," *J. Clin. Invest.*, vol. 118, no. 9, pp. 3065–74, Sep. 2008.
- [118] M. S. Lee and B. H. O'Neil, "Summary of emerging personalized medicine in neuroendocrine tumors: are we on track?," *J. Gastrointest. Oncol.*, vol. 7, no. 5, pp. 804–818, Oct. 2016.
- [119] J. C. Yao, M. H. Shah, T. Ito, C. L. Bohas, E. M. Wolin, E. Van Cutsem, T. J. Hobday, T. Okusaka, J. Capdevila, E. G. E. de Vries, P. Tomassetti, M. E. Pavel, S. Hoosen, T. Haas, J. Lincy, D. Lebwohl, K. Öberg, and T. T. (RADIANT-3) S. G. RAD001 in Advanced Neuroendocrine Tumors, "Everolimus for advanced pancreatic neuroendocrine tumors," *N. Engl. J. Med.*, vol. 364, no. 6, pp. 514–23, Feb. 2011.

- [120] J. C. Yao, N. Fazio, S. Singh, R. Buzzoni, C. Carnaghi, E. Wolin, J. Tomasek, M. Raderer, H. Lahner, M. Voi, L. B. Pacaud, N. Rouyrre, C. Sachs, J. W. Valle, G. Delle Fave, E. Van Cutsem, M. Tesselaar, Y. Shimada, D.-Y. Oh, J. Strosberg, M. H. Kulke, M. E. Pavel, and F. T. (RADIANT-4) S. G. RAD001 in Advanced Neuroendocrine Tumours, "Everolimus for the treatment of advanced, non-functional neuroendocrine tumours of the lung or gastrointestinal tract (RADIANT-4): a randomised, placebo-controlled, phase 3 study.," *Lancet (London, England)*, vol. 387, no. 10022, pp. 968–77, Mar. 2016.
- [121] M. E. Pavel, J. D. Hainsworth, E. Baudin, M. Peeters, D. Hörsch, R. E. Winkler, J. Klimovsky, D. Lebowitz, V. Jehl, E. M. Wolin, K. Öberg, E. Van Cutsem, and J. C. Yao, "Everolimus plus octreotide long-acting repeatable for the treatment of advanced neuroendocrine tumours associated with carcinoid syndrome (RADIANT-2): a randomised, placebo-controlled, phase 3 study," *Lancet*, vol. 378, no. 9808, pp. 2005–2012, 2011.
- [122] J. C. Yao, C. Lombard-Bohas, E. Baudin, L. K. Kvols, P. Rougier, P. Ruzsniwski, S. Hoosen, J. St Peter, T. Haas, D. Lebowitz, E. Van Cutsem, M. H. Kulke, T. J. Hobday, T. M. O'Dorisio, M. H. Shah, G. Cadiot, G. Luppi, J. A. Posey, and B. Wiedenmann, "Daily oral everolimus activity in patients with metastatic pancreatic neuroendocrine tumors after failure of cytotoxic chemotherapy: a phase II trial.," *J. Clin. Oncol.*, vol. 28, no. 1, pp. 69–76, Jan. 2010.
- [123] I. Duran, J. Kortmansky, D. Singh, H. Hirte, W. Kocha, G. Goss, L. Le, A. Oza, T. Nicklee, J. Ho, D. Birle, G. R. Pond, D. Arboine, J. Dancey, S. Aviel-Ronen, M.-S. Tsao, D. Hedley, and L. L. Siu, "A phase II clinical and pharmacodynamic study of temsirolimus in advanced neuroendocrine carcinomas.," *Br. J. Cancer*, vol. 95, no. 9, pp. 1148–54, Nov. 2006.
- [124] M. B. Atkins, U. Yasothan, and P. Kirkpatrick, "Everolimus.," *Nat. Rev. Drug Discov.*, vol. 8, no. 7, pp. 535–6, Jul. 2009.
- [125] B. Rini, S. Kar, and P. Kirkpatrick, "Temsirrolimus.," *Nat. Rev. Drug Discov.*, vol. 6, p. 599, Aug. 2007.
- [126] P. G. Claringbold and J. H. Turner, "NeuroEndocrine Tumor Therapy with Lutetium-177-octreotate and Everolimus (NETTLE): A Phase I Study.," *Cancer Biother. Radiopharm.*, vol. 30, no. 6, pp. 261–9, Aug. 2015.
- [127] S. Mehta, P. R. de Reuver, P. Gill, J. Andrici, L. D'Urso, A. Mittal, N. Pavlakis, S. Clarke, J. S. Samra, and A. J. Gill, "Somatostatin Receptor SSTR-2a Expression Is a Stronger Predictor for Survival Than Ki-67 in Pancreatic Neuroendocrine Tumors.," *Medicine (Baltimore)*, vol. 94, no. 40, p. e1281, Oct. 2015.
- [128] J. C. Reubi and B. Waser, "Concomitant expression of several peptide receptors in neuroendocrine tumours: molecular basis for in vivo multireceptor tumour targeting.," *Eur. J. Nucl. Med. Mol. Imaging*, vol. 30, no. 5, pp. 781–93, May 2003.
- [129] O. Eriksson, I. Velikyan, R. K. Selvaraju, F. Kandeel, L. Johansson, G. Antoni, B. Eriksson, J. Sörensen, and O. Korsgren, "Detection of metastatic insulinoma by positron emission tomography with [(68)ga]exendin-4-a case report.," *J. Clin. Endocrinol. Metab.*, vol. 99, no. 5, pp. 1519–24, May 2014.
- [130] J. C. Reubi, E. Krenning, S. W. J. Lamberts, and L. Kvols, "In vitro detection of somatostatin receptors in human tumors," *Metabolism*, vol. 41, no. 9, pp. 104–110, Sep. 1992.
- [131] L. J. Hofland and S. W. J. Lamberts, "The pathophysiological consequences of somatostatin receptor internalization and resistance.," *Endocr. Rev.*, vol. 24, no. 1, pp. 28–47, Feb. 2003.
- [132] S. W. J. Lamberts, A.-J. van der Lely, W. W. de Herder, and L. J. Hofland, "Octreotide," *N. Engl. J. Med.*, vol. 334, no. 4, pp. 246–254, Jan. 1996.

- [133] C. Hassenius, M. Bäder, H. Meinhold, M. Böhmig, S. Faiss, J. C. Reubi, and B. Wiedenmann, "Vasoactive intestinal peptide receptor scintigraphy in patients with pancreatic adenocarcinomas or neuroendocrine tumours.," *Eur. J. Nucl. Med.*, vol. 27, no. 11, pp. 1684–93, Nov. 2000.
- [134] J. C. Reubi, J. C. Schaer, and B. Waser, "Cholecystikinin(CCK)-A and CCK-B/gastrin receptors in human tumors.," *Cancer Res.*, vol. 57, no. 7, pp. 1377–86, Apr. 1997.
- [135] M. Körner, M. Stöckli, B. Waser, and J. C. Reubi, "GLP-1 receptor expression in human tumors and human normal tissues: potential for in vivo targeting.," *J. Nucl. Med.*, vol. 48, no. 5, pp. 736–43, May 2007.
- [136] B. Waser, R. Rehmann, C. Sanchez, D. Fourmy, and J. C. Reubi, "Glucose-dependent insulinotropic polypeptide receptors in most gastroenteropancreatic and bronchial neuroendocrine tumors.," *J. Clin. Endocrinol. Metab.*, vol. 97, no. 2, pp. 482–8, Feb. 2012.
- [137] J. C. Reubi and B. Waser, "Triple-peptide receptor targeting in vitro allows detection of all tested gut and bronchial NETs.," *J. Nucl. Med.*, vol. 56, no. 4, pp. 613–5, Apr. 2015.
- [138] S. E. Burdall, A. M. Hanby, M. R. J. Lansdown, and V. Speirs, "Breast cancer cell lines: friend or foe?," *Breast Cancer Res.*, vol. 5, no. 2, pp. 89–95, 2003.
- [139] R. J. Geraghty, A. Capes-Davis, J. M. Davis, J. Downward, R. I. Freshney, I. Knezevic, R. Lovell-Badge, J. R. W. Masters, J. Meredith, G. N. Stacey, P. Thraves, and M. Vias, "Guidelines for the use of cell lines in biomedical research," *Br. J. Cancer*, vol. 111, no. 6, pp. 1021–1046, Sep. 2014.
- [140] M. de Jong, J. Essers, and W. M. van Weerden, "Imaging preclinical tumour models: improving translational power," *Nat. Rev. Cancer*, vol. 14, p. 481, Jun. 2014.
- [141] T. G. Meijer, K. A. Naipal, A. Jager, and D. C. van Gent, "Ex vivo tumor culture systems for functional drug testing and therapy response prediction," *Futur. Sci. OA*, vol. 3, no. 2, p. FSO190, May 2017.
- [142] C. A. Pettaway, S. Pathak, G. Greene, E. Ramirez, M. R. Wilson, J. J. Killion, and I. J. Fidler, "Selection of highly metastatic variants of different human prostatic carcinomas using orthotopic implantation in nude mice.," *Clin. Cancer Res.*, vol. 2, no. 9, pp. 1627–36, Sep. 1996.
- [143] T. Kubota, "Metastatic models of human cancer xenografted in the nude mouse: the importance of orthotopic transplantation.," *J. Cell. Biochem.*, vol. 56, no. 1, pp. 4–8, Sep. 1994.
- [144] D. Siolas and G. J. Hannon, "Patient-derived tumor xenografts: transforming clinical samples into mouse models.," *Cancer Res.*, vol. 73, no. 17, pp. 5315–9, Sep. 2013.
- [145] L. D. Shultz, F. Ishikawa, and D. L. Greiner, "Humanized mice in translational biomedical research," *Nat. Rev. Immunol.*, vol. 7, no. 2, pp. 118–130, Feb. 2007.
- [146] L. D. Shultz, N. Goodwin, F. Ishikawa, V. Hosur, B. L. Lyons, and D. L. Greiner, "Human cancer growth and therapy in immunodeficient mouse models.," *Cold Spring Harb. Protoc.*, vol. 2014, no. 7, pp. 694–708, Jul. 2014.
- [147] L. Pompili, M. Porru, C. Caruso, A. Biroccio, and C. Leonetti, "Patient-derived xenografts: a relevant preclinical model for drug development," *J. Exp. Clin. Cancer Res.*, vol. 35, no. 1, p. 189, Dec. 2016.
- [148] J. Rygaard and C. O. Povlsen, "Heterotransplantation of a human malignant tumour to 'Nude' mice.," *Acta Pathol. Microbiol. Scand.*, vol. 77, no. 4, pp. 758–60, 1969.

- [149] D. Benten, Y. Behrang, L. Unrau, V. Weissmann, G. Wolters-Eisfeld, S. Burdak-Rothkamm, F. R. Stahl, M. Anlauf, P. Grabowski, M. Möbs, J. Dieckhoff, B. Sipos, M. Fahl, C. Eggers, D. Perez, M. Bockhorn, J. R. Izbicki, A. W. Lohse, and J. Schrader, "Establishment of the First Well-differentiated Human Pancreatic Neuroendocrine Tumor Model," *Mol. Cancer Res.*, Jan. 2018.
- [150] A. Schroeder, O. Mueller, S. Stocker, R. Salowsky, M. Leiber, M. Gassmann, S. Lightfoot, W. Menzel, M. Granzow, and T. Ragg, "The RIN: an RNA integrity number for assigning integrity values to RNA measurements.," *BMC Mol. Biol.*, vol. 7, p. 3, Jan. 2006.
- [151] K. J. Livak and T. D. Schmittgen, "Analysis of Relative Gene Expression Data Using Real-Time Quantitative PCR and the $2^{-\Delta\Delta CT}$ Method," *Methods*, vol. 25, no. 4, pp. 402–408, Dec. 2001.
- [152] M. W. Pfaffl, "A new mathematical model for relative quantification in real-time RT-PCR.," *Nucleic Acids Res.*, vol. 29, no. 9, p. e45, May 2001.
- [153] J. Hellemans, G. Mortier, A. De Paepe, F. Speleman, and J. Vandesompele, "qBase relative quantification framework and software for management and automated analysis of real-time quantitative PCR data.," *Genome Biol.*, vol. 8, no. 2, p. R19, 2007.
- [154] A. Krishan, "Rapid flow cytofluorometric analysis of mammalian cell cycle by propidium iodide staining.," *J. Cell Biol.*, vol. 66, no. 1, pp. 188–93, Jul. 1975.
- [155] R. P. Wersto, F. J. Chrest, J. F. Leary, C. Morris, M. A. Stetler-Stevenson, and E. Gabrielson, "Doublet discrimination in DNA cell-cycle analysis.," *Cytometry*, vol. 46, no. 5, pp. 296–306, Oct. 2001.
- [156] C. Guzmán, M. Bagga, A. Kaur, J. Westermarck, and D. Abankwa, "ColonyArea: An ImageJ Plugin to Automatically Quantify Colony Formation in Clonogenic Assays," *PLoS One*, vol. 9, no. 3, p. e92444, Mar. 2014.
- [157] F. C. Greenwood, W. M. Hunter, and J. S. Glover, "The preparation of I-131-labelled human growth hormone of high specific radioactivity.," *Biochem. J.*, vol. 89, pp. 114–23, Oct. 1963.
- [158] D. J. R. Lane and D. R. Richardson, "William Hunter and radioiodination: revolutions in the labelling of proteins with radionuclides of iodine," *Biochem. J.*, vol. 2011, no. 4, pp. c1-4, Oct. 2011.
- [159] M. J. Kuhar, "In Vitro Autoradiography," in *Current Protocols in Pharmacology*, Hoboken, NJ, USA: John Wiley & Sons, Inc., 2001, p. 8.1.1-8.1.9.
- [160] S. Constant, S. Huang, L. Wiszniewski, and C. Mas, "Colon Cancer: Current Treatments and Preclinical Models for the Discovery and Development of New Therapies," in *Drug Discovery*, InTech, 2013.
- [161] T. N. M. Schumacher and T. J. Tsomides, "In Vitro Radiolabeling of Peptides and Proteins," in *Current Protocols in Protein Science*, vol. Chapter 3, Hoboken, NJ, USA: John Wiley & Sons, Inc., 1995, p. 3.3.1-3.3.19.
- [162] W. A. Pettinger, K. Keeton, and K. Tanaka, "Radioimmunoassay and pharmacokinetics of saralasin in the rat and hypertensive patients.," *Clin. Pharmacol. Ther.*, vol. 17, no. 2, pp. 146–58, Feb. 1975.
- [163] A. Markham and K. L. Goa, "Valsartan. A review of its pharmacology and therapeutic use in essential hypertension.," *Drugs*, vol. 54, no. 2, pp. 299–311, Aug. 1997.

- [164] F. R. E. Nobels, D. J. Kwekkeboom, W. Coopmans, C. H. H. Schoenmakers, J. Lindemans, W. W. De Herder, E. P. Krenning, R. Bouillon, and S. W. J. Lamberts, "Chromogranin A as Serum Marker for Neuroendocrine Neoplasia: Comparison with Neuron-Specific Enolase and the α -Subunit of Glycoprotein Hormones," *J. Clin. Endocrinol. Metab.*, vol. 82, no. 8, pp. 2622–2628, Aug. 1997.
- [165] T. Yamamori, H. Yasui, M. Yamazumi, Y. Wada, Y. Nakamura, H. Nakamura, and O. Inanami, "Ionizing radiation induces mitochondrial reactive oxygen species production accompanied by upregulation of mitochondrial electron transport chain function and mitochondrial content under control of the cell cycle checkpoint.," *Free Radic. Biol. Med.*, vol. 53, no. 2, pp. 260–70, Jul. 2012.
- [166] E. I. Azzam, J.-P. Jay-Gerin, and D. Pain, "Ionizing radiation-induced metabolic oxidative stress and prolonged cell injury.," *Cancer Lett.*, vol. 327, no. 1–2, pp. 48–60, Dec. 2012.
- [167] R. Cescato, J. Erchegyi, B. Waser, V. Piccand, H. R. Maecke, J. E. Rivier, and J. C. Reubi, "Design and in vitro characterization of highly sst2-selective somatostatin antagonists suitable for radiotargeting.," *J. Med. Chem.*, vol. 51, no. 13, pp. 4030–7, Jul. 2008.
- [168] T. Dolley-Hitze, F. Jouan, B. Martin, S. Mottier, J. Edeline, O. Moranne, P. Le Pogamp, M.-A. Belaud-Rotureau, J.-J. Patard, N. Rioux-Leclercq, and C. Vigneau, "Angiotensin-2 receptors (AT1-R and AT2-R), new prognostic factors for renal clear-cell carcinoma?," *Br. J. Cancer*, vol. 103, no. 11, pp. 1698–1705, Nov. 2010.
- [169] O. Arrieta, B. Pineda-Olvera, P. Guevara-Salazar, N. Hernández-Pedro, D. Morales-Espinosa, T. L. Cerón-Lizarraga, C. H. González-De la Rosa, D. Rembao, B. Segura-Pacheco, and J. Sotelo, "Expression of AT1 and AT2 angiotensin receptors in astrocytomas is associated with poor prognosis," *Br. J. Cancer*, vol. 99, no. 1, pp. 160–166, Jul. 2008.
- [170] A. W. Piastowska-Ciesielska, E. Płuciennik, K. Wójcik-Krowiranda, A. Bieńkiewicz, A. Bednarek, and T. Ochędalski, "Analysis of the expression of angiotensin II type 1 receptor and VEGF in endometrial adenocarcinoma with different clinicopathological characteristics.," *Tumour Biol.*, vol. 33, no. 3, pp. 767–74, Jun. 2012.
- [171] V. Fendrich, C. L. Lopez, J. Manoharan, K. Maschuw, S. Wichmann, A. Baier, J. P. Holler, A. Ramaswamy, D. K. Bartsch, and J. Waldmann, "Enalapril and ASS inhibit tumor growth in a transgenic mouse model of islet cell tumors.," *Endocr. Relat. Cancer*, vol. 21, no. 5, pp. 813–24, Oct. 2014.
- [172] M. Herrera, M. A. Sparks, A. R. Alfonso-Pecchio, L. M. Harrison-Bernard, and T. M. Coffman, "Lack of specificity of commercial antibodies leads to misidentification of angiotensin type 1 receptor protein.," *Hypertens. (Dallas, Tex. 1979)*, vol. 61, no. 1, pp. 253–8, Jan. 2013.
- [173] J. Benicky, R. Hafko, E. Sanchez-Lemus, G. Aguilera, and J. M. Saavedra, "Six commercially available angiotensin II AT1 receptor antibodies are non-specific.," *Cell. Mol. Neurobiol.*, vol. 32, no. 8, pp. 1353–65, Nov. 2012.
- [174] M. Jo and S. T. Jung, "Engineering therapeutic antibodies targeting G-protein-coupled receptors," *Exp. Mol. Med.*, vol. 48, no. 2, pp. e207–e207, Feb. 2016.
- [175] M. C. Michel, T. Wieland, and G. Tsujimoto, "How reliable are G-protein-coupled receptor antibodies?," *Naunyn. Schmiedeberg's Arch. Pharmacol.*, vol. 379, no. 4, pp. 385–388, 2009.
- [176] C. Vogel and E. M. Marcotte, "Insights into the regulation of protein abundance from proteomic and transcriptomic analyses.," *Nat. Rev. Genet.*, vol. 13, no. 4, pp. 227–32, Mar. 2012.

- [177] U. Rudloff, U. Bhanot, W. Gerald, D. S. Klimstra, W. R. Jarnagin, M. F. Brennan, and P. J. Allen, "Biobanking of human pancreas cancer tissue: impact of ex-vivo procurement times on RNA quality.," *Ann. Surg. Oncol.*, vol. 17, no. 8, pp. 2229–36, Aug. 2010.
- [178] S. Pan, T. A. Brentnall, K. Kelly, and R. Chen, "Tissue proteomics in pancreatic cancer study: discovery, emerging technologies, and challenges.," *Proteomics*, vol. 13, no. 3–4, pp. 710–21, Feb. 2013.
- [179] C. Shao, I. H. Zucker, and L. Gao, "Angiotensin type 2 receptor in pancreatic islets of adult rats: a novel insulinotropic mediator.," *Am. J. Physiol. Endocrinol. Metab.*, vol. 305, no. 10, pp. E1281-91, Nov. 2013.
- [180] N. A.-H. Sadik, N. S. Metwally, O. G. Shaker, M. S. Soliman, A. A. Mohamed, and M. M. Abdelmoaty, "Local renin-angiotensin system regulates the differentiation of mesenchymal stem cells into insulin-producing cells through angiotensin type 2 receptor.," *Biochimie*, vol. 137, pp. 132–138, Jun. 2017.
- [181] B. Ulmasov, Z. Xu, L. H. Tetri, T. Inagami, and B. A. Neuschwander-Tetri, "Protective role of angiotensin II type 2 receptor signaling in a mouse model of pancreatic fibrosis.," *Am. J. Physiol. Gastrointest. Liver Physiol.*, vol. 296, no. 2, pp. G284-94, Feb. 2009.
- [182] C. Doi, N. Egashira, A. Kawabata, D. K. Maurya, N. Ohta, D. Uppalapati, R. Ayuzawa, L. Pickel, Y. Isayama, D. Troyer, S. Takekoshi, and M. Tamura, "Angiotensin II type 2 receptor signaling significantly attenuates growth of murine pancreatic carcinoma grafts in syngeneic mice.," *BMC Cancer*, vol. 10, no. 1, p. 67, Jan. 2010.
- [183] J. Shirani and V. Dilsizian, "Novel Molecular Angiotensin Converting Enzyme and Angiotensin Receptor Imaging Techniques," *Curr. Cardiol. Rep.*, vol. 16, no. 4, p. 466, Apr. 2014.
- [184] M.-O. Guimond, M. Hallberg, N. Gallo-Payet, and C. Wallinder, "Saralasin and Sarile Are AT2 Receptor Agonists," *ACS Med. Chem. Lett.*, vol. 5, no. 10, pp. 1129–1132, Oct. 2014.
- [185] G. Vauquelin and S. J. Charlton, "Long-lasting target binding and rebinding as mechanisms to prolong in vivo drug action," *Br. J. Pharmacol.*, vol. 161, no. 3, pp. 488–508, Oct. 2010.
- [186] G. R. Jang, R. Z. Harris, and D. T. Lau, "Pharmacokinetics and its role in small molecule drug discovery research," *Med. Res. Rev.*, vol. 21, no. 5, pp. 382–396, Sep. 2001.
- [187] J. Fan and I. A. M. de Lannoy, "Pharmacokinetics.," *Biochem. Pharmacol.*, vol. 87, no. 1, pp. 93–120, Jan. 2014.
- [188] E. B. Hunter, S. P. Powers, L. J. Kost, D. I. Pinon, L. J. Miller, and N. F. LaRusso, "Physicochemical determinants in hepatic extraction of small peptides.," *Hepatology*, vol. 12, no. 1, pp. 76–82, Jul. 1990.
- [189] Novartis Pharmaceuticals Corporation, "Diovan (valsartan) tablets for oral use: prescribing information," 2018. [Online]. Available: <https://www.pharma.us.novartis.com/product-list/products/d>. [Accessed: 12-Feb-2018].
- [190] L. Criscione, H. Thomann, S. Whitebread, M. de Gasparo, P. Bühlmayer, P. Herold, F. Ostermayer, and B. Kamber, "Binding characteristics and vascular effects of various angiotensin II antagonists.," *J. Cardiovasc. Pharmacol.*, vol. 16 Suppl 4, pp. S56-9, 1990.
- [191] H. A. Lehr, M. Skelly, K. Buhler, B. Anderson, H. M. Delisser, and A. M. Gown, "Microvascular endothelium of human tumor xenografts expresses mouse (= host) CD31.," *Int. J. Microcirc. Clin. Exp.*, vol. 17, no. 3, pp. 138–42.

- [192] B. L. Hylander, N. Punt, H. Tang, J. Hillman, M. Vaughan, W. Bshara, R. Pitoniak, and E. A. Repasky, "Origin of the vasculature supporting growth of primary patient tumor xenografts," *J. Transl. Med.*, vol. 11, no. 1, p. 110, 2013.
- [193] K. Egami, T. Murohara, T. Shimada, K. Sasaki, S. Shintani, T. Sugaya, M. Ishii, T. Akagi, H. Ikeda, T. Matsuishi, and T. Imaizumi, "Role of host angiotensin II type 1 receptor in tumor angiogenesis and growth," *October*, vol. 112, no. 1, pp. 67–75, 2003.
- [194] J. U. N. Kinoshita, S. Fushida, S. Harada, Y. Yagi, H. Fujita, S. Kinami, I. Ninomiya, T. Fujimura, M. Kayahara, M. Yashiro, K. Hirakawa, and T. Ohta, "Local angiotensin II-generation in human gastric cancer: Correlation with tumor progression through the activation of ERK1 / 2, NF- κ B and survivin," *Cancer Res.*, pp. 1573–1582, 2009.
- [195] T. Walther, A. Menrad, H.-D. Orzechowski, G. Siemeister, M. Paul, and M. Schirner, "Differential regulation of in vivo angiogenesis by angiotensin II receptors.," *FASEB J.*, vol. 17, no. 14, pp. 2061–7, Nov. 2003.
- [196] N. Clere, I. Corre, S. Faure, A.-L. Guihot, E. Vessières, M. Chalopin, A. Morel, O. Coqueret, L. Hein, Y. Delneste, F. Paris, and D. Henrion, "Deficiency or blockade of angiotensin II type 2 receptor delays tumorigenesis by inhibiting malignant cell proliferation and angiogenesis.," *Int. J. cancer*, vol. 127, no. 10, pp. 2279–91, Nov. 2010.
- [197] S. Kossatz, R. Mansi, M. Béhé, P. Czerney, and I. Hilger, "Influence of d-glutamine and d-glutamic acid sequences in optical peptide probes targeted against the cholecystokinin-2/gastrin-receptor on binding affinity, specificity and pharmacokinetic properties," *EJNMMI Res.*, vol. 3, no. 1, p. 75, 2013.
- [198] R. H. Kimura, Z. Cheng, S. S. Gambhir, and J. R. Cochran, "Engineered knottin peptides: a new class of agents for imaging integrin expression in living subjects.," *Cancer Res.*, vol. 69, no. 6, pp. 2435–42, Mar. 2009.
- [199] W. S. Tummers, R. H. Kimura, L. Abou-Elkacem, A. L. Vahrmeijer, R.-J. Swijnenburg, J. K. Willmann, and S. S. Gambhir, "Development and preclinical validation of a cysteine knottin peptide targeting Integrin $\alpha\beta 6$ for near-infrared fluorescent-guided surgery in pancreatic cancer.," *Clin. Cancer Res.*, Jan. 2018.
- [200] H. R. Balon, T. L. Y. Brown, S. J. Goldsmith, E. B. Silberstein, E. P. Krenning, O. Lang, G. Dillehay, J. Tarrance, M. Johnson, M. G. Stabin, and Society of Nuclear Medicine, "The SNM practice guideline for somatostatin receptor scintigraphy 2.0.," *J. Nucl. Med. Technol.*, vol. 39, no. 4, pp. 317–24, Dec. 2011.
- [201] N. Prevarskaya, R. Skryma, and Y. Shuba, "Calcium in tumour metastasis: new roles for known actors," *Nat. Rev. Cancer*, vol. 11, no. 8, pp. 609–618, Aug. 2011.
- [202] M. J. Berridge, "The Inositol Trisphosphate/Calcium Signaling Pathway in Health and Disease.," *Physiol. Rev.*, vol. 96, no. 4, pp. 1261–96, Oct. 2016.
- [203] M. C. X. Pinto, A. H. Kihara, V. A. M. Goulart, F. M. P. Tonelli, K. N. Gomes, H. Ulrich, and R. R. Resende, "Calcium signaling and cell proliferation.," *Cell. Signal.*, vol. 27, no. 11, pp. 2139–49, Nov. 2015.
- [204] M. J. Berridge, P. Lipp, and M. D. Bootman, "The versatility and universality of calcium signalling," *Nat. Rev. Mol. Cell Biol.*, vol. 1, no. 1, pp. 11–21, Oct. 2000.
- [205] C. Cui, R. Merritt, L. Fu, and Z. Pan, "Targeting calcium signaling in cancer therapy," *Acta Pharm. Sin. B*, vol. 7, no. 1, pp. 3–17, Jan. 2017.

- [206] S. Mergler, O. Strauss, M. Strowski, J. Prada, A. Drost, J. Langrehr, P. Neuhaus, B. Wiedenmann, and U. Ploeckinger, "Insulin-like growth factor-1 increases intracellular calcium concentration in human primary neuroendocrine pancreatic tumor cells and a pancreatic neuroendocrine tumor cell line (BON-1) via R-type Ca²⁺ channels and regulates chromogranin a secretion in BO," *Neuroendocrinology*, vol. 82, no. 2, pp. 87–102, Jan. 2005.
- [207] S. Mergler, B. Wiedenmann, and J. Prada, "R-type Ca(2+)-channel activity is associated with chromogranin A secretion in human neuroendocrine tumor BON cells.," *J. Membr. Biol.*, vol. 194, no. 3, pp. 177–86, Aug. 2003.
- [208] H. Uemura, H. Ishiguro, N. Nakaigawa, Y. Nagashima, Y. Miyoshi, K. Fujinami, A. Sakaguchi, and Y. Kubota, "Angiotensin II receptor blocker shows antiproliferative activity in prostate cancer cells: A possibility of tyrosine kinase inhibitor of growth factor.," *Mol. Cancer Ther.*, vol. 2, no. 11, pp. 1139–1147, 2003.
- [209] S. Greco, A. Muscella, M. G. Elia, P. Salvatore, C. Storelli, A. Mazzotta, C. Manca, and S. Marsigliante, "Angiotensin II activates extracellular signal regulated kinases via protein kinase C and epidermal growth factor receptor in breast cancer cells," *J. Cell. Physiol.*, vol. 196, no. 2, pp. 370–377, 2003.
- [210] B. H. Shah, A. Yesilkaya, J. A. Olivares-Reyes, H.-D. Chen, L. Hunyady, and K. J. Catt, "Differential pathways of angiotensin II-induced extracellularly regulated kinase 1/2 phosphorylation in specific cell types: role of heparin-binding epidermal growth factor.," *Mol. Endocrinol.*, vol. 18, no. 8, pp. 2035–48, Aug. 2004.
- [211] W. G. Thomas, Y. Brandenburger, D. J. Autelitano, T. Pham, H. Qian, and R. D. Hannan, "Adenoviral-directed expression of the type 1A angiotensin receptor promotes cardiomyocyte hypertrophy via transactivation of the epidermal growth factor receptor.," *Circ. Res.*, vol. 90, no. 2, pp. 135–42, Feb. 2002.
- [212] M.-H. Lee, H. M. El-Shewy, D. K. Luttrell, and L. M. Luttrell, "Role of beta-arrestin-mediated desensitization and signaling in the control of angiotensin AT1a receptor-stimulated transcription.," *J. Biol. Chem.*, vol. 283, no. 4, pp. 2088–97, Jan. 2008.
- [213] J. Kim, S. Ahn, K. Rajagopal, and R. J. Lefkowitz, "Independent beta-arrestin2 and Gq/protein kinase Czeta pathways for ERK stimulated by angiotensin type 1A receptors in vascular smooth muscle cells converge on transactivation of the epidermal growth factor receptor.," *J. Biol. Chem.*, vol. 284, no. 18, pp. 11953–62, May 2009.
- [214] A. Di Florio, V. Sancho, P. Moreno, G. D. Fave, and R. T. Jensen, "Gastrointestinal hormones stimulate growth of Foregut Neuroendocrine Tumors by transactivating the EGF receptor.," *Biochim. Biophys. Acta - Mol. Cell Res.*, vol. 1833, no. 3, pp. 573–582, Mar. 2013.
- [215] B. Papouchado, L. A. Erickson, A. L. Rohlinger, T. J. Hobday, C. Erlichman, M. M. Ames, and R. V Lloyd, "Epidermal growth factor receptor and activated epidermal growth factor receptor expression in gastrointestinal carcinoids and pancreatic endocrine carcinomas.," *Mod. Pathol.*, vol. 18, no. 10, pp. 1329–35, Oct. 2005.
- [216] M. Höpfner, A. P. Sutter, B. Gerst, M. Zeitz, and H. Scherübl, "A novel approach in the treatment of neuroendocrine gastrointestinal tumours. Targeting the epidermal growth factor receptor by gefitinib (ZD1839).," *Br. J. Cancer*, vol. 89, no. 9, pp. 1766–75, Nov. 2003.
- [217] U. Wulbrand, M. Wied, P. Zöfel, B. Göke, R. Arnold, and H. Fehmann, "Growth factor receptor expression in human gastroenteropancreatic neuroendocrine tumours.," *Eur. J. Clin. Invest.*, vol. 28, no. 12, pp. 1038–49, Dec. 1998.

- [218] C. A. Grimes and R. S. Jope, "The multifaceted roles of glycogen synthase kinase 3beta in cellular signaling.," *Prog. Neurobiol.*, vol. 65, no. 4, pp. 391–426, Nov. 2001.
- [219] T. C. Sudhof, "Calcium Control of Neurotransmitter Release," *Cold Spring Harb. Perspect. Biol.*, vol. 4, no. 1, pp. a011353–a011353, Jan. 2012.
- [220] C. Münzberg, K. Höhn, D. Krndija, U. Maaß, D. K. Bartsch, E. P. Slater, F. Oswald, P. Walther, T. Seufferlein, and G. von Wichert, "IGF-1 drives chromogranin A secretion via activation of Arf1 in human neuroendocrine tumour cells.," *J. Cell. Mol. Med.*, vol. 19, no. 5, pp. 948–59, May 2015.
- [221] G. Rindi and B. Wiedenmann, "Neuroendocrine neoplasms of the gut and pancreas: new insights.," *Nat. Rev. Endocrinol.*, vol. 8, no. 1, pp. 54–64, Jan. 2012.
- [222] G. von Wichert, T. Edenfeld, J. von Blume, H. Krisp, D. Krndija, H. Schmid, F. Oswald, U. Lothar, P. Walther, G. Adler, and T. Seufferlein, "Protein kinase D2 regulates chromogranin A secretion in human BON neuroendocrine tumour cells.," *Cell. Signal.*, vol. 20, no. 5, pp. 925–34, May 2008.
- [223] G. von Wichert, P. M. Jehle, A. Hoeflich, S. Koschnick, H. Dralle, E. Wolf, B. Wiedenmann, B. O. Boehm, G. Adler, and T. Seufferlein, "Insulin-like growth factor-I is an autocrine regulator of chromogranin A secretion and growth in human neuroendocrine tumor cells.," *Cancer Res.*, vol. 60, no. 16, pp. 4573–81, Aug. 2000.
- [224] J. Li, K. L. O'Connor, M. R. Hellmich, G. H. Greeley, C. M. Townsend, and B. M. Evers, "The role of protein kinase D in neurotensin secretion mediated by protein kinase C-alpha/delta and Rho/Rho kinase.," *J. Biol. Chem.*, vol. 279, no. 27, pp. 28466–74, Jul. 2004.
- [225] Y. Zhao, X. Chen, L. Cai, Y. Yang, G. Sui, and S. Fu, "Angiotensin II/angiotensin II type I receptor (AT1R) signaling promotes MCF-7 breast cancer cells survival via PI3-kinase/Akt pathway.," *J. Cell. Physiol.*, vol. 225, no. 1, pp. 168–73, Oct. 2010.
- [226] K. Amaya, T. Ohta, H. Kitagawa, M. Kayahara, H. Takamura, T. Fujimura, G.-I. Nishimura, K. Shimizu, and K. Miwa, "Angiotensin II activates MAP kinase and NF-kappaB through angiotensin II type I receptor in human pancreatic cancer cells.," *Int. J. Oncol.*, vol. 25, no. 4, pp. 849–56, Oct. 2004.
- [227] S. Grozinsky-Glasberg, I. Shimon, and H. Rubinfeld, "The role of cell lines in the study of neuroendocrine tumors.," *Neuroendocrinology*, vol. 96, no. 3, pp. 173–87, Jan. 2012.
- [228] K. E. Forsten and D. A. Lauffenburger, "Autocrine ligand binding to cell receptors. Mathematical analysis of competition by solution 'decoys,'" *Biophys. J.*, vol. 61, no. 2, pp. 518–529, 1992.
- [229] M. Fujita, I. Hayashi, S. Yamashina, M. Itoman, and M. Majima, "Blockade of angiotensin AT1a receptor signaling reduces tumor growth, angiogenesis, and metastasis.," *Biochem. Biophys. Res. Commun.*, vol. 294, no. 2, pp. 441–7, Jun. 2002.
- [230] M. Fujita, I. Hayashi, S. Yamashina, A. Fukamizu, M. Itoman, and M. Majima, "Angiotensin type 1a receptor signaling-dependent induction of vascular endothelial growth factor in stroma is relevant to tumor-associated angiogenesis and tumor growth.," *Carcinogenesis*, vol. 26, no. 2, pp. 271–9, Feb. 2005.
- [231] M. Lundqvist and K. Oberg, "In vitro culture of neuroendocrine tumors of the pancreas and gut.," *Acta Oncol.*, vol. 28, no. 3, pp. 335–9, 1989.
- [232] V. Babu, N. Paul, and R. Yu, "Animal models and cell lines of pancreatic neuroendocrine tumors.," *Pancreas*, vol. 42, no. 6, pp. 912–23, Aug. 2013.

- [233] M. Mattie, A. Christensen, M. S. Chang, W. Yeh, S. Said, Y. Shostak, L. Capo, A. Verlinsky, Z. An, I. Joseph, Y. Zhang, S. Kumar-Ganesan, K. Morrison, D. Stover, and P. Challita-Eid, "Molecular Characterization of Patient-Derived Human Pancreatic Tumor Xenograft Models for Preclinical and Translational Development of Cancer Therapeutics," *Neoplasia*, vol. 15, no. 10, p. 1138–IN17, 2013.
- [234] C. Pauli, B. D. Hopkins, D. Prandi, R. Shaw, T. Fedrizzi, A. Sboner, V. Sailer, M. Augello, L. Puca, R. Rosati, T. J. McNary, Y. Churakova, C. Cheung, J. Triscott, D. Pisapia, R. Rao, J. M. Mosquera, B. Robinson, B. M. Faltas, B. E. Emerling, V. K. Gadi, B. Bernard, O. Elemento, H. Beltran, F. Demichelis, C. J. Kemp, C. Grandori, L. C. Cantley, and M. A. Rubin, "Personalized in vitro and in vivo cancer models to guide precision medicine," *Cancer Discov.*, vol. 7, no. 5, pp. 462–477, 2017.
- [235] A. Bruna, O. M. Rueda, W. Greenwood, A. S. Batra, M. Callari, R. N. Batra, K. Pogrebniak, J. Sandoval, J. W. Cassidy, A. Tufegdizic-Vidakovic, S.-J. Sammut, L. Jones, E. Provenzano, R. Baird, P. Eirew, J. Hadfield, M. Eldridge, A. McLaren-Douglas, A. Barthorpe, H. Lightfoot, M. J. O'Connor, J. Gray, J. Cortes, J. Baselga, E. Marangoni, A. L. Welm, S. Aparicio, V. Serra, M. J. Garnett, and C. Caldas, "A Biobank of Breast Cancer Explants with Preserved Intra-tumor Heterogeneity to Screen Anticancer Compounds.," *Cell*, vol. 167, no. 1, p. 260–274.e22, Sep. 2016.
- [236] D. J. Kwkkeboom and E. P. Krenning, "Peptide Receptor Radionuclide Therapy in the Treatment of Neuroendocrine Tumors.," *Hematol. Oncol. Clin. North Am.*, vol. 30, no. 1, pp. 179–91, Feb. 2016.
- [237] M. Cremonesi, M. Ferrari, L. Bodei, G. Tosi, and G. Paganelli, "Dosimetry in Peptide radionuclide receptor therapy: a review.," *J. Nucl. Med.*, vol. 47, no. 9, pp. 1467–75, 2006.
- [238] S. J. Goldsmith, "Radioimmunotherapy of lymphoma: Bexxar and Zevalin.," *Semin. Nucl. Med.*, vol. 40, no. 2, pp. 122–35, Mar. 2010.
- [239] M. Luster, H. Hänscheid, L. S. Freudenberg, and F. A. Verburg, "Radioiodine therapy of metastatic lesions of differentiated thyroid cancer.," *J. Endocrinol. Invest.*, vol. 35, no. 6 Suppl, pp. 21–9, 2012.
- [240] R. Nassim, J. J. Mansure, S. Chevalier, F. Cury, and W. Kassouf, "Combining mTOR Inhibition with Radiation Improves Antitumor Activity in Bladder Cancer Cells In Vitro and In Vivo: A Novel Strategy for Treatment," *PLoS One*, vol. 8, no. 6, 2013.
- [241] J. M. Albert, K. W. Kim, C. Cao, and B. Lu, "Targeting the Akt/mammalian target of rapamycin pathway for radiosensitization of breast cancer.," *Mol. Cancer Ther.*, vol. 5, no. 5, pp. 1183–9, May 2006.
- [242] B. Shor, W.-G. Zhang, L. Toral-Barza, J. Lucas, R. T. Abraham, J. J. Gibbons, and K. Yu, "A new pharmacologic action of CCI-779 involves FKBP12-independent inhibition of mTOR kinase activity and profound repression of global protein synthesis.," *Cancer Res.*, vol. 68, no. 8, pp. 2934–43, Apr. 2008.
- [243] S. A. Hurvitz, O. Kalous, D. Conklin, A. J. Desai, J. Dering, L. Anderson, N. A. O'Brien, T. Kolarova, R. S. Finn, R. Linnartz, D. Chen, and D. J. Slamon, "In vitro activity of the mTOR inhibitor everolimus, in a large panel of breast cancer cell lines and analysis for predictors of response," *Breast Cancer Res. Treat.*, vol. 149, no. 3, pp. 669–680, Feb. 2015.
- [244] K. Zitzmann, E. N. De Toni, S. Brand, B. Göke, J. Meinecke, G. Spöttl, H. H. D. Meyer, and C. J. Auernhammer, "The novel mTOR inhibitor RAD001 (everolimus) induces antiproliferative effects in human pancreatic neuroendocrine tumor cells.," *Neuroendocrinology*, vol. 85, no. 1, pp. 54–60, 2007.

- [245] G. Cooper, *The Cell: A Molecular Approach*, 2nd ed. Sunderland (MA): Sinauer Associates; The Eukaryotic Cell Cycle., 2000.
- [246] M. Grewe, F. Gansauge, R. M. Schmid, G. Adler, and T. Seufferlein, "Regulation of cell growth and cyclin D1 expression by the constitutively active FRAP-p70s6K pathway in human pancreatic cancer cells," *Cancer Res.*, vol. 59, no. 15, p. 3581 LP-3587, Aug. 1999.
- [247] S. Kawamata, H. Sakaida, T. Hori, M. Maeda, and T. Uchiyama, "The upregulation of p27Kip1 by rapamycin results in G1 arrest in exponentially growing T-cell lines.," *Blood*, vol. 91, no. 2, p. 561 LP-569, Jan. 1998.
- [248] S. Hashemolhosseini, Y. Nagamine, S. J. Morley, S. Desrivie, L. Mercep, and S. Ferrari, "Rapamycin Inhibition of the G 1 to S Transition Is Mediated by Effects on Cyclin D1 mRNA and Protein Stability.," *J. Biol. Chem.*, vol. 273, no. 23, pp. 14424–14429, 1998.
- [249] E. Missiaglia, I. Dalai, S. Barbi, S. Beghelli, M. Falconi, M. della Peruta, L. Piemonti, G. Capurso, A. Di Florio, G. delle Fave, P. Pederzoli, C. M. Croce, and A. Scarpa, "Pancreatic Endocrine Tumors: Expression Profiling Evidences a Role for AKT-mTOR Pathway," *J. Clin. Oncol.*, vol. 28, no. 2, pp. 245–255, Jan. 2010.
- [250] S. Serra, L. Zheng, M. Hassan, A. T. Phan, L. J. Woodhouse, J. C. Yao, S. Ezzat, and S. L. Asa, "The FGFR4-G388R single-nucleotide polymorphism alters pancreatic neuroendocrine tumor progression and response to mTOR inhibition therapy.," *Cancer Res.*, vol. 72, no. 22, pp. 5683–91, Nov. 2012.
- [251] B. Weigelt, P. H. Warne, and J. Downward, "PIK3CA mutation, but not PTEN loss of function, determines the sensitivity of breast cancer cells to mTOR inhibitory drugs.," *Oncogene*, vol. 30, no. 29, pp. 3222–33, Jul. 2011.
- [252] M. C. Zatelli, G. Fanciulli, P. Malandrino, V. Ramundo, A. Faggiano, A. Colao, and NIKE Group, "Predictive factors of response to mTOR inhibitors in neuroendocrine tumours.," *Endocr. Relat. Cancer*, vol. 23, no. 3, pp. R173-83, Mar. 2016.
- [253] M. D. Garrett and I. Collins, "Anticancer therapy with checkpoint inhibitors: what, where and when?," *Trends Pharmacol. Sci.*, vol. 32, no. 5, pp. 308–16, May 2011.
- [254] M. T. Dillon, J. S. Good, and K. J. Harrington, "Selective targeting of the G2/M cell cycle checkpoint to improve the therapeutic index of radiotherapy.," *Clin. Oncol. (R. Coll. Radiol.)*, vol. 26, no. 5, pp. 257–65, May 2014.
- [255] N. Bucher and C. D. Britten, "G2 checkpoint abrogation and checkpoint kinase-1 targeting in the treatment of cancer.," *Br. J. Cancer*, vol. 98, no. 3, pp. 523–8, Feb. 2008.
- [256] R. S. DiPaola, "To arrest or not to G(2)-M Cell-cycle arrest : commentary re: A. K. Tyagi et al., Silibinin strongly synergizes human prostate carcinoma DU145 cells to doxorubicin-induced growth inhibition, G(2)-M arrest, and apoptosis. Clin. cancer res., 8: 3512-3519, 2," *Clin. Cancer Res.*, vol. 8, no. 11, pp. 3311–4, Nov. 2002.
- [257] T. Chen, P. A. Stephens, F. K. Middleton, and N. J. Curtin, "Targeting the S and G2 checkpoint to treat cancer.," *Drug Discov. Today*, vol. 17, no. 5–6, pp. 194–202, Mar. 2012.
- [258] I. Vitale, L. Galluzzi, M. Castedo, and G. Kroemer, "Mitotic catastrophe: a mechanism for avoiding genomic instability.," *Nat. Rev. Mol. Cell Biol.*, vol. 12, no. 6, pp. 385–92, Jun. 2011.
- [259] T. Kawabe, "G2 checkpoint abrogators as anticancer drugs.," *Mol. Cancer Ther.*, vol. 3, no. 4, pp. 513–9, Apr. 2004.

- [260] Y.-C. Su, C.-C. Yu, F.-T. Hsu, S.-L. Fu, J.-J. Hwang, L.-C. Hung, M.-S. Lee, W.-Y. Chiou, H.-Y. Lin, and S.-K. Hung, "Everolimus sensitizes Ras-transformed cells to radiation in vitro through the autophagy pathway.," *Int. J. Mol. Med.*, vol. 34, no. 5, pp. 1417–22, Nov. 2014.
- [261] T. M. Pawlik and K. Keyomarsi, "Role of cell cycle in mediating sensitivity to radiotherapy," *Int. J. Radiat. Oncol.*, vol. 59, no. 4, pp. 928–942, 2004.
- [262] Z. Wang, S.-T. Lai, N.-Y. Ma, Y. Deng, Y. Liu, D.-P. Wei, J.-D. Zhao, and G.-L. Jiang, "Radiosensitization of metformin in pancreatic cancer cells via abrogating the G2 checkpoint and inhibiting DNA damage repair," *Cancer Lett.*, Aug. 2015.
- [263] S.-C. Li, C. Martijn, T. Cui, A. Essaghir, R. M. Luque, J.-B. Demoulin, J. P. Castaño, K. Öberg, and V. Giandomenico, "The somatostatin analogue octreotide inhibits growth of small intestine neuroendocrine tumour cells.," *PLoS One*, vol. 7, no. 10, p. e48411, 2012.
- [264] M. Kidd, A. V Schally, R. Pfragner, M. V Malfertheiner, and I. M. Modlin, "Inhibition of proliferation of small intestinal and bronchopulmonary neuroendocrine cell lines by using peptide analogs targeting receptors.," *Cancer*, vol. 112, no. 6, pp. 1404–14, Mar. 2008.
- [265] S. Jonas, M. John, J. Boese-Landgraf, R. Häring, G. Prevost, F. Thomas, S. Rosewicz, E. O. Riecken, B. Wiedenmann, and P. Neuhaus, "Somatostatin receptor subtypes in neuroendocrine tumor cell lines and tumor tissues.," *Langenbecks Arch. Chir.*, vol. 380, no. 2, pp. 90–5, 1995.
- [266] H. Iguchi, I. Hayashi, and A. Kono, "A somatostatin-secreting cell line established from a human pancreatic islet cell carcinoma (somatostatinoma): release experiment and immunohistochemical study.," *Cancer Res.*, vol. 50, no. 12, pp. 3691–3, Jun. 1990.
- [267] J. C. Reubi, B. Waser, H. Mäcke, and J. Rivier, "Highly Increased 125 I-JR11 Antagonist Binding In Vitro Reveals Novel Indications for sst 2 Targeting in Human Cancers," *J. Nucl. Med.*, vol. 58, no. 2, pp. 300–306, Feb. 2017.
- [268] R. Cescato, B. Waser, M. Fani, and J. C. Reubi, "Evaluation of 177Lu-DOTA-sst2 antagonist versus 177Lu-DOTA-sst2 agonist binding in human cancers in vitro.," *J. Nucl. Med.*, vol. 52, no. 12, pp. 1886–90, Dec. 2011.
- [269] I. Dude, Z. Zhang, J. Rousseau, N. Hundal-Jabal, N. Colpo, H. Merkens, K.-S. Lin, and F. Bénard, "Evaluation of agonist and antagonist radioligands for somatostatin receptor imaging of breast cancer using positron emission tomography," *EJNMMI Radiopharm. Chem.*, vol. 2, no. 1, p. 4, 2017.
- [270] S. E. Pool, S. Bison, S. J. Koelewijn, L. M. van der Graaf, M. Melis, E. P. Krenning, and M. de Jong, "mTOR inhibitor RAD001 promotes metastasis in a rat model of pancreatic neuroendocrine cancer.," *Cancer Res.*, vol. 73, no. 1, pp. 12–8, Jan. 2013.
- [271] S. M. Bison, S. E. Pool, S. J. Koelewijn, L. M. van der Graaf, H. C. Groen, M. Melis, and M. de Jong, "Peptide receptor radionuclide therapy (PRRT) with [(177)Lu-DOTA(0),Tyr(3)]octreotate in combination with RAD001 treatment: further investigations on tumor metastasis and response in the rat pancreatic CA20948 tumor model.," *EJNMMI Res.*, vol. 4, p. 21, Jan. 2014.

PUBLICATIONS AND PRESENTATIONS

Publications

S. Exner, V. Prasad, B. Wiedenmann, C. Grötzing

Octreotide does not inhibit proliferation in five neuroendocrine tumor cell lines.

Front Endocrinol (Lausanne). 2018 Apr 6; 9:146.

S. Nölting, J. Rentsch, H. Freitag, K. Detjen, F. Briest, M. Möbs, V. Weissmann, B. Siegmund, C.J. Auernhammer, E.T. Aristizabal Prada, M. Lauseker, A. Grossmann, S. Exner, C. Fischer, C. Grötzing, J. Schrader, P. Grabowski; GERMAN NET-Z study group

The selective PI3K α inhibitor BYL719 as a novel therapeutic option for neuroendocrine tumors: Results from multiple cell line models.

PLoS One. 2017 Aug 11; 12(8): e0182852.

S. Bandholtz, S. Erdmann, J. L. v. Hacht, S. Exner, G. Krause, G. Kleinau, C. Grötzing

Urolinin: The First Linear Peptidic Urotensin-II Receptor Agonist.

J Med Chem. 2016 Nov 23; 59(22): 10100–10112. Epub 2016 Nov 4.

Oral presentations

S. Exner, S. Erdmann, V. Prasad, S. Prasad, E. Koziolk, B. Wiedenmann, C. Grötzing

The effect of combined mTOR inhibitor treatment and peptide receptor radiotherapy on neuroendocrine tumor cells.

DKTK Retreat Berlin: Deutsches Konsortium für translationale Krebsforschung, September 2017, Potsdam, Germany

S. Exner, J. Du, C. Schuldt, Y. Giesecke, B. Wiedenmann, C. Grötzing

Identification and validation of the angiotensin II receptor type 1 as a possible anti-cancer target in neuroendocrine tumors.

PostDoc Day, May 2017, Berlin, Germany, *Awarded as best talk with BIH travel grant*

S. Exner, S. Erdmann, V. Prasad, C. Grötzing

The mTOR inhibitor temsirolimus acts as a radiosensitizer in neuroendocrine tumor cells.

EANM '16: Annual Congress of the European Association of Nuclear Medicine, October 2016, Barcelona, Spain

S. Exner, J. Du, C. Schuldt, Y. Giesecke, B. Wiedenmann, C. Grötzing

Identification and validation of AGTR1 as a possible anti-cancer target in neuroendocrine tumors.

32. Deutscher Krebskongress, February 2016, Berlin, Germany

S. Exner, S. Pönick, V. Prasad, C. Grötzinger

Potential radioprotectors and radiosensitizers in neuroendocrine tumor cells.

EANM '15: Annual Congress of the European Association of Nuclear Medicine, October 2015, Hamburg, Germany

Poster presentations

S. Exner, J. Du, C. Schuldt, Y. Giesecke, B. Wiedenmann, C. Grötzinger

Identification and validation of the angiotensin II receptor type 1 as a possible anti-cancer target in neuroendocrine tumors.

40th FEBS Meeting, July 2015, Berlin, Germany

S. Exner, S. Erdmann, V. Prasad, C. Grötzinger

The mTOR inhibitor temsirolimus acts as a radiosensitizer in neuroendocrine tumor cells.

DKTK Retreat Heidelberg: Deutsches Konsortium für translationale Krebsforschung, October 2017, Heidelberg, Germany

SELBSTÄNDIGKEITSERKLÄRUNG

Hiermit erkläre ich, dass ich die vorliegende Arbeit selbständig und ohne fremde Hilfe verfasst und keine anderen Hilfsmittel als angegeben verwendet habe. Insbesondere versichere ich, dass ich alle wörtlichen und sinngemäßen Übernahmen aus anderen Werken als solche kenntlich gemacht habe.

Ich erkläre außerdem, dass ich diese Dissertation weder in gleicher noch in ähnlicher Form in einem anderen Prüfungsverfahren vorgelegt habe.

Berlin, den 06.03.2018

Samantha Exner

SUPPLEMENTARY

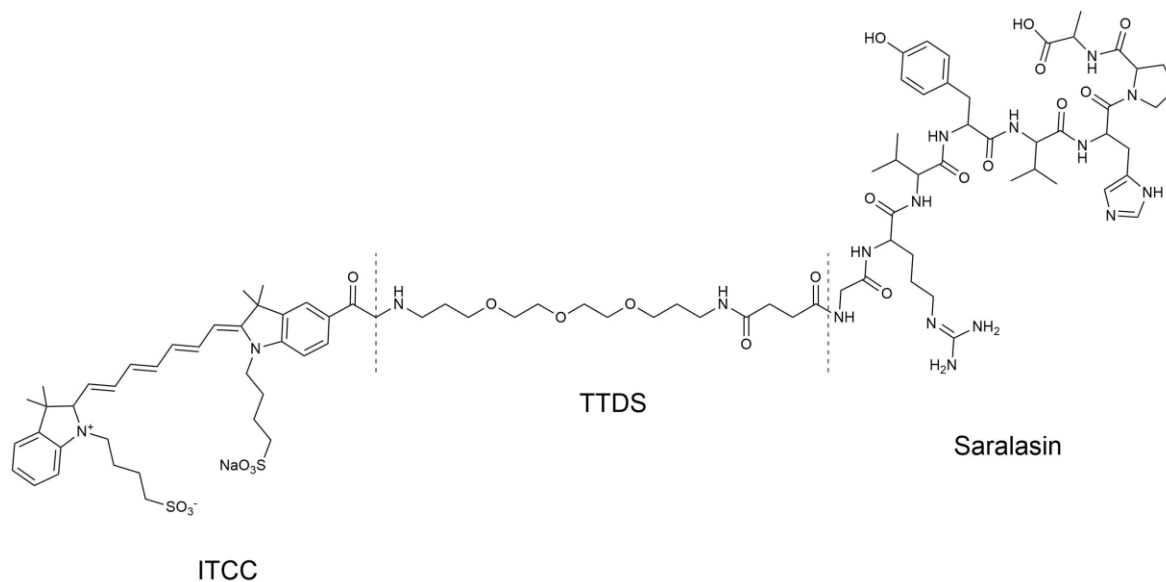


Figure S1 | Structure of saralasin-ITCC. The angiotensin II analog saralasin was coupled to the near-infrared dye indotricarbocyanine (ITCC) by the linker molecule trioxatridecane succinic acid (TTDS).

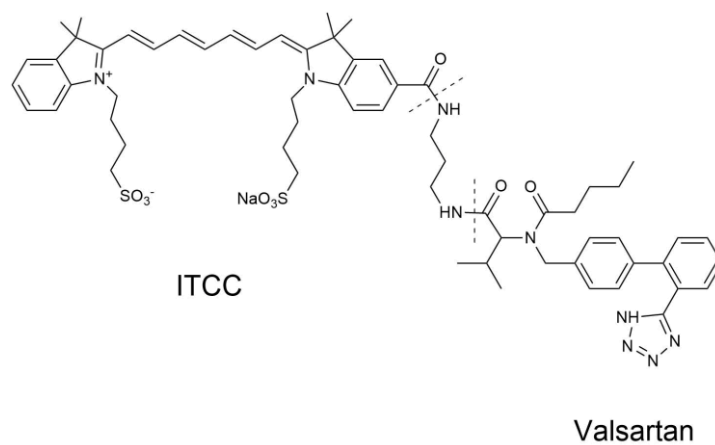


Figure S2 | Structure of valsartan-ITCC. The AGTR1 antagonist valsartan was directly coupled to the near-infrared dye indotricarbocyanine (ITCC) by a short diaminopropane linker.

Table S1 | Amino acid code.

name	one letter code	three letter code
<i>natural</i>		
Alanine	A	Ala
Cysteine	C	Cys
Aspartic acid	D	Asp
Glutamic acid	E	Glu
Phenylalanine	F	Phe
Glycine	G	Gly
Histidine	H	His
Isoleucine	I	Ile
Lysine	K	Lys
Leucine	L	Leu
Methionine	M	Met
Asparagine	N	Asn
Proline	P	Pro
Glutamine	Q	Gln
Arginine	R	Arg
Serine	S	Ser
Threonine	T	Thr
Valine	V	Val
Tryptophan	W	Trp
Tyrosine	Y	Tyr
<i>non-natural</i>		
Threoninol		Thr(ol)
2-Naphtylalanine		2Nal
Sarcosine		Sar
4-Chlorophenylalanine		Cpa
4-Amino-L-hydroxyphenylalanine		Aph(Hor)
4-Aminocarbamoylphenylalanine		Aph(Cbm)

Table S2 | Clinical characteristics of the tissues analyzed by in vitro receptor autoradiography.

no	ID	Sex	Age at surgery	Tissue type	Primary	Origin of tissue	Ki67	Grade
1	7	m	75	primary	pancreas	pancreas	3 %	-
2	31	m	67	metastasis	pancreas	liver	2 %	-
3	57	m	28	primary	pancreas	pancreas	6 %	G2
4	51	f	43	metastasis	pancreas	liver	5 %	-
5	39	f	44	metastasis	pancreas	liver	25 %	-
6	35	f	51	primary	pancreas	pancreas	1 %	-
7	13	f	38	metastasis	pancreas	liver	80 %	-
8	22	f	65	primary	pancreas	pancreas	15 %	G2
1		m	58	normal		pancreas		
2		m	67	normal		pancreas		
3		m	50	normal		pancreas		
4		f	65	normal		pancreas		
5		m	65	normal		pancreas		
1	62	m	34	primary	ileum	ileum	10 %	G2
2	74	m	74	metastasis	ileum	liver	3 %	G2
3	71	f	54	metastasis	ileum	liver	-	-
4	90	m	76	metastasis	ileum	liver	2 %	-
5	71	f	54	primary	ileum	ileum	5 %	G2
6	94	m	49	primary	ileum	ileum	-	-
7	64	f	57	metastasis	ileum	liver	-	-
8	72	f	62	primary	ileum	ileum	1-2 %	G1
9	83	f	53	primary	ileum	ileum	1 %	G1
1	62	m	34	normal		ileum		
2	121	f	65	normal		duodenum		
3	69	m	72	normal		lymph node ileum		
4	122	f	69	normal		ileum		
5	117	m	65	normal		duodenum		

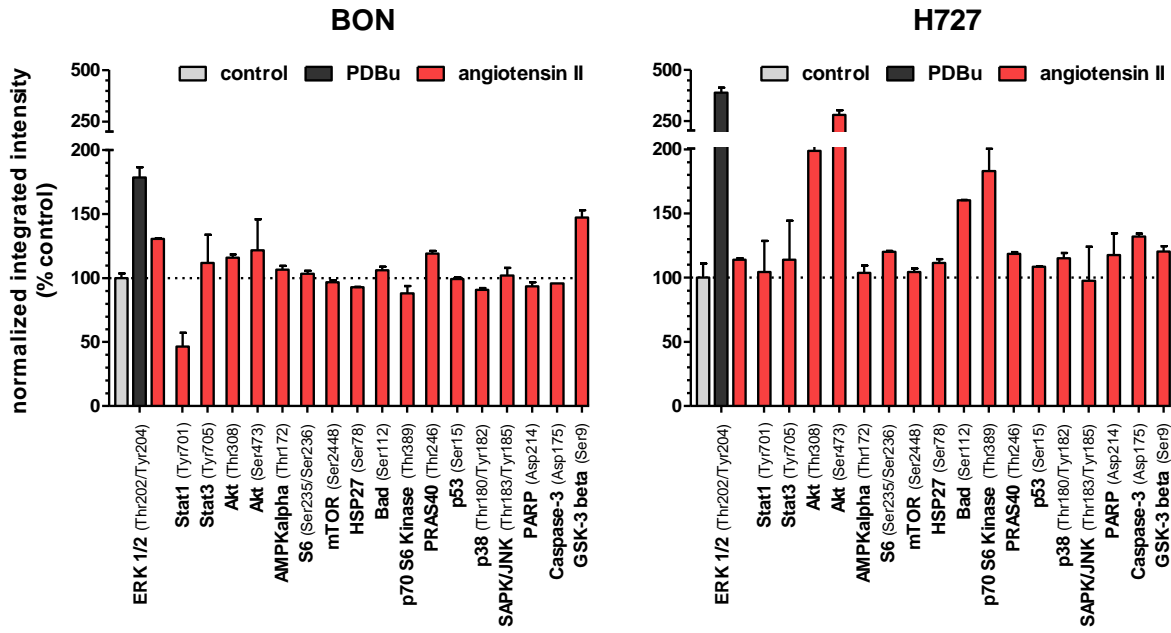


Figure S3 | Intracellular signaling array after 10 min of angiotensin II stimulation. BON and H727 cells were incubated with vehicle, 1 μ M PDBu or 1 μ M angiotensin II for 10 min. Cell lysates were analyzed for the phosphorylation and cleavage status of intracellular molecules. For each target, fluorescence intensities were normalized on the untreated control lysate, here exemplarily shown for ERK 1/2. Data showing mean \pm S.D. of one experiment, measured in duplicates. PDBu, phorbol 12,13-dibutyrate.

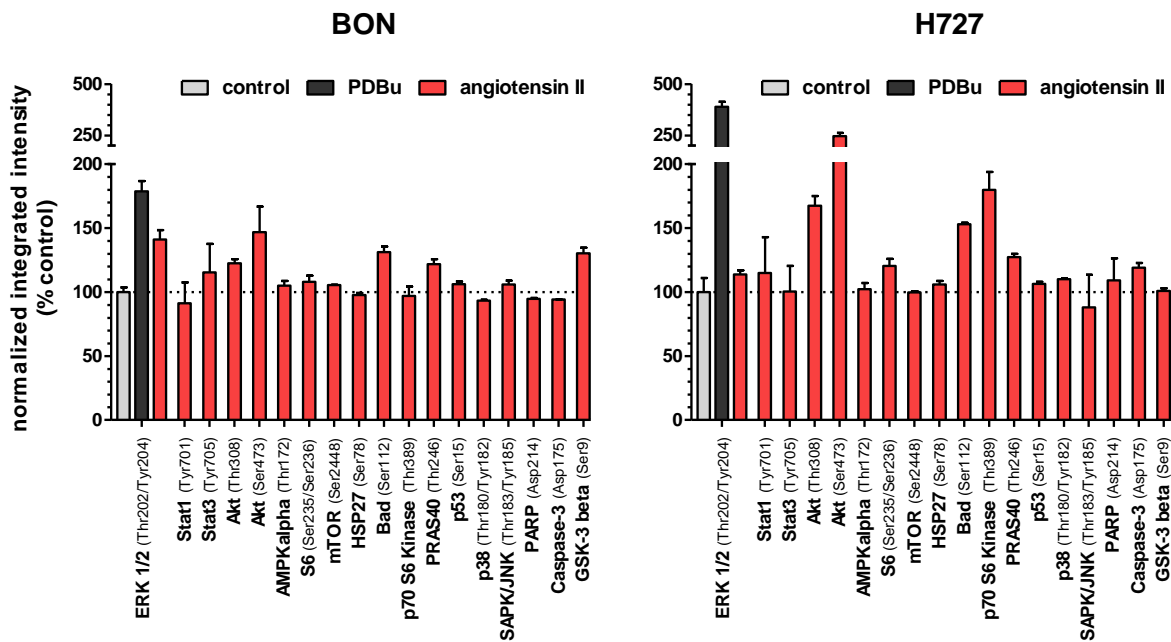


Figure S4 | Intracellular signaling array after 15 min of angiotensin II stimulation. BON and H727 cells were incubated with vehicle, 1 μ M PDBu or 1 μ M angiotensin II for 15 min. Cell lysates were analyzed for the phosphorylation and cleavage status of intracellular molecules. For each target, fluorescence intensities were normalized on the untreated control lysate, here exemplarily shown for ERK 1/2. Data showing mean \pm S.D. of one experiment, measured in duplicates. PDBu, phorbol 12,13-dibutyrate.

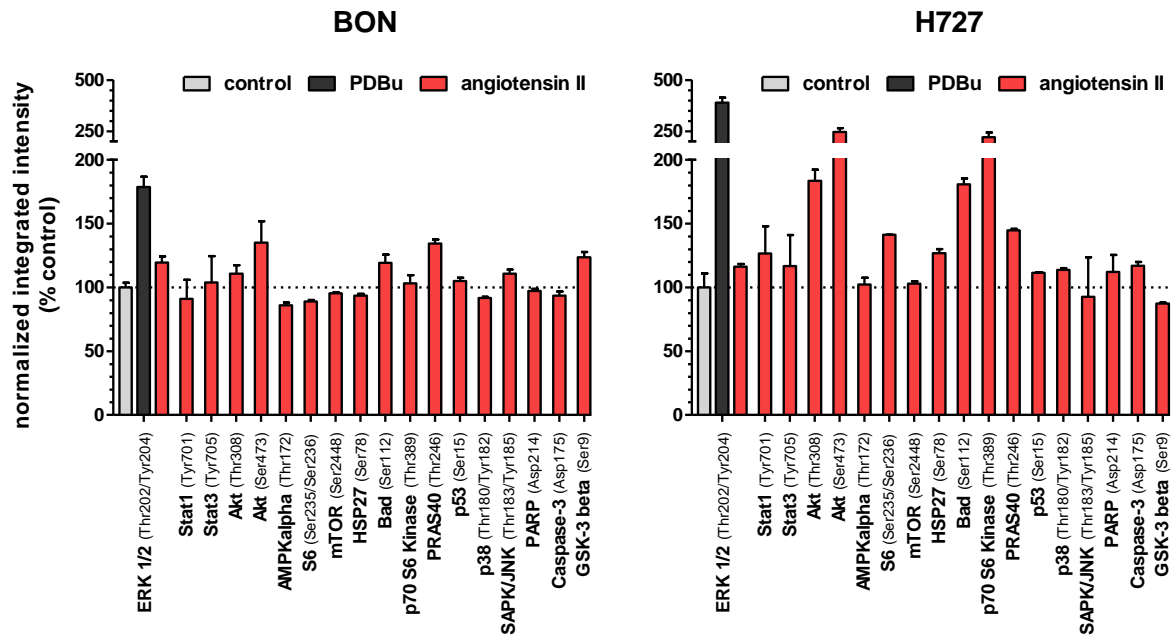


Figure S5 | Intracellular signaling array after 30 min of angiotensin II stimulation. BON and H727 cells were incubated with vehicle, 1 μ M PDBu or 1 μ M angiotensin II for 30 min. Cell lysates were analyzed for the phosphorylation and cleavage status of intracellular molecules. For each target, fluorescence intensities were normalized on the untreated control lysate, here exemplarily shown for ERK 1/2. Data showing mean \pm S.D. of one experiment, measured in duplicates. PDBu, phorbol 12,13-dibutyrate.

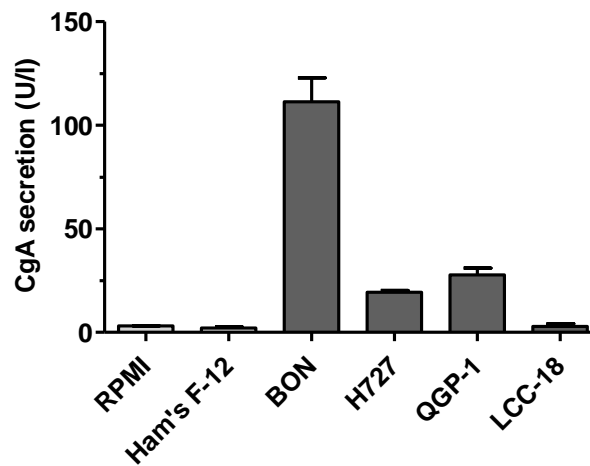


Figure S6 | Chromogranin A secretion of NET cell lines. The indicated NET cell lines were tested for their basal chromogranin A (CgA) secretion. After 24 h incubation, cell culture supernatants were measured with ELISA. Data show mean \pm S.D. of duplicates (n=1).

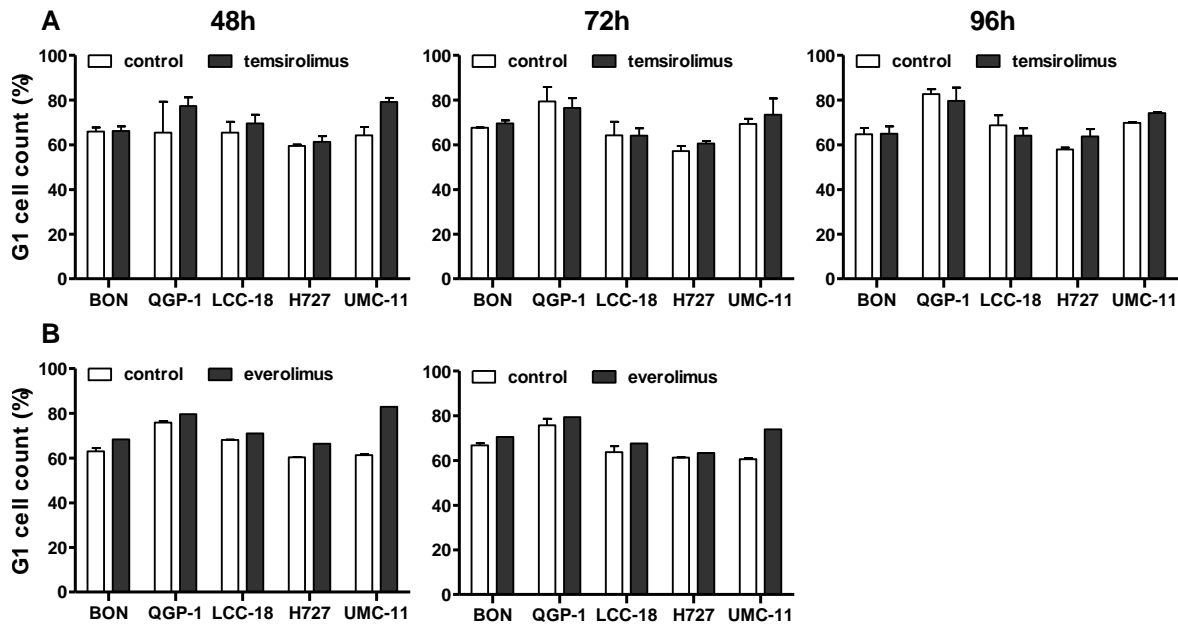


Figure S7 | Accumulation of cells in G1 after mTOR inhibitor treatment after 48, 72 and 96 h. NET cell lines were treated with vehicle and 1 μ M temsirolimus (A) or everolimus (B). After the indicated incubation time, samples were collected for cell cycle analysis by flow cytometry. Data are shown as bar diagrams with mean \pm S.E.M. of n=2-3 (A) or n=1-2 (B).

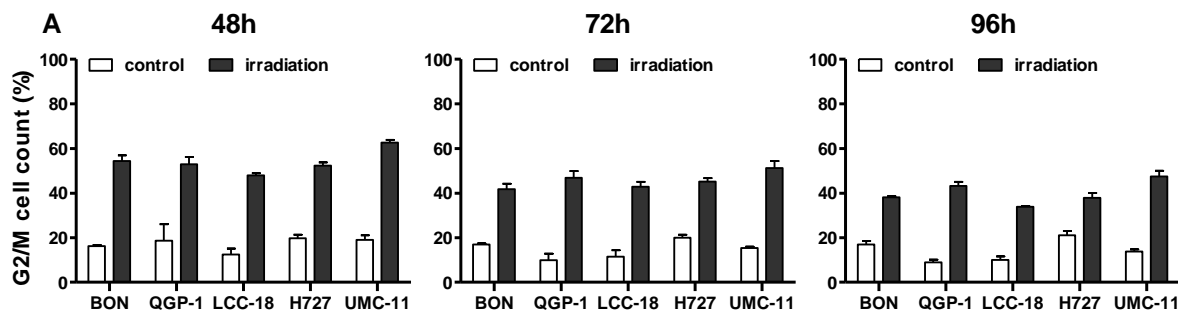


Figure S8 | Irradiation leads to G2/M accumulation of NET cells after 48, 72 and 96 h. NET cell lines were irradiated with 10 Gy and samples were collected after the indicated time points for cell cycle analysis by flow cytometry. Data are shown as bar diagrams with mean \pm S.E.M. (n=2-3).

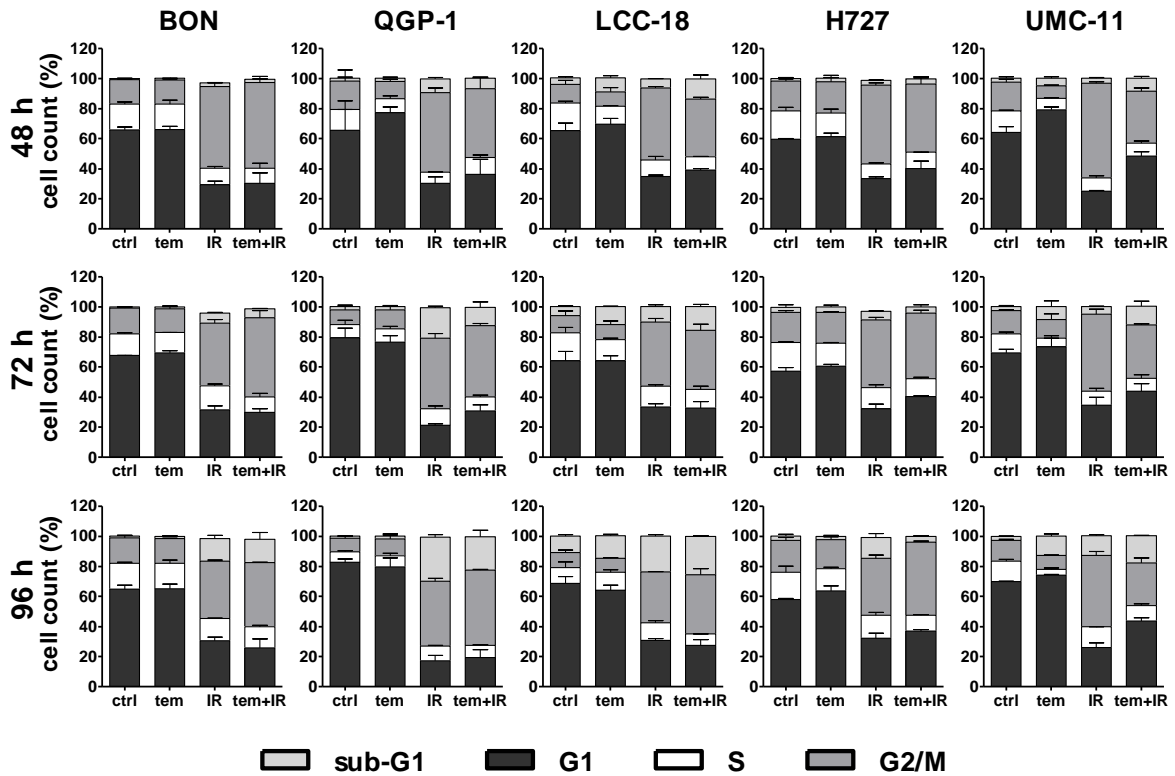


Figure S9 | Cell cycle distribution at 48, 72 and 96 h after combined treatment. NET cell lines were incubated with 1 μ M temsirolimus (tem) or vehicle (ctrl) for 24 h before irradiation. For assessment of cell cycle distribution pretreated NET cells were collected 48, 72 or 96 h after irradiation with 10 Gy (IR, tem+IR), stained with propidium iodide and analyzed by flow cytometry. Data show mean \pm S.E.M. (n=2-3).

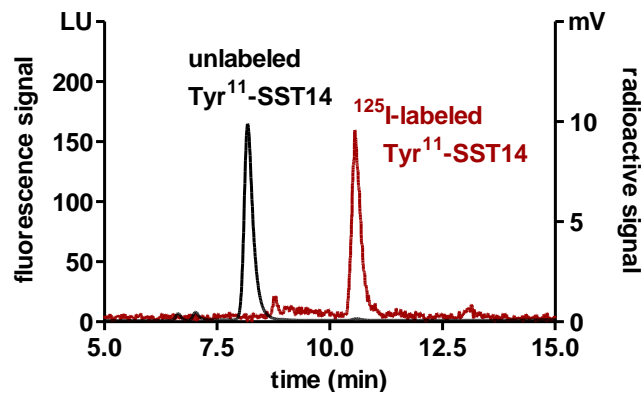


Figure S10 | Chromatographic purification of radioiodinated somatostatin-14. Tyr¹¹-somatostatin-14 (SST14) was radioactively labeled with iodine-125 and purified from unlabeled peptide by HPLC. Chromatogram showing peptide peaks as recorded by fluorescence detector (black line, ex=280 nm, em=340 nm) and radioactive detector (red line).